

44

Synthesis and Reactivity of Copper(I) and Iron(II) Carboxylate-Bridged Dimetallic Complexes

by

Daniel D. LeCloux

B.S., University of Minnesota- Twin Cities (1992)

SUBMITTED TO THE DEPARTMENT OF CHEMISTRY IN PARTIAL
FULFILLMENT OF THE REQUIREMENTS FOR THE DEGREE OF

DOCTOR OF PHILOSOPHY IN CHEMISTRY
AT THE
MASSACHUSETTS INSTITUTE OF TECHNOLOGY

February 1998

© Massachusetts Institute of Technology, 1998

All rights reserved

Signature of Author: _____

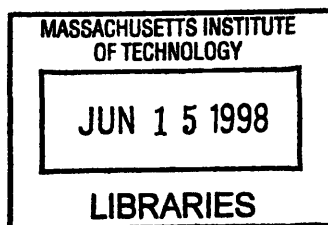
Department of Chemistry
February 11, 1998

Certified by: _____

Stephen J. Lippard
Thesis Supervisor

Accepted by: _____

Dietmar Seyferth
Chairman, Departmental Committee on Graduate Studies



Science

This doctoral thesis has been examined by a Committee of the Department of Chemistry as follows: —

Christopher C. Cummins
Professor of Chemistry
Committee Chairman

Stephen J. Lippard
Arthur Amos Noyes Chair and Professor of Chemistry
Thesis Supervisor

Daniel G. Nocera
Professor of Chemistry

Synthesis, Characterization and Reactivity of Copper(I) and Iron(II) Bis(carboxylate)-Bridged Complexes

by

Daniel D. LeCloux

Submitted to the Department of Chemistry on February 11, 1998, in partial fulfillment of the requirements for the Degree of Doctor of Philosophy.

Abstract

Chapter 1. Synthesis and Characterization of a Novel Class of Dicopper(I) Bis(carboxylate)-Bridged Complexes

The syntheses, spectroscopic properties, crystal and molecular structures, and bonding of several dicopper(I) bis(carboxylate)-bridged complexes are described in which the bridging dicarboxylate ligand is the dianion of *m*-xylylenediamine bis(Kemp's triacid imide) (H₂XDK, **1**). A sterically demanding benzyl derivative of H₂XDK was prepared, H₂BXDK (**6**). Reaction of these two ligands as well as the propyl analog, H₂PXDK (**2**), with thallium ethoxide provided dithallium salts Tl₂L (L = XDK, **7**; PXDK, **8**; and BXDK, **9**). Reaction of **7**, **8**, or **9** with excess CuBr(Me₂S) in CH₂Cl₂/MeCN afforded dinuclear acetonitrile adducts [Cu₂L(MeCN)] (L = XDK, **10**; PXDK, **11**; and BXDK, **12**) in high yield and multigram quantities. The coordination chemistry of the Cu₂(XDK) platform was explored with a range of ancillary ligands. Treatment of **10**, **11**, or **12** with an excess of the specified neutral donor ligand provided complexes [Cu₂(XDK)(PPh₃)₂] (**13**), [Cu₂(XDK)(2,6-Me₂PhNC)₃] (**14a**), [Cu₂(XDK)(μ-2,6-Me₂PhNC)(2,6-Me₂PhNC)₂] (**14b**), [Cu₂(XDK)(NB)₂] (**15**, NB = norbornene), [Cu₂(XDK)(tmeda)] (**17**), [Cu₂(PXDK)(tmeda)] (**18**), [Cu₂(BXDK)(tmeda)] (**19**), and [Cu(4,4'-Me₂bpy)₂][Cu(XDK)] (**20**). Reaction of **10** with an excess of cyclohexene resulted in the loss of the acetonitrile ligand, affording the parent unsubstituted complex [Cu₂(XDK)] (**16**). Attempts to prepare anionic carbon-bridged dicopper(I) complexes with alkyl or aryl lithium compounds or cyanide reagents resulted instead in extraction of one of the Cu(I) ions, affording (Et₄N)[Cu(PXDK)] (**21**) and [CuLi(XDK)(THF)₂] (**22**). Crystallographic chemical analysis of the complexes revealed linear two-coordinate, trigonal three-coordinate, and pseudotetrahedral four-coordinate copper(I), depending upon the composition, and variable degrees of Cu-Cu bonding (d_{Cu-Cu} range, 2.5697(8)-3.4211(6) Å).

Chapter 2. Synthesis and Characterization of Cu(I)-Cu(II) Mixed-Valence and Cu(I)-M(II) Heterodimetallic Bis(carboxylate-bridged) Complexes: Structural, Electrochemical, and Spectroscopic Investigations

The synthesis, spectroscopic, electrochemical, and structural properties of a series of Cu(I)Cu(II) bis(carboxylate-bridged) complexes are described, as well as

related investigations with Cu(I)M(II) (M = Fe and Zn) analogs, utilizing the dianionic *m*-xylylenediamine bis(Kemp's triacid imide) ligand system. Treatment of previously reported [Cu₂(XDK)(MeCN)] (1) or [Cu₂(PXDK)(MeCN)] (2, PXDK = the propyl derivative of XDK) with one equivalent of silver(I) triflate, trifluoroacetate, or tetrafluoroborate in THF afforded mixed valence complexes [Cu₂L(μ-X)(THF)₂] (X = triflate, L = XDK, 4, or PXDK, 5; X = trifluoroacetate and L = XDK, 6); or [Cu₂L(THF)₄]X (X = tetrafluoroborate, L = XDK, 7, or PXDK, 8). Complex 8 was also prepared from equimolar (Et₄N)[Cu(PXDK)] (3) and copper(II) triflate. Solid state structural investigations on 4, 6, and 8 revealed symmetric square pyramidal coordination environments about each copper atom and short Cu–Cu distances ranging from 2.3988(8)-2.4246(12) Å, features which taken together imply significant metal-metal bonding character. The nature of the Cu–Cu bonding in this series of complexes was further interrogated by (a) comparative structural and ligand exchange studies with mixed-metal analogs [CuZn(PXDK)(OTf)(THF)₂(H₂O)] (9), [CuFe(PXDK)(OTf)(NB)MeCN]₂ (10a, NB = norbornene), and CuZn(PXDK)(OTf)(NB)(H₂O) (11), all of which exhibited longer metal–metal distances ranging from 3.294(2)-3.732(2) Å and monodentate, terminal triflate ligation; (b) by variable temperature and field EPR studies, which showed that complexes 4-8 possess a fully delocalized electronic structure in the solid state and solution down to liquid helium temperatures; and (c) by molecular orbital calculations on simplified models of 4-8, which revealed a Cu–Cu bonding interaction in the SHOMO and SOMO, comprised mainly of σ-type overlap between the d_{x²-y²} orbitals. In addition, complex 4 was shown by cyclic voltammetry to under go a chemically reversible and electrochemically quasireversible one-electron reduction that is markedly positive for a Cu(I)Cu(II) complex with an all-oxygen, dianionic donor set. Overall, we provide definitive evidence that, utilizing the XDK scaffold, an unusual series of class III mixed-valence dicopper complexes has been accessed. These studies should aid in understanding an electronically similar Cu–Cu bonded system at the biological Cu_A site.

Chapter 3. Preparation of Sterically Hindered Diiron(II) Tetracarboxylate Complexes, and Their Reactivity Toward Dioxygen

A family of diferric peroxo-bridged complexes has been prepared which matches exactly the combination of carboxylate and imidazole donors of the H_{peroxo} intermediate in sMMO. A variety of methods including UV-Vis, EPR, Resonance Raman, and Mössbauer spectroscopies have been employed to elucidate their structures. These adducts have inequivalent iron coordination environments, a feature which is attributed either to an asymmetric peroxide bridge, a disproportionate arrangement of the ancillary carboxylate and nitrogen donor ligands about each iron center, or a combination of the two. Kinetic studies revealed that the rate of peroxo formation is first order in diiron(II) complex and O₂, implicating a rate-determining bimolecular collision between the reaction components. Moreover, the rate of peroxo formation tracks inversely with the steric

demands of the carboxylate substituents, implying that a carboxylate shift is associated with the rate-determining step. The oxygenation rate is affected much more dramatically by the basicity of the N-donor ligand, however, with a difference of $>10^5 \text{ s}^{-1}$ noted for the pseudo-first-order rate constants with 1-alkylimidazole versus pyridine ligation.

Chapter 4. Biomimetic Oxidation Studies With Discrete Diiron(III) Bis(carboxylate)-Bridged Peroxo Complexes: Toward Functional Models of Oxygen Intermediates of Soluble Methane Monooxygenase

The reactivity properties of two diiron(III) peroxo complexes have been fully elucidated. These adducts behave as nucleophilic/basic peroxides, exhibiting no propensity to serve as oxygen atom donors for even potent acceptors such as triphenylphosphine. The 1-butylimidazole ligands in **1** enhance the nucleophilicity/basicity of the peroxo compared to the pyridine analog, probably because the former ligand is a superior σ -donor. This feature imparts more electron density to the iron centers, which in turn is transmitted to the peroxo ligand. Thermolysis of the peroxo adducts in a variety of media results in solvent oxidation, providing ketone and alcohol products in modest yield based on the complex. A detailed analysis of cyclopentane oxidation provided evidence for a radical chain autoxidation mechanism, a reactivity manifold which does not mimic the hydrocarbon oxidation chemistry of sMMO.

Thesis Supervisor: Stephen J. Lippard

Title: Arthur Amos Noyes Professor of Chemistry

This thesis is dedicated to my family for all your love, support and patience,
and in memory of my grandfather, Roland C. LeCloux.

Acknowledgments

I write this section of my thesis with the utmost pleasure, not only because I have saved it for last, but more importantly, it also gives me the opportunity to thank all those that have helped to make my experience at MIT so professionally and personally rewarding. First and foremost I would like to thank my advisor, Steve Lippard, for giving me virtually complete freedom to develop my research projects, while constantly instilling in me the fundamentals of scientific thinking, writing, and presentation. Former Lippard group members have reminded me how much I will value having acquired these skills once I pursue an independent career. I must say that I came to appreciate all of them when writing the thesis, and I know they will serve me well in the future, whatever that may hold.

I also must acknowledge my undergraduate advisor, William B. Tolman, at the University of Minnesota-Twin Cities. I first met Bill when taking his introductory organic chemistry course as a junior. At the time I was very committed to going to medical school, but I had enjoyed the subject immensely and wanted to obtain some practical lab experience. He enthusiastically agreed to allow me to work in his lab, and over the next two years helped to instill in me a love for chemistry which I will never relinquish. Needless to say the thought of medical school soon thereafter became a distant memory. Bill continues to provide me with much practical advice concerning all facets of my career, and he is a great friend.

There seems to be a countless number of colleagues that I need to thank for helping me professionally over the past five years. When I first arrived, fellow Subgroup 5 members Linda Doerrer, Joanne Yun, Tomoaki Tanase, and Jackie Aho helped get me started in lab. Laura Pence taught an anxious and often times overbearing young graduate student the basics of X-ray crystallography; her knowledge and patience are much appreciated. Although I never worked with him directly, Andrew Feig was always willing to answer my questions and to engage in spirited scientific debates, both of which are necessary for building the enthusiasm and confidence of a young student.

Many helped to bring together the stories described in these thesis chapters. Mike Scott and Peter Fuhrmann were always there to aid with difficult X-ray structures. Dave Coufal kindly ran liquid helium EPR samples for me, since I was always a tad too lazy to learn how to use the instrument. Maria Bautista and Linda Doerrer taught me some of the finer points of cyclic voltammetry and high vacuum line techniques. Marc Johnson and Mike Fickes of the Cummins group helped with

the MO calculations, and Mike also ran several high field, variable temperature NMR experiments for me. Kathy Franz acquired SQUID magnetic data on the copper complexes. Amy Barrios helped with many Resonance Raman studies. Jack Mizoguchi and Dongwhan Lee devoted many hours to my Mössbauer samples over at Northeastern. Ann Valentine cheerfully taught me the joys of low-temperature, stopped-flow UV-vis spectroscopy and GC-MS. Dietrich Steinhuebel always provided an extra steady pair of hands for preparing thermally unstable peroxo samples. Finally, I thank Mike Fickes, Ann Valentine, Dietrich Steinhuebel, and Justin Du Bois for a countless number of enlightening scientific discussions. I have learned much from each one of them concerning my research and chemistry in general.

Of course my personal experiences at MIT are inextricably tied to professional ones, so there will be quite a bit of repetition here. As I have preached over the years to just about anyone who will listen to me, I firmly believe single greatest attribute of MIT is one's colleagues, as they must be one of the brightest collections of people anywhere, and many in the chemistry department have become my very close friends. First I would like to thank the entire Lippard group. You are a wonderfully bright, enthusiastic, and fun-loving bunch that always seemed to put up with my intense, although good-hearted, demeanor. For this and all of the fun we had outside of the lab, I am very grateful. In addition, I must give a special thank you to Ann Valentine for being a great friend over our years at MIT, and in particular for helping me get through the thesis writing process. Everyone needs to be able to share this equally euphoric and frustrating experience with someone, lest go insane, and you certainly provided that for me. Finally, there are "the guys", as Jonas Peters has dubbed us, which includes Jonas, Mike Fickes, Robert Baumann, and Dietrich Steinhuebel. I must also throw Seble Wagaw in there as a ceremonial member, since she too has partaken in our escapades with much enthusiasm. I am confident that our paths will cross again on many occasions in the future, yet I will greatly miss our time at MIT.

Table of Contents

Abstract.....	3
Dedication.....	6
Acknowledgements.....	7
Table of Contents	9
List of Tables.....	12
List of Schemes.....	14
List of Figures.....	15
Chapter I. Synthesis and Characterization of a Novel Class of Dicopper(I) Bis(carboxylate)-Bridged Complexes	19
Introduction.....	20
Experimental Section.....	22
General Considerations.....	22
Physical Measurements.....	22
Synthesis.....	23
Collection and Reduction of X-ray Data.....	33
Results and Discussion.....	35
Ligand Synthesis	35
Preparation and Reactivity of Dicopper(I) Bis(carboxylate)- Bridged Complexes.....	37
Conclusions.....	46
Acknowledgement	46
References and Notes.....	47
Chapter II. Synthesis and Characterization of Cu(I)-Cu(II) Mixed- Valence and Cu(I)-M(II) Heterodimetallic Bis(carboxylate)- bridged) Complexes: Structural, Electrochemical, and Spectroscopic Investigations.....	86
Introduction.....	87
Experimental Section.....	90
General Considerations.....	90
Physical Measurements.....	91
Extended Hückel Molecular Orbital Calculations.....	92
Preparation of Compounds	92
Collection and Reduction of X-ray Data.....	95
Results and Discussion.....	96

Preparation and Structural Characterization of Mixed-Valence Complexes	97
Preparation and Structural Characterization of Heterodimetallic Complexes.....	100
Electrochemical Properties of the Mixed-Valence Complexes	103
EPR Studies	106
Molecular Orbital Calculations.....	108
Conclusions.....	110
Acknowledgement	111
References and Notes.....	112
Chapter III. Modeling the H_{peroxo} Intermediate of Soluble Methane Monooxygenase: Preparation of Sterically Hindered Diiron(II) Tetracarboxylate Complexes, and Their Reactivity Toward Dioxygen.....	159
Introduction.....	160
Experimental Section.....	165
General Considerations.....	165
Synthesis.....	166
Collection and Reduction of X-ray Data.....	170
Physical Measurements.....	171
Results and Discussion.....	175
Preparation and Characterization of Complexes	175
Reactions of the Diferrous Complexes Toward Dioxygen.....	178
EPR and ¹ H NMR Studies.....	181
Resonance Raman Studies of the Peroxo Adducts.....	181
Mössbauer Spectroscopy	183
Kinetic Studies of the Reaction of the Diferrous Complexes With O ₂ and a Proposed Mechanism for Peroxo Formation.....	185
Conclusions.....	188
Acknowledgement	188
References and Notes.....	190
Chapter IV. The Reactivity of Well Defined Diiron(III) Peroxo Complexes Towards Substrates: Addition to Electrophiles and Hydrocarbon Oxidation	244

Introduction.....	245
Experimental Section.....	246
General Considerations.....	246
Physical Measurements.....	247
Synthetic Methods.....	248
Intermolecular Kinetic Isotope Measurements	250
Results and Discussion.....	250
Reactions of Peroxide Complexes 1 and 2 With Various Reagents at -77 °C.....	250
Thermolysis Reactions Leading to Solvent Oxidation.....	254
Conclusions.....	260
References and Notes.....	261
Biographical Note.....	284

List of Tables

Table 1.1. Summary of X-ray Crystallographic Data	51
Table 1.2. Selected Bond Distance and Angles.....	53
Table 1.3. Atomic Coordinates and Equivalent Isotropic Thermal Parameters for H ₂ (BXDK) (6).....	56
Table 1.4. Atomic Coordinates and Equivalent Isotropic Thermal Parameters for [Cu ₂ (XDK)(MeCN)] (10)	58
Table 1.5. Atomic Coordinates and Equivalent Isotropic Thermal Parameters for [Cu ₂ (XDK)(PPh ₃) ₂] (13).....	60
Table 1.6. Atomic Coordinates and Equivalent Isotropic Thermal Parameters for [Cu ₂ (XDK)(2,6-Me ₂ C ₆ H ₃ NC) ₃] (14a)	63
Table 1.7. Atomic Coordinates and Equivalent Isotropic Thermal Parameters for [Cu ₂ (XDK) (μ-2,6-Me ₂ C ₆ H ₃ NC)(2,6- Me ₂ C ₆ H ₃ NC) ₂] (14b)	65
Table 1.8. Atomic Coordinates and Equivalent Isotropic Thermal Parameters for [Cu ₂ (XDK)(NB) ₂] (15).....	67
Table 1.9. Atomic Coordinates and Equivalent Isotropic Thermal Parameters for [Cu ₂ (XDK)] ₂ (16).....	69
Table 1.10. Atomic Coordinates and Equivalent Isotropic Thermal Parameters for [Cu ₂ (XDK)(tmeda)] (17).....	72
Table 1.11. Atomic Coordinates and Equivalent Isotropic Thermal Parameters for (Et ₄ N)[Cu(XDK)] (21).....	74
Table 1.12. Atomic Coordinates and Equivalent Isotropic Thermal Parameters for [CuLi(XDK)(THF) ₂] (22)	77
Table 2.1. Summary of pertinent spectroscopic and structural data on known class III mixed-valence copper systems.....	117
Table 2.2. Summary of X-ray Crystallographic Data	118
Table 2.3. Selected Bond Distances and Angles	119
Table 2.4. Atomic coordinates (x 10 ⁴) and equivalent isotropic displacement parameters (A ² x 10 ³) for 4	121
Table 2.5. Atomic coordinates (x 10 ⁴) and equivalent isotropic displacement parameters (A ² x 10 ³) for 6	123
Table 2.6. Atomic coordinates (x 10 ⁴) and equivalent isotropic displacement parameters (A ² x 10 ³) for 8	125
Table 2.7. Atomic coordinates (x 10 ⁴) and equivalent isotropic displacement parameters (A ² x 10 ³) for 9	127

Table 2.8. Atomic coordinates ($\times 10^4$) and equivalent isotropic displacement parameters ($\text{Å}^2 \times 10^3$) for 11	129
Table 2.9. Selected electrochemical data for a range of copper redox couples.....	131
Table 2.10. EPR g values and copper hyperfine coupling constants for 7	132
Table 3.1. Summary of data acquired for selected RR and sMMO model complexes.....	194
Table 3.2. Summary of X-ray Crystallographic Data	195
Table 3.3. Selected Bond Distances and Angles	196
Table 3.4. Atomic coordinates ($\times 10^4$) and equivalent isotropic displacement parameters ($\text{Å}^2 \times 10^3$) for 6	199
Table 3.5. Atomic coordinates ($\times 10^4$) and equivalent isotropic displacement parameters ($\text{Å}^2 \times 10^3$) for 7	202
Table 3.6. Atomic coordinates ($\times 10^4$) and equivalent isotropic displacement parameters ($\text{Å}^2 \times 10^3$) for 12	205
Table 3.7. Atomic coordinates ($\times 10^4$) and equivalent isotropic displacement parameters ($\text{Å}^2 \times 10^3$) for 13	208
Table 3.8. Atomic coordinates ($\times 10^4$) and equivalent isotropic displacement parameters ($\text{Å}^2 \times 10^3$) for 16	212
Table 3.9. Effect of ligand steric and electronic properties and solvent on stable peroxo adduct formation.....	215
Table 3.10. Manometric studies of the dioxygen uptake for 13 , 16 , and $[\text{Fe}(\text{Tp}^{3,5\text{-iPr}_2})(\text{O}_2\text{CH}_2\text{Ph})]$ vs. equimolar Vaska's complex.....	216
Table 3.11. A summary of resonance Raman data obtained for the peroxo adducts.....	217
Table 3.12. Mössbauer parameters for the peroxo adducts.....	218
Table 3.13. Summary of kinetic data for the reaction of the diferrous complexes with oxygen at $-77\text{ }^\circ\text{C}$	219
Table 4.1. A summary of reagents and solvents used for the stoichiometric reactions.....	264
Table 4.2. A survey of solvent oxidation reactions mediated by peroxo 1	265
Table 4.3. Cyclopentane oxidation reactions carried out with peroxo 1	266

List of Schemes

Scheme 1.1.....	79
Scheme 1.2.....	80
Scheme 2.1.....	133
Scheme 3.1.....	220
Scheme 3.2.....	221
Scheme 4.1.....	267

List of Figures

Figure 1.1. ORTEP (50% thermal ellipsoids) and space-filling diagrams of H ₂ BXDK (6).....	81
Figure 1.2. ORTEP diagram of [Cu ₂ (XDK)(MeCN)] (10) with 50% thermal ellipsoids.....	82
Figure 1.3. ORTEP diagrams with 50% thermal ellipsoids for (clockwise from top left) [Cu ₂ (XDK)(PPh ₃) ₂] (13), [Cu ₂ (XDK)(2,6-Me ₂ PhNC) ₃] (14a), [Cu ₂ (XDK)(μ-2,6-Me ₂ PhNC)(2,6-Me ₂ PhNC) ₂] (14b), and [Cu ₂ (XDK)(NB) ₂] (15).....	83
Figure 1.4. ORTEP diagrams with 50% thermal ellipsoids for (clockwise from top left) [Cu ₂ (XDK)] ₂ (16), [Cu ₂ (XDK)(tmeda)] (17), (Et ₄ N)[Cu(PXDK)] (21), and [CuLi(XDK)(THF) ₂] (22).....	84
Figure 2.1. Electronic absorption spectrum of [Cu ₂ (XDK)(μ-OTf)(THF) ₂] (4), 0.74 mM in THF.....	134
Figure 2.2. Electronic absorption spectrum of [Cu ₂ (XDK)(μ-O ₂ CCF ₃)(THF) ₂] (6), 0.74 mM in THF.....	135
Figure 2.3. Electronic absorption spectrum of [Cu ₂ (XDK)(THF) ₄](BF ₄) (7), 0.47 mM in THF.....	136
Figure 2.4. Conductivity plots for [Cu ₂ (XDK)(μ-OTf)(THF) ₂] (4) and Bu ₄ NPF ₆ in THF at 296 K.....	137
Figure 2.5. Conductivity plots for [Cu ₂ (XDK)(THF) ₄](BF ₄) (7) in THF and Bu ₄ NPF ₆ in THF at 296 K.....	138
Figure 2.6. ORTEP diagram of [Cu ₂ (XDK)(μ-OTf)(THF) ₂] (4) with 50% thermal ellipsoids.....	139
Figure 2.7. ORTEP diagram of [Cu ₂ (XDK)(μ-O ₂ CCF ₃)(THF) ₂] (6) with 50% thermal ellipsoids.....	140
Figure 2.8. ORTEP diagram of [Cu ₂ (PXDK)(THF) ₄](BF ₄) (8) with 50% thermal ellipsoids.....	141
Figure 2.9. (Top) Stacked IR spectra of 10a and 10b in the carboxylate-ν _{CO} and the triflate-ν _{SO} regions.....	142
Figure 2.10. ORTEP diagram of [CuZn(PXDK)(OTf)(THF) ₂ (H ₂ O)] (9) with 50% thermal ellipsoids.....	143
Figure 2.11. ORTEP diagrams of [CuZn(PXDK)(OTf)(NB)(H ₂ O)] (11) with 50% thermal ellipsoids.....	144
Figure 2.12. Cyclic voltammogram of 10 mM [Cu ₂ (XDK)] in THF.....	145
Figure 2.13. Plot of anodic and cathodic currents versus (scan speed) ^{1/2} for [Cu ₂ (XDK)].....	146
Figure 2.14. Cyclic voltammogram of 10 mM [Cu ₂ (XDK)(THF) ₄](BF ₄) (7) in THF.....	147

Figure 2.15. Plot of anodic and cathodic currents versus (scan speed) ^{1/2} for [Cu ₂ (XDK)(THF) ₄](BF ₄) (7).....	148
Figure 2.16. Cyclic voltammogram of 10 mM [Cu ₂ (XDK)(μ-OTf)(THF) ₂] (4) in THF.....	149
Figure 2.17. Plot of anodic and cathodic currents versus (scan speed) ^{1/2} for [Cu ₂ (XDK)(μ-OTf)(THF) ₂] (4).....	150
Figure 2.18. Cyclic voltammogram of 10 mM [Cu ₂ (XDK)(μ-OTf)(THF) ₂] (4) in THF.....	151
Figure 2.19. Cyclic voltammogram of 10 mM [Cu ₂ (XDK)(μ-O ₂ CCF ₃)(THF) ₂] (4) in THF.....	152
Figure 2.20. X-band EPR spectra of 1 mM [Cu ₂ (XDK)(THF) ₄](BF ₄) (7) as a frozen solution at 77 and 9 K, along with a simulation.....	153
Figure 2.21. X-band EPR spectra of [Cu ₂ (XDK)(THF) ₄](BF ₄) (7) as a powdered solid at 296, 77, and 9 K, along with a simulation.....	154
Figure 2.22. Q-band EPR spectrum of [Cu ₂ (XDK)(THF) ₄](BF ₄) (7)	155
Figure 2.23. Contour plots derived from extended Hückel calculations for the SOMO of [Cu ₂ (μ-O ₂ CCH ₃) ₂ (OMe ₂) ₄].....	156
Figure 2.24. Contour plot derived from extended Hückel calculations for the SHOMO of [Cu ₂ (μ-O ₂ CCH ₃) ₂ (OMe ₂) ₄].....	157
Figure 2.25. Fragment molecular orbital diagram and a Walsh diagram for [Cu ₂ (OH) ₂ (OH ₂) ₂ (OMe ₂) ₄].....	158
Figure 3.1. Chemdraw representations of the active site structures of: (A) reduced R ₂ , (B) reduced MMOH (H _{red}), and (C) oxidized MMOH (H _{ox}).....	222
Figure 3.2. A summary of the ribonucleotide reductase and sMMO catalytic cycles.....	223
Figure 3.3. ORTEP diagram of [Fe ₂ (BXDK)(μ-O ₂ Ctert-Bu)(O ₂ Ctert-Bu)(py) ₂] (6) with 50% thermal ellipsoids.....	224
Figure 3.4. Space-filling models of [Fe ₂ (PXDK)(O ₂ Ct-Bu)(μ-O ₂ Ct-Bu)(Me-Im) ₂] and [Fe ₂ (BXDK)(O ₂ Ct-Bu)(μ-O ₂ Ct-Bu)(py) ₂] (6).....	225
Figure 3.5. ORTEP diagram of [Fe ₂ (XDK)(μ-O ₂ CPhCy)(O ₂ CPhCy)(py) ₂] (7) with 50% thermal ellipsoids.....	226
Figure 3.6. Space-filling representation of [Fe ₂ (XDK)(μ-O ₂ CPhCy)(O ₂ CPhCy)(py) ₂] (7)	227
Figure 3.7. ORTEP diagram of [Fe ₂ (XDK)(μ-O ₂ CPhCy)(O ₂ CPhCy)(py) ₂] (7) with 50% thermal ellipsoids.....	228

Figure 3.8. ORTEP diagram of $[\text{Fe}_2(\text{BXDK})(\mu\text{-O}_2\text{CPh})(\text{O}_2\text{CPh})(\text{py})_2]$ (12) with 50% thermal ellipsoids.....	229
Figure 3.9. ORTEP diagram of $[\text{Fe}_2(\text{BXDK})(\mu\text{-O}_2\text{CPhCy})(\text{O}_2\text{CPhCy})(\text{py})_2]$ (13) with 50% thermal ellipsoids.....	230
Figure 3.10. ORTEP diagram of $[\text{Fe}_2(\text{PXDK})(\mu\text{-O}_2\text{PhCy})(\text{O}_2\text{PhCy})(\text{Bu-Im})_2]$ (16) with 50% thermal ellipsoids.....	231
Figure 3.11. A schematic illustration of the effect of ligand substituent steric repulsion on the orientation of the bridging ancillary carboxylate.....	232
Figure 3.12. Representative UV-Vis spectra for the reaction of diferrous complexes 6-15 with O_2 at $-80\text{ }^\circ\text{C}$	233
Figure 3.13. Resonance Raman spectra obtained with 647 nm excitation on fluid toluene solutions ($-80\text{ }^\circ\text{C}$) of: (A) $[\text{Fe}_2(^{16}\text{O}_2)(\text{PXDK})(\text{O}_2\text{CPhCy})_2(\text{Bu-Im})_2]$ (16- $^{16}\text{O}_2$), (B) $[\text{Fe}_2(^{18}\text{O}_2)(\text{PXDK})(\text{O}_2\text{CPhCy})_2(\text{Bu-Im})_2]$ (16- $^{18}\text{O}_2$), and toluene	234
Figure 3.14. Solvent subtracted resonance Raman spectra.	235
Figure 3.15. (A) Resonance Raman spectrum obtained with 647 nm excitation on a fluid toluene solution ($-80\text{ }^\circ\text{C}$) of $[\text{Fe}_2(\text{O}_2)(\text{PXDK})(\text{O}_2\text{CPhCy})_2(\text{Bu-Im})_2]$ (16- O_2), prepared from 16 and a 1:2:1 mixture of $^{16}\text{O}_2$, $^{16}\text{O}^{18}\text{O}$, and $^{18}\text{O}_2$. (B) Toluene solvent background subtracted from the spectrum in A	236
Figure 3.16. Mössbauer spectra of $[\text{Fe}_2(\text{BXDK})(\mu\text{-O}_2\text{CPhCy})(\text{O}_2\text{CPhCy})(\text{py})_2]$ (13)	237
Figure 3.17. Mössbauer spectrum of $[\text{Fe}_2(\text{XDK})(\mu\text{-O}_2\text{CPhCy})(\text{O}_2\text{CPhCy})(\text{Me-Im})_2]$ (15).....	238
Figure 3.18. Mössbauer spectrum of 13- O_2	239
Figure 3.19. Kinetic data for the reaction of $[\text{Fe}_2(\text{BXDK})(\mu\text{-O}_2\text{Ct-Bu})(\text{O}_2\text{Ct-Bu})(\text{py})_2]$ (6) with O_2 in THF at $-77\text{ }^\circ\text{C}$	240
Figure 3.20. Kinetic data for the reaction of $[\text{Fe}_2(\text{XDK})(\mu\text{-O}_2\text{CPhCy})(\text{O}_2\text{CPhCy})(\text{py})_2]$ (7) with O_2 in THF at $-77\text{ }^\circ\text{C}$	241
Figure 3.21. Kinetic data for the reaction of $[\text{Fe}_2(\text{BXDK})(\mu\text{-O}_2\text{CPhCy})(\text{O}_2\text{CPhCy})(\text{py})_2]$ (13) with O_2 in THF at $-77\text{ }^\circ\text{C}$	242
Figure 3.22. Kinetic data for the reaction of $[\text{Fe}_2(\text{BXDK})(\mu\text{-O}_2\text{CAr})(\text{O}_2\text{CAr})(\text{py})_2]$ (14) with O_2 in THF at $-77\text{ }^\circ\text{C}$	243
Figure 4.1. Electronic absorption spectrum of 1 in THF at $-77\text{ }^\circ\text{C}$ (0.98 mM) and with 1.0 equiv of 2,4-di- <i>t</i> -butylphenol added.....	268

Figure 4.2. Electronic absorption spectrum of 2 in CH ₂ Cl ₂ at -77 °C (0.82 mM) and with 1.2 equiv of 2,4-di- <i>t</i> -butylphenol added.....	269
Figure 4.3. Electronic absorption spectrum of 1 in THF at -77 °C (0.90 mM) and with 1.2 equiv of phenol added.....	270
Figure 4.4. Electronic absorption spectrum of 1 in THF at -77 °C (0.63 mM) and with 1.1 equiv of pentafluorophenol added.....	271
Figure 4.5. Resonance Raman spectra of 1- ¹⁶ O ₂ and 1- ¹⁶ O ₂ + 1.1 equiv of 2,4-di- <i>tert</i> -butylphenol.....	272
Figure 4.6. Resonance Raman spectra of 1- ¹⁸ O ₂) and (B) 1- ¹⁸ O ₂ + 1.1 equiv of 2,4-di- <i>tert</i> -butylphenol.....	273
Figure 4.7. Electronic absorption spectrum of 1 in cyclopentane at -77 °C (0.84 mM) and with 2 equiv of 2,4,6-tri- <i>tert</i> -butylphenol added.....	274
Figure 4.8. Electronic absorption spectrum of 1 in toluene at -77 °C (0.86 mM), and after 1.1 equiv of HO ₂ CPhCy was added.....	275
Figure 4.9. Electronic absorption spectrum of 1 in Et ₂ O at -77 °C (0.98 mM) and after CO ₂ addition.....	276
Figure 4.10. Electronic absorption spectrum of 2 in CH ₂ Cl ₂ at -77 °C (0.82 mM) in the presence of excess CO ₂	277
Figure 4.11. Electronic absorption spectrum of 1 in Et ₂ O at -77 °C (0.79 mM), and in the presence of 1.1 equiv of Cp ₂ *Fe.....	278
Figure 4.12. Electronic absorption spectrum of 1 in THF at -77 °C (0.79 mM), and after 1.1 equiv of Cp ₂ Co was added.....	279
Figure 4.13. A representative GC chromatogram for cyclopentane oxidation reactions with peroxo 1.....	280
Figure 4.14. A representative GC chromatogram for THF oxidation reactions with peroxo 1.....	281
Figure 4.15. A GC-MS chromatogram for a competitive deuterium isotope effect measurement for THF oxidation by peroxo 1.....	282
Figure 4.16. A GC-MS chromatogram for a competitive deuterium isotope effect measurement for toluene oxidation by peroxo 1.....	283

Chapter I

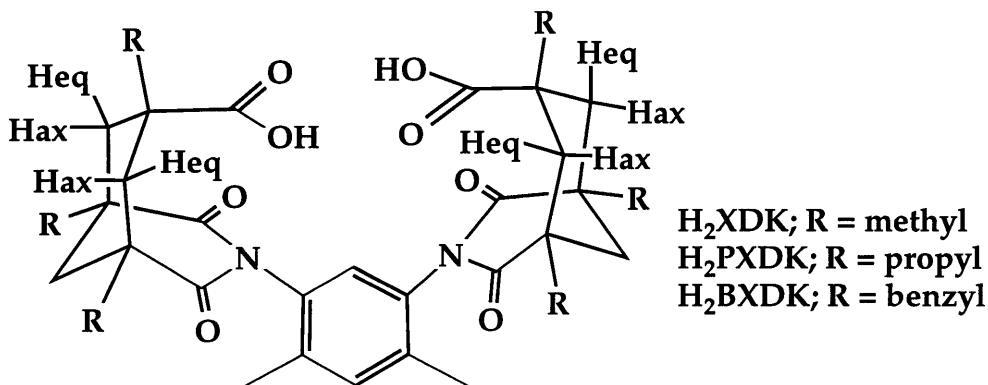
Synthesis and Characterization of a Novel Class of Dicopper(I) Bis(carboxylate)- Bridged Complexes^{1,2}

Introduction

The preparation of multinuclear complexes of transition metal ions in low oxidation states for the reductive activation of small molecules is of fundamental and practical importance in bioinorganic chemistry. Many metalloenzymes utilize this strategy to achieve atom transfer reactions which pose a formidable challenge to the synthetic chemist. For example, soluble methane monooxygenase (sMMO) contains a diiron active site and catalyzes the reaction of dioxygen with methane to produce methanol and water.³⁻⁵ Particulate pMMO carries out the same reaction with a tricopper,⁶⁻⁹ or possibly a copper-iron,¹⁰ active site. Dopamine β -monooxygenase contains a dicopper active site and catalyzes the O₂-promoted hydroxylation of a benzylic CH bond in phenethylamine derivatives.^{11,12} Tyrosinase utilizes a dinuclear copper active site to catalyze the orthohydroxylation of monophenols and the oxidation of catechol derivatives to orthoquinones.⁶ Inspired by these natural successes, we seek to prepare functional model complexes of some of the forgoing enzymes to gain a general mechanistic understanding of how two or more metal ions can work in concert to activate dioxygen reductively and harness its oxidizing equivalents for oxygen atom transfer reactions to a suitable substrate molecule. The specific reactions of interest are the hydroxylation of aliphatic, aromatic, and olefinic hydrocarbons where the oxygen atom equivalent is derived from O₂. Because we are primarily concerned with exploring the basic *principles* of multimetal-mediated oxidation reactions, our choice of ancillary ligands is not restricted to mimic the active site residues in any particular enzyme. The target complexes for examining these reactions are required only to have discrete dinuclear units with sufficient kinetic stability toward metal ion rearrangements to avoid thermodynamically viable and catalytically inactive species along an oxidation reaction pathway.

As an initial approach to this objective we have assembled dimetallic complexes with a class of convergent bis(carboxylate) ligands derived from xylene di-

amine Kemp's triacid.¹³⁻²⁰ Its attributes include: (a) the carboxylate functional group, which forms a host of bridged dinuclear complexes having the desired 2-5 Å



metal-metal distance;²¹ (b) a pair of preorganized and conformationally rigid carboxylates, which tightly bind two metal ions and resist the formation of higher metal aggregates;¹⁹ and (c) variable substituents (R) peripheral to the metal binding sites, which provide more steric protection than simple carboxylate ligands.

The reduced metal ion pairs of particular interest to us for exploring O-atom transfer chemistry following reductive activation of dioxygen are homo- and heterodimetallic combinations of Cu(I) and Fe(II). Copper²²⁻²⁶ and iron^{3,13,27-29} oxygenases and hydroxylases have been the subject of an enormous body of structural and functional modeling literature. We are particularly interested in the effects of the basic carboxylate ligand environment for stabilizing oxygen intermediates and for inducing oxo transfer reactivity. A program to investigate the diiron(II) chemistry of this bis(carboxylate) ligand system for the functional modeling of sMMO, in particular, is in progress.^{13,14,30}

In the present paper, we report the preparation and characterization of a new class of dicopper(I) bis(carboxylate) complexes carried out as a prelude to an evaluation of their potential to promote hydrocarbon oxidation. The synthesis of a sterically more demanding derivative of H₂XDK,³¹ H₂BXDK, is described. Both of these

ligands as well as H₂PXDK have been used to prepare complexes with Cu(I). The reactivity of the resulting dicopper(I) XDK species with neutral ancillary ligands has been explored to elucidate fully the electronic nature of this platform and to map out its coordination chemistry. Several unprecedented copper(I) carboxylates were obtained. The dicopper(I) complexes of all three carboxylate ligands have been used in O₂ reactivity studies, affording some stable peroxo intermediates at low temperature. These investigations will be described elsewhere.³²

Experimental Section

General Considerations. The H₂XDK (1)³³ and H₂PXDK (2)¹³ ligands were prepared according to literature procedures. All reagents were obtained from commercial sources unless otherwise noted. THF, benzene, toluene, pentane, and Et₂O were distilled from sodium benzophenone ketyl under nitrogen. Dichloromethane and chlorobenzene were distilled from CaH₂ under nitrogen. Acetonitrile was pre-distilled from CaH₂ and then from P₂O₅. The NMR solvents CDCl₃, CD₂Cl₂, and C₆D₆ were degassed, passed through activated basic alumina, and stored over 3 Å molecular sieves prior to use. All other solvents and reagents are commercially available and were used as received. All air sensitive manipulations were carried out either in a nitrogen filled Vacuum Atmospheres drybox or by standard Schlenk line techniques at room temperature unless otherwise noted.

Physical Measurements. NMR spectra were recorded on Bruker AC-250, Varian XL-300, or Varian VXR-500 NMR spectrometers. ¹H and ¹³C{¹H} NMR chemical shifts are reported versus tetramethylsilane and referenced to the residual solvent peak. ³¹P NMR chemical shifts are reported versus external H₃PO₄ (85%). FTIR spectra were recorded on a BioRad FTS-135 FTIR spectrometer, and mass spectra were determined by using a Finnigan 4000 mass spectrometer with 70-eV impact ionization. UV-vis spectra were recorded on a Cary 1E spectrophotometer.

Conductivity measurements were carried out in CH₂Cl₂ at 296 K with a Fisher Scientific conductivity bridge model 9-326 with a platinum black electrode. Elemental analyses were performed by Microlytics, South Deerfield, MA.

Synthesis. Trimethyl-*cis,cis*-1,3,5-tribenzylcyclohexane-1,3,5-tricarboxylate (Benzyl Kemp's Triester, 3). To a mechanically stirred solution of lithium diisopropyl amide (1.5 M in THF, 200 mL, 297 mmol) and toluene (400 mL) at 0 °C under N₂ was added trimethyl-1,3,5-cyclohexyltricarboxylate (24.0 g, 92.9 mmol) in toluene (300 mL) dropwise over 1 h. The mixture was allowed to stir an additional 0.5 h, and then benzyl bromide (35.4 mL, 297 mmol) was added via syringe in one portion. The mixture was warmed to room temperature and then refluxed for 7 h. After this time the reaction was cooled to room temperature and quenched with H₂O (200-300 mL). The organic phase was collected and concentrated in vacuo. The resulting oily residue was taken up in CH₂Cl₂ (200 mL) and extracted with 2 M HCl (2 X 100 mL) and brine (100 mL). The combined organic extracts were dried with MgSO₄, and the volatile components were removed in vacuo. The resulting orange-brown solid was suspended in dry Et₂O (200-300 mL) and then isolated by filtration to yield 3 (>95% pure by ¹H NMR) as a light yellow solid (31.9 g, 65%). Recrystallization from toluene/pentane provided 3 as colorless blocks. ¹H NMR (250 MHz, DMSO, 296 K) δ 7.32-7.20 (9H, m), 7.07 (6H, d, *J* = 6.6 Hz), 3.43 (9H, s), 2.82 (6H, s), 2.41 (3H, d, *J* = 14.1 Hz), 1.46 (3H, d, *J* = 14.1 Hz) ppm; IR (KBr) 3060, 3027, 3000, 2946, 2895, 1738, 1602, 1495, 1451, 1383, 1233, 1206, 1121, 1038, 993, 874, 770, 698, 549 cm⁻¹. High resolution MS (FAB) Calcd for C₃₃H₃₆O₆ (M): *m/e* 528.2512. Found: 528.2505. Anal. Calcd for C₃₃H₃₆O₆: C, 74.98; H, 6.86. Found: C, 75.35; H, 6.85.

***cis,cis*-1,3,5-Tribenzylcyclohexane-1,3,5-tricarboxylic acid (Benzyl Kemp's Triacid, 4).** To a stirred solution of 3 (25.3 g, 47.8 mmol) in EtOH/THF (1:1, 500 mL total volume) was added KOH (63.0 g, 955 mmol) in a minimum amount of H₂O, and the mixture was refluxed for 6 h. The mixture was concentrated in vacuo to a vis-

cous oily solid. It was redissolved in H₂O (300 mL), cooled to 0 °C, and acidified to pH 1 with concentrated HCl. The resulting yellow precipitate was isolated by filtration, washed with H₂O (300-400 mL), and dried in vacuo at 110 °C for 2 h. The powder was then suspended in dry Et₂O and isolated by filtration to yield **4** (>95% pure by ¹H NMR) as a white solid (18.4 g, 79%). Recrystallization from acetone/DMSO/Et₂O afforded **4** as colorless blocks. ¹H NMR (300 MHz, DMSO, 296 K) δ 12.04 (1H, s), 7.29-7.14 (15H, m), 2.86 (6H, s), 2.39 (3H, d, *J* = 14.7 Hz), 1.47 (3H, d, *J* = 13.8 Hz) ppm; IR (KBr) 3010, 2615, 1729, 1698, 1603, 1496, 1457, 1291, 1198, 1127, 1031, 915, 767, 699, 553 cm⁻¹. Anal. Calcd for C₃₄H₄₂O₈S₂ (4·2DMSO): C, 63.53; H, 6.59. Found: C, 63.44; H, 6.54. The 4·2DMSO stoichiometry was determined by X-ray crystallography.

***cis,cis*-1,3,5-Tribenzylcyclohexane-1,3-anhydride-5-acid chloride (Tribenzyl Kemp's Anhydride Acid Chloride, 5)**. This compound was prepared from **4** (22.3 g, 45.8 mmol) and excess SOCl₂ (100 mL) by a procedure analogous to one used for the synthesis of the parent trimethyl derivative³³ to yield **5** (>95% pure by ¹H NMR) as a white solid (22.3 g, 100%). ¹H NMR (250 MHz, CDCl₃, 296 K) δ 7.40-7.25 (10H, m), 7.10-7.03 (5H, m), 3.21 (2H, d, *J* = 13.6 Hz), 2.91-2.84 (4H, m), 2.70 (2H, d, *J* = 14.4 Hz), 1.87 (1H, d, *J* = 12.9 Hz), 1.45 (2H, d, *J* = 14.4 Hz), 1.16 (1H, d, *J* = 13.2 Hz) ppm; IR (KBr) 3062, 3030, 2961, 2928, 1803, 1767, 1604, 1496, 1455, 1445, 1213, 1099, 1057, 1000, 991, 898, 760, 701, 609, 537 cm⁻¹. High resolution MS (FAB) Calcd for C₃₀H₂₇O₄Cl (M): *m/e* 486.1598. Found: 486.1598.

Benzyl Xylene Diamine Kemp's Triacid (H₂BXDK, 6). This compound was prepared from **5** (22.3 g, 45.8 mmol), 1,3-dimethyl-4,6-diaminobenzene (3.27 g, 24.0 mmol), and 4-dimethylaminopyridine (300 mg, 2.40 mmol) by a procedure analogous to that used to prepare H₂XDK (**1**).³³ Recrystallization from MeOH yielded **6** (>95% pure by ¹H NMR) as a white microcrystalline solid (16.6 g, 70%). Recrystallization from CHCl₃/pentane provided **6** as colorless blocks which ap-

peared suitable for X-ray crystallography. ^1H NMR (300 MHz, CDCl_3 , 296 K) δ 7.32-7.28 (4H, m), 7.21-6.95 (27 H, m), 6.54 (1H, s), 3.40 (4H, d, $J = 13.2$ Hz), 2.75 (4H, d, $J = 13.8$ Hz), 2.56 (4H, s), 2.31 (4H, d, $J = 13.5$ Hz), 2.02 (2H, d, $J = 13.0$ Hz), 1.18 (6H, s), 1.03 (4H, d, $J = 14.1$ Hz), 0.89 (2H, d, $J = 13.2$ Hz) ppm; $^{13}\text{C}\{^1\text{H}\}$ NMR (125 mHz, CDCl_3 , 296 K) δ 181.6, 173.7, 136.0, 135.4, 135.0, 133.0, 132.9, 131.2, 130.0, 128.4, 128.0, 127.6, 126.8, 126.2, 50.2, 47.3, 45.0, 44.4, 41.8, 36.9, 16.0 ppm; IR (KBr) 3027, 2955, 2924, 2863, 1795, 1707, 1603, 1495, 1461, 1368, 1326, 1231, 1178, 1031, 934, 744, 700, 585, 517 cm^{-1} . High resolution MS (FAB) Calcd for $\text{C}_{68}\text{H}_{64}\text{N}_2\text{O}_8$ (M): m/e 1036.4663. Found: 1036.4652. Anal. Calcd for $\text{C}_{68}\text{H}_{64}\text{N}_2\text{O}_8$: C, 78.74; H, 6.22; N, 2.70. Found: C, 78.18; H, 6.22; N, 2.67. This sample and others with the BXDK ligand repeatedly analyzed low for carbon, perhaps due to its highly unsaturated composition.

$\text{Tl}_2(\text{XDK})$ (7). To a rapidly stirred suspension of **1** (4.00 g, 6.89 mM) in dry THF (100 mL) under N_2 was added TIOEt (1.0 mL, 14 mM) by syringe. The solution initially clarified and then a white precipitate formed immediately. The mixture was stirred for 4 h, and the volatile components were removed in vacuo, affording **7** (> 95% pure by ^1H NMR) as a white powder (6.80 g, 100%). ^1H NMR (300 MHz, CDCl_3 , 296 K) δ 7.64 (1H, s), 7.08 (1H, s), 2.72 (4H, d, $J = 13.0$ Hz), 2.08 (2H, d, $J = 13.2$ Hz), 1.90 (6H, s), 1.44 (2H, d, $J = 13.2$ Hz), 1.27 (12H, s), 1.16 (6H, s), 1.12 (4H, d, $J = 14.1$ Hz) ppm; IR(KBr) 2958, 2909, 2877, 1728, 1686, 1584, 1459, 1354, 1190, 1086, 958, 884, 761, 632 cm^{-1} . High resolution MS (FAB) Calcd for $\text{C}_{32}\text{H}_{38}\text{N}_2\text{O}_8\text{Tl}_2$ (M): m/e 988.2116. Found 989.2195 (MH^+).

$\text{Tl}_2(\text{PXDK})$ (8). This compound was prepared from **2** (8.00 g, 10.7 mmol) and TIOEt (1.54 mL, 21.4 mmol) by a procedure analogous to that used to prepare **7**. Compound **8** was obtained (>95% pure by ^1H NMR) as a white powder (12.3 g, 100%). ^1H NMR (250 MHz, CD_2Cl_2 , 296 K) δ 7.38 (1H, s), 7.13 (1H, s), 2.61 (4H, d, $J = 13.0$ Hz), 2.36 (2H, d, $J = 13.0$ Hz), 2.10-1.90 (10 H, m), 1.55-1.10 (26 H, m), 1.00-0.80 (18H, m) ppm; $^{13}\text{C}\{^1\text{H}\}$ NMR (75 mHz, CDCl_3 , 296 K) δ 181.9, 177.0, 134.8, 133.5, 133.2, 128.7,

48.4, 44.3, 43.8, 42.4, 37.7, 25.8, 18.2, 17.9, 17.3, 14.8 ppm; IR (KBr) 2959, 2871, 1734, 1685, 1558, 1499, 1436, 1391, 1361, 1310, 1246, 1185, 1163, 1106, 1035, 930, 861, 760, 629 cm^{-1} . High resolution MS (FAB) Calcd for $\text{C}_{44}\text{H}_{62}\text{N}_2\text{O}_8\text{Tl}_2$ (M): m/e 1156.3994. Found: 1157.4065 (MH^+).

$\text{Tl}_2(\text{BXDK})$ (9). This compound was prepared from crude **6** (3.00 g, 2.89 mmol) and TlOEt (418 μL , 5.78 mmol) by a procedure analogous to that used to prepare **7**, affording **9** (>95% pure by ^1H NMR) as a tan powder. Recrystallization from $\text{CH}_2\text{Cl}_2/\text{Et}_2\text{O}$ gave **9** as a white microcrystalline solid (3.38 g, 81%). ^1H NMR (300 MHz, C_6D_6 , 296 K) δ 7.88 (1H, s), 7.30-7.23 (4H, m), 7.21-6.98 (26H, m), 6.51 (1H, s), 3.48 (4H, s, $J = 12.9$ Hz), 2.97 (4H, d, $J = 12.9$ Hz), 2.82 (4H, s), 2.49 (4H, d, $J = 12.9$ Hz), 2.07 (4H, d, $J = 12.9$ Hz), 1.18 (4H, d, $J = 12.9$ Hz), 1.02 (2H, d, $J = 13.2$ Hz), 0.96 (6H, s) ppm; $^{13}\text{C}\{^1\text{H}\}$ NMR (75 MHz, CDCl_3 , 296 K) δ 180.4, 176.2, 138.6, 136.9, 135.6, 133.5, 133.4, 131.8, 131.3, 128.8, 128.6, 128.4, 127.2, 127.1, 51.0, 50.5, 45.9, 45.4, 43.5, 37.9, 16.6 ppm; IR (KBr) 3083, 3027, 2916, 1731, 1681, 1559, 1453, 1357, 1187, 1031, 937, 865, 741, 700, 602, 508 cm^{-1} . High resolution MS (FAB) Calcd for $\text{C}_{68}\text{H}_{62}\text{N}_2\text{O}_8\text{Tl}_2$ (M): m/e 1444.3994. Found: 1445.4061.

$[\text{Cu}_2(\text{XDK})(\text{MeCN})]$ (10). To a stirred solution of **7** (3.67 g, 3.72 mmol) in $\text{CH}_2\text{Cl}_2/\text{MeCN}$ (3:1, 300 mL) under N_2 was added solid $\text{CuBr}(\text{Me}_2\text{S})$ (2.32 g, 11.1 mmol), and the mixture was rapidly stirred for 3 h. The salts were then removed by filtration through celite. The filtrate was treated with three more equiv of $\text{CuBr}(\text{Me}_2\text{S})$ and stirred for 1 h. The solvent was removed in vacuo, and the solid residue was extracted with CH_2Cl_2 (200 mL) followed by filtration through celite. The precipitate was extracted with additional CH_2Cl_2 (100 mL) and filtered through celite. The combined filtrates were concentrated in vacuo to yield a solid residue. It was suspended in Et_2O , and the precipitate was recovered by filtration to yield **10** (> 95% pure by ^1H NMR) as a white solid (2.50 g, 90%). The crude powder was used without further purification for subsequent reactions. Recrystallization from $\text{MeCN}/\text{CH}_2\text{Cl}_2$ -

/Et₂O afforded **10** as colorless blocks which appeared suitable for X-ray crystallography. ¹H NMR (300 MHz, C₆D₆, 296 K) δ 8.47 (1H, s), 6.70 (1H, s), 2.83 (4H, d, *J* = 13.1 Hz), 2.05 (3H, br s), 1.77 (6H, s), 1.71 (2H, d, *J* = 15.0 Hz), 1.20 (12H, s), 0.82 (2H, d, *J* = 13.1 Hz), 0.75 (4H, d, *J* = 13.5 Hz), 0.63 (6H, s) ppm; ¹³C{¹H} NMR (75 MHz, CD₂Cl₂, 296 K) δ 186.4, 177.1, 135.7, 134.9, 133.7, 128.5, 117.6, 45.7, 45.2, 43.4, 41.7, 31.5, 26.5, 17.5, 2.6 ppm; IR(KBr) 2963, 2921, 1738, 1704, 1568, 1463, 1403, 1357, 1176, 1086, 957, 891, 849, 759, 734, 622 cm⁻¹. Anal. Calcd for C₃₄H₄₁N₃O₈Cu₂: C, 54.68; H, 5.53; N, 5.63. Found: C, 54.39; H, 5.58; N, 5.94.

[Cu₂(PXDK)(MeCN)] (**11**). This compound was prepared from **8** (500 mg, 0.433 mmol) and CuBr(Me₂S) (241 mg, 130 mmol) by a procedure analogous to that used to synthesize **10**, affording **11** (>95% pure by ¹H NMR) as a white powder (360 mg, 91%). The crude powder was used without further purification for subsequent reactions. Recrystallization from CH₂Cl₂/MeCN/Et₂O gave **11** as colorless needles. ¹H NMR (500 MHz, CD₂Cl₂, 296 K) δ 8.23 (1H, s), 7.17 (1H, s), 2.69 (4H, d, *J* = 13.5 Hz), 2.39 (2H, d, *J* = 12.5 Hz), 2.00-1.92 (13H, m), 1.42-1.18 (26H, m), 0.92 (12H, t, *J* = 7.0 Hz), 0.84 (6H, t, *J* = 7.2 Hz) ppm; ¹³C{¹H} NMR (75 MHz, CDCl₃, 296 K) δ 185.4, 176.3, 135.5, 134.9, 133.7, 129.1, 117.8, 48.1, 46.9, 44.7, 42.6, 38.2, 18.0, 17.6, 15.7, 15.0, 14.8, 2.5 ppm (18 of the expected 19 peaks were observed); IR(KBr) 2959, 2872, 1734, 1695, 1566, 1458, 1359, 1247, 1182, 1035, 924, 863, 759, 583 cm⁻¹. Anal. Calcd for C₄₄H₆₂N₂O₈Cu₂Cl₂ (**11** minus 1MeCN): C, 60.46; H, 7.15; N, 3.20. Found: C, 60.01; H, 7.32; N, 3.22. This sample was heated at 90 °C for 12 h to remove any residual CH₂Cl₂. The MeCN ligand was removed in the process.

[Cu₂(BXDK)(MeCN)] (**12**). This compound was synthesized from **9** (1.00 g, 0.692 mmol) and CuBr(Me₂S) (435 mg, 2.08 mmol) by a procedure analogous to that used to prepare **10**, to yield **12** (> 95% pure by ¹H NMR) as a white solid. The crude powder was used without further purification for subsequent reactions.

Recrystallization from MeCN/CH₂Cl₂/Et₂O afforded **12** as colorless thin plates (600 mg, 72%). ¹H NMR (300 MHz, C₆D₆, 296 K) δ 8.22 (1H, s), 7.25-6.95 (30 H, m), 6.54 (1H, s), 3.51 (4H, d, *J* = 13.2 Hz), 2.85 (4H, d, *J* = 13.2 Hz), 2.59 (4H, s), 2.41 (4H, d, *J* = 12.9 Hz), 2.04 (2H, d, *J* = 12.6 Hz), 1.90 (3H, br s), 1.10 (4H, d, *J* = 14.1 Hz), 0.94 (2H, d, *J* = 13.2 Hz), 0.82 (6H, s) ppm; ¹³C{¹H} NMR (75 mHz, CDCl₃, 296 K) δ 182.5, 175.3, 137.6, 136.7, 135.9, 134.3, 134.0, 132.0, 130.9, 128.5, 128.4, 128.3, 127.4, 127.1, 117.5, 50.1, 49.0, 46.2, 45.2, 43.6, 38.1, 15.8, 2.6 ppm; IR(KBr) 3084, 3061, 3028, 2926, 2860, 2251, 1732, 1700, 1565, 1494, 1413, 1359, 1231, 1178, 1031, 928, 844, 749, 698 cm⁻¹. Anal. Calcd for C₆₈H₆₂N₂O₈Cu₂ (**12** minus 1MeCN): C, 70.27; H, 5.38; N, 2.41. Found: C, 67.67; H, 5.30; N, 2.68. This sample was heated at 90 °C for 12 h to remove any residual CH₂Cl₂. The MeCN ligand was removed in the process.

[Cu₂(XDK)(PPh₃)₂] (**13**). To a stirred suspension of **10** (50 mg, 0.067 mmol) in THF (2 mL) was added PPh₃ (35 mg, 0.13 mmol) in THF (1 mL). The mixture clarified immediately and after 0.5 h the solvent was removed in vacuo. The solid residue was recrystallized from chlorobenzene/Et₂O to yield **13** as colorless blocks which appeared suitable for X-ray crystallography (45 mg, 55 %). ¹H NMR (300 MHz, C₆D₆, 296 K) δ 8.05 (1H, s), 7.50-7.43 (10 H, m), 7.04-7.00 (20H, m), 6.80 (1H, s), 2.98 (4H, d, *J* = 13.2 Hz), 1.89 (6H, s), 1.79 (2H, d, *J* = 12.5 Hz), 1.22 (12 H, s), 0.90 (2H, d, *J* = 13.2 Hz), 0.92-0.78 (10H, m) ppm; ¹³C{¹H} NMR (75 mHz, CD₂Cl₂, 296 K) δ 182.5, 176.8, 135.2, 135.1, 134.5 (d, *J*_{CP} = 15.8 Hz), 133.6, 133.1 (d, *J*_{CP} = 15.1 Hz), 130.4, 129.1 (d, *J*_{CP} = 9.3 Hz), 128.8, 45.6, 45.4, 43.5, 41.3, 32.8, 26.5, 17.5 ppm; ³¹P NMR (121 mHz, CD₂Cl₂, 296 K) δ 5.43 (br s, Δ*v*_{1/2} = 45.4 Hz) ppm; IR(KBr) 3070, 2961, 2926, 1733, 1695, 1571, 1461, 1435, 1400, 1359, 1195, 1097, 958, 851, 745, 694 cm⁻¹. Anal. Calcd for C₆₈H₆₈N₂O₈P₂Cu₂: C, 66.38; H, 5.57; N, 2.28. Found: C, 66.07; H, 5.79; N, 2.15.

[Cu₂(XDK)(2,6-Me₂PhNC)₃] (**14a**) and [Cu₂(XDK)(μ-2,6-Me₂PhNC)(2,6-Me₂PhNC)₂] (**14b**). This compound was prepared from **10** (100 mg, 0.13 mmol) and 2,6-dimethylphenyl isocyanide (54 mg, 0.40 mmol) by a procedure analogous to that

used to make **13**. Recrystallization from PhCl/Et₂O (vapor diffusion) afforded blocks of colorless **14a** and yellow **14b** in distinct crystal fields, both of which appeared suitable for X-ray crystallography (96 mg, 65%). ¹H NMR (300 MHz, C₆D₆, 296 K) δ 8.05 (1H, s), 7.50-7.43 (10H, m), 7.04-7.00 (20H, m), 6.80 (1H, s), 2.98 (4H, d, *J* = 13.2 Hz), 1.89 (6H, s), 1.79 (2H, d, *J* = 12.5 Hz), 1.22 (12H, s), 0.90 (2H, d, *J* = 13.2 Hz), 0.92-0.78 (10H, m) ppm; ¹³C{¹H} NMR (75 MHz, CD₂Cl₂, 296 K) δ 182.9, 176.8, 135.7, 135.1, 134.6, 132.0, 130.2, 129.9, 129.0, 128.4, 127.1, 45.9, 45.8, 43.3, 41.3, 33.0, 26.7, 19.0, 17.6 ppm; IR (KBr) 2957, 2926, 2877, 2134, 1736, 1701, 1592, 1462, 1356, 1197, 1085, 960, 887, 793, 749, 720, 635 cm⁻¹. Anal. Calcd for C₅₉H₆₅N₅O₈Cu₂: C, 64.46; H, 5.96; N, 6.37. Found: C, 64.54; H, 5.94; N, 6.04.

[Cu₂(XDK)(NB)₂] (**15**). This compound was prepared from **10** (80 mg, 0.11 mmol) and excess norbornene (650 mg, 6.9 mmol) by a procedure analogous to that used to make **13**. Recrystallization from NB/CH₂Cl₂/Et₂O provided **15** as colorless blocks (69 mg, 72%). ¹H NMR (300 MHz, CD₂Cl₂, 296 K) δ 7.24 (1H, s), 7.10 (1H, s), 5.41 (4H, s), 2.85-2.77 (8H, m), 2.06 (2H, d, *J* = 13.2 MHz), 2.83 (6H, s), 1.58-1.41 (8H, m), 1.32-1.25 (18H, m), 1.20 (4H, d, *J* = 13.8 Hz), 1.01 (2H, d, *J* = 8.7 Hz), 0.80 (4H, dd, *J* = 7.5, 2.4 Hz) ppm; ¹³C{¹H} NMR (75 MHz, CD₂Cl₂, 296 K) δ 186.4, 176.8, 135.5, 134.8, 133.6, 127.7, 120.2, 47.4, 45.4, 45.1, 43.7, 42.7, 41.6, 32.4, 26.3, 24.8, 17.5 ppm; IR (KBr) 2957, 2926, 2877, 2134, 1736, 1701, 1592, 1462, 1356, 1197, 1085, 960, 887, 793, 749, 720, 635 cm⁻¹. Prolonged exposure of powdered **15** to high vacuum resulted in removal of 1 equiv of NB, as judged by ¹H NMR and elemental analysis. ¹H NMR for [Cu₂(XDK)(NB)]: (300 MHz, CD₂Cl₂, 296 K): δ 7.58 (1H, s), 7.13 (1H, s), 5.27 (2H, s), 2.85-2.74 (6H, m), 2.08 (2H, d, *J* = 13.5 Hz), 1.89 (6H, s), 1.59-1.51 (4H, m), 1.47 (2H, d, *J* = 13.2 Hz), 1.28 (12H, s), 1.25 (6H, s), 1.17 (4H, d, *J* = 12.6 Hz), 1.00 (2H, d, *J* = 13.1 Hz), 0.91 (2H, dd, *J* = 7.4, 2.4 Hz); IR (KBr) 2966, 2928, 1733, 1696, 1592, 1460, 1407, 1356, 1335, 1223, 1136, 957, 851, 760, 684, 638 cm⁻¹. Anal. Calcd for C₅₉H₆₅N₅O₈Cu₂ (**15** minus 1NB): C, 64.46; H, 5.96; N, 6.37. Found: C, 64.54; H, 5.94; N, 6.04.

Cu₂(XDK) (16). This compound was prepared from **10** (290 mg, 0.38 mmol) and excess cyclohexene (5.0 ml, 49 mmol) by a procedure analogous to that used to prepare **15**. Upon removal of the volatile components in vacuo, all the cyclohexene was driven off to afford **16** as a white solid. Recrystallization from CH₂Cl₂/pentane provided **16** as colorless needles (220 mg, 81%). ¹H NMR (300 MHz, CD₂Cl₂, 295 K) δ 8.08 (1H, s), 7.14 (1H, s), 2.77 (4H, d, *J* = 13.2 Hz), 2.09 (2H, d, *J* = 13.2 Hz), 1.90 (6H, s), 1.46 (2H, d, *J* = 13.2 Hz), 1.27 (12H, s), 1.23-1.15 (10H, m) ppm; ¹³C{¹H} NMR (75 MHz, CD₂Cl₂, 296 K) δ 187.7, 177.1, 135.8, 134.8, 134.1, 130.4, 45.7, 45.2, 43.6, 41.7, 31.4, 26.4, 17.5 ppm; IR (KBr) 2965, 2924, 1734, 1697, 1559, 1501, 1411, 1341, 1228, 1179, 1087, 956, 848, 761, 700, 623 cm⁻¹. Anal. Calcd for C₃₂H₃₈N₂O₈Cu₂: C, 54.46; H, 5.43; N, 3.97. Found: C, 54.67; H, 5.36; N, 3.75.

[Cu₂(XDK)(tmeda)] (17). This compound was prepared by addition of tmeda (23 μL, 0.15 mmol) to **10** (94 mg, 0.13 mmol) in THF (1 mL), followed by recrystallization from THF/pentane at -30 °C, to afford **17** as colorless blocks (81 mg, 78 %). ¹H NMR (295 K, 300 MHz, C₆D₆) δ 8.45 (1H, s), 6.69 (1H, s), 2.94 (4H, d, *J* = 13.1 Hz), 2.10 (12 H, s), 1.86 (4H, s), 1.85-1.78 (8H, m), 1.26 (12H, s), 1.05 (6H, s), 0.92 (2H, d, *J* = 13.1 Hz), 0.84 (4H, d, *J* = 13.8 Hz); ¹³C{¹H} NMR (75 MHz, CD₂Cl₂, 296 K) δ 184.2, 176.8, 135.2, 133.5, 129.2, 58.5, 47.3, 45.9, 45.5, 42.9, 41.6, 31.9, 26.6, 17.5 ppm (14 of the expected 15 peaks were observed); IR(KBr) 2984, 2930, 2882, 1735, 1695, 1561, 1461, 1355, 1189, 1086, 957, 850, 697 cm⁻¹. Anal. Calcd for C₃₈H₅₄N₄O₈Cu₂: C, 55.53; H, 6.62; N, 6.82. Found: C, 55.39; H, 6.80; N, 6.81.

[Cu₂(PXDK)(tmeda)] (18). This compound was prepared from **11** (57 mg, 0.062 mmol) and tmeda (19 μL, 0.50 mmol) by a procedure analogous to that used to obtain **17**. Recrystallization from THF/pentane provided **18** as colorless needles (39 mg, 72%). ¹H NMR (250 MHz, CD₂Cl₂, 295 K) δ 8.02 (1H, s), 7.10 (1H, s), 2.73 (4H, d, *J* = 12.9 Hz), 2.36 (4H, s), 2.23 (12H, s), 2.00-1.85 (8H, m), 1.50-1.12 (30H, m), 0.91 (12H, d, *J* = 6.6 Hz), 0.77 (6H, t, *J* = 6.7 Hz) ppm; ¹³C{¹H} NMR (75 MHz, CD₂Cl₂, 296 K) δ 138.2, 176.0,

135.2, 135.1, 133.4, 129.9, 58.6, 48.2, 47.2, 46.4, 44.5, 42.8, 38.5, 18.0, 17.6, 15.1, 14.6 ppm (17 of the expected 19 peaks were observed); IR(KBr) 2958, 2871, 2780, 1733, 1691, 1579, 1459, 1361, 1192, 923, 758, 582 cm^{-1} . Anal. Calcd for $\text{C}_{50}\text{H}_{78}\text{N}_4\text{O}_8\text{Cu}_2$: C, 60.64; H, 7.94; N, 5.66. Found: C, 59.99; H, 8.32; N, 6.56.

[Cu₂(BXDK)(tmeda)] (19). This compound was prepared from **12** (200 mg, 0.17 mmol) and tmeda (75 μL , 0.50 mmol) by a procedure analogous to that used to synthesize **17**. Recrystallization from THF/pentane provided **19** as colorless needles (138 mg, 65%). ^1H NMR (300 MHz, CD_2Cl_2 , 295 K) δ 7.91 (1H, s), 7.38-7.22 (6H, m), 7.20-7.05 (24H, m), 6.66 (1H, s), 3.30 (4H, d, $J = 12.9$ Hz), 2.81 (4H, s), 2.76 (4H, d, $J = 13.2$ Hz), 2.55-2.45 (8H, m), 2.40 (12 H, s), 1.99 (2H, d, $J = 12.6$ Hz), 1.36 (4H, d, $J = 13.2$ Hz), 1.00 (2H, d, $J = 12.9$ Hz), 0.62 (6H, s) ppm; $^{13}\text{C}\{^1\text{H}\}$ NMR (75 MHz, CD_2Cl_2 , 296 K) δ 183.9, 175.0, 137.0, 136.9, 135.2, 134.5, 133.9, 132.0, 131.9, 129.4, 128.5, 128.2, 127.2, 126.9, 58.5, 48.8, 48.1, 47.7, 45.7, 45.3, 41.5, 38.0, 16.0 ppm; IR(KBr) 3027, 2920, 2828, 1733, 1694, 1577, 1495, 1361, 1184, 1032, 932, 759, 701, 596 cm^{-1} . Anal. Calcd for $\text{C}_{74}\text{H}_{78}\text{N}_4\text{O}_8\text{Cu}_2$: C, 69.52; H, 6.15; N, 4.38. Found: C, 68.72; H, 6.45; N, 4.42.

[Cu(4,4'-Me₂bpy)₂][Cu(XDK)] (20). To a stirred solution of **10** (250 mg, 0.355 mmol) in CH_2Cl_2 (5 mL) was added 4,4'-dimethyl-2,2'-dipyridine (125 mg, 0.670 mmol). The solution immediately turned dark red, and after 0.5 h the volatile components were removed in vacuo. The dried residue was suspended in pentane (10 mL), and the precipitate was recovered by filtration. Recrystallization from THF/ CH_2Cl_2 /pentane provided **20** as a dark red-brown microcrystalline solid (345 mg, 96%). ^1H NMR (250 MHz, CD_2Cl_2 , 296 K) δ 8.43 (4H, d, $J = 5.1$ Hz), 8.02 (4H, s), 7.98 (1H, s), 7.33 (4H, d, $J = 5.1$ Hz), 7.06 (1H, s), 2.71 (4H, d, $J = 13.2$ Hz), 2.51 (12 H, s), 2.02 (2H, d, $J = 12.8$ Hz), 1.81 (6H, s), 1.37 (2H, d, $J = 13.0$ Hz), 1.21 (12H, s), 1.12-0.90 (10H, m); $^{13}\text{C}\{^1\text{H}\}$ NMR (75 MHz, CD_2Cl_2 , 296 K) δ 181.6, 176.9, 152.7, 150.2, 149.0, 135.1, 134.9, 132.5, 130.0, 127.5, 122.8, 46.2, 45.9, 42.5, 41.6, 31.6, 26.8, 21.9, 17.7 ppm; IR(KBr) 2958, 2926, 1734, 1696, 1611, 1460, 1345, 1226, 1193, 1086, 956, 823, 886, 626, 517

cm⁻¹. UV-vis (CH₂Cl₂) (λ_{max} , nm (ϵ , M⁻¹ cm⁻¹): 329 (sh, 2800), 397 (2200), 529 (sh, 630). Anal. Calcd for C₅₆H₆₂N₆O₈Cu₂: C, 62.61; H, 5.82; N, 7.82. Found: C, 62.30; H, 5.58; N, 7.69.

(Et₄N)[Cu(PXDK)] (**21**). To a stirred solution of **11** (1.50 g, 1.64 mmol) in CH₂Cl₂ (25 mL) was added Et₄N(CN) (272 mg, 1.64 mmol) in CH₂Cl₂ (5 mL). The mixture was rapidly stirred for 0.5 h and then filtered through celite. The colorless filtrate was dried to yield pure **21** (>95% by ¹H NMR) as a white powder (1.42 g, 92 %) Recrystallization from MeCN/THF/Et₂O afforded **21** as colorless blocks. ¹H NMR (250 MHz, CD₂Cl₂, 296 K) δ 7.99 (1H, s), 7.06 (1H, s), 3.26 (8H, m), 2.66 (4H, d, J = 13.0 Hz), 2.32 (2H, d, J = 12.9 Hz), 2.02-1.70 (10H, m), 1.50-1.00 (38 H, m), 0.93-0.70 (18H, m); ¹³C{¹H} NMR (75 MHz, CD₂Cl₂, 296 K) δ 180.4, 176.6, 135.3, 135.0, 132.4, 130.7, 51.8, 48.2, 46.0, 45.1, 44.7, 43.1, 38.6, 19.4, 18.3, 18.0, 17.7, 15.1, 7.8 ppm; IR(KBr) 2933, 2872, 1731, 1700, 1626, 1498, 1458, 1392, 1346, 1257, 1172, 1107, 1003, 924, 860, 826, 782, 759, 734, 539 cm⁻¹. Anal. Calcd for C₅₂H₈₄N₃O₈Cu: C, 66.39; H, 8.79; N, 4.47. Found: C, 66.32; H, 9.02; N, 4.53.

[CuLi(XDK)(THF)₂] (**22**). Method A: To a stirred solution of **10** (50 mg, 0.067 mmol) and 12-crown-4 (43 mL, 0.27 mmol) in THF (3 mL) was added PhLi (37 mL, 1.8 M in cyclohexane/Et₂O). The resulting brown mixture was stirred for 2 h, and then the volatile components were removed in vacuo. The residue was recrystallized from THF/pentane to yield a dark brown precipitate and large colorless blocks. Crystals of **22** separated from the dark residue in Paratone-N (Exxon) and were suitable for X-ray crystallography, but a large scale purification for spectroscopic and elemental analysis was unsuccessful by this method.

Method B: To a stirred solution of **10** (100 mg, 0.13 mmol) in THF (5 mL) was added LiCN (0.5 M in DMF, 268 μ l, 0.13 mmol) via syringe in one portion. An off-white precipitate formed immediately, and after 5 min the mixture was filtered through celite. The volatile components were removed from the filtrate in vacuo.

The resulting tan solid was washed with pentane (5-10 ml) to remove residual DMF. The dried residue was redissolved in CH₂Cl₂ (0.5 ml) and filtered through celite to remove a fine white precipitate. An equal volume of THF was added, and slow diffusion of pentane into this solution provided **22** as large colorless blocks. When crystalline **22** was isolated from the mother liquor, followed by drying at atmospheric pressure under N₂, one of the THF molecules was lost as judged by ¹H NMR and elemental analysis (75 mg, 78%). ¹H NMR for [CuLi(XDK)(THF)] (300 MHz, CD₂Cl₂, 296 K) δ 7.64 (1H, s), 7.14 (1H, s), 3.69 (4H, t, *J* = 6.3 Hz), 2.72 (4H, d, *J* = 13.2 Hz), 2.08 (2H, d, *J* = 13.2 Hz), 1.91 (6H, s), 1.87-1.80 (4H, m), 1.45 (2H, d, *J* = 12.9 Hz), 1.34-1.05 (22H, m); ¹³C{¹H} NMR (75 MHz, CD₂Cl₂, 296 K) δ 185.1, 177.5, 135.6, 134.7, 133.2, 128.2, 45.7, 45.2, 43.1, 41.7, 32.3, 31.7, 26.5, 26.1, 17.6 ppm; IR(KBr) 2959, 2868, 1736, 1702, 1402, 1376, 1352, 1227, 1184, 1048, 956, 889, 760, 624 cm⁻¹. Anal. Calcd for C₃₆H₄₆N₂O₉CuLi (**22** minus 1THF): C, 59.95; H, 6.43; N, 3.88. Found: C, 59.64; H, 7.10; N, 3.43.

Collection and Reduction of X-ray Data

All crystals were mounted on the tips of quartz fibers with Paratone-N (Exxon), cooled to low temperature (~ -85 °C), and placed on Siemens CCD X-ray diffraction system controlled by a Pentium-based PC running the SMART software package.³⁴ The general procedures for data collection and reduction follow those reported previously.³⁵ All structures were solved by use of the direct methods programs SIR-92³⁶ or XS, part of the TEXSAN³⁷ and SHELXTL³⁸ program packages, respectively. Structure refinements were carried out with XL, part of the SHELXTL program package.³⁸ All remaining non-hydrogen atoms were located and their positions refined by a series of least-squares cycles and Fourier syntheses. Enantiomorph checks were carried out on **17** and **21** by using the Flack parameter refinement³⁹ in the XL program. Selection of the correct enantiomer for complex **17** was determined to be unreliable, so it was refined as a racemic twin, resulting in lower *R* and *wR*²

values than were obtained when refining with either of the two enantiomers. Selection of the correct enantiomer for **21** was unambiguous. All hydrogen atoms for **6**, **10**, and **21** were located from difference Fourier maps and refined isotropically. For **15**, the four olefinic hydrogen atoms of the coordinated norbornene molecules were located from difference maps and refined isotropically. The remaining hydrogen atoms of **15**, and all the hydrogen atoms for **13**, **14a**, **14b**, **16**, **17**, and **22**, were assigned idealized positions and given a thermal parameter 1.2 times the thermal parameter of the carbon atom to which each was attached. Empirical absorption corrections were calculated and applied for each structure using SADABS, part of the SHELXTL program package.³⁸

The structures of **14a**, **14b**, and **16** contain a disordered chlorobenzene molecule. The chlorine atom in each case is disordered across an inversion center positioned on the centroid of the phenyl ring. Each chlorine atom was refined with a site occupancy of 0.5. The other chlorobenzene in **16** contains two carbon atoms with large thermal parameters. The structure of **17** contains two disordered THF molecules in which the oxygen atoms could not be determined reliably, so both were refined at partial occupancy as cyclopentane molecules. The structure of **21** contains a lattice THF molecule disordered over two positions. It was refined as a cyclopentane molecule with two of the carbon atoms at full occupancy, and the occupancy of the other three carbon atoms was distributed over two positions and refined. One of the propyl groups of **21** is disordered. The carbon atom attached to the cyclohexyl ring was refined at full occupancy, and the occupancy of the other two carbon atoms was distributed over two positions and refined.

Important crystallographic information for each complex including refinement residuals is given in Table 1.1, along with core distances and angles in Table 1.2. Final positional and equivalent isotropic thermal parameters are provided in Tables 1.3-1.12.

Results and Discussion

At the inception of this research, very few well characterized copper(I) carboxylate complexes had been described. The most notable work came from Floriani's lab, which reported the synthesis of carbon monoxide,⁴⁰ isonitrile,⁴¹ and alkyne⁴² complexes incorporating Cu(I) benzoate. Copper(I) carboxylate complexes without π -acceptor ligands, except for oligomeric homoleptic complexes, are rare owing to disproportionation to Cu metal and Cu(II) products. In addition, accounts of the reactivity toward dioxygen of any well defined Cu(I) carboxylate derivatives were non-existent. Our initial goals were therefore to develop a facile synthesis of a discrete dicopper(I) XDK complex and ascertain its kinetic stability, and to understand the chemical properties of this bis(carboxylate)-bridged "platform" by fully elucidating its coordination chemistry with a range of ancillary ligands, ranging from π -acceptor to sigma-only donors. From these studies has emerged a detailed picture of the electronic nature of the dicopper(I) XDK platform and a host of complexes for O₂ reactivity studies.

Ligand Synthesis. Exposure of most dicopper(I) and diiron(II) complexes of XDK and PXDK to dioxygen at low temperature produces transiently stable intermediates at best.^{13,43} A possible decomposition pathway in these reactions is the intermolecular reaction between an O₂-derived intermediate and one or more {M₂(XDK)} units.^{27,28} A more sterically demanding XDK derivative might block this pathway by impeding access to the intermediate or transition state. This strategy presumes that the decomposition pathway does not involve complete dissociation of the metal O₂-derived species from XDK, which may occur in some cases. Nevertheless it represents a reasonable starting point, and we were therefore interested to prepare a sterically more hindered XDK analog.

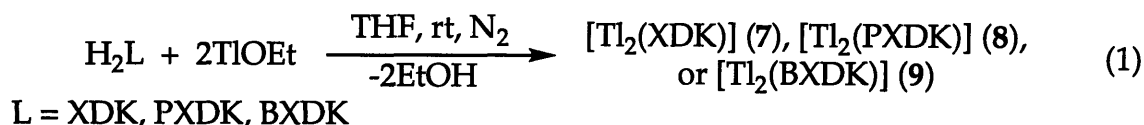
Derivatization of Kemp's triacid has been achieved by alkylation of trimethyl 1,3,5-cyclohexyltricarboxylate carboxylate with benzyl chloromethyl ether⁴⁴ and allyl

bromide,⁴⁵ both potent electrophiles. A more sterically demanding and robust substituent than the benzyloxy group was sought which would place a bulky group closer to the metal binding sites and resist oxidative cleavage. Both neopentyl and benzyl functionalities fulfill these requirements, but efforts to alkylate with neopentyl iodide failed owing to its modest electrophilicity. Reaction of trithio trimethyl-1,3,5-cyclohexyltricarboxylate with three equivalents of benzyl bromide under relatively forcing conditions proceeded in good yield, however, affording multigram quantities of trimethyl-*cis,cis*-1,3,5-tribenzylcyclohexane-1,3,5-tricarboxylate (benzyl Kemp's triester, **3**, Scheme 1.1). Deprotection of **3** in refluxing KOH followed by acidification with HCl provided *cis,cis*-1,3,5-tribenzylcyclohexane-1,3,5-tricarboxylic acid (benzyl Kemp's triacid, **4**). Under identical conditions but in the absence of THF, only intractable decomposition products were obtained. The tripotassium salt of **4** precipitates out of solution when a 1:1 EtOH/THF solvent mixture is used, and this property may protect it from further degradation. The final ether wash also proved crucial for obtaining pure product, for it removed significant quantities of partially deprotected **3** and other decomposition products. The triacid is soluble in neat DMSO or DMSO solvent mixtures. Synthesis of *cis,cis*-1,3,5-tribenzylcyclohexane-1,3-anhydride-5-acid chloride (tribenzyl Kemp's anhydride acid chloride, **5**) proceeded by standard procedures³³ in quantitative yield.

Condensation of **5** with 0.5 equivalents of 1,3-dimethyl-4,6-diaminobenzene followed by recrystallization from MeOH provided benzyl xylene diamine Kemp's triacid (H₂BXDK, **6**) in moderate yield and high purity as judged by the ¹H NMR spectrum of the bulk product. This spectrum also revealed that the benzyl Kemp's cyclohexyl fragments were in equivalent magnetic environments, supporting the assignment of C_{2v} symmetry for the product and confirming that the desired U-shaped isomer had been obtained. An X-ray structural determination of **6** confirmed this assignment (Figure 1.1). The space filling representation reveals that the

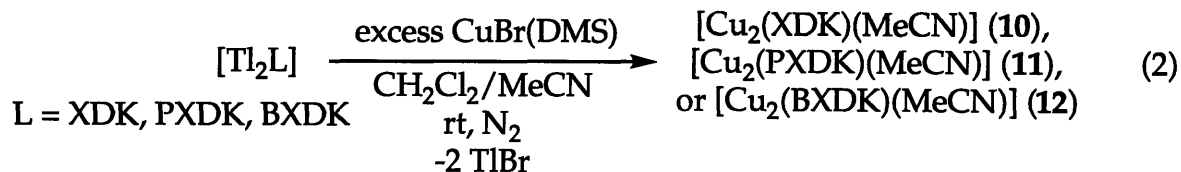
peripheral benzyl groups shroud the bis(carboxylate) oxygen plane and the metal binding sites from above, although rotation toward the outside of the molecule in solution appears facile. This flexibility would preclude steric protection from the sides of a BXDK complex. Nevertheless the benzyl groups are still forced to point up owing to the geometric constraints of the quaternary cyclohexyl carbon atoms and this property should provide added steric protection at the carboxylate binding sites compared to XDK and PXDK.

Preparation and Reactivity of Dicopper(I) Bis(carboxylate)-Bridged Complexes: Synthesis of [Tl₂L], L = XDK (7), PXDK (8), and BXDK (9); and [Cu₂L(MeCN)], L = XDK (10), PXDK (11), and BXDK (12). Convenient, high-yield procedures were desired for the bis(carboxylate) dicopper(I) starting materials. Other Cu(I) carboxylates have been prepared from their Tl(I) salts and a copper halide,⁴⁶ so this approach was adopted (eq 1). Treatment of 1, 2, or 6 with 2 equiv of TlOEt afforded 7-9, respectively, as



white powders in quantitative yields. The ¹H NMR spectra of each dithallium(I) complex showed one set of cleanly shifted resonances and the disappearance of the broad singlet due to the carboxylic acid protons. Complex 7 is only slightly soluble in THF and CH₂Cl₂, whereas 8 and 9 are readily soluble.

Treatment of 7, 8 or 9 with excess CuBr(DMS) in CH₂Cl₂/MeCN provided 10-12, respectively, as crude off-white powders in 90% yield (eq 2). The ¹H NMR



spectrum of each product exhibited a single shifted set of dicarboxylate and MeCN ligand resonances in a 1:1 ratio. A xylene spacer aromatic proton experiences a significant downfield shift, presumably the one ortho to both imide nitrogen atoms, which is in close proximity to the metal-binding sites. Recrystallization from CH₂Cl₂/MeCN/Et₂O afforded colorless blocks or needles. Spectroscopic and analytical data confirm the purity of each complex. Complexes 10-12 are all non-electrolytes in CH₂Cl₂ solution, supporting that the metal ions are strongly coordinated by the carboxylate groups in solution. An X-ray structural determination of 10 confirmed that both Tl ions were displaced in eq 2 to form a dinuclear copper(I) carboxylate-bridged complex. As illustrated in Figure 1.2, one copper atom is ligated by an acetonitrile and two carboxylate oxygen atoms in a trigonal planar geometry, and the other is coordinated in a nearly linear, two-coordinate fashion to the other two carboxylate oxygen atoms. A linear two-coordinate geometry is not uncommon for Cu(I),⁴⁷ which appears to have the ideal ionic radius to be "skewered" by the two rigidly positioned XDK oxygen atoms. The relatively short Cu...Cu distance of 2.6287 (5) Å signifies weak metal-metal bonding, a formulation which is supported by molecular orbital calculations on a tetrameric Cu(I) trimethylsilyl complex with similar copper-copper distances.⁴⁸

Reactivity of the Dicopper(I) Acetonitrile Complexes. The reactivity of 10-12 with a spectrum of reagents, weak sigma donors (π -acceptors), basic neutral sigma donors, and anionic donors was investigated and the results are summarized in Scheme 1.2. ORTEP diagrams of the structurally characterized products are shown in Figures 1.3 and 1.4, and selected bond distances and angles are reported in Table 1.2. The coordination chemistry proved to be essentially identical for all three diacids, so only that for XDK will be described in detail.

Neutral Donor Adducts: Preparation of [Cu₂(XDK)(PPh₃)₂] (13), [Cu₂(XDK)(2,6-Me₂PhNC)₃] (14a), [Cu₂(XDK)(μ -2,6-Me₂PhNC)(2,6-Me₂PhNC)₂] (14b), [Cu₂(XDK)-

(NB)₂] (15), [Cu₂(XDK)] (16), [Cu₂(XDK)(tmeda)] (17), [Cu₂(PXDK)(tmeda)] (18), [Cu₂(BXDK)(tmeda)] (19), and [Cu(4,4'-Me₂bpy)₂][Cu(XDK)] (20). All of these complexes were prepared by allowing **10** or **11** to react with 2-4 equiv or an excess of the appropriate ancillary ligand, followed by washing with pentane or Et₂O to remove residual free ligand. All were recrystallized to afford analytically pure material.

Treatment of **10** with two equivalents of triphenylphosphine followed by recrystallization afforded bis(phosphine) adduct **13** as colorless blocks. Conductivity measurements revealed **13** to be a non-electrolyte in CH₂Cl₂ solution. The ¹H NMR spectrum exhibited one set of XDK resonances and a complicated set of triphenylphosphine resonances in a 2:1 ratio. The proton-decoupled ¹³C NMR spectrum showed single sets of XDK and triphenylphosphine resonances, and phosphorus coupling to three of the four phenyl ring proton resonances, as is found in free triphenylphosphine in CD₂Cl₂. The ³¹P NMR spectrum showed one broad singlet at room temperature, shifted slightly downfield from that of free triphenylphosphine (δ 5.1 ppm, $\Delta\nu_{1/2}$ = 24.7 Hz, CD₂Cl₂). X-ray structural analysis revealed solid **13** to be composed two inequivalent trigonal planar copper atoms, with one copper displaced laterally from the four-oxygen carboxylate plane and the other lying above the plane (Figure 1.3). The copper-phosphorus bond lengths are normal for Cu(I) triphenylphosphine complexes having one phosphine ligand per copper atom.⁴⁹ Simple Cu(I) carboxylate-triphenylphosphine complexes have been prepared and structurally characterized previously, with [Cu(OAc)(PPh₃)₂] being a representative example.⁵⁰ This mononuclear complex consists of a tetrahedrally coordinated copper atom with a chelating acetate and two triphenylphosphine ligands. The dissimilar reactivity of **10** is probably due to steric effects and the convergent nature of the XDK carboxylate ligands.

Exposure of **10** to excess 2,6-dimethylphenylisocyanide followed by recrystallization provided the tris(isonitrile) adduct **14**. The ¹H NMR spectrum exhibited

single sets of cleanly shifted XDK and isonitrile resonances in the expected ratios. The IR spectrum showed one broad isonitrile C≡N stretch at 2134 cm⁻¹. The complex is a non-electrolyte in CH₂Cl₂ solution. X-ray structural analysis on two different crystals, obtained under identical crystallization conditions, revealed that the tris(isonitrile) complex can exist as two isomers (Figure 1.3). In all-terminal colorless **14a**, one copper is trigonal and the other tetrahedral, essentially as found in a bis(carboxylate) tris(isonitrile) complex prepared from Cu(I) benzoate and *p*-tolyl isocyanide.⁴¹ The other isomer, yellow **14b**, has the isonitrile ligands coordinated in a symmetrical fashion, with one bridging the two copper atoms and one terminal on each. The bridging isonitrile in **14b** enforces a relatively close Cu...Cu distance of 2.7278 (9) Å compared to the value of 3.2560(5) Å for **14a**. A bridging isonitrile derivative similar to **14b** has not been reported for other Cu(I) carboxylates. The isomers appear to be in rapid equilibrium in solution at room temperature since only one set of ¹H NMR resonances is observed for the XDK and isonitrile ligands.

Treatment of **10** with excess norbornene followed by recrystallization provided bis(norbornene) adduct **15** as colorless blocks. The X-ray structure was analogous to that determined for bis(triphenylphosphine) adduct **13**, with each trigonal planar copper atom ligated to XDK in a different fashion (Figure 1.3). Both norbornene ligands are coordinated via the exo face, as has been observed in other Cu(I) norbornene adducts, with characteristic Cu(I)-olefin bond distances.⁵¹ When crystals of **15** are allowed to dry fully under an atmosphere of N₂ at room temperature, one of the norbornene ligands is lost, as judged by ¹H NMR spectroscopy and elemental analysis. This complex does not lose the remaining norbornene ligand when exposed to high vacuum. It is probably composed of trigonal planar and linear two coordinate copper atoms, although an X-ray structure has not been obtained.

Treatment of **10** with excess cyclohexene, followed by evaporation of the volatile components under high vacuum, provided the desolvated parent complex

16. The ^1H and ^{13}C NMR and IR spectra showed no cyclohexene or acetonitrile peaks, and the product is a non-electrolyte in CH_2Cl_2 solution. X-ray quality crystals of **16** were grown from either CH_2Cl_2 /pentane or PhCl /pentane. A low resolution structure was obtained on crystals grown from CH_2Cl_2 /pentane. (X-ray data for **16** from CH_2Cl_2 /pentane: $P2_1/n$, $a = 14.0015(3)$, $b = 12.8639(2)$, $c = 22.3936(3)$, $\beta = 106.621(1)$, $V = 3832.8(1)$, $Z = 4$, $T = 188\text{ K}$, $R = 0.121$, $wR^2 = 0.355$. This structure was not fully refined due to major disorder of the two lattice CH_2Cl_2 molecules.) This homoleptic dinuclear complex consists of two nearly linear two coordinate copper ions with no intermolecular bonding to any neighboring Cu_2XDK (Scheme 2, $n = 1$). Structural analysis of the crystals grown from PhCl /pentane showed that two $\{\text{Cu}_2\text{XDK}\}$ units in this isomer are linked by a bond between an XDK imide carbonyl oxygen and a neighboring copper atom (Cu2-O504, Figure 1.4). One of the $\{\text{Cu}_2\text{XDK}\}$ units consists of two linearly coordinated copper atoms with a $\text{Cu}_3\cdots\text{Cu}_4$ distance of $2.6106(9)\text{ \AA}$. Each copper atom is pulled laterally out of the four-oxygen carboxylate plane. The other Cu_2XDK unit contains two- and three-coordinate copper atoms, with a slightly shorter $\text{Cu}_1\cdots\text{Cu}_2$ distance of $2.5697(8)\text{ \AA}$. Instead of being displaced in a lateral direction from the four-oxygen plane, the two-coordinate Cu_1 atom lies slightly above the plane, thus accounting for the slightly shorter $\text{Cu}\cdots\text{Cu}$ distance in this $\{\text{Cu}_2(\text{XDK})\}$ unit. These structures may be contrasted to those of polymeric $\text{Cu}(\text{I})$ acetate⁵² and tetrameric $\text{Cu}(\text{I})$ benzoate,⁵³ where oligomerization via the bridging carboxylate oxygen atoms occurs, presumably because of the greater conformational flexibility of these ligands. Apparently the convergent nature of the XDK ligand coupled with the chelate effect cause the carboxylate ligands to bind the copper ions more tightly compared to simple $\text{Cu}(\text{I})$ carboxylates, thus inhibiting oligomerization.

Exposure of **10** to CO in THF or CH_2Cl_2 solution followed by solvent removal afforded no product, as judged by IR and NMR spectroscopy. These results are in contrast to the stable CO adducts obtained with $\text{Cu}(\text{I})$ benzoate and other simple car-

boxylates.^{40,46} Carbon monoxide is a very poor sigma donor, and the Cu(I) ions in the {Cu₂(XDK)} platform must also be unable to engage in π backbonding with this ligand. Both factors preclude stable adduct formation.

Reaction of **10**, **11**, or **12** with excess tmeda followed by recrystallization from THF/pentane provided mono(tmeda) adducts **17-19** as colorless blocks or needles. These reactions do not occur for Cu(I) acetate or benzoate, which upon exposure to excess tmeda under identical conditions immediately disproportionates to Cu metal and uncharacterized Cu(II) products. An X-ray structure was obtained for **17**. This complex is composed of one linear two-coordinate copper, analogous to that observed for acetonitrile complex **10**, and a tetrahedrally ligated copper with a chelating tmeda molecule. The Cu...Cu distances in **10** and **17** are also nearly identical.

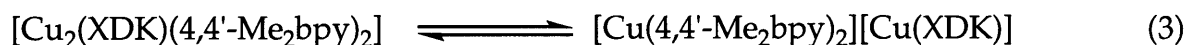
Because tmeda adducts **17-19** react with dioxygen at low temperature to afford stable peroxo intermediates in some cases,⁴³ detailed knowledge of their solution properties was desired. Of particular interest was to determine whether the Cu(I) ions remained coordinated to the XDK ligand in solution, and whether the tmeda ligand exhibited fluxional behavior. All of the tmeda adducts are non-electrolytes in CH₂Cl₂ solution, even in the presence of a 20-fold excess of tmeda, confirming that the Cu(I) ions remain coordinated to the carboxylates in solution. The ¹H NMR spectrum of each of the tmeda adducts exhibits a single set of XDK resonances, suggesting that the approximate C_s symmetry of the solid state structure of **17** may not be maintained in solution. If it were, the pair of four-proton doublets assigned to the XDK methylene groups (H_{ax} and H_{eq}, below) might split into four, two-proton doublets. This phenomenon has been observed for other asymmetrically ligated M₂XDK and heterodimetallic MM'(XDK) complexes, when one of the mirror planes of the C_{2v}-symmetric XDK ligand is lost.⁴³ The psuedo C_{2v}-symmetric spectral pattern observed for **17** suggests that the tmeda ligand exchanges between the two copper sites

in $\text{Cu}_2(\text{XDK})$ by an intra- and/or intermolecular fashion, resulting in one set of averaged H_{ax} and H_{eq} resonances.

Additional ^1H NMR experiments were carried out to help elucidate the nature of this exchange process. The ^1H NMR spectrum of recrystallized **17** in the presence of one additional equiv of tmeda still displayed a single set of tmeda and XDK resonances, slightly shifted from those in **17**, suggesting that free and coordinated tmeda exchange rapidly on the ^1H NMR timescale. To determine whether the tmeda ligand in **17** could be exchanging intermolecularly between different $\{\text{Cu}_2(\text{XDK})\}$ units, a ^1H NMR spectrum of an equimolar mixture of **17** and parent complex **16** was recorded at room temperature. The spectrum exhibited one set of XDK and tmeda resonances, and the chemical shifts of the XDK resonances were the average of those observed for pure **16** and **17**. A variable temperature (VT) ^1H NMR spectroscopic study was carried out on pure **17**. As the temperature was decreased, the two sharp tmeda singlets (methyl and methylene protons) broadened and overlapped one another. The tmeda resonances appeared to coalesce between -70 and -80 $^\circ\text{C}$. Below this temperature one broad singlet was observed for the tmeda methyl groups, and the tmeda methylene resonances appeared to be split into two broad singlets in an approximately 3:1 ratio. One sharp set of XDK resonances was observed down to -85 $^\circ\text{C}$, accompanied by small changes in their chemical shifts. A more detailed interpretation of the VT data was hampered by overlap of the tmeda resonances with each other and with the XDK resonances. Although no detailed mechanistic information could be gleaned from the VT experiments, the broadening and shifting of the tmeda resonances with decreasing temperature does support the occurrence of some fluxional tmeda exchange process(es), perhaps involving copper-nitrogen bond breaking and/or different conformations of the five-membered tmeda chelate ring. Taken together, these additional ^1H NMR experiments

support the conclusion that the tmeda ligands in complexes **17-19** are exchanging rapidly between copper sites, but do not reveal the mechanism.

Treatment of **10** with two equiv of 4,4'-dimethyldipyridine afforded **20** as a dark brick-red solid. This color is characteristic of the $[\text{Cu}(\text{bpy})_2]^+$ cation,⁵⁴ and immediately suggested that one of the copper ions had been extracted from the bis(carboxylate) platform. Neutral and ionic species may be in equilibrium, as indicated by eq 3. A similar equilibrium was suggested to explain the solution



behavior of $[\text{Cu}(\text{phen})_2]_2[\text{Cu}(\text{OAc})_2]$, specifically based on its crystal structure and solution conductivity properties.^{54,55} Determination of the molar conductivity from a plot of the measured conductivity versus concentration for complex **20** in CH_2Cl_2 solution (Figure 1.5) gave approximately the same value as those obtained for Bu_4NPF_6 and $[\text{Cu}(\text{MeCN})_4]\text{ClO}_4$, consistent with the equilibrium in eq 3 lying completely to the right. Suitable crystals of **20** could not be obtained for X-ray crystallography. Based on the similarity of its UV-vis spectral features to those of $[\text{Cu}(\text{phen})_2]_2[\text{Cu}(\text{OAc})_2]$ and its conductivity properties, **20** is probably composed of a bis(dipyridyl) cation and a linear two coordinate $\text{Cu}(\text{XDK})$ anion.

Anionic Donors: Preparation of $(\text{Et}_4\text{N})[\text{Cu}(\text{PXDK})]$ (21**) and $[\text{CuLi}(\text{XDK})(\text{THF})_2]$ (**22**).** We attempted to prepare a class of anionic-bridged dicopper(I) XDK complexes in order to explore further the chemistry of this system. Attempts to synthesize thio- late- or cyanide-bridged $\{\text{Cu}_2(\text{XDK})\}$ complexes from $\text{Et}_4\text{N}(\text{SR})$ ($\text{R} = \text{Ph}, \text{Me}$) and $\text{Et}_4\text{N}(\text{CN})$, respectively, were unsuccessful. The former reagents invariably yielded copper(I) sulfide and intractable XDK-containing products. Reaction of acetonitrile adduct **11** with tetraethylammonium cyanide in CH_2Cl_2 immediately resulted in precipitation of Cu(I) cyanide and formation of **21**, as judged by IR and ^1H NMR

spectroscopic analyses. The solid state structure of **21** is composed of two crystallographically independent clusters which differ only in the orientation of the peripheral propyl groups. Each contains linear two-coordinate copper ligated by cis-carboxylate oxygen atoms. This mononuclear complex is unreactive toward additional cyanide, attesting to the effectiveness of the XDK ligand for retaining the remaining copper atom in the "skewered" two coordinate arrangement.

Alkyl- and aryl-bridged cuprate complexes of XDK were sought for studies of conjugate addition and other R⁻ transfer reactions. The only structurally characterized Cu(I) carboxylate-alkyl or aryl complex reported to date is [Cu₃(μ-Mes)(μ-O₂CPh)₂], a neutral trinuclear cluster isolated upon exposure of Cu(I) benzoate to pentameric mesitylcopper(I).⁵⁶ No well characterized Cu(I) carboxylate alkyl or aryl cuprates have been described. Treatment of **10** with one equiv of PhLi in THF afforded heterodimetallic complex **22** as the only XDK-containing product isolated, even when a large excess of 12-crown-4 was added. Much difficulty was experienced in trying to purify **22** from the phenylcopper(I) coproduct and large amounts of an intractable brown material. As in the preparation of mononuclear **21**, this complex was obtained more conveniently from **10** and lithium cyanide. The solid state structure consists of a linear two coordinate copper atom and a tetrahedrally ligated lithium atom bridged by XDK. Crystals of **22** lose one of the coordinated THF molecules upon isolation and drying, as judged by integration of the ¹H NMR spectrum and elemental analysis, presumably to afford [CuLi(XDK)(THF)]. The solid state structure is unknown, but by analogy to other heterodimetallic alkali metal XDK complexes,⁵⁷ the lithium ion is probably coordinated to one or more of the XDK imide carbonyl oxygens. Compounds **21** and **22** provided the ideal kinetic stability for the preparation of a host of Cu(I)/Cu(II) mixed valent and Cu(I)M(II) heterodimetallic bis(carboxylate)-bridged complexes, which are the subject of a separate report.³²

Conclusions

A more sterically demanding version of XDK and PXDK has been prepared in multigram quantities and high purity. The kinetic stability imparted by the convergent nature of the XDK ligand system provides an excellent template for the synthesis of discrete dinuclear Cu(I) complexes. All three XDK derivatives afford complexes, some heretofore unknown for Cu(I) carboxylates, of π acceptor and sigma donor ligands. Disproportionation reactions which occur with the simple Cu(I) carboxylates are not observed with XDK. Attempts to prepare anionic-bridged Cu_2XDK complexes resulted instead in extrusion of one Cu(I) ion and formation of mono-copper(I) XDK products.

Acknowledgement. This work was supported by a grant from the National Science Foundation.

References and Notes

- (1) Most of this work has appeared previously in a slightly altered form in reference (2), © American Chemical Society.
- (2) LeCloux, D. D.; Lippard, S. J. *Inorg. Chem.* **1997**, *36*, 4035-4046.
- (3) Feig, A. L.; Lippard, S. J. *Chem. Rev.* **1994**, *94*, 759-805.
- (4) Liu, K. E.; Lippard, S. J. In *Adv. Inorg. Chem.*; A. G. Sykes, Ed.; Academic Press, Inc.: San Diego, CA, 1995; Vol. 42; pp 263-289.
- (5) Wallar, B. J.; Lipscomb, J. D. *Chem. Rev.* **1996**, *96*, 2625-2657.
- (6) Solomon, E. I.; Sundaram, U. M.; Machonkin, T. E. *Chem. Rev.* **1996**, *96*, 2563-2605.
- (7) Semrau, J. D.; Zolanz, D.; Lidstrom, M. E.; Chan, S. I. *J. Inorg. Biochem.* **1995**, *58*, 235-244.
- (8) Nguyen, H. T.; Shiemke, A. K.; Jacobs, S. J.; Hales, B. J.; Lidstrom, M. E.; Chan, S. I. *J. Biol. Chem.* **1994**, *269*, 14995-15005.
- (9) Chan, S. I.; Nguyen, H. T.; Shiemke, A. K.; Lidstrom, M. E. In *Bioinorganic Chemistry of Copper*; K. D. Karlin and Z. Tyeklar, Ed.; Chapman and Hall: New York, 1993; pp 184-195.
- (10) Zahn, J. A.; DiSpirito, A. A. *J. Bacteriol.* **1996**, *178*, 1018-1029.
- (11) Klinman, J. P. *Chem. Rev.* **1996**, *96*, 2541-2561.
- (12) Klinman, J. P.; Berry, J. A.; Tian, G. In *Bioinorganic Chemistry of Copper*; K. D. Karlin and Z. Tyeklar, Ed.; Chapman and Hall: New York, 1993; pp 151-163.
- (13) Herold, S. H.; Lippard, S. J. *J. Am. Chem. Soc.* **1997**, *119*, 145-156.
- (14) Herold, S. H.; Lippard, S. J. *Inorg. Chem.* **1997**, *36*, 50-58.
- (15) Tanase, T. T.; Yun, J. W.; Lippard, S. J. *Inorg. Chem.* **1996**, *35*, 3585.
- (16) Tanase, T.; Lippard, S. J. *Inorg. Chem.* **1995**, *34*, 4682-4690.
- (17) Tanase, T.; Yun, J. W.; Lippard, S. J. *Inorg. Chem.* **1995**, *34*, 4220-4229.

- (18) Yun, J. W.; Tanase, T.; Pence, L. E.; Lippard, S. J. *J. Am. Chem. Soc.* **1995**, *117*, 4407.
- (19) Watton, S. P.; Masschelein, A.; Rebek, J., Jr.; Lippard, S. J. *J. Am. Chem. Soc.* **1994**, *116*, 5196-5205.
- (20) Goldberg, G. P.; Watton, S. P.; Masschelein, A.; Wimmer, L.; Lippard, S. J. *J. Am. Chem. Soc.* **1993**, *115*, 5346-5347.
- (21) Rardin, R. L.; Tolman, W. B.; Lippard, S. J. *New J. Chem.* **1991**, *15*, 417-430.
- (22) Karlin, K. D.; Kaderli, S.; Zuberbühler, A. D. *Acc. Chem. Res.* **1997**, *30*, 139-147.
- (23) Fox, S.; Karlin, K. D. In *Reactive Oxygen in Biochemistry*; J. S. Valentine, C. S. Foote, A. Greenberg and J. F. Liebman, Ed.; Blackie Academic and Professional, Chapman & Hall: Glasgow, 1995; pp 188-231.
- (24) Kitajima, N.; Moro-oka, Y. *Chem. Rev.* **1994**, *94*, 737-757.
- (25) Mahapatra, S.; Halfen, J. A.; Wilkinson, E. C.; Pan, G.; Wang, X.; Jr., V. G. Y.; Cramer, C. J.; Jr., L. Q.; Tolman, W. B. *J. Am. Chem. Soc.* **1996**, *118*, 11555-11574.
- (26) Mahapatra, S.; Halfen, J. A.; Tolman, W. B. *J. Am. Chem. Soc.* **1996**, *118*, 11575-11586.
- (27) Feig, A. L.; Masschelein, A.; Bakac, A.; Lippard, S. J. *J. Am. Chem. Soc.* **1997**, *119*, 334-342.
- (28) Feig, A. L.; Becker, M.; Schindler, S.; Eldik, R. v.; Lippard, S. J. *Inorg. Chem.* **1996**, *35*, 2590-2601.
- (29) Que, L., Jr.; Dong, Y. *Acc. Chem. Res.* **1996**, *29*, 190-196.
- (30) Herold, S.; Pence, L. E.; Lippard, S. J. *J. Am. Chem. Soc.* **1995**, *117*, 6134-6135.
- (31) Abbreviations used: H₂XDK, *m*-xylylenediamine bis(Kemp's triacid imide); H₂PXDK, *m*-xylylenediamine bis(propyl Kemp's triacid imide); H₂BXDK, *m*-xylylenediamine bis(benzyl Kemp's triacid imide); NB, norbornene; tmeda,

N,N,N',N'-tetramethylethylenediamine; 4,4'-Me₂bpy, 4,4'-dimethyl-2,2'-dipyridine; phen, 1,10-phenanthroline.

- (32) LeCloux, D. D.; Lippard, S. J., Manuscript In Preparation.
- (33) Rebek, J., Jr.; Marshall, L.; Wolak, R.; Parris, K.; Killoran, M.; Askew, B.; Nemeth, D.; Islam, N. *J. Am. Chem. Soc.* **1985**, *107*, 7476-7481.
- (34) *SMART: Version 4.0*; Siemens Industrial Automation, Inc.: Madison, WI, 1995.
- (35) Feig, A. L.; Bautista, M. T.; Lippard, S. J. *Inorg. Chem.* **1996**, *35*, 6892-6898.
- (36) Burla, M. C.; Camalli, M.; Cascarano, G.; Giacovazzo, C.; Polidori, G.; Spagna, R.; Viterbo, D. *J. Appl. Crystallogr.* **1989**, *22*, 389-393.
- (37) *TEXSAN: Single Crystal Structure Analysis Software. 1.6c*; Molecular Structure Corporation.: The Woodlands, TX, 1995.
- (38) *SHELXTL: Structure Analysis Program. 5.0*; Siemens Industrial Automation, Inc.: Madison, WI, 1995.
- (39) Flack, H. D. *Acta Crystallogr.* **1983**, *A39*, 876-881.
- (40) Pasquali, M.; Floriani, C.; Venturi, G.; Gaetani-Manfredotti, A.; Chiesi-Villa, A. *J. Am. Chem. Soc.* **1982**, *104*, 4092-4099.
- (41) Toth, A.; Floriani, C.; Chiesi-Villa, A.; Guastini, C. *Inorg. Chem.* **1987**, *26*, 236-241.
- (42) Pasquali, M.; Leoni, P.; Floriani, C.; Gaetani-Manfredotti, A. *Inorg. Chem.* **1982**, *21*, 4324-4328.
- (43) LeCloux, D. D.; Lippard, S. J., Unpublished results.
- (44) Kato, Y.; Conn, M. M.; Rebek, J., Jr. *J. Am. Chem. Soc.* **1994**, *116*, 3279-3284.
- (45) Jeong, K. S.; Muehldorf, A. V.; Rebek, J., Jr. *J. Am. Chem. Soc.* **1990**, *112*, 6144-6145.
- (46) Doyle, G.; Erikson, K. A.; Modrick, M.; Ansell, G. *Organometallics* **1982**, *1*, 1613-1618.

- (47) Hathaway, B. J. In *Comprehensive Coordination Chemistry*; G. Wilkinson, Ed.; Pergamon: New York, 1987; Vol. 5; pp 533-774.
- (48) Mehrotra, P. K.; Hoffmann, R. *Inorg. Chem.* **1978**, *17*, 2187-2189.
- (49) Gill, J. T.; Mayerle, J. J.; Welcker, P. S.; Lewis, D. F.; Ucko, D. A.; Barton, D. J.; Stowens, D.; Lippard, S. J. *Inorg. Chem.* **1976**, *15*, 1155-1168.
- (50) Darensbourg, D. J.; Holtcamp, M. W.; Longridge, E. M.; Klausmeyer, K. K.; Reibenspies, J. H. *Inorg. Chim. Acta* **1994**, *227*, 223-232.
- (51) Hakansson, M.; Jagner, S.; Clot, E.; Eisenstein, O. *Inorg. Chem.* **1992**, *31*, 5389-5394.
- (52) Drew, M. G. B.; Edwards, D. A.; Richards, R. J. *Chem. Soc., Chem. Commun.* **1973**, 124-125.
- (53) Drew, M. G. B.; Edwards, D. A.; Richards, R. J. *Chem. Soc., Dalton Trans.* **1977**, 299-303.
- (54) Edwards, D. A.; Richards, R. J. *Chem. Soc. Dalton Trans.* **1975**, 637.
- (55) Darensbourg, D. J.; Longridge, E. M.; Atnip, E. V.; Reibenspies, J. H. *Inorg. Chem.* **1992**, *31*, 3951-3955.
- (56) Aalten, H. L.; van Koten, G.; Goublitz, K.; Stam, C. H. *Organometallics* **1989**, *8*, 2293-2299.
- (57) Watton, S. P.; Davis, M. I.; Pence, L. E.; Rebek, J., Jr. *Inorg. Chim. Acta* **1995**, *235*, 195-204.

Table 1.1. Summary of X-ray Crystallographic Data.

	H ₂ BXDK (6)	[Cu ₂ (XDK)(MeCN)] (10)·1CH ₃ CN	[Cu ₂ (XDK)(PPh ₃) ₂] (13)·1PhCl	[Cu ₂ (XDK)(ArNC) ₃] (14a)·0.5PhCl	[Cu ₂ (XDK)(μ-ArNC) (ArNC) ₂] (14b)·0.5PhCl·1Et ₂ O
formula	C ₆₂ H ₆₄ N ₂ O ₈	C ₃₆ H ₄₄ N ₄ O ₈ Cu ₂	C ₇₄ H ₇₃ N ₂ O ₈ ClP ₂ Cu ₂	C ₆₂ H _{67.5} N ₅ O ₈ Cl _{0.5} Cu ₂	C ₆₆ H _{77.5} N ₅ O ₉ Cl _{0.5} Cu ₂
fw	965.15	787.83	1342.81	1155.51	1229.64
space group	<i>P</i> 2 ₁ / <i>c</i>	<i>P</i> 2 ₁ / <i>c</i>	<i>C</i> 2/ <i>c</i>	<i>P</i> 1	<i>P</i> 2 ₁ / <i>n</i>
a, Å	11.91550(10)	13.6100(2)	41.7699(6)	11.8747(2)	22.5777(3)
b, Å	28.7491(4)	16.1248(3)	20.07040(10)	13.8800(2)	12.3144(2)
c, Å	17.2033(2)	17.69810(10)	16.2744(2)	18.50390(10)	23.6382(4)
α, deg				97.5001(9)	
β, deg	108.4970(10)	112.2098(7)	102.9530(10)	90.9158(10)	109.96(1)
γ, deg				106.1093(8)	
V, Å ³	5588.72(11)	3595.83(9)	13296.3(3)	2900.64(7)	6190.8(2)
Z	4	4	8	2	4
ρ _{calcd} , g/cm ³	1.147	1.455	1.342	1.323	1.319
T, °C	-85	-85	-85	-85	-85
μ(Mo Kα), mm ⁻¹	0.075	1.239	0.785	0.814	0.769
transmission coeff	0.854-1.000	0.828-1.000	0.831-1.000	0.857-1.000	0.852-1.000
2θ limits, deg	3-57	3-46	3-57	3-57	3-57
total no. of data	33729	13960	39721	17531	35986
no. of unique data	12738	5089	15154	12211	14149
observed data ^a	9442	4355	10375	8121	8708
no. of parameters	959	627	797	703	728
R(%) ^b	5.15	3.41	5.67	4.97	8.00
wR ² (%) ^c	11.26	7.59	15.25	11.26	21.65
max, min peaks, e/Å ³	0.302, -0.227	0.730, -0.633	1.039, -1.138	0.494, -0.463	1.240, -1.037

^aObservation criterion: $I > 2\sigma(I)$. ^b $R = \sum ||F_o| - |F_c|| / \sum |F_o|$. ^c $wR^2 = \{\sum [w(F_o^2 - F_c^2)^2] / \sum [w(F_o^2)]\}^{1/2}$.

Table 1.1 (cont'd.) Summary of X-ray Crystallographic Data.

	[Cu ₂ (XDK)(NB) ₂] (15)·1Et ₂ O	[Cu ₂ (XDK) ₂] (16)·1.5PhCl	[Cu ₂ (XDK)(tmeda)] (17)·2THF	(Et ₄ N)[Cu(XDK)] (21)·0.5CH ₃ CN	[CuLi(XDK)(THF) ₂] (22)·1THF
formula	C ₅₀ H ₆₈ N ₂ O ₉ Cu ₂	C ₇₃ H _{83.5} N ₄ O ₁₆ Cl _{1.5} Cu ₄	C ₄₆ H ₇₀ N ₄ O ₁₀ Cu ₂	C ₅₃ H _{83.5} N _{3.5} O ₈ Cu ₁	C ₄₄ H ₆₂ N ₂ O ₁₁ Li ₁ Cu ₁
fw	968.14	1580.27	966.14	961.27	865.44
space group	<i>P</i> $\bar{1}$	<i>P</i> $\bar{1}$	<i>Pna</i> 2 ₁	<i>P</i> 2 ₁	<i>P</i> $\bar{1}$
a, Å	12.4880(7)	13.7573(6)	21.3272(4)	10.6886(2)	11.75850(10)
b, Å	13.0087(8)	16.5180(7)	18.0465(3)	16.3952(3)	12.11510(10)
c, Å	15.0250(9)	17.8154(7)	12.4138(2)	30.5770(1)	16.73070(10)
α, deg	93.8052(8)	67.6240(10)			102.1888(2)
β, deg	94.5239(11)	70.5980(10)		96.12(1)	96.4520(6)
γ, deg	98.6628(10)	89.0870(10)			108.5870(2)
V, Å ³	2397.9(2)	3502.5(3)	4777.84(14)	5327.87(14)	2166.22(3)
Z	2	2	4	4	2
ρ _{calcd} , g/cm ³	1.341	1.498	1.343	1.198	1.327
T, °C	-85	-85	-85	-85	-85
μ(Mo Kα), mm ⁻¹	0.943	1.326	0.949	0.463	0.565
transmission coeff	0.736-1.000	0.795-1.000	0.845-1.000	0.856-1.000	0.900-1.000
2θ limits, deg	3-46	3-57	3-57	3-57	3-57
total no. of data	9589	21334	28775	33173	13402
no. of unique data	6570	14903	9880	22720	9309
observed data ^a	5445	9646	8203	16140	7405
no. of parameters	584	862	512	1179	736
R(%) ^b	3.78	6.14	5.01	5.21	5.37
wR ² (%) ^c	9.58	14.92	12.87	13.99	14.18
max, min peaks, e/Å ³	0.474, -0.378	0.960, -1.016	0.834, -0.399	0.482, -0.331	1.150, -0.573

^aObservation criterion: $I > 2\sigma(I)$. ^b $R = \sum ||F_O| - |F_C|| / \sum |F_O|$. ^c $wR^2 = \{\sum [w(F_O^2 - F_C^2)^2] / \sum [w(F_O^2)]\}^{1/2}$.

Table 2.2. Selected Bond Distances and Angles.^a

	<u>Distances</u>		<u>Angles</u>	
6	O101-C101	1.311(2)	O102-C101-O101	123.2(2)
	O102-C101	1.222(2)	O201-C201-O202	123.09(14)
	O201-C201	1.224(2)		
	O202-C201	1.308(2)		
	O101...O201	2.651(2)		
	O102...O202	2.678(2)		
10	Cu1...Cu2	2.6287(5)	O102-Cu1-O202	172.00(8)
	Cu1-O102	1.857(2)	O101-Cu2-O201	141.37(9)
	Cu1-O202	1.880(2)	O101-Cu2-N1	94.45(11)
	Cu2-O101	2.002(2)	O201-Cu2-N1	123.93(11)
	Cu2-O201	1.919(2)		
	Cu2-N1	1.989(3)		
13	Cu1...Cu2	3.1171(6)	O102-Cu1-O202	138.07(10)
	Cu1-O102	1.963(2)	O101-Cu2-O201	116.93(10)
	Cu1-O202	1.957(2)	O102-Cu1-P1	107.65(8)
	Cu2-O101	1.977(2)	O202-Cu1-P1	113.79(7)
	Cu2-O201	1.998(2)	O101-Cu2-P2	122.21(7)
	Cu1-P1	2.2427(9)	O201-Cu2-P2	120.81(7)
	Cu2-P2	2.1652(9)		
14a	Cu1...Cu2	3.2560(5)	O102-Cu1-O202	117.80(10)
	Cu1-O102	1.972(2)	O101-Cu2-O201	107.41(10)
	Cu1-O202	1.981(2)	O102-Cu1-C1	119.77(12)
	Cu2-O101	2.069(2)	O202-Cu1-C1	121.82(12)
	Cu2-O201	2.084(2)	O101-Cu2-C2	110.96(12)
	Cu1-C1	1.842(3)	O201-Cu2-C2	111.09(12)
	Cu2-C2	1.877(3)	O101-Cu2-C3	98.83(11)
	Cu2-C3	1.930(3)	O201-Cu2-C3	97.12(11)
	C1-N1	1.157(4)	C1-N1-C4	176.1(3)
	C2-N2	1.158(4)	C2-N2-C12	172.9(3)

Table 2.2. (cont'd.) Selected Bond Distances and Angles.^a

	<u>Distances</u>		<u>Angles</u>	
14a	C3-N3	1.156(4)	C3-N3-C20	168.0(3)
14b	Cu1...Cu2	2.7278(9)	O102-Cu1-O202	114.05(13)
	Cu1-O102	2.059(3)	O101-Cu2-O201	117.56(13)
	Cu1-O202	2.035(3)	O102-Cu1-C1	109.1(2)
	Cu2-O101	2.071(3)	O102-Cu1-C2	99.3(2)
	Cu2-O201	2.022(3)	O101-Cu2-C2	99.1(2)
	Cu1-C1	1.921(7)	O101-Cu2-C3	98.8(2)
	Cu1-C2	2.001(6)	C1-N1-C4	173.1(6)
	Cu2-C2	2.135(5)	C2-N2-C12	175.3(5)
	Cu2-C3	1.908(6)	C3-N3-C20	172.0(5)
15	Cu1...Cu2	3.4211(6)	O102-Cu1-O202	126.86(10)
	Cu1-O102	1.965(2)	O101-Cu2-O201	105.17(9)
	Cu1-O202	1.963(2)	O102-Cu1-C8	133.95(13)
	Cu2-O101	1.978(2)	O102-Cu1-C9	96.70(13)
	Cu2-O201	1.981(2)	O101-Cu2-C1	108.2(2)
	Cu1-C8	2.070(4)	O101-Cu2-C2	146.6(2)
	Cu1-C9	2.076(4)		
	Cu2-C1	2.023(4)		
	Cu2-C2	2.033(3)		
16	Cu1...Cu2	2.5697(8)	O102-Cu1-O202	168.9(2)
	Cu3...Cu4	2.6106(9)	O101-Cu2-O201	160.85(12)
	Cu1-O102	1.855(3)	O101-Cu2-O504	94.65(11)
	Cu1-O202	1.859(3)	O201-Cu2-O504	98.50(12)
	Cu2-O101	1.970(3)	O402-Cu3-O502	170.87(14)
	Cu2-O201	1.942(3)	O401-Cu4-O501	165.8(2)
	Cu2-O504	2.191(3)		
	Cu3-O402	1.873(3)		
	Cu3-O502	1.871(3)		

Table 2.2. (cont'd.) Selected Bond Distances and Angles.^a

	<u>Distances</u>		<u>Angles</u>	
16	Cu4-O401	1.875(3)		
	Cu4-O501	1.869(3)		
17	Cu1...Cu2	2.6245(7)	O102-Cu1-O202	175.4(2)
	Cu1-O102	1.857(3)	O101-Cu2-O201	143.36(11)
	Cu1-O202	1.859(3)	O101-Cu2-N1	99.50(13)
	Cu2-O101	2.014(3)	O101-Cu2-N2	105.32(13)
	Cu2-O201	1.999(3)	O201-Cu2-N1	101.63(13)
	Cu2-N1	2.165(3)	O201-Cu2-N2	106.25(14)
	Cu2-N2	2.201(4)		
21	Cu1-O102	1.850(3)	O102-Cu1-O202	176.70(14)
	Cu1-O202	1.848(3)		
22	Cu1...Li1	3.023(4)	O102-Cu1-O202	171.63(8)
	Cu1-O102	1.855(2)	O101-Li1-O201	128.3(3)
	Cu1-O202	1.862(2)	O101-Li1-O1	106.0(2)
	Li1-O101	1.901(5)	O101-Li1-O2	107.0(2)
	Li1-O201	1.908(5)	O201-Li1-O1	104.5(2)
	Li-O1	1.986(5)	O201-Li1-O2	103.9(2)
	Li1-O2	1.971(5)		

^aNumbers in parentheses are estimated standard deviations of the last significant figure. Atoms are labeled as indicated in Figures 1-4.

Table 1.3. Atomic coordinates ($\times 10^4$) and equivalent isotropic displacement parameters ($\text{Å}^2 \times 10^3$) for **6**.^a

atom	x	y	z	U(eq)
O(101)	1173(1)	8450(1)	5419(1)	34(1)
O(102)	1818(1)	8145(1)	4447(1)	32(1)
O(201)	1470(1)	9234(1)	4696(1)	30(1)
O(202)	1840(1)	8929(1)	3613(1)	27(1)
O(103)	-1655(1)	8158(1)	4993(1)	35(1)
O(104)	-185(1)	7542(1)	3094(1)	31(1)
O(203)	-251(1)	9023(1)	1891(1)	31(1)
O(204)	-1353(1)	9666(1)	3939(1)	31(1)
N(101)	-1014(1)	7821(1)	4022(1)	22(1)
N(201)	-845(1)	9362(1)	2884(1)	22(1)
C(101)	1505(1)	8100(1)	5054(1)	25(1)
C(102)	-1147(1)	7833(1)	4804(1)	24(1)
C(103)	-323(1)	7496(1)	3754(1)	22(1)
C(104)	2853(2)	7655(1)	6127(1)	33(1)
C(105)	351(2)	6669(1)	3836(1)	28(1)
C(106)	-1373(2)	7342(1)	5955(1)	30(1)
C(107)	1564(1)	7633(1)	5487(1)	25(1)
C(108)	1483(1)	7231(1)	4887(1)	26(1)
C(109)	220(1)	7098(1)	4341(1)	23(1)
C(110)	-545(1)	7001(1)	4887(1)	24(1)
C(111)	-616(1)	7433(1)	5385(1)	24(1)
C(112)	640(1)	7576(1)	5933(1)	27(1)
C(113)	3158(1)	7252(1)	6719(1)	34(1)
C(114)	3562(2)	6832(1)	6518(1)	42(1)
C(115)	3771(2)	6455(1)	7052(2)	54(1)
C(116)	3616(2)	6503(1)	7805(2)	56(1)
C(117)	3246(2)	6923(1)	8026(1)	53(1)
C(118)	3008(2)	7295(1)	7485(1)	45(1)
C(119)	-760(1)	6478(1)	3222(1)	27(1)
C(120)	-1015(2)	6568(1)	2390(1)	33(1)
C(121)	-2013(2)	6387(1)	1813(1)	39(1)
C(122)	-2786(2)	6113(1)	2067(1)	40(1)
C(123)	-2546(2)	6013(1)	2890(1)	38(1)
C(124)	-1536(2)	6191(1)	3464(1)	32(1)
C(125)	-2635(2)	7191(1)	5535(1)	30(1)
C(126)	-3542(2)	7516(1)	5290(2)	51(1)
C(127)	-4700(2)	7383(1)	4917(2)	69(1)
C(128)	-4979(2)	6922(1)	4776(2)	71(1)
C(129)	-4106(2)	6593(1)	5019(2)	66(1)
C(130)	-2935(2)	6725(1)	5404(1)	46(1)
C(201)	1695(1)	9281(1)	4054(1)	22(1)
C(202)	-840(1)	9721(1)	3442(1)	22(1)
C(203)	-225(1)	9363(1)	2309(1)	23(1)
C(204)	3206(1)	9887(1)	4270(1)	27(1)
C(205)	445(2)	9855(1)	1348(1)	29(1)
C(206)	-729(2)	10582(1)	3679(1)	27(1)

Table 1.3. (con't) Atomic coordinates ($\times 10^4$) and equivalent isotropic displacement parameters ($\text{Å}^2 \times 10^3$) for **6**.^a

atom	x	y	z	U(eq)
C(207)	1904(1)	9758(1)	3743(1)	22(1)
C(208)	1747(1)	9767(1)	2818(1)	24(1)
C(209)	444(1)	9806(1)	2246(1)	23(1)
C(210)	-150(1)	10223(1)	2504(1)	24(1)
C(211)	-162(1)	10163(1)	3382(1)	23(1)
C(212)	1122(1)	10127(1)	3965(1)	24(1)
C(213)	4195(1)	9557(1)	4273(1)	28(1)
C(214)	4496(2)	9189(1)	4824(1)	37(1)
C(215)	5453(2)	8898(1)	4845(1)	50(1)
C(216)	6111(2)	8979(1)	4339(2)	60(1)
C(217)	5820(2)	9347(1)	3791(2)	55(1)
C(218)	4867(2)	9629(1)	3759(1)	40(1)
C(219)	-758(2)	9934(1)	724(1)	31(1)
C(220)	-1205(2)	10383(1)	546(1)	45(1)
C(221)	-2317(2)	10462(1)	-7(2)	63(1)
C(222)	-3007(2)	10092(1)	-396(1)	62(1)
C(223)	-2573(2)	9645(1)	-237(1)	52(1)
C(224)	-1457(2)	9567(1)	314(1)	39(1)
C(225)	-1933(2)	10734(1)	3140(1)	31(1)
C(226)	-2037(2)	11072(1)	2551(1)	51(1)
C(227)	-3131(2)	11236(1)	2075(2)	69(1)
C(228)	-4144(2)	11059(1)	2171(2)	73(1)
C(229)	-4058(2)	10726(1)	2763(2)	70(1)
C(230)	-2961(2)	10564(1)	3240(2)	48(1)
C(301)	-995(1)	8596(1)	3455(1)	23(1)
C(302)	-1516(1)	8943(1)	2906(1)	22(1)
C(303)	-2645(1)	8889(1)	2351(1)	28(1)
C(304)	-3204(2)	8464(1)	2352(1)	33(1)
C(305)	-2704(1)	8103(1)	2890(1)	29(1)
C(306)	-1585(1)	8182(1)	3446(1)	22(1)
C(307)	-3234(2)	9271(1)	1765(1)	40(1)
C(308)	-3341(2)	7648(1)	2861(2)	49(1)

^aNumbers in parentheses are estimated standard deviations of the last significant figure. ^bU(eq) is defined as one third of the trace of the orthogonalized U_{ij} tensor.

Table 1.4. Atomic coordinates ($\times 10^4$) and equivalent isotropic displacement parameters ($\text{Å}^2 \times 10^3$) for **10**.^a

atom	x	y	z	U(eq)
Cu(1)	3694(1)	5078(1)	-505(1)	28(1)
Cu(2)	2209(1)	5613(1)	-15(1)	38(1)
O(103)	-36(2)	6313(2)	-2632(2)	34(1)
O(104)	2780(2)	5087(2)	-2943(2)	36(1)
O(203)	5084(2)	7255(2)	-1245(2)	41(1)
O(204)	2356(2)	8201(2)	-614(2)	37(1)
N(101)	1348(2)	5703(2)	-2826(2)	24(1)
N(201)	3732(2)	7721(2)	-915(2)	25(1)
N(1)	1509(3)	5007(3)	624(2)	59(1)
N(2)	3250(4)	3795(3)	2339(3)	81(2)
O(101)	1296(2)	5108(2)	-1083(1)	31(1)
O(102)	2641(2)	4413(1)	-1225(1)	30(1)
O(201)	3287(2)	6440(2)	439(2)	35(1)
O(202)	4622(2)	5874(2)	173(2)	31(1)
C(101)	1658(3)	4552(2)	-1401(2)	24(1)
C(102)	305(3)	5704(2)	-2841(2)	26(1)
C(103)	1861(3)	5022(2)	-3015(2)	26(1)
C(104)	801(3)	3218(2)	-1471(2)	34(1)
C(105)	1611(3)	3819(3)	-3940(2)	43(1)
C(106)	-1509(3)	5176(3)	-3570(2)	41(1)
C(107)	882(3)	3947(2)	-2007(2)	25(1)
C(108)	1313(3)	3629(2)	-2641(2)	30(1)
C(109)	1201(3)	4239(2)	-3337(2)	29(1)
C(110)	38(3)	4483(2)	-3756(2)	31(1)
C(111)	-346(3)	4918(2)	-3153(2)	28(1)
C(112)	-230(3)	4321(2)	-2444(2)	29(1)
C(201)	4233(3)	6432(2)	491(2)	26(1)
C(202)	3309(3)	8136(2)	-404(2)	28(1)
C(203)	4823(3)	7607(2)	-748(2)	29(1)
C(204)	5475(3)	6691(2)	1877(2)	37(1)
C(205)	6622(3)	8185(2)	-97(3)	43(1)
C(206)	3605(3)	9281(2)	602(2)	41(1)
C(207)	4979(3)	7097(2)	1024(2)	28(1)
C(208)	5877(3)	7330(2)	739(2)	31(1)
C(209)	5604(3)	7966(2)	40(2)	29(1)
C(210)	5119(3)	8733(2)	262(2)	33(1)
C(211)	4104(3)	8507(2)	386(2)	29(1)
C(212)	4371(3)	7880(2)	1092(2)	32(1)
C(301)	2532(3)	6721(2)	-1878(2)	25(1)
C(302)	3012(3)	7493(2)	-1732(2)	25(1)
C(303)	2840(3)	8060(2)	-2363(2)	29(1)
C(304)	2197(3)	7816(2)	-3145(2)	32(1)
C(305)	1712(3)	7040(2)	-3317(2)	28(1)
C(306)	1890(3)	6501(2)	-2663(2)	25(1)
C(307)	3348(3)	8908(2)	-2208(3)	41(1)
C(308)	1000(3)	6812(3)	-4178(2)	40(1)

Table 1.4. (con't) Atomic coordinates ($\times 10^4$) and equivalent isotropic displacement parameters ($\text{\AA}^2 \times 10^3$) for **10**.^a

atom	x	y	z	U(eq)
C(1)	1136(3)	4445(3)	820(3)	48(1)
C(2)	679(4)	3723(3)	1057(3)	57(1)
C(3)	3844(4)	4089(3)	2093(3)	55(1)
C(4)	4609(4)	4463(3)	1813(3)	63(1)

^aNumbers in parentheses are estimated standard deviations of the last significant figure. ^bU(eq) is defined as one third of the trace of the orthogonalized U_{ij} tensor.

Table 1.5. Atomic coordinates ($\times 10^4$) and equivalent isotropic displacement parameters ($\text{Å}^2 \times 10^3$) for **13**.^a

atom	x	y	z	U(eq)
Cu(1)	1481(1)	2368(1)	1940(1)	40(1)
Cu(2)	826(1)	2110(1)	2504(1)	38(1)
P(1)	1865(1)	2432(1)	1176(1)	34(1)
P(2)	499(1)	1548(1)	1529(1)	37(1)
O(101)	839(1)	3095(1)	2502(1)	39(1)
O(102)	1242(1)	3218(1)	1815(2)	50(1)
O(201)	1145(1)	1647(1)	3426(1)	39(1)
O(202)	1509(1)	1558(1)	2622(2)	50(1)
O(103)	828(1)	4031(1)	4155(2)	50(1)
O(104)	1731(1)	4475(1)	3157(2)	49(1)
O(203)	2131(1)	2255(1)	4200(2)	62(1)
O(204)	1285(1)	1983(2)	5485(2)	58(1)
N(101)	1273(1)	4236(1)	3626(2)	36(1)
N(201)	1721(1)	2117(2)	4889(2)	40(1)
C(101)	989(1)	3412(2)	2046(2)	37(1)
C(102)	938(1)	4308(2)	3622(2)	38(1)
C(103)	1438(1)	4557(2)	3074(2)	41(1)
C(104)	656(1)	3878(2)	759(3)	59(1)
C(105)	1462(1)	5562(2)	2214(3)	60(1)
C(106)	450(1)	5048(2)	3294(3)	55(1)
C(107)	839(1)	4074(2)	1661(2)	42(1)
C(108)	1099(1)	4603(2)	1599(2)	45(1)
C(109)	1236(1)	5008(2)	2410(2)	44(1)
C(110)	953(1)	5304(2)	2742(3)	47(1)
C(111)	733(1)	4754(2)	2945(2)	41(1)
C(112)	587(1)	4357(2)	2139(2)	45(1)
C(201)	1383(1)	1376(2)	3220(2)	38(1)
C(202)	1505(1)	1721(2)	5227(2)	47(1)
C(203)	1983(1)	1874(2)	4556(2)	47(1)
C(204)	1406(1)	170(2)	3049(3)	58(1)
C(205)	2443(1)	1069(3)	4849(4)	79(2)
C(206)	1439(2)	700(3)	6028(3)	80(2)
C(207)	1527(1)	734(2)	3681(2)	43(1)
C(208)	1904(1)	742(2)	3892(3)	50(1)
C(209)	2065(1)	1136(2)	4684(3)	53(1)
C(210)	1940(1)	868(2)	5426(3)	63(1)
C(211)	1568(1)	975(2)	5279(2)	55(1)
C(212)	1396(1)	601(2)	4475(2)	50(1)
C(301)	1493(1)	3177(2)	4267(2)	37(1)
C(302)	1687(1)	2827(2)	4929(2)	41(1)
C(303)	1861(1)	3161(2)	5650(2)	49(1)
C(304)	1835(1)	3846(2)	5671(2)	54(1)
C(305)	1645(1)	4214(2)	5016(2)	45(1)
C(306)	1474(1)	3866(2)	4315(2)	37(1)
C(307)	2075(1)	2778(3)	6369(3)	67(1)
C(308)	1632(1)	4966(2)	5053(3)	61(1)

Table 1.5.(con't) Atomic coordinates ($\times 10^4$) and equivalent isotropic displacement parameters ($\text{Å}^2 \times 10^3$) for **13**.^a

atom	x	y	z	U(eq)
C(1)	456(1)	663(2)	1745(2)	42(1)
C(2)	413(1)	167(2)	1139(3)	59(1)
C(3)	388(1)	-497(2)	1365(3)	74(1)
C(4)	395(1)	-662(2)	2179(4)	76(1)
C(5)	435(1)	-180(2)	2785(3)	69(1)
C(6)	471(1)	482(2)	2573(3)	55(1)
C(7)	639(1)	1544(2)	545(2)	42(1)
C(8)	458(1)	1810(2)	-196(3)	62(1)
C(9)	589(1)	1807(3)	-911(3)	82(2)
C(10)	891(1)	1523(3)	-896(4)	76(2)
C(11)	1069(1)	1268(2)	-166(3)	67(1)
C(12)	949(1)	1278(2)	559(3)	56(1)
C(13)	80(1)	1856(2)	1249(2)	37(1)
C(14)	24(1)	2505(2)	1460(3)	51(1)
C(15)	-294(1)	2767(2)	1258(3)	59(1)
C(16)	-552(1)	2385(2)	850(2)	52(1)
C(17)	-500(1)	1740(2)	639(3)	55(1)
C(18)	-184(1)	1473(2)	836(2)	49(1)
C(19)	1724(1)	2432(2)	22(2)	40(1)
C(20)	1855(1)	2027(2)	-510(2)	49(1)
C(21)	1742(1)	2058(3)	-1377(3)	64(1)
C(22)	1497(1)	2496(3)	-1724(3)	74(1)
C(23)	1360(1)	2895(2)	-1210(3)	71(1)
C(24)	1470(1)	2863(2)	-330(3)	55(1)
C(25)	2106(1)	3194(2)	1363(2)	36(1)
C(26)	2152(1)	3492(2)	2147(2)	50(1)
C(27)	2342(1)	4066(2)	2321(3)	63(1)
C(28)	2477(1)	4350(2)	1710(3)	56(1)
C(29)	2430(1)	4064(2)	922(3)	50(1)
C(30)	2246(1)	3490(2)	748(2)	44(1)
C(31)	2177(1)	1780(2)	1361(2)	32(1)
C(32)	2081(1)	1142(2)	1543(2)	41(1)
C(33)	2303(1)	621(2)	1656(2)	44(1)
C(34)	2624(1)	729(2)	1607(2)	46(1)
C(35)	2727(1)	1365(2)	1446(2)	46(1)
C(36)	2503(1)	1884(2)	1323(2)	40(1)
C(37)	348(2)	3646(3)	5924(4)	88(2)
C(38)	174(2)	3283(5)	6398(5)	128(3)
C(39)	335(3)	2606(6)	6817(8)	182(4)
C(40)	682(2)	2395(6)	6721(5)	162(4)
C(41)	800(2)	2896(3)	6274(4)	91(2)
C(42)	662(1)	3456(3)	5843(3)	73(1)
Cl(1)	166(1)	4329(1)	5434(1)	126(1)

^aNumbers in parentheses are estimated standard deviations of the last significant figure. ^b $U(eq)$ is defined as one third of the trace of the orthogonalized U_{ij} tensor.

Table 1.6. Atomic coordinates ($\times 10^4$) and equivalent isotropic displacement parameters ($\text{\AA}^2 \times 10^3$) for **14a**.^a

atom	x	y	z	U(eq)
Cu(1)	526(1)	1357(1)	8260(1)	33(1)
Cu(2)	-441(1)	2072(1)	6822(1)	29(1)
O(101)	721(2)	1258(2)	6480(1)	40(1)
O(102)	1236(2)	669(2)	7468(1)	39(1)
O(201)	528(2)	3412(2)	7451(1)	38(1)
O(202)	1066(2)	2856(2)	8449(1)	38(1)
O(103)	3320(2)	2134(2)	5574(1)	49(1)
O(104)	4130(2)	852(2)	7577(1)	39(1)
O(203)	3861(2)	3961(2)	9114(1)	39(1)
O(204)	3104(2)	5202(2)	7071(1)	45(1)
N(101)	3693(2)	1482(2)	6572(1)	28(1)
N(201)	3471(2)	4587(2)	8096(1)	29(1)
N(1)	-1012(2)	130(2)	9276(1)	34(1)
N(2)	-2369(2)	866(2)	7675(2)	40(1)
N(3)	-540(2)	3030(2)	5423(1)	34(1)
C(101)	1061(3)	633(2)	6791(2)	31(1)
C(102)	3278(3)	1382(3)	5842(2)	34(1)
C(103)	3739(3)	671(2)	6949(2)	30(1)
C(104)	-80(3)	-1051(3)	6263(2)	49(1)
C(105)	4035(3)	-1029(3)	6831(2)	43(1)
C(106)	3020(3)	377(3)	4615(2)	50(1)
C(107)	1171(3)	-329(2)	6302(2)	33(1)
C(108)	2009(3)	-840(2)	6639(2)	35(1)
C(109)	3319(3)	-388(2)	6532(2)	31(1)
C(110)	3506(3)	-345(3)	5719(2)	36(1)
C(111)	2821(3)	318(2)	5429(2)	34(1)
C(112)	1510(3)	-127(3)	5527(2)	37(1)
C(201)	818(3)	3511(2)	8119(2)	30(1)
C(202)	3011(3)	5224(2)	7723(2)	33(1)
C(203)	3404(3)	4528(2)	8852(2)	31(1)
C(204)	-551(3)	4292(3)	8742(2)	45(1)
C(205)	3356(4)	5462(3)	10081(2)	50(1)
C(206)	2638(3)	6899(2)	7810(2)	45(1)
C(207)	758(3)	4495(2)	8589(2)	31(1)
C(208)	1480(3)	4710(2)	9322(2)	34(1)
C(209)	2806(3)	5220(2)	9299(2)	33(1)
C(210)	2986(3)	6184(2)	8954(2)	38(1)
C(211)	2440(3)	5936(2)	8173(2)	33(1)
C(212)	1111(3)	5428(2)	8189(2)	34(1)
C(301)	3587(3)	3037(2)	7334(2)	29(1)
C(302)	4144(3)	3997(2)	7686(2)	30(1)
C(303)	5347(3)	4421(2)	7665(2)	37(1)
C(304)	5977(3)	3847(3)	7267(2)	41(1)
C(305)	5458(3)	2882(3)	6900(2)	36(1)
C(306)	4253(3)	2494(2)	6945(2)	28(1)
C(307)	5947(3)	5476(3)	8043(2)	56(1)

Table 1.6. (con't) Atomic coordinates ($\times 10^4$) and equivalent isotropic displacement parameters ($\text{Å}^2 \times 10^3$) for **14a**.^a

atom	x	y	z	U(eq)
C(308)	6165(3)	2290(3)	6456(2)	51(1)
C(1)	-437(3)	606(2)	8878(2)	34(1)
C(2)	-1614(3)	1321(3)	7360(2)	36(1)
C(3)	-600(3)	2637(2)	5940(2)	33(1)
C(4)	-1649(3)	-411(3)	9796(2)	34(1)
C(5)	-2053(3)	114(3)	10378(2)	45(1)
C(6)	-2633(4)	-454(4)	10904(2)	61(1)
C(7)	-2817(4)	-1471(4)	10836(2)	68(1)
C(8)	-2436(4)	-1967(3)	10246(2)	61(1)
C(9)	-1836(3)	-1457(3)	9711(2)	42(1)
C(10)	-1415(4)	-2016(3)	9065(2)	64(1)
C(11)	-1881(4)	1233(3)	10425(2)	67(1)
C(12)	-3179(3)	261(3)	8090(2)	35(1)
C(13)	-3765(3)	733(3)	8607(2)	38(1)
C(14)	-4520(3)	106(3)	9029(2)	43(1)
C(15)	-4672(3)	-927(3)	8937(2)	46(1)
C(16)	-4091(3)	-1366(3)	8408(2)	43(1)
C(17)	-3327(3)	-782(3)	7974(2)	38(1)
C(18)	-2668(4)	-1239(3)	7400(2)	59(1)
C(19)	-3595(4)	1851(3)	8705(2)	55(1)
C(20)	-212(3)	3554(2)	4824(2)	29(1)
C(21)	962(3)	3764(2)	4652(2)	36(1)
C(22)	1285(3)	4281(3)	4065(2)	48(1)
C(23)	482(4)	4598(3)	3680(2)	49(1)
C(24)	-669(3)	4387(2)	3866(2)	41(1)
C(25)	-1052(3)	3843(2)	4440(2)	32(1)
C(26)	-2310(3)	3592(3)	4636(2)	47(1)
C(27)	1839(3)	3455(3)	5098(2)	58(1)
Cl(1)	5235(3)	6700(4)	6246(3)	172(2)
C(28)	5058(5)	5761(6)	5582(5)	105(2)
C(29)	5048(5)	5938(5)	4830(5)	103(2)
C(30)	4991(5)	5132(8)	4275(3)	101(2)

^aNumbers in parentheses are estimated standard deviations of the last significant figure. ^bU(eq) is defined as one third of the trace of the orthogonalized U_{ij} tensor.

Table 1.7. Atomic coordinates ($\times 10^4$) and equivalent isotropic displacement parameters ($\text{Å}^2 \times 10^3$) for **14b**.^a

atom	x	y	z	U(eq)
Cu(1)	7335(1)	1501(1)	247(1)	47(1)
Cu(2)	8362(1)	2495(1)	122(1)	49(1)
O(101)	7881(2)	3887(3)	195(2)	56(1)
O(102)	7059(2)	3065(3)	332(2)	56(1)
O(201)	8097(1)	1748(2)	-688(1)	41(1)
O(202)	7208(2)	1054(3)	-615(1)	45(1)
O(103)	7404(2)	6193(3)	-701(1)	48(1)
O(104)	5732(2)	4447(3)	-486(2)	49(1)
O(203)	5863(1)	1606(2)	-1773(1)	44(1)
O(204)	7510(1)	3210(2)	-2114(2)	44(1)
N(101)	6583(2)	5294(3)	-574(1)	30(1)
N(201)	6689(2)	2385(3)	-1948(1)	31(1)
N(1)	6306(2)	-106(4)	343(2)	70(1)
N(2)	8525(2)	1386(3)	1319(2)	48(1)
N(3)	9661(2)	3565(4)	539(2)	49(1)
C(101)	7435(3)	3831(4)	398(2)	50(1)
C(102)	7098(2)	6009(3)	-382(2)	35(1)
C(103)	6174(2)	5054(3)	-260(2)	37(1)
C(104)	7838(4)	4322(6)	1457(2)	88(2)
C(105)	5682(3)	5733(5)	465(3)	64(2)
C(106)	7533(3)	7649(4)	221(3)	63(2)
C(107)	7408(3)	4745(4)	839(2)	55(1)
C(108)	6741(3)	4901(4)	857(2)	53(1)
C(109)	6307(2)	5596(4)	348(2)	44(1)
C(110)	6611(2)	6689(4)	343(2)	42(1)
C(111)	7228(2)	6548(4)	227(2)	42(1)
C(112)	7673(2)	5830(4)	721(2)	53(1)
C(201)	7631(2)	1119(3)	-854(2)	38(1)
C(202)	7224(2)	2377(3)	-2127(2)	33(1)
C(203)	6311(2)	1485(3)	-1936(2)	35(1)
C(204)	8052(3)	-645(4)	-975(2)	56(1)
C(205)	5877(3)	-251(4)	-2426(3)	62(1)
C(206)	7699(3)	1534(4)	-2824(2)	54(1)
C(207)	7600(2)	261(3)	-1342(2)	40(1)
C(208)	6947(2)	-232(3)	-1631(2)	44(1)
C(209)	6486(2)	411(3)	-2150(2)	43(1)
C(210)	6794(2)	630(4)	-2622(2)	45(1)
C(211)	7389(2)	1303(3)	-2351(2)	39(1)
C(212)	7865(2)	680(3)	-1820(2)	40(1)
C(301)	6632(2)	3843(3)	-1265(2)	29(1)
C(302)	6471(2)	3447(3)	-1844(2)	30(1)
C(303)	6096(2)	4029(3)	-2340(2)	32(1)
C(304)	5900(2)	5053(3)	-2231(2)	36(1)
C(305)	6055(2)	5489(3)	-1662(2)	36(1)
C(306)	6420(2)	4867(3)	-1180(2)	29(1)
C(307)	5908(2)	3583(4)	-2969(2)	43(1)

Table 1.7.(con't) Atomic coordinates ($\times 10^4$) and equivalent isotropic displacement parameters ($\text{Å}^2 \times 10^3$) for **14b**.^a

atom	x	y	z	U(eq)
C(308)	5837(2)	6606(4)	-1570(2)	51(1)
C(1)	6746(3)	512(5)	393(3)	70(2)
C(2)	8220(3)	1566(4)	826(2)	55(1)
C(3)	9197(2)	3066(4)	391(2)	49(1)
C(4)	5755(3)	-785(4)	210(3)	61(1)
C(5)	5568(3)	-1108(5)	692(3)	75(2)
C(6)	5019(4)	-1723(5)	551(4)	85(2)
C(7)	4672(4)	-2018(5)	-37(4)	86(2)
C(8)	4889(3)	-1687(5)	-505(3)	77(2)
C(9)	5424(3)	-1071(5)	-386(3)	68(2)
C(10)	5665(4)	-725(6)	-874(3)	82(2)
C(11)	5946(4)	-768(7)	1314(3)	100(2)
C(12)	8868(2)	1087(4)	1919(2)	47(1)
C(13)	9325(2)	1794(4)	2280(2)	51(1)
C(14)	9647(2)	1458(5)	2862(2)	59(1)
C(15)	9512(3)	503(6)	3074(2)	69(2)
C(16)	9052(3)	-161(6)	2719(3)	77(2)
C(17)	8720(3)	118(5)	2123(2)	68(2)
C(18)	8214(4)	-605(6)	1701(4)	114(3)
C(19)	9455(3)	2868(5)	2048(3)	76(2)
C(20)	10167(2)	4296(5)	695(2)	52(1)
C(21)	10056(3)	5333(5)	875(2)	56(1)
C(22)	10552(3)	6063(5)	1007(3)	71(2)
C(23)	11119(3)	5780(7)	964(3)	73(2)
C(24)	11216(3)	4760(7)	792(3)	71(2)
C(25)	10740(2)	3967(5)	649(2)	58(1)
C(26)	10825(3)	2834(5)	468(3)	75(2)
C(27)	9429(3)	5632(5)	915(3)	72(2)
Cl(1)	4796(3)	5971(4)	-3912(2)	126(2)
C(32)	4927(4)	5442(7)	-4505(5)	114(3)
C(33)	5421(4)	5784(8)	-4662(6)	124(4)
C(34)	5492(4)	5296(8)	-5218(6)	124(4)
O(1)	8246(4)	-3031(6)	2418(3)	140(3)
C(28)	9278(7)	-3190(13)	2320(7)	176(5)
C(29)	8832(7)	-3430(12)	2658(7)	168(5)
C(30)	7795(8)	-3228(12)	2741(7)	172(5)
C(31)	7249(6)	-2801(10)	2370(6)	141(4)

^aNumbers in parentheses are estimated standard deviations of the last significant figure. ^bU(eq) is defined as one third of the trace of the orthogonalized U_{ij} tensor.

Table 1.8. Atomic coordinates ($\times 10^4$) and equivalent isotropic displacement parameters ($\text{Å}^2 \times 10^3$) for **15**.^a

atom	x	y	z	U(eq)
Cu(2)	976(1)	5981(1)	5196(1)	28(1)
Cu(1)	2591(1)	7789(1)	6674(1)	36(1)
O(101)	-26(2)	6718(2)	5861(2)	33(1)
O(102)	1156(2)	8155(2)	6319(2)	38(1)
O(201)	1640(2)	5145(2)	6080(1)	34(1)
O(202)	3037(2)	6410(2)	6511(2)	38(1)
O(103)	-1629(2)	6162(2)	7688(2)	39(1)
O(104)	879(2)	9050(2)	8389(2)	40(1)
O(203)	3664(2)	6552(2)	8697(2)	46(1)
O(204)	888(2)	3872(2)	8038(2)	36(1)
N(101)	-375(2)	7608(2)	8014(2)	25(1)
N(201)	2285(2)	5205(2)	8352(2)	26(1)
C(101)	217(3)	7679(3)	6077(2)	28(1)
C(102)	-1375(3)	7077(2)	7601(2)	29(1)
C(103)	10(3)	8684(2)	8008(2)	31(1)
C(104)	-693(3)	8579(3)	4955(2)	44(1)
C(105)	-550(4)	10426(3)	7995(3)	52(1)
C(106)	-3278(3)	7179(3)	7079(3)	51(1)
C(107)	-695(3)	8349(3)	5951(2)	31(1)
C(108)	-464(3)	9384(3)	6536(2)	36(1)
C(109)	-741(3)	9326(2)	7518(2)	35(1)
C(110)	-1924(3)	8819(3)	7525(2)	39(1)
C(111)	-2097(3)	7718(3)	7076(2)	34(1)
C(112)	-1814(3)	7751(3)	6097(2)	35(1)
C(201)	2617(3)	5471(3)	6372(2)	29(1)
C(202)	1852(3)	4180(2)	8036(2)	29(1)
C(203)	3398(3)	5653(3)	8420(2)	33(1)
C(204)	3768(3)	4506(3)	5524(2)	43(1)
C(205)	5287(3)	5301(4)	8696(3)	54(1)
C(206)	2180(3)	2349(3)	7838(3)	49(1)
C(207)	3379(3)	4649(3)	6473(2)	31(1)
C(208)	4381(3)	5045(3)	7136(2)	35(1)
C(209)	4196(3)	4943(3)	8131(2)	36(1)
C(210)	3743(3)	3821(3)	8267(2)	41(1)
C(211)	2653(3)	3482(3)	7714(2)	35(1)
C(212)	2798(3)	3596(3)	6714(2)	36(1)
C(301)	956(2)	6411(2)	8193(2)	25(1)
C(302)	1540(2)	5830(2)	8737(2)	26(1)
C(303)	1417(3)	5813(3)	9651(2)	30(1)
C(304)	708(3)	6419(3)	10002(2)	33(1)
C(305)	133(3)	7037(2)	9487(2)	31(1)
C(306)	267(2)	7010(2)	8572(2)	26(1)
C(307)	2033(3)	5160(3)	10235(2)	42(1)
C(308)	-634(3)	7693(3)	9897(2)	45(1)
C(1)	859(4)	6359(4)	3911(3)	57(1)
C(2)	1537(4)	5661(3)	3990(2)	48(1)

Table 1.8.(con't) Atomic coordinates ($\times 10^4$) and equivalent isotropic displacement parameters ($\text{Å}^2 \times 10^3$) for **15**.^a

atom	x	y	z	U(eq)
C(3)	2638(3)	6202(3)	3835(3)	54(1)
C(4)	2610(4)	7250(4)	4222(3)	70(2)
C(5)	1557(4)	7365(3)	3731(3)	74(2)
C(6)	1828(4)	7168(4)	2744(3)	69(1)
C(7)	2599(4)	6379(3)	2831(3)	52(1)
C(8)	4073(3)	8643(3)	7180(3)	46(1)
C(9)	3270(3)	9234(3)	7307(3)	45(1)
C(10)	3424(3)	10104(3)	6690(3)	47(1)
C(11)	3858(3)	9569(3)	5904(3)	53(1)
C(12)	4723(3)	9135(3)	6479(3)	53(1)
C(13)	5372(3)	10167(3)	6975(4)	64(1)
C(14)	4463(3)	10835(3)	7114(4)	64(1)
O(1)	6568(4)	10099(4)	9554(3)	116(2)
C(15)	6222(5)	8327(6)	9726(4)	111(2)
C(16)	6625(7)	9456(6)	10162(4)	123(3)
C(17)	6834(6)	11166(5)	9939(5)	122(2)
C(18)	6643(5)	11848(4)	9240(3)	90(2)

^aNumbers in parentheses are estimated standard deviations of the last significant figure. ^bU(eq) is defined as one third of the trace of the orthogonalized U_{ij} tensor.

Table 1.9. Atomic coordinates ($\times 10^4$) and equivalent isotropic displacement parameters ($\text{Å}^2 \times 10^3$) for **16**.^a

atom	x	y	z	U(eq)
Cu(1)	5019(1)	8923(1)	759(1)	33(1)
Cu(2)	4018(1)	7367(1)	1436(1)	28(1)
Cu(3)	617(1)	6239(1)	853(1)	32(1)
Cu(4)	1361(1)	7272(1)	1388(1)	35(1)
O(101)	2812(2)	8014(2)	1651(2)	24(1)
O(102)	3765(2)	9318(2)	1181(2)	31(1)
O(201)	5432(2)	7076(2)	1214(2)	28(1)
O(202)	6270(2)	8453(2)	555(2)	39(1)
O(103)	1696(2)	6957(2)	3849(2)	31(1)
O(104)	3547(3)	9448(2)	3362(2)	39(1)
O(203)	6727(3)	8313(2)	2565(2)	38(1)
O(204)	5278(3)	5607(2)	3120(2)	37(1)
N(101)	2695(3)	8227(2)	3465(2)	22(1)
N(201)	5994(3)	6968(2)	2821(2)	25(1)
O(401)	1597(3)	8100(2)	258(2)	33(1)
O(402)	970(3)	7215(2)	-209(2)	34(1)
O(501)	924(2)	6289(2)	2445(2)	29(1)
O(502)	392(2)	5369(2)	1960(2)	29(1)
O(403)	4054(3)	8443(2)	-286(2)	37(1)
O(404)	3247(3)	6605(2)	-1391(2)	36(1)
O(503)	2363(2)	4136(2)	1523(2)	32(1)
O(504)	3210(2)	6104(2)	2484(2)	27(1)
N(401)	3638(3)	7537(2)	-846(2)	24(1)
N(501)	2799(3)	5104(2)	2015(2)	21(1)
C(101)	2908(3)	8818(3)	1536(3)	23(1)
C(102)	1776(3)	7750(3)	3581(3)	23(1)
C(103)	2809(4)	9134(3)	3296(3)	27(1)
C(104)	1747(4)	9726(3)	912(3)	31(1)
C(105)	1975(5)	10488(3)	3265(4)	45(1)
C(106)	-126(4)	7656(3)	3969(3)	39(1)
C(107)	1938(3)	9260(3)	1774(3)	22(1)
C(108)	2100(4)	9971(3)	2103(3)	28(1)
C(109)	1952(4)	9663(3)	3066(3)	30(1)
C(110)	912(4)	9077(3)	3625(3)	31(1)
C(111)	885(3)	8274(3)	3398(3)	25(1)
C(112)	981(3)	8592(3)	2449(3)	24(1)
C(201)	6246(3)	7621(3)	852(3)	26(1)
C(202)	6034(4)	6150(3)	2739(3)	29(1)
C(203)	6843(3)	7644(3)	2440(3)	27(1)
C(204)	7783(4)	7461(3)	-243(3)	36(1)
C(205)	8734(4)	7982(4)	2000(4)	43(1)
C(206)	7138(4)	4972(3)	2596(4)	42(1)
C(207)	7305(3)	7275(3)	731(3)	26(1)
C(208)	8032(3)	7776(3)	950(3)	29(1)
C(209)	7883(3)	7468(3)	1918(3)	31(1)
C(210)	7949(4)	6471(3)	2293(3)	33(1)

Table 1.9.(con't) Atomic coordinates ($\times 10^4$) and equivalent isotropic displacement parameters ($\text{Å}^2 \times 10^3$) for **16**.^a

atom	x	y	z	U(eq)
C(211)	7079 (3)	5970 (3)	2219 (3)	30 (1)
C(212)	7206 (4)	6271 (3)	1256 (3)	31 (1)
C(301)	4326 (3)	7585 (3)	3156 (3)	22 (1)
C(302)	5062 (3)	7093 (3)	3438 (3)	26 (1)
C(303)	4938 (4)	6723 (3)	4315 (3)	34 (1)
C(304)	4057 (4)	6866 (3)	4895 (3)	36 (1)
C(305)	3316 (3)	7359 (3)	4635 (3)	28 (1)
C(306)	3462 (3)	7707 (3)	3759 (3)	24 (1)
C(307)	5735 (4)	6198 (4)	4635 (4)	53 (2)
C(308)	2396 (4)	7517 (4)	5293 (3)	39 (1)
C(401)	1406 (3)	7933 (3)	-317 (3)	27 (1)
C(402)	3792 (3)	8385 (3)	-847 (3)	29 (1)
C(403)	3350 (3)	7359 (3)	-1458 (3)	28 (1)
C(404)	680 (4)	9087 (3)	-1219 (4)	41 (1)
C(405)	3464 (5)	7901 (4)	-2990 (3)	50 (2)
C(406)	4376 (4)	9957 (3)	-1749 (4)	46 (1)
C(407)	1701 (4)	8687 (3)	-1223 (3)	28 (1)
C(408)	2065 (4)	8350 (3)	-1946 (3)	35 (1)
C(409)	3207 (4)	8146 (3)	-2194 (3)	31 (1)
C(410)	3921 (4)	8951 (3)	-2387 (3)	36 (1)
C(411)	3651 (4)	9168 (3)	-1588 (3)	29 (1)
C(412)	2524 (4)	9396 (3)	-1358 (3)	33 (1)
C(501)	593 (3)	5533 (3)	2539 (3)	24 (1)
C(502)	2758 (3)	5388 (3)	2675 (3)	23 (1)
C(503)	2287 (3)	4303 (3)	2141 (3)	27 (1)
C(504)	-796 (3)	4768 (3)	3927 (3)	29 (1)
C(505)	1671 (4)	2731 (3)	3143 (4)	48 (2)
C(506)	2698 (4)	4922 (3)	4185 (3)	33 (1)
C(507)	371 (3)	4778 (3)	3422 (3)	24 (1)
C(508)	529 (3)	3885 (3)	3356 (3)	28 (1)
C(509)	1663 (4)	3684 (3)	3080 (3)	29 (1)
C(510)	2185 (3)	3818 (3)	3671 (3)	28 (1)
C(511)	2167 (3)	4764 (3)	3609 (3)	25 (1)
C(512)	1023 (3)	4952 (3)	3902 (3)	22 (1)
C(601)	3227 (3)	6289 (3)	571 (3)	22 (1)
C(602)	3548 (3)	5623 (3)	1155 (3)	22 (1)
C(603)	4564 (3)	5442 (3)	942 (3)	21 (1)
C(604)	5269 (3)	5967 (3)	125 (3)	24 (1)
C(605)	4987 (3)	6668 (3)	-464 (3)	23 (1)
C(606)	3949 (3)	6810 (3)	-232 (3)	23 (1)
C(607)	4918 (3)	4718 (3)	1597 (3)	29 (1)
C(608)	5788 (3)	7270 (3)	-1320 (3)	31 (1)
Cl(1)	9484 (5)	3434 (3)	1900 (3)	116 (2)
C(1)	9785 (6)	4341 (5)	814 (5)	70 (2)
C(2)	10807 (6)	4754 (5)	310 (6)	72 (2)
C(3)	11012 (6)	5419 (5)	-511 (5)	67 (2)

Table 1.9.(con't) Atomic coordinates ($\times 10^4$) and equivalent isotropic displacement parameters ($\text{Å}^2 \times 10^3$) for **16**.^a

atom	x	y	z	U(eq)
C1(2)	8700(3)	10480(3)	4073(2)	164(2)
C(4)	7690(10)	9726(8)	4383(8)	127(4)
C(5)	6721(11)	9819(8)	5046(8)	142(4)
C(6)	5741(15)	9427(12)	5228(12)	210(7)
C(7)	5772(16)	8791(12)	4684(13)	219(8)
C(8)	6701(12)	8810(8)	4172(9)	140(4)
C(9)	7586(10)	9281(8)	3892(8)	137(4)

^aNumbers in parentheses are estimated standard deviations of the last significant figure. ^bU(eq) is defined as one third of the trace of the orthogonalized Uij tensor.

Table 1.10. Atomic coordinates ($\times 10^4$) and equivalent isotropic displacement parameters ($\text{\AA}^2 \times 10^3$) for **17**.^a

atom	x	y	z	U(eq)
Cu(1)	-257(1)	1625(1)	6842(1)	43(1)
Cu(2)	656(1)	2275(1)	7898(1)	38(1)
O(101)	236(1)	1646(1)	9027(3)	44(1)
O(102)	-385(1)	969(2)	7974(3)	50(1)
O(201)	489(1)	2971(2)	6679(3)	44(1)
O(202)	-197(2)	2305(2)	5721(3)	51(1)
O(103)	-385(2)	2753(2)	10933(3)	50(1)
O(104)	-1823(1)	1662(2)	8779(3)	49(1)
O(203)	-1621(1)	3389(2)	6021(3)	51(1)
O(204)	-29(1)	4530(2)	7762(3)	44(1)
N(1)	1254(2)	2940(2)	8923(3)	44(1)
N(2)	1530(2)	1689(2)	7492(3)	48(1)
N(101)	-1120(2)	2209(2)	9886(3)	35(1)
N(201)	-810(1)	3944(2)	6876(3)	34(1)
C(1)	974(3)	3085(3)	9976(5)	66(1)
C(2)	1407(2)	3649(2)	8392(5)	53(1)
C(3)	1818(2)	2468(2)	9040(4)	49(1)
C(4)	2024(2)	2141(2)	7971(5)	50(1)
C(5)	1521(2)	949(2)	7999(6)	68(2)
C(6)	1626(3)	1619(3)	6315(5)	62(1)
C(101)	-136(2)	1127(2)	8874(3)	38(1)
C(102)	-679(2)	2200(2)	10740(3)	42(1)
C(103)	-1484(2)	1606(2)	9560(4)	40(1)
C(104)	123(2)	-82(2)	9639(5)	65(1)
C(105)	-2117(2)	550(3)	10233(5)	66(2)
C(106)	-458(4)	1702(3)	12548(5)	77(2)
C(107)	-301(2)	609(2)	9819(4)	46(1)
C(108)	-982(2)	355(2)	9798(4)	48(1)
C(109)	-1468(2)	907(2)	10269(4)	48(1)
C(110)	-1282(2)	1113(3)	11397(4)	54(1)
C(111)	-636(2)	1487(2)	11402(4)	52(1)
C(112)	-139(2)	957(2)	10927(4)	52(1)
C(201)	158(2)	2868(2)	5873(4)	39(1)
C(202)	-264(2)	4394(2)	6908(4)	34(1)
C(203)	-1150(2)	3752(2)	5946(3)	37(1)
C(204)	668(2)	3075(3)	4153(4)	58(1)
C(205)	-1464(2)	4146(3)	4099(4)	58(1)
C(206)	282(2)	5452(2)	6071(4)	53(1)
C(207)	196(2)	3428(2)	4944(4)	43(1)
C(208)	-436(2)	3520(2)	4353(3)	44(1)
C(209)	-903(2)	4059(2)	4874(3)	43(1)
C(210)	-587(2)	4800(2)	5084(3)	43(1)
C(211)	-30(2)	4710(2)	5841(3)	40(1)
C(212)	451(2)	4185(2)	5302(4)	44(1)
C(301)	-961(2)	3090(2)	8393(3)	34(1)
C(302)	-1087(2)	3758(2)	7900(3)	32(1)

Table 1.10. (con't) Atomic coordinates ($\times 10^4$) and equivalent isotropic displacement parameters ($\text{Å}^2 \times 10^3$) for **17**.^a

atom	x	y	z	U(eq)
C(303)	-1485(2)	4275(2)	8395(3)	39(1)
C(304)	-1740(2)	4094(2)	9379(3)	39(1)
C(305)	-1625(2)	3429(2)	9896(3)	40(1)
C(306)	-1233(2)	2920(2)	9366(3)	33(1)
C(307)	-1626(2)	5003(2)	7860(4)	49(1)
C(308)	-1904(2)	3268(3)	10986(4)	55(1)
C(7)	-1898(8)	1055(9)	4271(16)	178(6)
C(8)	-1622(6)	1604(6)	4966(12)	129(4)
C(9)	-1903(6)	1568(7)	5992(13)	138(4)
C(10)	-2509(6)	1216(7)	5845(12)	140(4)
C(11)	-2435(5)	738(6)	4908(10)	113(3)
C(12)	-1586(7)	-502(8)	6540(14)	192(6)
C(13)	-2025(7)	-445(8)	7500(13)	184(5)
C(13)	-1812(6)	-1162(8)	8151(14)	189(5)
C(15)	-1493(8)	-1660(9)	7219(17)	213(7)
C(16)	-1490(4)	-1307(5)	6345(8)	108(3)

^aNumbers in parentheses are estimated standard deviations of the last significant figure. ^bU(eq) is defined as one third of the trace of the orthogonalized U_{ij} tensor.

Table 1.11. Atomic coordinates ($\times 10^4$) and equivalent isotropic displacement parameters ($\text{\AA}^2 \times 10^3$) for **21**.^a

atom	x	y	z	U(eq)
Cu(1)	-455(1)	3253(1)	5588(1)	32(1)
O(101)	-1875(3)	3557(2)	6313(1)	41(1)
O(102)	-430(3)	4159(2)	5950(1)	35(1)
O(201)	-2152(3)	1915(2)	5475(1)	49(1)
O(202)	-380(3)	2353(2)	5228(1)	37(1)
O(103)	-1090(3)	2713(2)	7270(1)	35(1)
O(104)	2224(3)	3631(2)	6610(1)	37(1)
O(203)	2102(3)	1286(2)	5646(1)	35(1)
O(204)	-1414(3)	368(2)	6189(1)	38(1)
N(101)	550(3)	3183(2)	6932(1)	28(1)
N(201)	341(3)	823(2)	5914(1)	26(1)
C(101)	-1143(4)	4120(2)	6259(1)	29(1)
C(102)	-467(4)	3293(3)	7182(1)	29(1)
C(103)	1376(4)	3805(3)	6821(1)	30(1)
C(104)	-1902(4)	5534(3)	6333(2)	39(1)
C(105)	2447(4)	5109(3)	7058(2)	45(1)
C(106)	-1379(4)	4116(3)	7769(1)	38(1)
C(107)	-1071(4)	4863(2)	6573(1)	33(1)
C(108)	293(4)	5162(2)	6664(1)	33(1)
C(109)	1161(4)	4672(3)	6995(1)	33(1)
C(110)	561(4)	4597(3)	7425(1)	35(1)
C(111)	-702(4)	4162(3)	7346(1)	33(1)
C(112)	-1582(4)	4647(3)	7008(1)	33(1)
C(113)	-3276(5)	5315(3)	6215(2)	52(1)
C(114)	-4084(6)	6001(4)	6010(3)	78(2)
C(115)	-691(5)	3731(3)	8167(2)	48(1)
C(116)	-1496(5)	3783(4)	8557(2)	56(1)
C(117)	3393(5)	4804(4)	7420(2)	55(1)
C(118)	4692(5)	5204(4)	7401(2)	73(2)
C(201)	-1290(4)	1839(3)	5243(1)	32(1)
C(202)	-789(4)	363(2)	5886(2)	31(1)
C(203)	1166(4)	867(2)	5586(1)	28(1)
C(204)	-2090(5)	1365(3)	4503(2)	45(1)
C(205)	2073(4)	110(3)	4980(2)	38(1)
C(206)	-1861(5)	-896(3)	5600(2)	48(1)
C(207)	-1278(4)	1102(3)	4925(1)	33(1)
C(208)	50(4)	868(3)	4821(1)	34(1)
C(209)	836(4)	360(3)	5170(1)	31(1)
C(210)	105(4)	-392(3)	5288(2)	37(1)
C(211)	-1126(4)	-134(2)	5466(1)	31(1)
C(212)	-1920(4)	364(3)	5115(2)	37(1)
C(213)	-1636(6)	2084(4)	4260(2)	64(2)
C(214)	-2554(8)	2336(6)	3868(2)	98(3)
C(215)	-2086(7)	-1562(5)	5281(3)	48(2)
C(216)	-2788(8)	-2291(5)	5439(3)	54(2)
C(1D)	-1261(17)	-1450(11)	5855(6)	62(5)

Table 1.11.(con't) Atomic coordinates ($\times 10^4$) and equivalent isotropic displacement parameters ($\text{A}^2 \times 10^3$) for **21**.^a

atom	x	y	z	U(eq)
C(2D)	-2197(24)	-2290(17)	5788(9)	97(8)
C(217)	2851(5)	-546(3)	5233(2)	49(1)
C(218)	4052(6)	-752(5)	5015(2)	70(2)
C(301)	385(3)	1986(2)	6434(1)	25(1)
C(302)	762(4)	1211(2)	6336(1)	28(1)
C(303)	1610(4)	772(3)	6625(1)	32(1)
C(304)	2073(4)	1163(3)	7014(1)	33(1)
C(305)	1732(4)	1937(3)	7121(1)	32(1)
C(306)	881(4)	2352(2)	6825(1)	27(1)
C(307)	1994(5)	-89(3)	6533(2)	43(1)
C(308)	2272(5)	2342(3)	7552(1)	42(1)
Cu(2)	-1049(1)	-1895(1)	9388(1)	33(1)
O(401)	-3104(3)	-1910(2)	8652(1)	36(1)
O(402)	-1335(3)	-2561(2)	8902(1)	37(1)
O(501)	-2424(3)	-644(2)	9655(1)	39(1)
O(502)	-644(3)	-1261(2)	9892(1)	38(1)
O(403)	-3133(3)	-678(2)	7795(1)	33(1)
O(404)	706(3)	-1679(2)	8276(1)	45(1)
O(503)	1391(3)	95(2)	9482(1)	34(1)
O(504)	-2571(3)	1042(2)	9162(1)	33(1)
N(401)	-1214(3)	-1188(2)	8030(1)	25(1)
N(501)	-545(3)	633(2)	9319(1)	25(1)
C(401)	-2306(4)	-2428(2)	8616(1)	30(1)
C(402)	-2408(4)	-1246(2)	7797(1)	28(1)
C(403)	-281(3)	-1795(3)	8054(1)	30(1)
C(404)	-2959(5)	-3824(3)	8386(2)	39(1)
C(405)	696(4)	-2877(3)	7650(2)	45(1)
C(406)	-3720(4)	-1857(3)	7155(1)	36(1)
C(407)	-2411(4)	-3026(2)	8221(1)	31(1)
C(408)	-1114(4)	-3230(3)	8071(2)	36(1)
C(409)	-560(4)	-2567(3)	7780(2)	34(1)
C(410)	-1508(4)	-2380(3)	7391(1)	33(1)
C(411)	-2721(4)	-2044(2)	7539(1)	28(1)
C(412)	-3288(4)	-2683(3)	7841(1)	32(1)
C(413)	-4243(5)	-3761(3)	8552(2)	50(1)
C(414)	-4668(7)	-4576(4)	8737(2)	73(2)
C(415)	-3348(5)	-1284(3)	6800(2)	49(1)
C(416)	-4452(6)	-1077(5)	6466(2)	67(2)
C(417)	1375(5)	-2292(4)	7351(2)	58(1)
C(418)	2762(5)	-2478(4)	7357(2)	67(2)
C(501)	-1476(4)	-703(2)	9914(1)	27(1)
C(502)	-1680(4)	979(2)	9441(1)	26(1)
C(503)	531(3)	470(2)	9610(1)	26(1)
C(504)	-1569(4)	-574(3)	10719(1)	36(1)
C(505)	1942(4)	1064(3)	10237(2)	36(1)
C(506)	-2552(4)	2031(2)	9900(1)	32(1)

Table 1.11.(con't) Atomic coordinates ($\times 10^4$) and equivalent isotropic displacement parameters ($\text{Å}^2 \times 10^3$) for **21**.^a

atom	x	y	z	U(eq)
C(507)	-1242(3)	-109(2)	10305(1)	28(1)
C(508)	149(4)	155(3)	10386(1)	31(1)
C(509)	568(3)	818(2)	10074(1)	27(1)
C(510)	-303(4)	1552(2)	10075(1)	28(1)
C(511)	-1653(3)	1299(2)	9908(1)	26(1)
C(512)	-2097(4)	649(2)	10221(1)	28(1)
C(513)	-2888(4)	-932(3)	10708(2)	41(1)
C(514)	-3099(5)	-1329(3)	11140(2)	54(1)
C(515)	-2251(5)	2753(3)	9609(2)	43(1)
C(516)	-3297(7)	3358(5)	9537(3)	102(3)
C(517)	2563(4)	1690(3)	9967(2)	40(1)
C(518)	3834(5)	1981(4)	10197(2)	54(1)
C(601)	-947(3)	-268(2)	8672(1)	24(1)
C(602)	-486(3)	457(2)	8858(1)	24(1)
C(603)	63(4)	1041(2)	8610(1)	28(1)
C(604)	125(4)	883(2)	8165(1)	30(1)
C(605)	-310(4)	164(2)	7966(1)	28(1)
C(606)	-837(3)	-410(2)	8228(1)	25(1)
C(607)	570(4)	1837(3)	8806(2)	39(1)
C(608)	-229(5)	13(3)	7482(2)	42(1)
N(1)	-4541(3)	2094(2)	6342(1)	31(1)
N(2)	-5894(3)	-358(2)	8780(1)	32(1)
N(3)	-4689(8)	2653(8)	7992(3)	163(5)
C(1)	-5273(4)	1343(3)	6187(2)	44(1)
C(2)	-4798(5)	930(4)	5793(2)	61(2)
C(3)	-4528(4)	2720(3)	5979(2)	39(1)
C(4)	-5831(4)	3013(4)	5791(2)	53(1)
C(5)	-5181(4)	2444(3)	6724(2)	39(1)
C(6)	-4561(5)	3195(4)	6931(2)	57(1)
C(7)	-3163(4)	1882(3)	6487(2)	34(1)
C(8)	-2974(4)	1267(3)	6851(2)	41(1)
C(9)	-6915(4)	-997(3)	8794(2)	47(1)
C(10)	-6418(5)	-1876(4)	8809(3)	75(2)
C(11)	-5230(5)	-434(4)	8369(2)	52(1)
C(12)	-6080(7)	-352(6)	7943(2)	88(3)
C(13)	-6568(4)	465(3)	8797(2)	40(1)
C(14)	-5760(6)	1203(4)	8791(3)	75(2)
C(15)	-4875(4)	-444(3)	9168(1)	39(1)
C(16)	-5364(5)	-359(6)	9610(2)	81(2)
C(17)	-3861(7)	2169(9)	8032(3)	130(5)
C(18)	-2795(6)	1616(5)	8089(2)	84(2)

^aNumbers in parentheses are estimated standard deviations of the last significant figure. ^bU(eq) is defined as one third of the trace of the orthogonalized U_{ij} tensor.

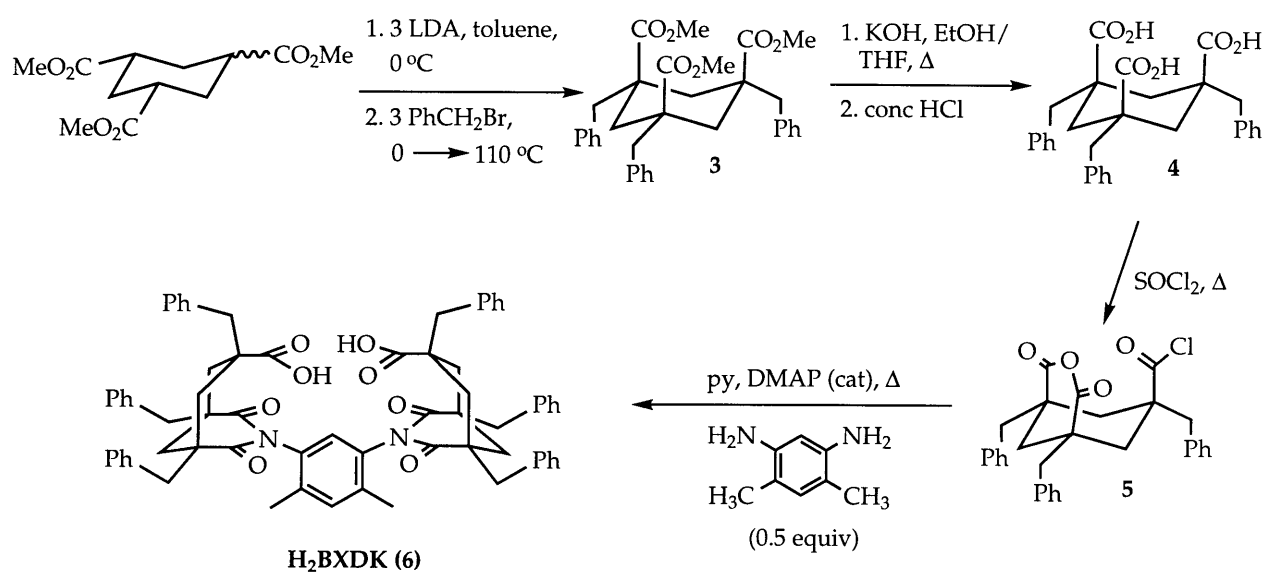
Table 1.12. Atomic coordinates ($\times 10^4$) and equivalent isotropic displacement parameters ($\text{\AA}^2 \times 10^3$) for **22**.^a

atom	x	y	z	U(eq)
Cu(1)	9329(1)	4813(1)	9061(1)	28(1)
Li(1)	8580(4)	6815(4)	8629(3)	26(1)
O(1)	8034(2)	7282(2)	9690(1)	40(1)
O(2)	8372(2)	7960(2)	7996(1)	38(1)
O(101)	7423(2)	5270(2)	8046(1)	33(1)
O(102)	7778(2)	3782(2)	8497(1)	31(1)
O(201)	10311(2)	7279(2)	8943(1)	27(1)
O(202)	10873(2)	5977(2)	9514(1)	29(1)
O(103)	7523(2)	4948(2)	5955(1)	35(1)
O(203)	12658(2)	4967(2)	8268(1)	37(1)
O(104)	8469(2)	2060(2)	6915(2)	45(1)
O(204)	11647(2)	7785(2)	7254(1)	31(1)
N(101)	7983(2)	3508(2)	6451(1)	24(1)
N(201)	12115(2)	6383(2)	7796(1)	22(1)
C(1)	8631(5)	8534(4)	10136(3)	59(1)
C(2)	8958(6)	8584(5)	11042(3)	73(1)
C(3)	8898(5)	7308(4)	11031(3)	66(1)
C(4)	7902(4)	6566(4)	10289(2)	45(1)
C(5)	7176(4)	7984(5)	7779(3)	65(1)
C(6)	6835(4)	7570(4)	6860(3)	68(1)
C(7)	8011(6)	8014(7)	6598(3)	80(2)
C(8)	8932(4)	7943(5)	7272(3)	63(1)
C(101)	7119(2)	4202(2)	8079(2)	25(1)
C(102)	7155(2)	4011(2)	6149(2)	27(1)
C(103)	7676(3)	2403(2)	6671(2)	29(1)
C(104)	5022(3)	3379(3)	8277(2)	35(1)
C(105)	6155(4)	331(3)	6362(3)	50(1)
C(106)	5072(3)	3584(4)	5361(2)	49(1)
C(107)	5844(2)	3304(2)	7626(2)	25(1)
C(108)	5826(3)	2007(2)	7363(2)	29(1)
C(109)	6312(3)	1677(2)	6563(2)	32(1)
C(110)	5605(3)	1955(3)	5856(2)	37(1)
C(111)	5791(3)	3292(3)	6064(2)	32(1)
C(112)	5343(3)	3663(3)	6876(2)	29(1)
C(201)	11074(2)	7000(2)	9351(2)	22(1)
C(202)	12264(2)	7579(2)	7791(2)	23(1)
C(203)	12827(2)	6027(2)	8353(2)	26(1)
C(204)	12232(3)	8567(3)	10619(2)	31(1)
C(205)	14859(3)	6564(3)	9246(2)	39(1)
C(206)	13707(3)	9687(3)	8132(2)	37(1)
C(207)	12353(2)	7954(2)	9742(2)	23(1)
C(208)	13330(2)	7376(2)	9826(2)	25(1)
C(209)	13823(2)	7028(2)	9032(2)	26(1)
C(210)	14287(2)	8134(3)	8696(2)	31(1)
C(211)	13249(2)	8580(2)	8472(2)	26(1)
C(212)	12716(3)	8914(2)	9251(2)	27(1)

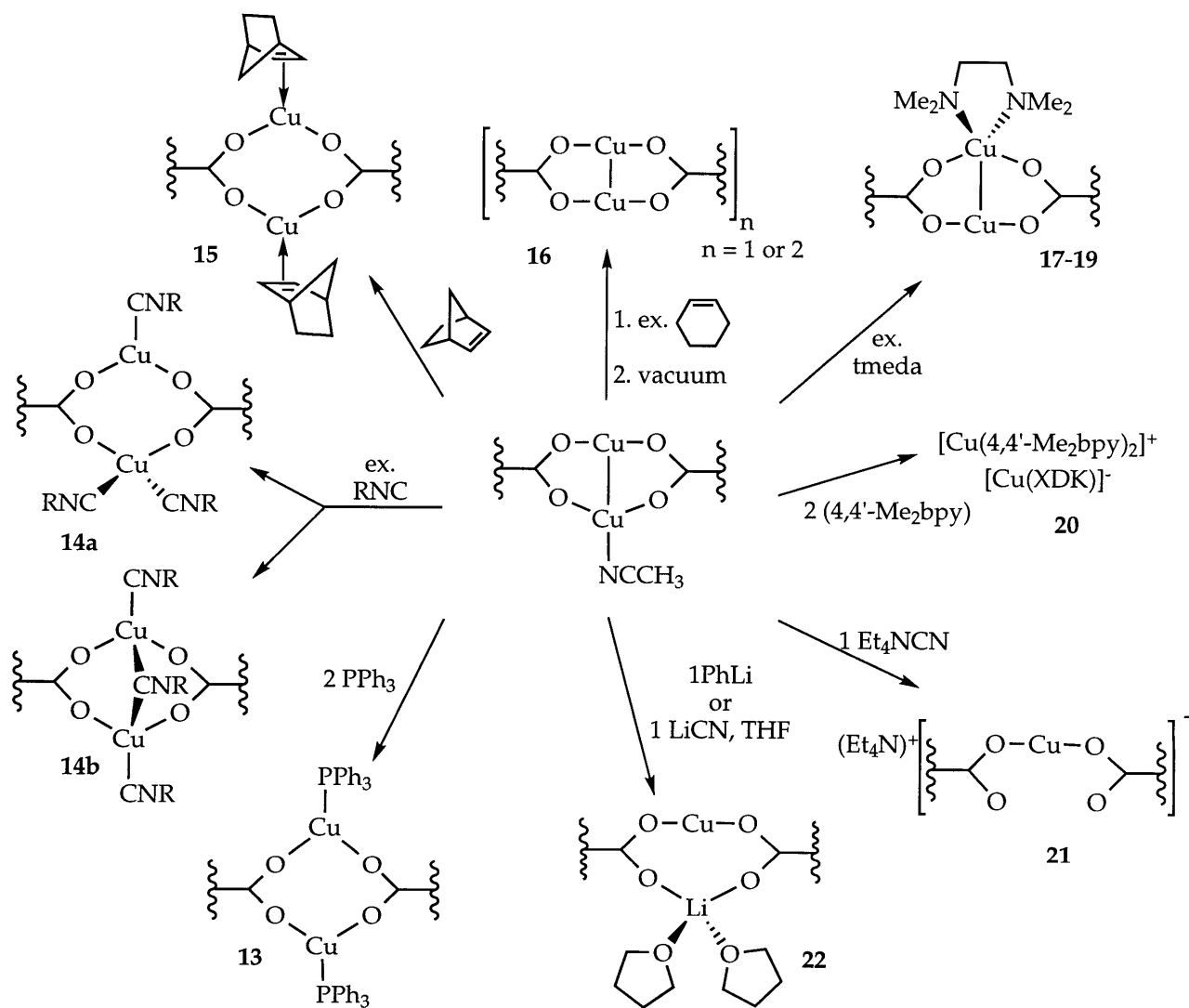
Table 1.12. (con't) Atomic coordinates ($\times 10^4$) and equivalent isotropic displacement parameters ($\text{Å}^2 \times 10^3$) for **22**.^a

atom	x	y	z	U(eq)
C(301)	10055(2)	4943(2)	7117(2)	22(1)
C(302)	11278(2)	5454(2)	7084(2)	22(1)
C(303)	11728(2)	5147(2)	6368(2)	27(1)
C(304)	10893(3)	4319(3)	5669(2)	29(1)
C(305)	9662(3)	3774(2)	5681(2)	27(1)
C(306)	9262(2)	4092(2)	6420(2)	23(1)
C(307)	13057(3)	5677(4)	6335(2)	38(1)
C(308)	8801(3)	2872(3)	4917(2)	37(1)
C(1D)	11518(6)	12041(6)	6625(4)	102(2)
C(2D)	11624(9)	11853(9)	5771(6)	152(3)
C(3D)	12339(8)	11357(8)	6907(5)	70(2)
C(4D)	12447(13)	11222(13)	5767(9)	116(4)
C(5D)	12028(7)	10304(7)	6240(5)	59(2)
C(6D)	11010(17)	10956(18)	6744(12)	113(6)
C(7D)	11784(12)	10505(12)	5550(8)	68(3)
C(8D)	11064(14)	10047(13)	6245(9)	86(4)

^aNumbers in parentheses are estimated standard deviations of the last significant figure. ^bU(eq) is defined as one third of the trace of the orthogonalized U_{ij} tensor.



Scheme 1.1.



Scheme 1.2.

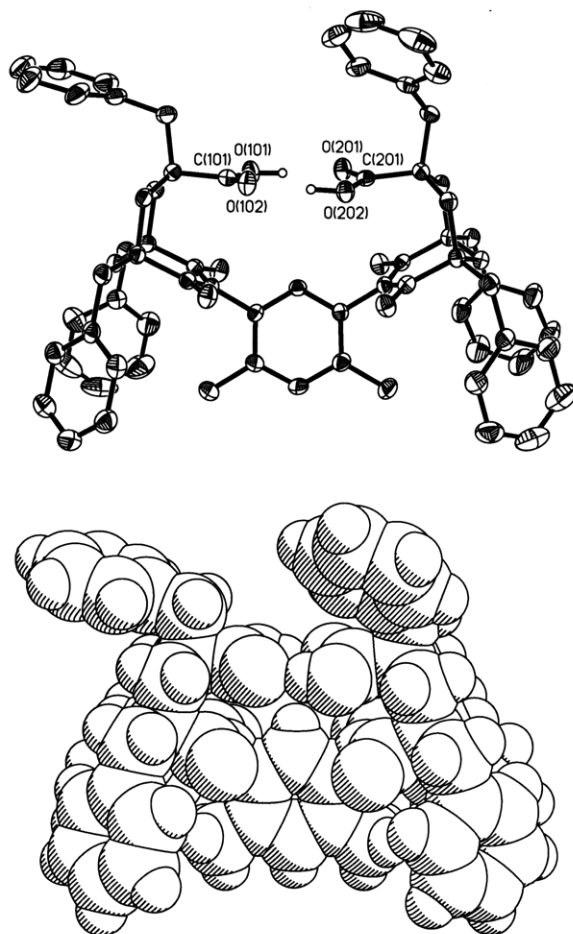


Figure 1.1. ORTEP (50% thermal ellipsoids) and space-filling diagrams of H₂BXDK (6).

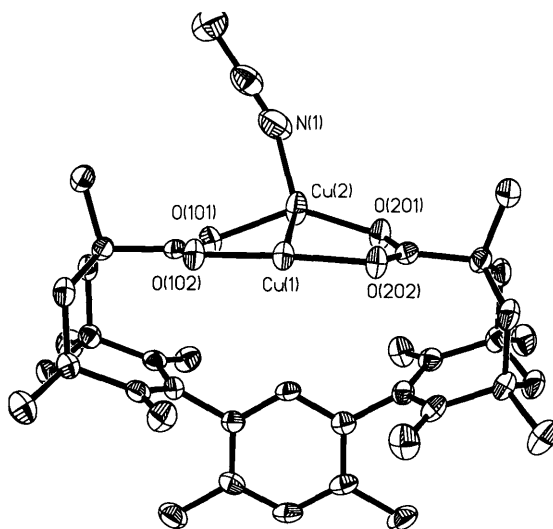


Figure 1.2. ORTEP diagram of [Cu₂(XDK)(MeCN)] (10) with 50% thermal ellipsoids.

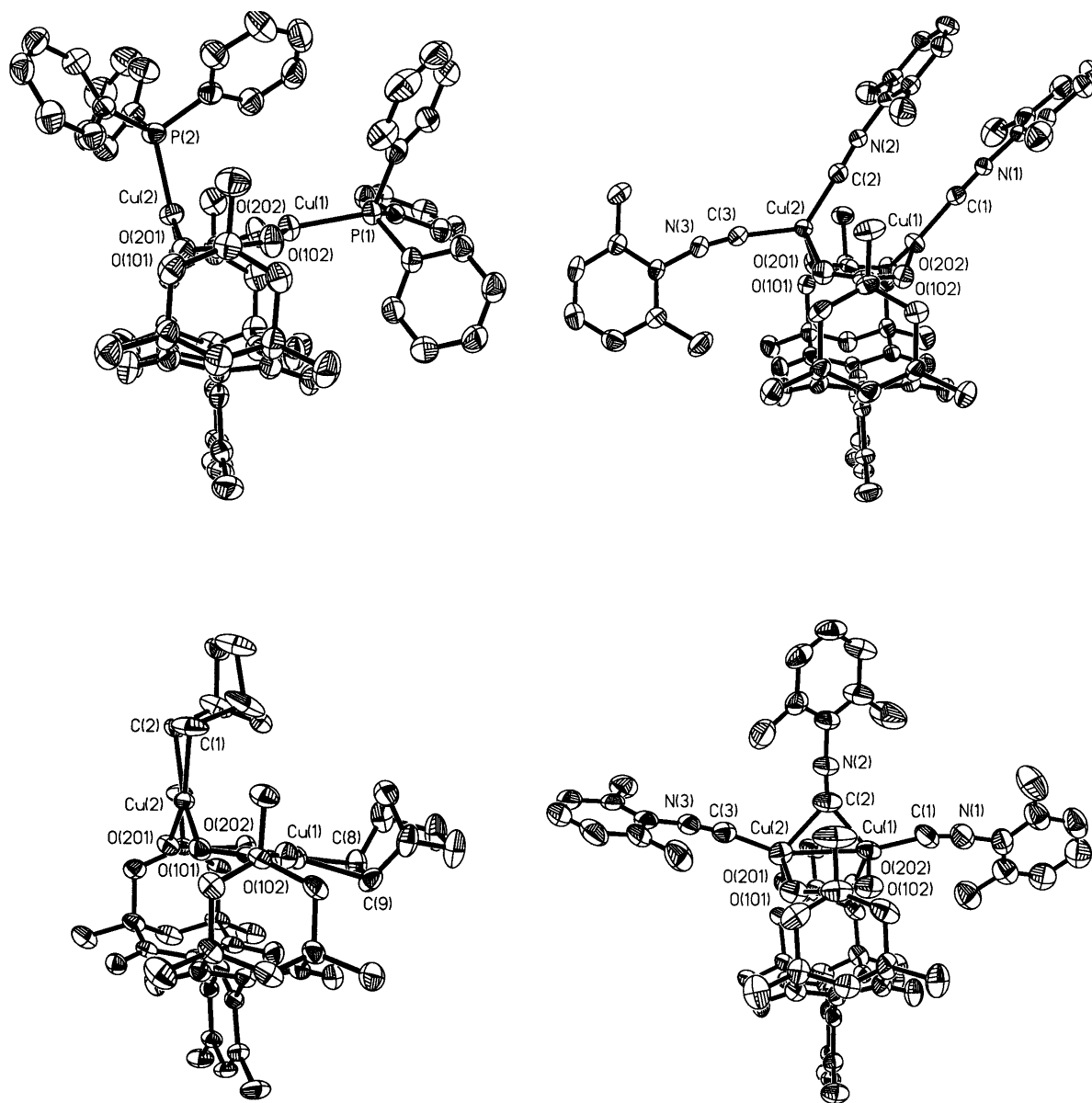


Figure 1.3. ORTEP diagrams with 50% thermal ellipsoids for (clockwise from top left) $[\text{Cu}_2(\text{XDK})(\text{PPh}_3)_2]$ (**13**), $[\text{Cu}_2(\text{XDK})(2,6\text{-Me}_2\text{PhNC})_3]$ (**14a**), $[\text{Cu}_2(\text{XDK})(\mu\text{-}2,6\text{-Me}_2\text{PhNC})(2,6\text{-Me}_2\text{PhNC})_2]$ (**14b**), and $[\text{Cu}_2(\text{XDK})(\text{NB})_2]$ (**15**).

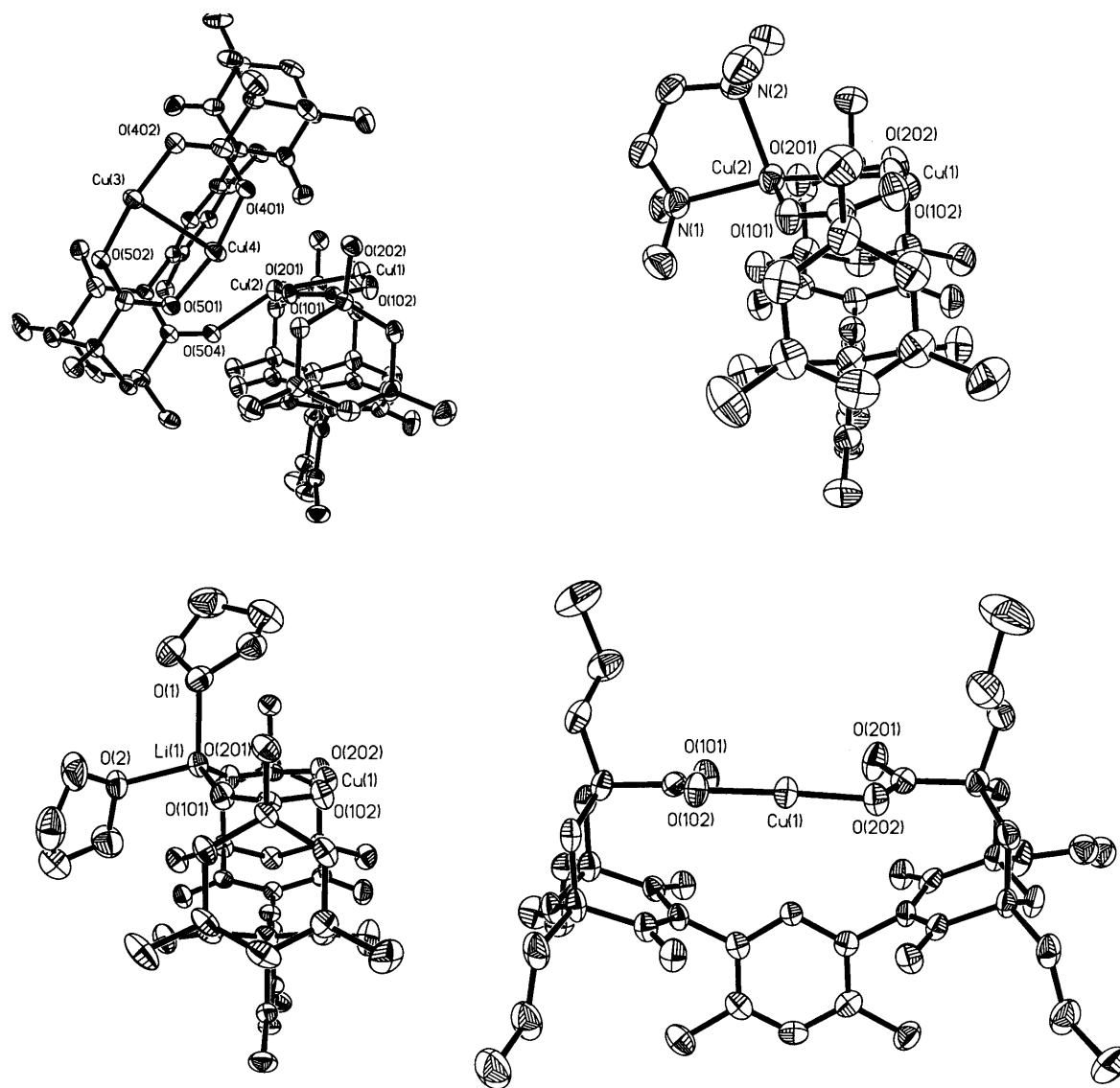


Figure 1.4. ORTEP diagrams with 50% thermal ellipsoids for (clockwise from top left) $[\text{Cu}_2(\text{XDK})_2]$ (**16**), $[\text{Cu}_2(\text{XDK})(\text{tmeda})]$ (**17**), $(\text{Et}_4\text{N})[\text{Cu}(\text{PXDK})]$ (**21**), and $[\text{CuLi}(\text{XDK})(\text{THF})_2]$ (**22**).

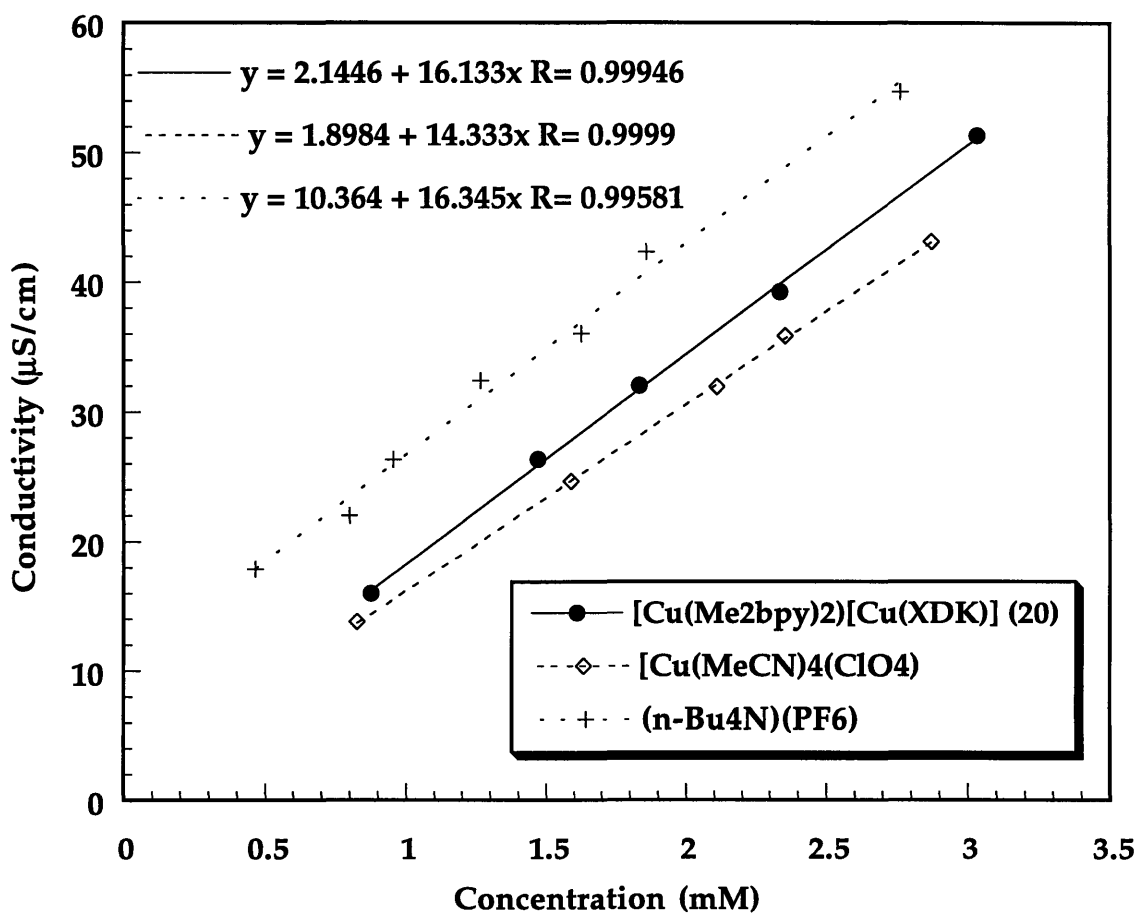


Figure 1.5. Conductivity plots for 20, Bu_4NPF_6 , and $[\text{Cu}(\text{MeCN})_4](\text{ClO}_4)$ in CH_2Cl_2 at 296 K.

Chapter II

Synthesis and Characterization of Cu(I)-Cu(II) Mixed-Valence and Cu(I)-M(II) Heterodimetallic Bis(carboxylate-bridged) Complexes: Structural, Electrochemical, and Spectroscopic Investigations

Introduction

The ubiquitous cellular respiratory protein cytochrome *c* oxidase (CcO) couples the catalytic reduction of dioxygen to water with the production of a proton electrochemical gradient across a cell membrane, providing the energy essential for ATP synthesis from ADP and inorganic phosphate.¹ Another respiratory protein, nitrous oxide reductase (N₂OR), plays an analogous role in denitrifying bacteria by catalyzing the reduction of N₂O to N₂ and water.² A common feature of both of these enzymes is their use of a unique electron transfer center, Cu_A. Recent spectroscopic³⁻⁸ and X-ray structural⁹⁻¹¹ studies have provided compelling evidence that Cu_A is a fully delocalized mixed-valence "class III"¹² dicopper center. The X-ray structural analyses revealed that each copper ion is ligated by two bridging thiolates and a terminal histidine nitrogen, with weaker contacts occurring between a methionine thioether and one copper and between a glutamate carboxylate oxygen atom and the other (Table 2.1). Most remarkably, the Cu_A site possesses an inter-metal distance of 2.5 Å, which is consistent with the presence of a genuine metal-metal bond. This feature is unprecedented in biological systems and is undoubtedly connected intimately with the highly unusual electronic properties and the function of the center.¹³

The recent identification of the Cu_A site has spawned interest in the structural and spectroscopic properties of well-defined complexes to model its electron transfer properties. Many mixed-valence dicopper complexes are known, but most are fully localized class I systems, with no electronic exchange between the d⁹ and d¹⁰ metal centers.^{12,14} A small number of class II dicopper complexes have been characterized.^{12,15-19} Some have been shown to exhibit temperature dependent electronic exchange phenomena, whereby the unpaired electron becomes spin-trapped upon cooling, as judged primarily by EPR spectroscopy.¹⁵⁻¹⁷ Fully

delocalized, type III mixed-valence copper complexes which remain delocalized at liquid helium temperatures are rare.

The two types of class III dicopper complexes described to date employ a tridentate N₂S ligand, LiPrdacoS,^{20,21} or octazacryptand macrobicyclic ligands, L¹-L³ (Table 2.1).²²⁻²⁴ In addition to having different bridging properties, the two ligands afford complexes with very different Cu...Cu distances and metal ion geometries. The N₂S ligand provides a Cu(1.5)Cu(1.5) complex of overall C_i-symmetry, each Cu having a distorted trigonal pyramidal geometry. The Cu...Cu distance of 2.9306(9) Å is long and there is presumably no metal-metal bond. Ligands L¹-L³ afford D_{3d}-symmetric complexes with trigonal bipyramidal Cu centers and Cu-Cu distances of 2.448(1), 2.415(1), and 2.419(1) Å, respectively. The identical coordination environments about the two copper ions within each complex suggest delocalized mixed-valence formulations for all in the solid state. The delocalization origins of these two classes of compounds is revealed by their frozen solution EPR (T = 4-20 K) and electronic absorption spectral properties, summarized in Table 2.1. The N₂S-derived complex exhibits a rhombic EPR spectrum with a seven-line hyperfine splitting of the two lower field components due to spin delocalization over both I = 3/2 Cu ions. In contrast, EPR spectra obtained for complexes with the octazacryptands are axial and display seven-line hyperfine coupling on the lower field, A_{||} component, indicating substantial d_{z²} character in the ground state. The electronic absorption spectra of all these complexes exhibit relatively intense ($\epsilon > 1000 \text{ M}^{-1}\text{cm}^{-1}$) features in the near-infrared (NIR) region, but the absorption maxima differs substantially for the two different types of complexes, again suggesting different electronic states.

Recently in two independent studies,²⁵⁻²⁷ detailed descriptions of the electronic structures of the Cu_A center and its models have been put forth based on thorough analyses of UV-vis, NIR, MCD, EPR, EXAFS, and X-ray structural data,

coupled with molecular orbital calculations. The singly occupied molecular orbital (SOMO) for the N₂S-derived mixed-valence complex is partly composed of weakly participating, π -bonding $d_{x^2-y^2}$ metal orbitals. It is dominated by the antibonding sulfur p-orbitals, however, as might be expected in this case since the Cu ions are too far apart for direct d-orbital overlap.^{25,26} At the other extreme, in the octazacryptand systems the σ^* SOMO is dominated by d_{z^2} - d_{z^2} out-of-phase overlap afforded by the short metal-metal distance and lack of an efficient superexchange pathway through the four-atom bridging groups.²⁶ The σ^* SOMO for Cu_A was assigned to be a composite of those deduced for these two models, with significant metal $d_{x^2-y^2}$ - $d_{x^2-y^2}$ out-of-phase and sulfur p_{π} - p_{π} in-phase overlap.^{25,26} Taken together, these studies suggest that the superexchange pathway in this set of class III mixed-valence complexes is comprised of overlap between metal d- or ligand p- orbitals, or both, depending on the energetic accessibility of a metal-metal compared to a bridging exchange pathway.

The above examples notwithstanding, the paucity of small molecule analogs of the Cu_A center hampers efforts to develop *general* principles that govern the assembly of dicopper mixed-valence cores and their class III behavior. For example it would be of interest to know (1) what spectrum of ligands will assemble the mixed-valence core and protect it from decomposition pathways such as disproportionation; (2) how the superexchange pathway is affected by Cu-Cu distance, and number and donor properties of bridging ligands, metal ion geometries, and the overall complex symmetry; and (3) how these properties affect the ease with which the mixed-valence core can cycle reversibly between the Cu(I)Cu(I) and Cu(1.5)Cu(1.5) oxidation states with minimal ligand reorganization and at biologically relevant potentials. An efficient approach to exploring these questions is to utilize a readily modified ligand system that will stabilize the Cu(1.5)Cu(1.5) and Cu(I)Cu(I) units, while leaving open coordination sites for

docking ancillary ligands with variable donor properties to perturb incrementally the overall electronic structure. This strategy will facilitate the construction of a family of closely related complexes from which the relative importance of the above factors can be evaluated.

In the present investigation, we have approached this goal by using the *m*-xylylenediamine bis(Kemp's triacid imide) (H₂XDK) ligand system,²⁸⁻³⁰ previously demonstrated to be an ideal platform for binding a variety of metal fragments with labile coordination sites in both bioinorganic^{29,31-37} and organometallic³⁸ applications. Previously we reported the synthesis and characterization of several bis(carboxylate)-bridged dicopper(I) complexes derived from XDK and π -acceptor and σ -donor ligands.²⁸ In these complexes the copper atoms have linear two-coordinate, trigonal three-coordinate, or pseudo four-coordinate geometries, and variable Cu–Cu distances ranging from 2.5697(8) to 3.4211(6) Å. Here we report a series of dicopper mixed-valence complexes having variable ancillary ligands which facilitate the analysis of the factors that influence their electronic behavior. The synthesis, solid state and solution characterization, and electrochemical behavior of these complexes and related Cu(I) heterodimetallic complexes are described, the latter serving to enhance our understanding of the electronic properties of the mixed-valence system.

Experimental Section

General Considerations. The complexes Cu₂(XDK)(MeCN) (1), Cu₂(PXDK)(MeCN) (2), and (Et₄N)[Cu(PXDK)] (3) were prepared according to literature procedures.²⁸ The compound [Fe(OTf)₂(MeCN)₂] was prepared according to a procedure used to obtain the Mn(II) analog.³⁹ All other reagents were procured from commercial sources and used as received unless otherwise noted. THF, benzene, toluene, pentane, and Et₂O were distilled from sodium benzophenone

ketyl under nitrogen. Dichloromethane and 1,2-dichloroethane were distilled from CaH_2 under nitrogen. The NMR solvent C_6D_6 was degassed, passed through activated basic alumina, and stored over 3 Å molecular sieves prior to use. All air sensitive manipulations were carried out either in a nitrogen filled Vacuum Atmospheres drybox or by standard Schlenk line techniques at room temperature unless otherwise noted.

Physical Measurements. NMR spectra were recorded on a Bruker AC-250 or Varian XL-300 spectrometer. ^1H NMR chemical shifts are reported versus tetramethylsilane and referenced to the residual solvent peak. FTIR spectra were recorded on a BioRad FTS-135 FTIR spectrometer. UV-vis-NIR spectra were recorded on a Cary 5E reference spectrophotometer. Conductivity measurements were carried out in THF or CH_2Cl_2 at 296 K with a Fisher Scientific conductivity bridge, model 9-326, outfitted with a platinum black electrode. Elemental analyses were performed by Microlytics, South Deerfield, MA.

Electrochemistry. Cyclic voltammetric measurements were carried out in a Vacuum Atmospheres drybox under N_2 with an EG&G Model 263 potentiostat. A three electrode configuration was used consisting of a 1.75 mm^2 platinum working electrode, a Ag/AgNO_3 (0.1 M in MeCN) reference electrode, and a coiled platinum wire auxiliary electrode. A 0.5 M solution of $\text{Bu}_4(\text{NPF}_6)$, triply recrystallized from acetone, was used as supporting electrolyte. Solute samples were typically 1-2 mM. Scan rate profiles were conducted for each sample, at scan speeds of 50-500 mV/s, and compared to that obtained for Cp_2Fe under identical conditions. All cyclic voltammograms were externally referenced to Cp_2Fe , for which $E_{1/2} = +143\text{ mV}$ in THF ($\Delta E_p = 68\text{ mV}$, scan rate = 50 mV/s).

EPR Spectroscopy. For measurements at 9 K, data were collected on a Bruker Model 300 ESP X-band spectrometer operating at 9.47 GHz. For measurements at 77 K, data were collected on a Varian E104 X-band spectrometer operating at 9.14 GHz.

The Q-band measurements were performed at 2K with a modified Varian E109 spectrometer operating at 35 GHz. Liquid helium temperatures were maintained with an Oxford Instruments EPR 900 cryostat, and liquid nitrogen temperatures with an EPR finger dewar. For all measurements 1 mM frozen solutions were prepared in 2-methyltetrahydrofuran, a solvent in which the samples glassed well. Solid samples (~1 mg) were prepared as finely ground powders. Simulations were carried out with the WINEPR SimFonia program package.⁴⁰ The fits incorporated coupling of the unpaired spin simultaneously to each $I = 3/2$ copper center.

Extended Hückel Molecular Orbital Calculations. These computations⁴¹ were carried out with the program YAeHMOP,⁴² operating on a Silicon Graphics Indy computer. Simplified models of the mixed-valence complexes **7** and **8** were implemented, $[\text{Cu}_2(\mu\text{-O}_2\text{CCH}_3)_2(\text{OMe}_2)]^+$ and $[\text{Cu}_2(\text{OH})_2(\text{OH}_2)(\text{OMe}_2)_4]^+$, and used the core crystallographic coordinates determined for **8**.

Preparation of Compounds. $[\text{Cu}_2(\text{XDK})(\mu\text{-OTf})(\text{THF})_2]$ (4**).** To a stirred solution of **1** (300 mg, 0.402 mmol) in THF (5 mL) was added a solution of AgOTf (105 mg, 0.402 mmol) in THF (1 mL) in one portion. The colorless solution immediately turned dark purple and an off-white precipitate formed. The mixture was filtered through Celite, and the filtrate was evaporated to dryness. Recrystallization from THF/pentane at $-30\text{ }^\circ\text{C}$ provided **4** as thin purple blocks which appeared suitable for X-ray crystallography (386 mg, 96%). IR (KBr) 2962, 2935, 2875, 1734, 1691, 1460, 1362, 1297, 1264, 1182, 1024, 868, 760, 637 cm^{-1} ; UV-vis (THF, λ_{max} , nm (ϵ , M^{-1} , cm^{-1})) 542 (1200), 768 (sh, 300), 956 (630). Anal. Calcd for $\text{C}_{45}\text{H}_{62}\text{N}_2\text{O}_{14}\text{Cu}_2\text{F}_3\text{S}_1$ (**4**· 1THF): C, 50.46; H, 5.83; N, 2.62. Found: C, 50.45; H, 6.08; N, 2.47.

$[\text{Cu}_2(\text{PXDK})(\mu\text{-OTf})(\text{THF})_2]$ (5**). Method A.** This compound was prepared from **2** (50 mg, 0.055 mmol) and AgOTf (14 mg, 0.055 mmol) by an analogous procedure to that used to prepare **4**. Recrystallization from pentane and a trace amount of THF at $-30\text{ }^\circ\text{C}$ afforded **5** as purple needles (29 mg, 45%).

Method B. To a stirred suspension of **3** (50 mg, 0.053 mmol) in THF (2 mL) was added Cu(OTf)₂ (19.6 mg, 0.053 mmol) in THF (1 mL) in one portion. Complex **3** was immediately consumed and the solution turned dark purple. After 15 min the THF was removed in vacuo. The solid residue was taken up in Et₂O (2-3 mL) and then filtered through Celite to remove the precipitated Et₄N(OTf). Solvent removal in vacuo followed by recrystallization provided **5** as purple needles. (25 mg, 40%). IR (KBr) 2962, 2935, 2875, 1733, 1691, 1534, 1460, 1362, 1296, 1182, 1024, 868, 637 cm⁻¹. Anal. Calcd for C₅₃H₇₈N₂O₁₃Cu₂F₃S₁: C, 54.53; H, 6.73; N, 2.40. Found: C, 54.34; H, 6.54; N, 2.61.

[Cu₂(XDK)(μ-O₂CCF₃)(THF)₂] (**6**). This compound was prepared from **1** (150 mg, 0.201 mmol) and AgO₂CCF₃ (44 mg, 0.20 mmol) by an analogous procedure to that used to prepare **4**. Recrystallization from THF/pentane provided **6** as purple blocks which appeared suitable for X-ray crystallography (152 mg, 79%). IR (KBr) 2980, 2933, 2878, 1734, 1695, 1662, 1500, 1467, 1421, 1381, 1353, 1336, 1230, 1183, 1141, 1035, 838, 761, 667, 477 cm⁻¹; UV-vis (THF, λ_{max}, nm (ε, M⁻¹, cm⁻¹)) 563 (2000), 806 (sh, 320), 942 (sh, 360), 1250 (500). Anal. Calcd for C₄₂H₅₄N₂O₁₂Cu₂F₃: C, 52.39; H, 5.65; N, 2.91. Found: C, 52.17; H, 5.63; N, 2.89.

[Cu₂(XDK)(THF)₄](BF₄) (**7**). This compound was prepared from **1** (100 mg, 0.134 mmol) and AgBF₄ (26 mg, 0.13 mmol) by an analogous procedure to that used to prepare **4**. Recrystallization from THF/pentane provided **7** as purple plates (120 mg, 82%). IR (KBr) 2969, 2927, 2875, 1734, 1698, 1540, 1462, 1423, 1353, 1230, 1028, 957, 864, 759, 676, 523 cm⁻¹; UV-vis (THF, λ_{max}, nm (ε, M⁻¹, cm⁻¹)) 536 (1600), 923 (1200). Anal. Calcd for C₄₈H₇₀N₂O₁₂Cu₂B₁F₄: C, 51.29; H, 5.81; N, 2.99. Found: C, 50.98; H, 5.92; N, 3.04.

[Cu₂(PXDK)(THF)₄](BF₄) (**8**). This compound was prepared from **2** (121 mg, 0.132 mmol) and AgBF₄ (26 mg, 0.132 mmol) by an analogous procedure to that used to prepare **4**. Recrystallization from THF/pentane provided **8** as purple needles

which appeared suitable for X-ray crystallography (101 mg, 61%). IR (KBr) 2962, 2933, 2869, 1734, 1692, 1540, 1459, 1362, 1314, 1264, 1182, 1034, 866, 759, 673, 586 cm^{-1} ; UV-vis (THF, λ_{max} , nm (ϵ , $\text{M}^{-1}\text{cm}^{-1}$)) 527 (1700), 878 (1200). Anal. Calcd for $\text{C}_{60}\text{H}_{94}\text{N}_2\text{O}_{12}\text{Cu}_2\text{B}_1\text{F}_4$: C, 57.68; H, 7.58; N, 2.24. Found: C, 56.84; H, 7.25; N, 2.42.

[CuZn(PXDK)(OTf)(THF)₂(H₂O)] (9). This compound was prepared from **3** (200 mg, 0.213 mmol) and $\text{Zn}(\text{OTf})_2$ (94 mg, 0.21 mmol) by a procedure analogous to method B used to prepare **5**, except that the reaction mixture was allowed to stir for 12 h. Recrystallization from pentane with a trace of THF provided **9** as colorless blocks which appeared suitable for X-ray crystallography. (154 mg, 61%). ^1H NMR (300 MHz, C_6D_6 , 296 K) δ 7.31 (1H, s), 6.63 (1H, s), 3.83 (8H, br s), 2.90-2.60 (4H, m), 2.30-1.92 (6H), 1.83 (6H, s), 1.68-1.03 (34H, m), 1.03-0.80 (16H, m), 0.75 (4H, d, $J = 12.6$ Hz); IR (KBr) 3451, 2963, 2933, 2874, 1734, 1676, 1577, 1459, 1365, 1309, 1184, 1027, 918, 761, 637 cm^{-1} . Anal. Calcd for $\text{C}_{53}\text{H}_{80}\text{N}_2\text{O}_{14}\text{Cu}_1\text{Zn}_1\text{F}_3\text{S}_1$: C, 53.62; H, 6.79; N, 2.36. Found: C, 54.22; H, 6.55; N, 2.34.

[CuFe(PXDK)(OTf)(NB)(MeCN)]₂ (10a). To a stirred suspension of **3** (200 mg, 0.213 mmol) in THF (3 mL) was added $[\text{Fe}(\text{OTf})_2(\text{MeCN})_2]$ (106 mg, 0.243 mmol) in THF (1 mL) in one portion. After 15 min the THF was removed in vacuo. The solid residue was taken up in Et_2O (2-3 mL) and then filtered through Celite. Solvent removal in vacuo followed by recrystallization from 1,2-dichloroethane/norbornene (NB, 1:1, v:w) and pentane afforded **10a** as small colorless blocks (146 mg, 60%) which appeared suitable for X-ray crystallography. IR (KBr) 3049, 2871, 2742, 1737, 1699, 1594, 1502, 1412, 1368, 1315, 1181, 1033, 926, 862, 762, 637 cm^{-1} . Anal. Calcd for $\text{C}_{54}\text{H}_{75}\text{N}_3\text{O}_{11}\text{Cu}_1\text{Fe}_1\text{F}_3\text{S}_1$: C, 56.47; H, 6.57; N, 3.65. Found: C, 55.58; H, 6.80; N, 3.38. This sample was heated in vacuo at 90 °C for 6 h in an attempt to remove completely the two lattice dichloroethane molecules, which were identified by X-ray crystallography. Apparently only partial elimination was

achieved, and subsequent heating at higher temperatures resulted in decomposition of the complex.

[CuZn(PXDK)(OTf)(NB)(H₂O)] (11). Compound **9** was prepared in situ from **3** (38 mg, 0.040 mmol) and Zn(OTf)₂ (15 mg, 0.040 mmol) and then recrystallized from benzene/norbornene (1:1, v:v) and pentane to afford **11** as colorless blocks which appeared suitable for X-ray crystallography (27 mg, 57%). ¹H NMR (250 MHz, C₆D₆, 296 K) δ 7.35 (1H, s), 6.61 (1H, s), 5.22 (2H, s), 3.82 (4H, br s), 2.95-2.72 (6H, m), 2.30-1.90 (8H, m), 1.79 (6H, s), 1.68-0.60 (46H, m); IR (KBr) 3314, 2964, 2933, 2875, 1737, 1682, 1603, 1505, 1459, 1410, 1367, 1334, 1236, 1201, 1018, 926, 762, 637 cm⁻¹. Anal. Calcd for C₅₂H₇₄N₂O₁₂Cu₁Zn₁F₃S₁: C, 54.92; H, 6.55; N, 2.46. Found: C, 55.63; H, 6.78; N, 2.42.

Collection and Reduction of X-ray Data. All crystals were mounted on the tips of quartz fibers with Paratone-N (Exxon), cooled to low temperature (~ -85 °C), and placed on Siemens CCD X-ray diffraction system controlled by a Pentium-based PC running the SMART software package.⁴³ The general procedures for data collection and reduction follow those reported previously.⁴⁴ All structures were solved with the direct methods programs SIR-92⁴⁵ or XS, part of the TEXSAN⁴⁶ and SHELXTL⁴⁷ program packages, respectively. Structure refinements were carried out with XL, part of the SHELXTL program package.⁴⁷ All remaining non-hydrogen atoms were located and their positions refined by a series of least-squares cycles and Fourier syntheses. Hydrogen atoms were assigned idealized positions and given a thermal parameter 1.2 times the thermal parameter of the carbon atom to which each was attached. Empirical absorption corrections were calculated and applied for each structure by using SADABS, part of the SHELXTL program package.⁴⁷

In the structure of **4**, each coordinated THF molecule as well as one of the two lattice THF molecules contain a carbon atom disordered over two positions. In each case the atom was distributed over two positions and refined. In the structure of **6** each coordinated THF molecule was disordered over two positions. In one

molecule, two of the carbon atoms and the oxygen atom were refined at full occupancy, and the occupancy of the remaining two carbon atoms was distributed over two positions and refined. In the other, the occupancy of one carbon atom was distributed over two positions and refined, and the remaining atoms were refined at full occupancy. The lattice THF molecule in **6** contains large thermal parameters, so each atom was refined at a site occupancy of 0.5. Two of the coordinated THF molecules in the structure of **8** were disordered over two positions. Two of the carbon atoms and the oxygen atom were refined at full occupancy, whereas the remaining carbon atoms were distributed over two positions and refined. The structure of **9** contains a coordinated THF molecule disordered over two positions, and it was refined in similar fashion to those described for the structure of **4**. Finally, in the structure of **11** the copper atom and norbornene ligand are disordered. The site occupancy of this fragment was distributed over two positions and refined. Bond distances and angles for each orientation of **11** are reported in Table 2.3. For both structures **9** and **11**, the assignment of the metal atom positions as Cu or Zn was based on chemically reasonable presumptions that (a) the overall neutral charge of each complex necessitates the assignment of one mono- and divalent metal ion; (b) the three-coordinate geometry for the metal coordinated to the norbornene ligand in **11** is quite common for Cu(I) but not for Zn(II); and (c) the Cu–C distances in **11** are nearly identical to those observed for $[\text{Cu}_2(\text{XDK})(\text{NB})_2]$.²⁸

Important crystallographic information for each complex, including refinement residuals, is available in Table 2.2. Selected bond distances and angles for the coordination spheres of each structurally characterized complex are displayed in Table 2.3, and final positional and equivalent isotropic displacement parameters are listed in Tables 2.4-2.8.

Results and Discussion

Preparation and Structural Characterization of Mixed-Valence Complexes $[\text{Cu}_2(\text{XDK})(\mu\text{-OTf})(\text{THF})_2]$ (4), $[\text{Cu}_2(\text{PXDK})(\mu\text{-OTf})(\text{THF})_2]$ (5), $[\text{Cu}_2(\text{XDK})(\mu\text{-O}_2\text{CCF}_3)(\text{THF})_2]$ (6), $[\text{Cu}_2(\text{XDK})(\text{THF})_4](\text{BF}_4)$ (7), and $[\text{Cu}_2(\text{PXDK})(\text{THF})_4](\text{BF}_4)$ (8). Each of these complexes was prepared by one electron oxidation of acetonitrile adducts 1 or 2 with the appropriate silver(I) salt in THF (Scheme 2.1). Removal of the resulting solids followed by recrystallization afforded 4-8 as deep purple compounds in moderate to excellent yield. Recovery of 5 and 8 was limited by their significant solubility under the recrystallization conditions. The products appeared to be stable in the presence of excess Ag^+ , suggesting that these mixed-valence complexes are resistant to disproportionation followed by further Ag^+ oxidation of the remaining equivalent of Cu(I). By contrast, oxidation of 1 or 2 with Ag^+ salts of more basic anions, such as benzoate, led to mixtures of intractable blue-green products. This result indicates that ancillary ligands more donating than trifluoroacetate are incompatible with the dicopper-XDK mixed-valence framework. The triflate adduct 5 could also be prepared from mononuclear PXDK complex 3 and $\text{Cu}(\text{OTf})_2$. Because of the propyl groups in PXDK, 5 is readily soluble in Et_2O , allowing the $\text{Et}_4\text{N}(\text{OTf})$ byproduct to be removed conveniently by filtration.

The IR spectra of compounds 4-8 display new features attributable to their respective anions. In addition, the XDK carboxylate stretch in the dicopper(I) starting materials 1 and 2 is shifted by 5-15 cm^{-1} to lower energy for each product, indicating a change in Cu geometry. The UV-vis spectra of each product exhibit a relatively sharp and intense ($\epsilon = 1200\text{-}2000 \text{ M}^{-1}\text{cm}^{-1}$) feature with a maximum at $\sim 545 \text{ nm}$ (Figures 2.1-2.3). For the three XDK complexes, this band is most intense for the trifluoroacetate derivative. In the visible/near-infrared region, all the complexes show broad absorptions between 700 and 1500 nm. Based on the peak shapes, this feature appears to arise from a single transition for the BF_4^- complexes, but is made up of overlapping components for the OTf^- and O_2CCF_3^- adducts. A similarly

intense ($\epsilon > 500 \text{ M}^{-1}\text{cm}^{-1}$) feature at low energy has been observed in other class II and III mixed-valence copper complexes. In the class II systems it has been assigned as an intervalence charge transfer,^{16,17} and in the class III complexes as a $\psi \rightarrow \psi^*$ transition within the $\text{Cu}(1.5)\text{Cu}(1.5)$ manifold.^{25,26} The relatively sharp transition observed for the BF_4^- adduct parallels those observed for the class III octaazacryptand complexes,^{24,26} but the multiple bands appearing in the spectrum of the triflate and O_2CCF_3^- derivatives are currently not understood. In the absence of additional information such as MCD or single crystal data, we choose neither to assign the NIR transitions nor make a definitive class II or III designation based on these spectra.

The solution stability of the mixed-valence complexes was assessed by UV-vis spectroscopic and conductivity measurements. In all cases, the optical spectra remained unchanged after standing in THF, benzene, or CH_2Cl_2 for several days under N_2 . Upon addition of a strongly coordinating solvent such as MeCN, however, the solutions immediately turned pale blue-green and absorption spectra typical of mononuclear Cu(II) were observed. The conductivity behavior of **4-8** similarly remained unchanged over the same time period in THF solution. The triflate and O_2CCF_3^- adducts are non-electrolytes, whereas the BF_4^- adducts are 1:1 electrolytes as judged by a comparison of conductivity vs. concentration plots for **7** and $\text{Bu}_4\text{N}(\text{PF}_6)$ (Figures 2.4 and 2.5). These results demonstrate that the $[\text{Cu}_2(\text{XDK})]^+$ mixed-valence core is highly resistant to disproportionation, even in the absence of excess THF, provided only weak field ligands are present.

The structures of **4**, **6**, and **8**, as determined by X-ray crystallography, are displayed in Figures 2.6-2.8. Selected bond distances and angles, atomic coordinates, and equivalent isotropic displacement parameters are listed in Tables 2.3 and 2.4-2.8, respectively. The structure of the triflate adduct **4** consists of two slightly distorted square pyramidal copper atoms, each ligated by two XDK carboxylate oxygens, a THF molecule, and an oxygen atom of a bridging triflate ion. The bond distances and

angles about each Cu atom are almost identical, and the dinuclear complex has idealized C_{2v} geometry, although no symmetry is crystallographically imposed on the molecule. Both copper atoms are nestled slightly above (0.241(2) Å) the rigidly disposed and coplanar XDK carboxylate oxygen atoms, with nearly identical $O_{XDK}-Cu-O_{XDK}$ angles. The fifth coordination site is filled by the adjacent copper fragment, the Cu–Cu distance being 2.4093(8) Å. This value is significantly smaller than the 2.6287(5) Å distance in the dicopper(I) in starting material **1** or in homoleptic $Cu_2(XDK)$, where the average Cu...Cu distance is 2.5901(9) Å.²⁸ The Cu–Cu bond in **4** is slightly shorter than that observed for the octaazacryptand class III mixed-valence complexes (Table 2.1).²⁷ The longest Cu–O distance is that to the triflate oxygen atom, which is ~0.2 Å longer than the Cu–O bond involving THF, which identifies the triflate as the axial ligand of the square pyramid. Because the ligand fields presented by the three different type donor atoms, the carboxylates, THF and copper, differ widely, the true symmetry at each metal center is rhombic, as reflected by EPR spectroscopy (vide infra).

The solid state structure for trifluoroacetate analog **6** (Figure 2.7) is quite similar to that of **4**, with a few important distinctions. Firstly, the Cu–Cu bond in **6** is 2.3988(8) Å, the shortest distance thus far observed for any dicopper mixed-valence complex. Secondly, the axial Cu–O bonds to the trifluoroacetate ligand have shortened by ~0.1 Å. Thirdly, the $O_{XDK}-Cu-O_{XDK}$ angles have contracted by ~10°, reflecting displacement of the copper atoms by 0.363(3) Å from the plane of the XDK carboxylate oxygen atoms. In addition, the Cu– O_{XDK} bond lengths are slightly longer in **6** versus **4**. All of these differences reflect the superior donor properties of the trifluoroacetate ligand compared to the triflate, their relative pK_a values being 0.3⁴⁸ and -5.9,⁴⁹ respectively. Trifluoroacetate provides a greater share of the overall electron density required by each copper ion, diminishing the bonding interaction to the XDK carboxylate oxygens in **6**. Overall the tris(carboxylate-bridged) motif

comprises a superior set of bridging ligands, however, a feature which accounts for the slightly shorter Cu–Cu distance in **6** compared to **4**.

In the structure of **8**, the bridging anion has been displaced in favor of THF ligands, due to the poor donor properties of the BF_4^- anion and its even rarer inclination to behave as a bridging ligand (Figure 2.8). Without the third bridge, the Cu–Cu distance in **8** has lengthened slightly compared to that in **4**. The axial Cu– O_{THF} bond lengths and the $\text{O}_{\text{XDK}}\text{–Cu–O}_{\text{XDK}}$ angles are quite similar to the analogous values in **4**, however.

Preparation and Structural Characterization of Heterodimetallic Complexes $[\text{CuZn}(\text{PXDK})(\text{OTf})(\text{THF})_2(\text{H}_2\text{O})]$ (**9**), $[\text{CuFe}(\text{PXDK})(\text{OTf})(\text{NB})(\text{MeCN})]_2$ (**10a**), and $[\text{CuZn}(\text{PXDK})(\text{OTf})(\text{NB})(\text{H}_2\text{O})]$ (**11**). Heterodimetallic complexes containing Cu(I) and divalent non-copper ions were sought to help delineate the significance of metal-metal bonding in the dicopper mixed-valence derivatives. If the close contact between copper atoms in the latter was only a consequence of the bridging XDK ligand, then a similar metal...metal distance might be expected for analogous Cu(I)M(II)(μ -XDK) complexes. Although it is difficult to duplicate exactly the ligand composition of the Cu(II) fragment in **4-8** to make such a comparison most relevant, the successful preparation of triflate complex **5** from mononuclear **3** and $\text{Cu}(\text{OTf})_2$ by Method B (Experimental Section) suggested a route to the desired mixed-metal complexes by substituting $\text{M}(\text{OTf})_2$ starting materials for copper(II) triflate under identical reaction conditions. Heterodimetallic Cu(I) complexes with Zn(II) and Fe(II) were of particular interest because these occur in the copper-iron active site in CcO^1 and the copper-zinc site in Cu, Zn superoxide dismutase.⁵⁰ Although neither active site complex involves carboxylate ligands, structurally characterized Cu(I)Fe(II) and Cu(I)Zn(II) complexes are virtually nonexistent,⁵¹ so their structures and reactivity are of intrinsic interest in the present context.

Exposure of **3** to a suspension of $\text{Zn}(\text{OTf})_2$ in THF resulted in gradual consumption of both reagents over 12 h (Scheme 2.1). As was the case for **5**, the purification of Cu(I)Zn(II) complex **9** was facilitated by its solubility in ether, which allowed insoluble $\text{Et}_4\text{N}(\text{OTf})$ to be filtered off. The analogous reaction with the XDK analog of **3** yielded an identical product, as judged by ^1H NMR spectroscopy, but it could not be separated from the byproduct salt. The water ligand in **9** might be derived from a trace amount of water in the $\text{Zn}(\text{OTf})_2$ reagent or the ethereal solvents; the synthesis proved to be quite reproducible, however.

The ^1H NMR spectrum of **9** displays a single set of XDK and THF resonances in a 1:1 ratio. Some of the upfield XDK resonances corresponding to protons adjacent to the metal binding sites, and the two THF resonances, were broadened at room temperature. We ascribe this behavior to dynamic exchange process(es) involving the THF ligand. A resonance that could be ascribed to water was presumably obscured by the ligand resonances, but the identity of this ligand was confirmed by X-ray crystallography, elemental analysis, and IR spectroscopy.

Complex **10a** was prepared from **3** and $[\text{Fe}(\text{OTf})_2(\text{MeCN})_2]$ in a similar fashion. The THF complex analogous to **9** did not afford crystalline material until excess norbornene was added, which presumably displaces the THF ligand bound to copper(I) in the precursor complex. A similar transformation was accomplished with the Cu(I)Zn(II) complex by recrystallizing it in the presence of excess norbornene to provide **11**. Triflate complex **4** was unreactive toward excess norbornene under similar conditions, as judged by UV-vis spectroscopy. This result suggests that delocalization in this complex may mask any reactivity as a copper(I) species, and that a Cu(1.5)Cu(1.5) oxidation state assignment is more appropriate for **4-8**. Alternatively, kinetic factors may explain the inertness of **4** towards norbornene.

To elaborate further the chemistry of the Cu(I)Fe(II) system, attempts were made to prepare an analog of the tris(carboxylate-bridged) complex **6**. Compound **10a**

was treated with 1 equivalent of $\text{Me}_4\text{N}[\text{O}_2\text{C}(4\text{-tert-Bu-Ph})]$ in CH_2Cl_2 , affording a white solid presumed to be $[\text{CuFe}(\text{PXDK})(\text{O}_2\text{C}(4\text{-tert-Bu-Ph})(\text{NB})(\text{MeCN}))_n]$ (**10b**, $n = 1$ or 2), once extracted with Et_2O to remove the salt byproduct. Attempts to recrystallize this complex for X-ray analysis were thwarted by its facile disproportionation to Fe(III) products and copper metal upon standing in solution for >2 h. The crude material was characterized by FTIR spectroscopy. A difference spectrum of **10b** and **10a** is consistent with displacement of the triflate ligand by the carboxylate (Figure 2.9). The increased basicity of the carboxylate compared to the triflate ligand must render the iron(II) center more reducing, thus accounting for the difference in stability of the two complexes.

The solid state structures of **9** and **11** are presented in Figures 2.10 and 2.11, respectively. The structure of **9** consists of a trigonal copper atom ligated by a THF and two carboxylate oxygen atoms. The zinc atom is trigonal bipyramidally coordinated by five oxygen atoms contributed by two from PXDK, a monodentate, terminal triflate, a THF, and a water molecule. The water is hydrogen bonded to the imide carbonyls of the PXDK ligand, a common feature in XDK complexes when water or alcohol ligands are present.^{32-34,36} The triflate ligand displays no affinity for Cu(I), and the metal–metal distance in this complex has lengthened to 2.8810(8) Å, compared to 2.4093(8) Å for the triflate analog **4**. The X-ray structure of **11** is somewhat analogous to that determined for **9** in that the copper atom is trigonal, the triflate ligand is coordinated in the same fashion, and the metal ions are well separated from one another. The copper-norbornene fragment is disordered over two positions with equal site occupancies in each orientation. These two binding modes were also observed within the same molecule of $[\text{Cu}_2(\text{XDK})(\text{NB})_2]$,²⁸ and are judged to be energetically similar.

The structure of **10a** was of only modest quality,⁵² but it served to identify the overall geometry and is depicted in Scheme 2.1. The complex dimerizes in the solid

state via bridging triflate groups, the two halves of the dimer being related by a center of inversion. Qualitatively, the Cu–Fe separation of 3.492(2) Å is similar to the Cu–Zn distances in **11**. Thus replacement of the Cu(II) ion in **5** with Zn(II) or Fe(II) provided complexes with reasonably similar composition but of different structures, particularly with respect to the metal···metal separation. Collectively, these structural and copper(I) ligand exchange studies lend credence to the supposition that the short Cu–Cu distances and approximate C_{2v} symmetry observed for **4-8** are a consequence of metal-metal bonding and valence delocalization, and not a function of the ligand architecture.

Electrochemical Properties of the Mixed-Valence Complexes. With the mixed-valence solvento complex **7** and the dicopper(I) analog²⁸ in hand, we were interested to determine whether they could be electrochemically interconverted. It was anticipated a priori that quasireversible behavior might be observed owing to molecular reorganization, since the copper ion geometries in **7** and $Cu_2(XDK)$ differ significantly. Moreover, it was of additional interest to determine whether the reduction potential of the $[Cu_2(XDK)]^+/Cu_2(XDK)$ couple deviates significantly from known trends for copper complexes because of the valence delocalized character of the mixed-valence form.⁵³

The homoleptic dicopper(I) complex exhibited a chemically reversible ($i_{pa}/i_{pc} \sim 1$) and electrochemically quasireversible ($\Delta E_p = 105$ mV, scan rate = 50 mV/s) cyclic voltammogram, with $E_{1/2} = -214$ mV vs. Cp_2Fe^+/Cp_2Fe (Figure 2.12). Plots of i_{pa} and i_{pc} vs. the square root of the scan rate are linear (Figure 2.13), as would be expected for a (nearly) reversible couple. The same electrochemical couple was observed for the oxidized complex **7** (Figures 2.14 and 2.15: $E_{1/2} = -222$ mV, $\Delta E_p = 132$ mV, scan rate = 50 mV/s, $i_{pa}/i_{pc} \sim 1$), confirming the one-electron nature of the process. An identical couple was also observed for the triflate complex **4** (Figures 2.16 and 2.17: $E_{1/2} = -218$ mV, $\Delta E_p = 147$ mV, scan rate = 50 mV/s, $i_{pa}/i_{pc} \sim 1$), suggesting that

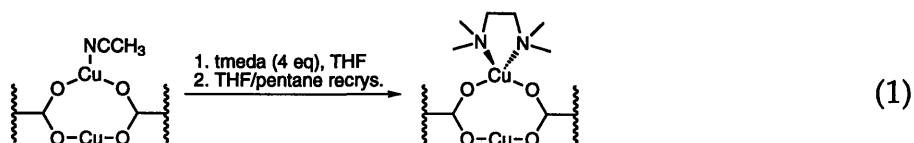
triflate is dissociated upon dissolution in the electrolyte media, or upon reduction to the Cu(I)Cu(I) species. At higher potentials an oxidation wave was detected, possibly signaling formation of a Cu(II)Cu(II) species, with $E_{pa} = 443$ mV (Figure 2.18). This feature could not be made reversible, even at high scan speeds (> 500 mV/s). Unlike the behavior noted for the more weakly coordinating triflate anion, the trifluoroacetate ligand in **6** might remain associated with the $Cu_2(XDK)^+$ fragment during cyclic voltammetry, because the analogous Cu(I)Cu(II)/Cu(I)Cu(I) reduction wave is completely irreversible (Figure 2.19).

In order to place the electrochemical data presented in a more general context, $E_{1/2}$ values for a variety of Cu(I) and Cu(I)Cu(I) complexes are compiled in Table 2.9. In each case the redox couple was chemically reversible and electrochemically reversible, or nearly so ($\Delta E_p < 150$ mV). The mononuclear complexes listed contain ligands ranging from a dianionic N_2 -bis(phenoxide) species (**a**) to neutral⁵⁴ or cationic⁵⁵⁻⁵⁷ donors with all nitrogen ligands (complexes **d**, **g**, **h-j**). For comparison to the results obtained for **7**, class I (**e**),⁵⁸ II (**b**),¹⁷ and III (**g**)²³ mixed-valence systems with well behaved electrochemistry were included. For **c**, the mixed-valence form has not been isolated and characterized, but the dicopper(II) form undergoes two sequential one-electron steps at the same potential.⁵⁹ To make the comparison more meaningful, potentials for each couple were referenced to the Cp_2Fe^+/Cp_2Fe couple in THF. Scaling was accomplished with the aid of literature data relating SHE to SCE,⁶⁰ AgCl/Ag to SCE,⁶⁰ and SCE to Cp_2Fe^+/Cp_2Fe (in THF)⁶¹. These normalized $E_{1/2}$ values can be used as a rough approximation only, since the potentials for each complex depend on experimental conditions, including choice of solvent, electrolyte and electrolyte concentration, solvation, and ion pairing.

As expected from previous electrochemical studies of a large series of copper complexes,⁵³ the compounds in Table 2.9 display the general trend that more negative reduction potentials occur as the ligand set becomes increasingly more

basic, with ligands which favor square planar or tetragonal over tetrahedral geometries, and with decreasing positive charge on the complex. From this standpoint all of the mixed-valence systems from the literature are unremarkable in the sense that their redox potentials are not anomalously affected by electronic coupling between adjacent copper atoms, except for **c**. Given the tetraanionic charge on the ligand and the rigidly planar structure of the dicopper(II) form, the $E_{1/2}$ values for this complex should more closely resemble that of **a**. Since little is known about the electronic and solid state structures of the mixed-valence and dicopper(I) forms of **c**, however, it is difficult to rationalize these findings.

For the $\text{Cu}_2(\text{XDK})/\text{Cu}_2(\text{XDK})^+$ couple, two competing factors unique to this system can be identified which tend to shift the reduction potential in opposite directions. One is the stability of the mixed-valence form due to its delocalized electronic structure, and the other is the resistance of the dicopper(I) variant to deviate from its linear, two-coordinate copper geometries. Judging from the large positive deviation of the redox potential from its expected position in the series of complexes (Table 2.9), the latter feature seems to predominate. Our previous studies of ligand substitution reactions with the $\text{Cu}_2(\text{XDK})$ scaffold revealed one of the copper(I) ions to be unreactive towards σ -donors. Even when exposed to excess tetramethylethylenediamine (tmeda, eq 1), it preferred to retain a



linear, two-coordinate "skewered" geometry. We suggest that the electrochemical oxidation of $\text{Cu}_2(\text{XDK})$ reaction involves coordination of two THF ligands to each copper ion, thus making it more difficult to oxidize compared to the other copper complexes with anionic oxygen donors which do not have the geometrical

constraints of XDK. In much the same way that ligands such as *i* and *j* prefer copper(I) by favoring a tetrahedral geometry, the XDK ligand enforces a linear, two-coordinate copper(I) structure. The magnitude of the positive $E_{1/2}$ shift appears to be much greater for **7**, however, since the all-oxygen $\text{Cu}_2(\text{XDK})$ donor set should place its $\text{Cu(I)Cu(II)}/\text{Cu(I)Cu(I)}$ potential near those found for **a-c**.

It is interesting that the $E_{1/2}$ value for $\text{Cu}_2(\text{XDK})$ falls approximately in the range found for blue copper proteins, $\sim +200$ to $+800$ mV vs. NHE, or ~ -600 to 0.0 mV vs. $\text{Cp}_2\text{Fe}^+/\text{Cp}_2\text{Fe}$ in THF, which employ a soft, monoanionic N_2S_2 ligand donor set while imposing a geometry intermediate between square planar and tetrahedral. Unlike our system, however, the rate of electron transfer is maximized at these biological electron transfer centers by requiring minimal ligand reorganization when cycling between the +1 and +2 oxidation states. Here we have achieved biologically relevant redox potentials through geometric constraints, at the cost of imparting a significant degree of reorganizational energy. Since these properties could readily be achieved in a protein matrix, the carboxylate-bridged dicopper(1.5) center would be a viable biological redox center.

EPR Studies of $[\text{Cu}_2(\text{XDK})(\text{THF})_4(\text{BF}_4)]$ (7**).** EPR spectroscopy is a key tool for characterizing electronic exchange in mixed-valence copper complexes because seven-line hyperfine coupling of the unpaired electron to a pair of $I = 3/2$ copper nuclei is diagnostic of spin delocalization.^{15-17,20,23} In class II systems, electron exchange is typically mediated by population of vibrationally excited states, which imparts sufficient kinetic energy for the electron to pass over the barrier separating the electronic ground states of the two metal ions. Thus the rate of electron transfer in these systems is temperature-dependent, and valence delocalization is observed when the rate exceeds the time scale of the EPR experiment. In contrast, class III mixed valence systems exhibit temperature independent delocalization behavior, at least on the EPR time scale and over the temperature range to which the sample

may be cooled. In this case the electronic structure is best defined by a single wavefunction encompassing both metal ions in which the unpaired electron resides. EPR studies of the present system were therefore undertaken in both the solid state and solution in order to probe the extent of electron delocalization, its temperature dependence, and the similarities between structures in the two different states.

A survey of the X-band frozen solution EPR spectra of **4**, **6** and **7** obtained at liquid helium temperature proved them to be quite similar, so a detailed investigation was undertaken with the solvento adduct **7**.⁶² EPR spectra for **7** are presented in Figures 2.20 and 2.21 for frozen solution and powdered samples, respectively, together with a simulation for each case, from which *g* values and copper hyperfine coupling constants were derived. The spectra of **7** at 9 and 77 K exhibited nearly identical rhombic signals with a readily discernible seven-line copper hyperfine coupling pattern on the lowest field component and overlapping hyperfine features on the two higher field components (Table 2.10). The X-band EPR spectra of powdered samples acquired at the same temperatures were extremely similar, albeit slightly broader, suggesting that the delocalized solid state structure is retained in solution. A frozen solution Q-band spectrum acquired at 2 K also exhibited seven distinct hyperfine lines on the lowest field component (Figure 2.22). Furthermore, power dependence saturation studies on both the frozen solution and powdered samples revealed that each spectrum corresponded to a single species. Taken together, the EPR studies provide compelling evidence that the $\text{Cu}_2(\text{XDK})^+$ mixed-valence series should be classified as a fully delocalized, class III system in both the solid state and solution. Moreover, these studies represent the first report of full delocalization for a dicopper mixed-valence species *at 2 K*, reinforcing its class III designation.

The rhombic signal and distinct hyperfine coupling constants at each g value were anticipated based on the approximate C_{2v} symmetry of the mixed-valence complexes and the significantly different ligand fields presented by the three types of ligands to each copper, the two carboxylate oxygens, the two THF oxygens, and the adjacent copper fragment.⁶³ The spectra may be compared with the rhombic spectra obtained for the Cu_A site⁶ and for $(CuL^{iPrdacoS})_2^+$,²⁰ each of which showed similar g values to those obtained for **7**, but the bis(μ -thiolato) model complex exhibited substantially smaller copper hyperfine coupling constants (Table 2.1). The larger copper hyperfine interactions in **7** may be explained in part by a greater amount of spin density residing at the metal centers because of the short Cu–Cu interaction and the absence of a superexchange pathway through bridging ligands. In contrast to these rhombic systems, the octazacryptand ligands afforded mixed-valence complexes with axial EPR spectra arising from its trigonal ligand field.

Molecular Orbital Calculations. An extended Hückel molecular orbital treatment of **7** was undertaken to elucidate its frontier molecular orbitals. The parameters of interest are the bonding and antibonding molecular orbitals responsible for the Cu–Cu interactions, their relative energies, and their copper orbital components. Net stabilization imparted to the dinuclear structure by Cu–Cu bonding was assessed by analyzing the interaction of the two mononuclear fragments as a function of Cu–Cu distance. Two simplified models were implemented, $[Cu_2(\mu-O_2CCH_3)_2(OMe_2)_4]$ and $[Cu_2(OH)_2(OH_2)_2(OMe_2)_4]$, each derived from the crystallographic coordinates of the dicopper core in **8**. The z -axis was taken along the apical copper- OMe_2 bond of one of the copper atoms, and the x - and y -axes along the copper-copper and copper-carboxylate (hydroxide/water) oxygen vectors, respectively.

Figures 2.23-2.24 display contour plots of the SOMO and second highest occupied molecular orbital (SHOMO) for $[Cu_2(\mu-O_2CCH_3)_2(OMe_2)_4]$. The SOMO has

considerable Cu $d_{x^2-y^2}$ /Cu $d_{x^2-y^2}$ σ -antibonding character (~60% for each copper), with a lobe from each metal pointed toward the other along the x-axis. The 4s (~11% for each copper) and d_{z^2} (~8% for each copper) orbitals also contribute significantly to the SOMO, having the same phases as the $d_{x^2-y^2}$ orbital on the two metals. In addition, the p orbital contribution from each ligand is out-of-phase with respect to the adjacent copper orbital lobe. The SHOMO in effect represents the bonding counterpart of the anti-bonding SOMO, but has more d_{z^2} (32%) and 4s (22%) character at the expense of the $d_{x^2-y^2}$ (36%). Again the ligand p orbitals are out-of-phase with respect to the adjacent copper orbital lobe, and in neither the SOMO nor the SHOMO are the carboxylate carbon atoms participating. An exchange pathway for electron delocalization therefore appears to be accessible only through the Cu–Cu interaction and not through the carboxylate ligands. Additional support for a net Cu–Cu bonding interaction is obtained from a reduced Mulliken overlap population analysis, which revealed that the overall Cu–Cu overlap population to be +0.1495 at the crystallographic Cu–Cu distance of 2.40 Å. This value may be compared to the average overlap population of +0.5362 for C–O single bonds in the same structure. Hence the short Cu–Cu distance in the mixed-valence complexes is indicative of a weak metal-metal bond.

A fragment molecular orbital (FMO) analysis was carried out on $[\text{Cu}_2(\text{OH})_2(\text{OH}_2)_2(\text{OMe}_2)_4]$, a simpler model which permits the two copper fragments to be separated without breaking any carbon–oxygen bonds (Figure 2.25). The frontier molecular orbitals for this model had essentially identical energies and orbital contributions as those obtained for $[\text{Cu}_2(\mu\text{-O}_2\text{CCH}_3)_2(\text{OMe}_2)_4]$. The FMO analysis revealed that a significant bonding/antibonding interaction results between the highest occupied molecular orbital (HOMO) of the Cu(I) and Cu(II) fragments when the two are brought together. This interaction is also observed in a Walsh diagram, where the molecular orbital energy is plotted as a function of the Cu–Cu

distance (Figure 2.25). The orbitals perturbed most dramatically are the SHOMO and SOMO, those suspected to play the greatest role in Cu–Cu bonding. The energy gap between the SOMO and SHOMO of $[\text{Cu}_2(\text{OH})_2(\text{OH}_2)_2(\text{OMe}_2)_4]$ is maximized at ~ 2.2 Å, reasonably close to the crystallographically determined distance of 2.40 Å. A minimum for the total energy of the molecular orbitals is reached at a Cu–Cu distance of ~ 2.9 Å. Greater error for this latter parameter is to be expected, since the total energy is made up of the individual energies of the 65 occupied molecular orbitals. Nevertheless, both the FMO and Walsh analyses support the idea that net stabilization is imparted to these mixed-valence complexes through Cu–Cu bonding. Furthermore, the bonding interaction principally utilizes the Cu $d_{x^2-y^2}$ orbitals. This outcome does not support a previous assertion that strong Cu–Cu bonding can only be mediated by Cu d_{z^2} /Cu d_{z^2} overlap, and that $(d_{x^2-y^2})^1$ dimers are always held together exclusively as a consequence of their ligand structures.²² Instead, we conclude that the only strict requirement for Cu–Cu bonding in these dimers is reasonable σ -type overlap between two adjacent metal orbitals and, depending on the geometry, this interaction can be achieved with $d_{x^2-y^2}$ orbitals.

Conclusions

A series of dicopper mixed-valence complexes have been assembled with the XDK ligand system. Their fully delocalized, class III behavior has been demonstrated experimentally through (a) X-ray crystallographic studies which show that the coordination environments about each copper atom are identical, and (b) solid state and solution EPR studies which demonstrate that the unpaired spin is coupled simultaneously to both $I = 3/2$ copper ions down to 2 K. Support for a stabilizing Cu–Cu bonding interaction in these complexes was provided by (a) the synthesis of Cu(I) heterodimetallic complexes with other divalent metal ions which are of similar composition but have much longer Cu(I)···M(II) distances; (b) the lack of

reactivity of the mixed-valence complexes with norbornene, which reacts quantitatively with the Cu(I) fragment of the heterodimetallic complexes; and (c) extended Hückel molecular orbital calculations, which show a Cu–Cu interaction in the SOMO and SHOMO that is composed primarily of Cu $d_{x^2-y^2}$ /Cu $d_{x^2-y^2}$ orbital overlap. Cyclic voltammetric studies revealed an electrochemically quasireversible Cu(I)Cu(II)/Cu(II)Cu(II) wave with a very positive $E_{1/2}$ value, tentatively attributed to the geometrical constraints imposed by the XDK ligand, which favors the linear two-coordinate Cu(I) geometry. In the aggregate, these studies significantly enhance our understanding of the assembly, stability, and electronic structure of class III mixed-valence Cu–Cu bonded systems. We suggest that this new structural and redox active motif would serve well as a biological electron transfer center in carboxylate-bridged environments.

Acknowledgement. This work was supported by grants from the National Science Foundation and AKZO Corp.

References and Notes

- (1) Ferguson-Miller, S.; Babcock, G. T. *Chem. Rev.* **1996**, *96*, 2889-2907.
- (2) Zumft, W. G.; Kroneck, P. M. H. *FEMS Symp. Ser.* **1990**, *56*, 37-55.
- (3) Blackburn, N. J.; deVries, S.; Barr, M. E.; Houser, R. P.; Tolman, W. B.; Sanders, D.; Fee, J. A. *J. Am. Chem. Soc.* **1997**, *119*, 6135-6143.
- (4) Farrar, J. A.; Neese, F.; Lappalainen, P.; Kroneck, P. M. H.; Saraste, M.; Zumft, W. G.; Thomson, A. J. *J. Am. Chem. Soc.* **1996**, *118*, 11501-11514.
- (5) von Wachenfeldt, C.; deVries, S.; van der Oost, J. *FEBS Lett.* **1994**, *340*, 109-113.
- (6) Neese, F.; Zumft, W. G.; Antholine, W. E.; Kroneck, P. M. H. *J. Am. Chem. Soc.* **1996**, *118*, 8692-8699.
- (7) Lappalainen, P.; Aasa, R.; Malmstrom, B. G.; Saraste, M. *J. Biol. Chem.* **1993**, *268*, 26416-26421.
- (8) Farrar, J. A.; Thomson, A. J.; Cheesman, M. R.; Dooley, D. M.; Zumft, W. G. *FEBS Lett.* **1991**, *294*, 11-15.
- (9) Iwata, S.; Ostermeier, C.; Ludwig, B.; Michel, M. *Nature* **1995**, *376*, 660-669.
- (10) Tsukihara, T.; Aoyama, H.; Yamashita, E.; Tomizake, T.; Yamaguchi, H.; Shinzawa-Itoh, K.; Nakashima, R.; Yaono, R.; Yoshikawa, S. *Science* **1995**, *269*, 1069-1074.
- (11) Tsukihara, T.; Aoyama, H.; Yamashita, E.; Tomizake, T.; Yamaguchi, H.; Shinzawa-Itoh, K.; Nakashima, R.; Yaono, R.; Yoshikawa, S. *Science* **1996**, *272*, 1136-1144.
- (12) Day, P.; Robin, M. B. *Adv. Inorg. Chem. Radiochem.* **1967**, *10*, 247-422.
- (13) Ramirez, B. E.; Malmstrom, B. G.; Winkler, J. R.; Gray, H. B. *Proc. Nat. Acad. Sci. U.S.A.* **1995**, *92*, 11949-11951.
- (14) Dunaj-Jurco, M.; Ondrejovic, G.; Melnik, M. *Coord. Chem. Rev.* **1988**, *83*, 1-28.

- (15) Hendrickson, D. N.; Long, R. C.; Hwang, Y. T.; Chang, H. In *Biological and Inorganic Copper Chemistry Volume I*; K. D. Karlin and J. Zubieta, Eds.; Adenine: Guilderland, NY, 1984; pp 223-238.
- (16) Long, R. C.; Hendrickson, D. N. *J. Am. Chem. Soc.* **1983**, *105*, 1513-1521.
- (17) Gagne, R. R.; Koval, C. A.; Smith, T. J.; Cimolino, M. C. *J. Am. Chem. Soc.* **1979**, *101*, 4571-4580.
- (18) Westmorland, T. D.; Wilcox, D. E.; Baldwin, M. J.; Mims, W. B.; Solomon, E. I. *J. Am. Chem. Soc.* **1989**, *111*, 6106-6123.
- (19) A Cu(I)Cu(II) mixed-valence "acetate/methanol" complex has been reported, and support for a delocalized structure at room temperature and at 77 K was acquired by EPR. This complex was never isolated, however, and it disproportionated to a large extent upon cooling below ~ -50 °C as judged by the presence of a significant mononuclear Cu(II) impurity in the EPR spectrum. See: Sigwart, C.; Hemmerich, P.; Spence, J. T. *Inorg. Chem.* **1968**, *7*, 2545-2548.
- (20) Houser, R. P.; Young, V. G., Jr.; Tolman, W. B. *J. Am. Chem. Soc.* **1996**, *118*, 2101-2102.
- (21) Abbreviations: $L^{iPrdacoS}$ = 1-isopropyl-5-ethylthiolato-1,5-diazocyclooctane; L^1 = $N(CH_2CH_2N=CH-CH=NCH_2CH_2)_3N$; L^2 = $N(CH_2CH_2NH-CH_2-CH_2-NHCH_2CH_2)_3N$; L^3 = $N(CH_2CH_2CH_2N=CH-CH=NCH_2CH_2CH_2)_3N$.
- (22) Harding, C.; Nelson, J.; Symons, M. C. R.; Wyatt, J. *J. Chem. Soc., Chem. Commun.* **1994**, 2499-2500.
- (23) Harding, C.; McKee, V.; Nelson, J. *J. Am. Chem. Soc.* **1991**, *113*, 9684-9685.
- (24) Barr, M. E.; Smith, P. H.; Antholine, D. E.; Spencer, B. *J. Chem. Soc., Chem. Commun.* **1993**, 1649-1652.

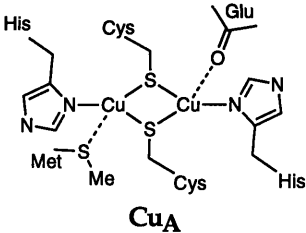
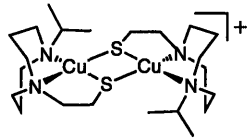
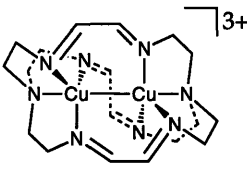
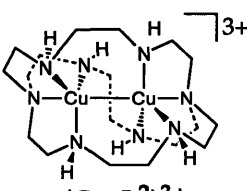
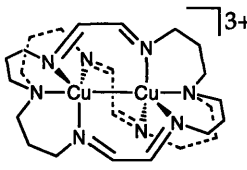
- (25) Williams, K. R.; Gamelin, D. R.; LaCroix, L. B.; Houser, R. P.; Tolman, W. B.; Mulder, T. C.; deVries, S.; Hedman, B.; Hodgson, K. O.; Solomon, E. I. *J. Am. Chem. Soc.* **1997**, *119*, 613-614.
- (26) Farrar, J. A.; Grinter, R.; Neese, F.; Nelson, J.; Thomson, A. J. *J. Chem. Soc., Dalton Trans.* **1997**, 4083-4087.
- (27) Farrar, J. A.; McKee, V.; Al-Obaidi, A. H. R.; McGarvey, J. J.; Nelson, J.; Thomson, A. J. *Inorg. Chem.* **1995**, *34*, 1302-1303.
- (28) LeCloux, D. D.; Lippard, S. J. *Inorg. Chem.* **1997**, *36*, 4035-4046.
- (29) Herold, S. H.; Lippard, S. J. *J. Am. Chem. Soc.* **1997**, *119*, 145-156.
- (30) Rebek, J., Jr.; Marshall, L.; Wolak, R.; Parris, K.; Killoran, M.; Askew, B.; Nemeth, D.; Islam, N. *J. Am. Chem. Soc.* **1985**, *107*, 7476-7481.
- (31) Mizoguchi, T. J.; Lippard, S. J. *Inorg. Chem.* **1997**, *36*, 4526-4533.
- (32) Tanase, T. T.; Yun, J. W.; Lippard, S. J. *Inorg. Chem.* **1996**, *35*, 3585-3594.
- (33) Tanase, T.; Lippard, S. J. *Inorg. Chem.* **1995**, *34*, 4682-4690.
- (34) Yun, J. W.; Tanase, T.; Pence, L. E.; Lippard, S. J. *J. Am. Chem. Soc.* **1995**, *117*, 4407-4408.
- (35) Tanase, T.; Yun, J. W.; Lippard, S. J. *Inorg. Chem.* **1995**, *34*, 4220-4229.
- (36) Watton, S. P.; Masschelein, A.; J. Rebek, J., Jr.; Lippard, S. J. *J. Am. Chem. Soc.* **1994**, *116*, 5196-5205.
- (37) Goldberg, G. P.; Watton, S. P.; Masschelein, A.; Wimmer, L.; Lippard, S. J. *J. Am. Chem. Soc.* **1993**, *115*, 5346-5347.
- (38) Steinhuebel, D. P.; Lippard, S. J. *Inorg. Chim. Acta* **1998**, *In Press*,
- (39) Bryan, P. S.; Dabrowiak, J. C. *Inorg. Chem.* **1975**, *14*, 296.
- (40) WINEPR-SimFonia. 1.25; Bruker Analytik GmbH: Karlsruhe, FRG, 1994-1996.
- (41) Hoffmann, R. *J. Chem. Phys.* **1963**, *39*, 1397-1412.

- (42) Landrum, G. A. *YAeHMOP: Yet Another extended Huckel Molecular Orbital Package. 2.0*; Cornell University: Ithaca, NY, 1995. YAeHMOP is freely available on the WWW at URL.
- (43) *SMART. 4.0*; Siemens Industrial Automation, Inc.: Madison, WI, 1994.
- (44) Feig, A. L.; Bautista, M. T.; Lippard, S. J. *Inorg. Chem.* **1996**, *35*, 6892-6898.
- (45) Burla, M. C.; Camalli, M.; Cascarano, G.; Giacovazzo, C.; Polidori, G.; Spagna, R.; Viterbo, D. *J. Appl. Crystallogr.* **1989**, *22*, 389-393.
- (46) *TEXSAN: Single Crystal Structure Analysis Software. 1.6c*; Molecular Structure Corporation: The Woodlands, TX, 1995.
- (47) *SHELXTL: Structure Analysis Program. 5.0*; Siemens Industrial Automation, Inc.: Madison, WI, 1995.
- (48) *The Merck Index, Twelfth Edition* S. Budavari, Ed.; Merck Research Laboratories: Whitehouse Station, NJ, 1996.
- (49) Guthrie, J. P. *Can. J. Chem.* **1978**, *56*, 2342-2354.
- (50) Valentine, J. S.; Pantoliano, M. W. In *Copper Proteins*; T. G. Spiro, Ed.; Wiley: New York, 1981.
- (51) (a) A Cambridge Structural Data Base (CSD) search yielded only Cu(I)Fe(II) complexes with ferrocenyl-phosphine ligands (See, for example: Neo, S. P.; Zhou, Z-Y.; Mak, T. C. W.; Hor, T. S. A. *J. Chem. Soc. Dalton Trans.* **1994**, 3451-3457). A Cu(I)Fe(II) trihydride bridged species was also reported, Van Der Sluys, L. S.; Miller, M. M.; Kubas, G. J.; Caulton, K.G. *J. Am. Chem. Soc.* **1991**, *113*, 2513-2520. (b) The only structurally characterized Cu(I)Zn(II) complex reported to date (CSD search) is a nitrite-bridged compound. See: Halfen, J. A.; Mahapatra, S.; Wilkinson, E. C.; Gengenbach, A. J.; Young, V.G., Jr.; Que, L., Jr.; Tolman, W. B. *J. Am. Chem. Soc.* **1996**, *118*, 763-776.
- (52) X-ray data for **10a** from dichloroethane/pentane: P2/n, a = 19.0883(5), b = 14.5289(3), c = 23.4342(6), β = 109.1900(10), V = 6137.9(3), Z = 4, T = 188 K, R =

14.12%, $wR^2 = 40.36$. This structure was not fully refined due to major disorder of the two lattice dichloroethane molecules.

- (53) Patterson, G. S.; Holm, R. H. *Bioinorg. Chem.* **1975**, *4*, 257-275.
- (54) Tolman, W. B. *Inorg. Chem.* **1991**, *30*, 4877-4880.
- (55) Wei, N.; Murthy, N. N.; Tyeklar, Z.; Karlin, K. D. *Inorg. Chem.* **1994**, *33*, 1177-1183.
- (56) Mahapatra, S.; Halfen, J. A.; Wilkinson, E. C.; Pan, G.; Wang, X.; Young, V.G., Jr.; Cramer, C. J.; Que, L., Jr.; Tolman, W. B. *J. Am. Chem. Soc.* **1996**, *118*, 11555-11574.
- (57) Sorrell, T. N.; Jameson, D. L. *Inorg. Chem.* **1982**, *21*, 1014-1019.
- (58) Mahroof-Tahir, M.; Karlin, K. D. *J. Am. Chem. Soc.* **1992**, *114*, 7599-7601.
- (59) Fenton, D. E.; Schroeder, R. R.; Lintvedt, R. L. *J. Am. Chem. Soc.* **1978**, *100*, 1931-1932.
- (60) Bard, A. J.; Faulkner, L. R. In *Electrochemical Methods Fundamentals and Applications* John Wiley & Sons: New York, 1980.
- (61) Connelly, N. G.; Geiger, W. E. *Chem. Rev.* **1996**, *96*, 877-910.
- (62) The detailed EPR analyses were carried out in collaboration with Dr. Roman Davydov of Northwestern University.
- (63) Hathaway, B. J.; Billing, D. E. *Coord. Chem. Rev.* **1970**, *5*, 143-207.

Table 2.1. Summary of pertinent spectroscopic and structural data on known class III mixed-valence copper systems.

Complex	Visible-NIR (λ_{\max} , nm (ϵ , M ⁻¹ , cm ⁻¹))	Cu-Cu Dist.(Å)	EPR ^b	ref.
 CuA	363 (1200), ^a 480 (3000), 532 (3000), 808 (1600)	2.5-2.7	g _{min} = 2.003, ^c g _{mid} = 2.005, g _{max} = 2.203, A _x ^{65-Cu} = 105 G, A _y ^{65-Cu} = 116 G, A _z ^{65-Cu} = 235 G	6,7, 9-11
 (CuLiPrdacoS) ₂ (OTf)	358 (2700), 602 (800), 786 (sh), 1466 (1200)	2.9306(9)	g ₁ = 2.010, g ₂ = 2.046, g ₃ = 2.204, A ₂ ^{Cu} = 36.3 G, A ₃ ^{Cu} = 49.9 G	20
 (Cu ₂ L ¹) ³⁺	600-650 (1500-3500), ^d 756 (5000)	2.448 ^e	g = 2.004, g _⊥ = 2.148, A = 11 G, A _⊥ = 111 G	22-23
 (Cu ₂ L ²) ³⁺	622 (2900), 736 (4500)	2.415(1)	g = 2.02, g _⊥ = 2.15, A = 22 G, A _⊥ = 115 G	24
 (Cu ₂ L ³) ³⁺	600-650 (1500-3500), ^d 750-780 (5000)	2.419(1)	g = 2.00, g _⊥ = 2.17, A = 11 G, A _⊥ = 92 G	22, 27

^aFrom *Paracoccus denitrificans* CcO (see ref. 7). ^bAll parameters were derived from simulated spectra. ^c⁶⁵Cu- and [15N]Histidine-Enriched N₂OR from *P. stutzeri* (see ref. 6). ^dOnly ranges were reported for the absorption maxima and molar absorptivities. ^eNo esd reported.

Table 2.2. Summary of X-ray Crystallographic Data.

	4·2THF	6·0.5THF	8·1THF	9·0.5THF	11
formula	C ₄₉ H ₇₀ N ₂ O ₁₅ Cu ₂ S ₁ F ₃	C ₄₄ H ₅₈ N ₂ O _{12.5} Cu ₂ F ₃	C ₆₄ H ₁₀₂ N ₂ O ₁₃ Cu ₂ B ₁ F ₄	C ₅₅ H ₈₄ N ₂ O _{14.5} Cu ₁ Zn ₁ F ₃ S ₁	C ₅₂ H ₇₄ N ₂ O ₁₂ Cu ₁ Zn ₁ F ₃ S ₁
fw	1143.21	4977.49(6)	1321.37	1223.21	1137.10
space group	<i>P</i> 2 ₁ / <i>n</i>	<i>P</i> 2 ₁ 2 ₁ 2 ₁	<i>P</i> 2 ₁ / <i>n</i>	<i>C</i> 2/ <i>c</i>	<i>P</i> 2 ₁ / <i>n</i>
a, Å	20.203(2)	11.02460(10)	17.4237(9)	25.0154(5)	15.5186(2)
b, Å	12.0901(10)	16.31380(10)	21.5206(12)	18.2877(2)	24.28620(10)
c, Å	22.130(2)	27.67530(10)	18.8570(10)	25.9855(5)	15.93940(10)
β, deg	94.522(5)		105.9970(10)	92.1000(10)	113.3850(10)
V, Å ³	5388.6(8)	4977.49(6)	6797.0(6)	11879.7(4)	5513.91(8)
Z	4	4	4	4	2
ρ _{calcd} , g/cm ³	1.409	1.333	1.291	1.368	1.370
T, °C	-85	-85	-85	-85	-85
μ(Mo Kα), mm ⁻¹	0.904	0.924	0.696	0.870	0.929
transmission coeff	0.817-1.000	0.668-1.000	0.806-1.000	0.885-1.000	0.718-1.000
2θ limits, deg	3-46	3-46	3-46	3-57	3-57
total no. of data	20000	19795	25459	33683	31387
no. of unique data	7456	7086	9533	13213	12392
observed data ^a	5684	6246	6996	8258	7881
no. of parameters	624	559	748	686	704
R(%) ^b	5.19	4.71	8.50	6.75	7.09
wR ² (%) ^c	12.59	12.45	18.14	16.37	17.60
max, min peaks, e/Å ³	0.533, -0.378	0.744, -0.380	1.112, -0.448	0.984, -0.613	0.792, -0.753

^aObservation criterion: $I > 2\sigma(I)$. ^b $R = \sum ||F_O| - |F_C|| / \sum |F_O|$. ^c $wR^2 = \{\sum [w(F_O^2 - F_C^2)^2] / \sum [w(F_O^2)^2]\}^{1/2}$.

Table 2.3. Selected Bond Distances and Angles.^a

	Distances (Å)		Angles (deg)	
4	Cu1-Cu2	2.4093(8)	O102-Cu1-O202	164.6(2)
	Cu1-O102	1.873(3)	O102-Cu1-O401	96.4(2)
	Cu1-O202	1.873(3)	O401-Cu1-O502	98.28(3)
	Cu1-O401	2.315(4)	O101-Cu2-O201	164.03(14)
	Cu1-O502	2.060(3)	O101-Cu2-O402	100.26(14)
	Cu2-O101	1.891(3)	O402-Cu2-O501	91.82(13)
	Cu2-O201	1.887(3)	Cu1-Cu2-O402	92.27(10)
	Cu2-O402	2.242(3)	Cu2-Cu1-O401	87.94(10)
	Cu2-O501	2.052(3)		
6	Cu1-Cu2	2.3988(8)	O102-Cu1-O202	157.9(2)
	Cu1-O102	1.910(4)	O102-Cu1-O401	99.9(2)
	Cu1-O202	1.908(4)	O401-Cu1-O502	97.5(2)
	Cu1-O401	2.150(4)	O101-Cu2-O201	156.6(2)
	Cu1-O502	2.050(4)	O101-Cu2-O402	105.8(2)
	Cu2-O101	1.891(3)	O402-Cu2-O501	97.7(2)
	Cu2-O201	1.889(3)	Cu1-Cu2-O402	87.03(12)
	Cu2-O402	2.166(4)	Cu2-Cu1-O401	88.27(13)
	Cu2-O501	2.083(3)		
8	Cu1-Cu2	2.4246(12)	O102-Cu1-O202	165.4(2)
	Cu1-O102	1.885(4)	O102-Cu1-O401	102.6(2)
	Cu1-O202	1.883(4)	O401-Cu1-O402	89.6(2)
	Cu1-O401	2.285(5)	O101-Cu2-O201	166.3(2)
	Cu1-O402	2.087(5)	O101-Cu2-O501	91.8(2)
	Cu2-O101	1.883(5)	O501-Cu2-O502	90.3(2)
	Cu2-O201	1.881(5)	Cu1-Cu2-O501	101.26(14)
	Cu2-O501	2.270(5)	Cu2-Cu1-O401	102.7(2)
	Cu2-O502	2.042(5)		

Table 2.3. (cont.) Selected Bond Distances and Angles.^a

	<u>Distances</u>		<u>Angles</u>	
9	Cu1...Zn1	2.8810(8)	O102-Cu1-O202	162.44(14)
	Cu1-O102	1.891(3)	O102-Cu1-O401	102.40(12)
	Cu1-O202	1.890(3)	O202-Cu1-O401	93.52(13)
	Cu1-O401	2.228(3)	O101-Zn1-O201	150.03(13)
	Zn1-O101	1.930(3)	O101-Zn1-O501	92.71(14)
	Zn1-O201	1.938(3)	O501-Zn1-O504	90.45(14)
	Zn1-O501	2.145(3)	O501-Zn1-O505	178.64(13)
	Zn1-O504	2.025(3)		
	Zn1-O505	2.189(3)		
11	Cu1...Zn1	3.732(2)	O102-Cu1-O202	109.84(14)
	Cu1'...Zn1	3.294(2)	O102-Cu1'-O202	107.0(2)
	Cu1-O102	1.981(3)	O102-Cu1-C401	104.3(4)
	Cu1-O202	1.973(3)	O102-Cu1'-C41	105.2(4)
	Cu1-C401	2.044(14)	O101-Zn1-O201	132.26(13)
	Cu1-C402	2.12(2)	O101-Zn1-O501	99.57(14)
	Cu1'-O102	1.998(3)	O101-Zn1-O504	103.15(12)
	Cu1'-O202	2.027(3)	O201-Zn1-O501	106.85(14)
	Cu1'-C41	2.024(12)	O201-Zn1-O504	105.59(12)
	Cu1'-C42	2.004(11)		
	Zn1-O101	1.911(3)		
	Zn1-O201	1.917(3)		
	Zn1-O501	2.021(3)		
	Zn1-O504	1.970(3)		

^aNumbers in parentheses are estimated standard deviations of the last significant figure. Atoms are labeled as indicated in Figures 2.6-2.10.

Table 2.4. Atomic coordinates ($\times 10^4$) and equivalent isotropic displacement parameters ($\text{Å}^2 \times 10^3$) for **4**.^a

atom	x	y	z	U(eq)
Cu(2)	2(1)	4179(1)	2107(1)	30(1)
Cu(1)	528(1)	5131(1)	2973(1)	32(1)
S(401)	1166(1)	5773(1)	1688(1)	45(1)
F(401)	1462(2)	7814(3)	1431(2)	76(1)
F(402)	1028(3)	6877(4)	679(2)	104(2)
F(403)	423(2)	7462(3)	1359(2)	96(1)
O(101)	-716(2)	5177(3)	2135(1)	34(1)
O(102)	-215(2)	6063(3)	2927(2)	38(1)
O(103)	-2058(2)	3708(3)	2509(2)	38(1)
O(104)	-1017(2)	5338(3)	4162(2)	46(1)
O(201)	624(2)	3035(3)	2278(2)	38(1)
O(202)	1104(2)	3921(3)	3083(2)	39(1)
O(203)	649(2)	2489(3)	4339(2)	49(1)
O(204)	-243(2)	829(3)	2630(2)	46(1)
O(401)	1128(2)	6126(3)	2309(2)	61(1)
O(402)	619(2)	5076(3)	1466(2)	53(1)
O(403)	1807(2)	5431(3)	1537(2)	72(1)
O(501)	-465(2)	3271(3)	1414(2)	43(1)
O(502)	911(2)	5846(3)	3770(2)	38(1)
O(601)	-2975(4)	5271(6)	5015(3)	139(3)
O(602)	-2851(4)	606(7)	4693(4)	157(3)
N(101)	-1529(2)	4545(3)	3324(2)	27(1)
N(201)	209(2)	1672(3)	3476(2)	31(1)
C(101)	-687(2)	5941(4)	2528(2)	32(1)
C(102)	-1968(2)	4551(4)	2801(2)	30(1)
C(103)	-1390(2)	5458(4)	3713(2)	33(1)
C(104)	-1001(3)	7716(4)	2090(3)	45(1)
C(105)	-1829(3)	7179(5)	4137(2)	52(2)
C(106)	-2990(2)	5396(4)	2290(3)	45(1)
C(107)	-1246(2)	6798(4)	2504(2)	33(1)
C(108)	-1337(2)	7272(4)	3134(2)	36(1)
C(109)	-1741(2)	6550(4)	3546(2)	36(1)
C(110)	-2413(2)	6286(4)	3210(2)	38(1)
C(111)	-2318(2)	5645(4)	2634(2)	33(1)
C(112)	-1905(2)	6347(4)	2217(2)	33(1)
C(201)	1061(2)	3117(4)	2718(2)	35(1)
C(202)	242(3)	982(4)	2969(2)	37(1)
C(203)	741(2)	1892(4)	3917(2)	35(1)
C(204)	2168(3)	2690(5)	2436(3)	53(2)
C(205)	1768(3)	1160(5)	4461(3)	54(2)
C(206)	767(3)	-689(4)	2557(3)	53(2)
C(207)	1594(2)	2222(4)	2791(2)	39(1)
C(208)	1838(2)	2059(4)	3459(2)	41(1)
C(209)	1404(2)	1331(4)	3835(2)	39(1)
C(210)	1276(3)	229(4)	3513(2)	43(1)
C(211)	913(2)	413(4)	2890(2)	38(1)

Table 2.4. (cont'd) Atomic coordinates ($\times 10^4$) and equivalent isotropic displacement parameters ($\text{Å}^2 \times 10^3$) for **4**.^a

atom	x	y	z	U(eq)
C(212)	1352(2)	1121(4)	2503(2)	40(1)
C(301)	-664(2)	3095(4)	3404(2)	29(1)
C(302)	-440(2)	2065(4)	3610(2)	29(1)
C(303)	-834(2)	1398(4)	3946(2)	33(1)
C(304)	-1450(2)	1807(4)	4079(2)	32(1)
C(305)	-1686(2)	2832(4)	3888(2)	30(1)
C(306)	-1286(2)	3469(4)	3540(2)	28(1)
C(307)	-602(3)	256(4)	4157(3)	51(1)
C(308)	-2345(2)	3250(4)	4061(2)	42(1)
C(401)	1012(3)	7036(5)	1268(3)	61(2)
C(501)	-62(3)	2737(6)	972(3)	67(2)
C(502)	-387(8)	1765(14)	750(10)	63(6)
C(50D)	-217(6)	1449(10)	1066(7)	56(5)
C(503)	-963(4)	1524(7)	1152(4)	115(4)
C(504)	-996(3)	2528(5)	1562(3)	56(2)
C(505)	640(3)	5431(5)	4320(2)	51(1)
C(506)	546(4)	6422(5)	4721(3)	75(2)
C(507)	541(9)	7380(11)	4332(6)	59(6)
C(51D)	974(9)	7362(11)	4442(6)	64(6)
C(508)	973(4)	7056(4)	3799(3)	62(2)
C(601)	-2525(6)	5435(10)	5517(6)	133(4)
C(602)	-2689(5)	4730(9)	6029(5)	126(4)
C(603)	-3380(6)	4355(10)	5848(5)	139(4)
C(604)	-3548(5)	4709(9)	5192(5)	123(3)
C(605)	-3367(6)	-155(10)	4476(6)	139(4)
C(606)	-4020(6)	472(11)	4575(6)	151(4)
C(607)	-3832(10)	1603(27)	4865(12)	180(8)
C(60D)	-3808(16)	1103(35)	5066(17)	50(19)
C(608)	-3116(6)	1205(10)	5202(6)	140(4)

^aNumbers in parentheses are estimated standard deviations of the last significant figure. ^bU(eq) is defined as one third of the trace of the orthogonalized U_{ij} tensor.

Table 2.5. Atomic coordinates ($\times 10^4$) and equivalent isotropic displacement parameters ($\text{Å}^2 \times 10^3$) for **6**.^a

atom	x	y	z	U(eq)
Cu(1)	-6207(1)	-4502(1)	-1033(1)	36(1)
Cu(2)	-7309(1)	-4784(1)	-1762(1)	31(1)
F(401)	-8136(7)	-1871(3)	-997(3)	148(3)
F(402)	-9671(6)	-2560(4)	-995(4)	189(4)
F(403)	-8999(7)	-2082(4)	-1631(3)	157(3)
O(101)	-8266(3)	-5517(2)	-1395(1)	36(1)
O(102)	-7230(3)	-5284(2)	-720(1)	40(1)
O(103)	-7524(3)	-7453(2)	-1747(1)	38(1)
O(104)	-5646(4)	-6934(3)	-331(1)	49(1)
O(201)	-5939(3)	-4428(2)	-2114(1)	36(1)
O(202)	-4942(3)	-4105(2)	-1441(1)	37(1)
O(203)	-2509(3)	-5346(2)	-1291(1)	48(1)
O(204)	-4579(4)	-5992(2)	-2645(1)	46(1)
O(401)	-7292(5)	-3417(3)	-946(2)	60(1)
O(402)	-8140(3)	-3590(3)	-1674(2)	51(1)
O(501)	-8229(3)	-5134(2)	-2386(1)	39(1)
O(502)	-5173(4)	-4371(3)	-422(1)	58(1)
N(101)	-6598(4)	-7188(2)	-1032(2)	30(1)
N(201)	-3533(4)	-5659(3)	-1969(2)	32(1)
C(101)	-8089(4)	-5614(3)	-948(2)	33(1)
C(102)	-7623(5)	-7403(3)	-1315(2)	32(1)
C(103)	-6576(5)	-7101(4)	-527(2)	37(1)
C(104)	-10017(5)	-5482(4)	-541(2)	44(1)
C(105)	-7459(6)	-7613(4)	245(2)	56(2)
C(106)	-9532(5)	-8212(4)	-1339(2)	46(2)
C(107)	-9015(5)	-6121(3)	-674(2)	34(1)
C(108)	-8508(5)	-6489(4)	-204(2)	42(1)
C(109)	-7754(5)	-7275(4)	-257(2)	40(1)
C(110)	-8491(5)	-7909(3)	-545(2)	41(1)
C(111)	-8795(4)	-7578(3)	-1036(2)	34(1)
C(112)	-9568(4)	-6791(3)	-996(2)	34(1)
C(201)	-5047(5)	-4111(3)	-1886(2)	31(1)
C(202)	-3847(5)	-5553(3)	-2458(2)	35(1)
C(203)	-2712(4)	-5180(3)	-1704(2)	36(1)
C(204)	-4558(5)	-2797(3)	-2246(2)	44(1)
C(205)	-848(5)	-4322(4)	-1740(3)	56(2)
C(206)	-3070(6)	-5134(4)	-3249(2)	51(2)
C(207)	-4085(4)	-3686(3)	-2198(2)	36(1)
C(208)	-2843(5)	-3678(3)	-1937(2)	40(1)
C(209)	-2090(4)	-4480(4)	-1975(2)	40(1)
C(210)	-1963(5)	-4715(4)	-2504(2)	42(1)
C(211)	-3208(5)	-4857(4)	-2730(2)	38(1)
C(212)	-3950(5)	-4069(3)	-2698(2)	35(1)
C(301)	-5062(4)	-6426(3)	-1499(2)	31(1)
C(302)	-3957(4)	-6413(3)	-1739(2)	30(1)
C(303)	-3226(4)	-7101(3)	-1770(2)	34(1)

Table 2.5. (cont'd) Atomic coordinates ($\times 10^4$) and equivalent isotropic displacement parameters ($\text{Å}^2 \times 10^3$) for **6**.^a

atom	x	y	z	U(eq)
C(304)	-3616(5)	-7803(3)	-1540(2)	34(1)
C(305)	-4721(5)	-7853(3)	-1284(2)	32(1)
C(306)	-5430(4)	-7147(3)	-1277(2)	31(1)
C(307)	-2050(5)	-7104(4)	-2055(2)	43(1)
C(308)	-5105(5)	-8627(3)	-1039(2)	40(1)
C(401)	-7949(6)	-3221(4)	-1279(3)	51(2)
C(402)	-8665(8)	-2435(5)	-1221(4)	80(2)
C(501)	-8212(7)	-4593(4)	-2805(2)	59(2)
C(502)	-8561(18)	-5162(10)	-3219(5)	82(6)
C(50D)	-7716(24)	-5118(12)	-3215(7)	79(8)
C(503)	-8092(12)	-5997(6)	-3063(3)	118(4)
C(504)	-8053(9)	-5956(5)	-2556(3)	86(3)
C(505)	-4364(14)	-5115(10)	-274(5)	164(5)
C(506)	-3472(11)	-4809(8)	81(4)	122(4)
C(51D)	-4754(25)	-4781(18)	383(9)	131(9)
C(52D)	-5715(19)	-4244(13)	51(7)	94(7)
C(507)	-3121(18)	-4013(12)	-221(7)	104(6)
C(508)	-4324(15)	-3708(10)	-350(6)	83(5)
O(601)	-8524(23)	-4476(15)	637(8)	196(8)
C(601)	-8202(38)	-3404(25)	443(14)	193(15)
C(602)	-8887(62)	-3160(36)	729(22)	287(27)
C(603)	-9999(48)	-3508(33)	606(18)	244(20)
C(604)	-9592(27)	-4169(18)	665(9)	128(8)

^aNumbers in parentheses are estimated standard deviations of the last significant figure. ^bU(eq) is defined as one third of the trace of the orthogonalized U_{ij} tensor.

Table 2.6. Atomic coordinates ($\times 10^4$) and equivalent isotropic displacement parameters ($\text{Å}^2 \times 10^3$) for **8**.^a

atom	x	y	z	U(eq)
Cu(1)	544(1)	2352(1)	7104(1)	32(1)
Cu(2)	-647(1)	2940(1)	6507(1)	34(1)
F(701)	2595(3)	4023(3)	4382(3)	79(2)
F(702)	1733(3)	4795(2)	4440(3)	72(2)
F(703)	2636(3)	4934(2)	3789(3)	68(1)
F(704)	1605(3)	4260(2)	3386(3)	71(1)
O(101)	-1155(3)	2468(2)	7086(3)	38(1)
O(102)	-95(3)	1870(2)	7554(3)	36(1)
O(103)	-2300(3)	1710(2)	5735(3)	42(1)
O(104)	-333(3)	355(2)	6799(3)	36(1)
O(201)	-114(3)	3226(2)	5827(3)	36(1)
O(202)	1010(3)	2748(2)	6433(3)	36(1)
O(203)	1337(3)	1530(2)	5505(3)	38(1)
O(204)	-842(3)	2519(2)	4095(3)	39(1)
O(401)	1194(3)	2998(3)	8036(3)	59(2)
O(402)	1470(3)	1712(2)	7431(3)	47(1)
O(501)	-521(3)	3769(2)	7274(3)	52(1)
O(502)	-1696(3)	3289(2)	5856(3)	50(1)
N(101)	-1352(3)	1001(2)	6246(3)	29(1)
N(201)	247(3)	2030(2)	4795(3)	26(1)
C(101)	-817(4)	2014(3)	7473(4)	30(2)
C(102)	-2051(4)	1344(3)	6231(4)	31(2)
C(103)	-949(4)	593(3)	6822(4)	29(2)
C(104)	-1182(4)	2008(3)	8639(4)	36(2)
C(105)	-1102(4)	-160(3)	7783(4)	33(2)
C(106)	-3374(4)	1267(3)	6486(4)	36(2)
C(107)	-1308(4)	1652(3)	7892(4)	29(2)
C(108)	-1030(4)	971(3)	8059(4)	28(2)
C(109)	-1343(4)	486(3)	7438(3)	26(2)
C(110)	-2248(4)	549(3)	7125(4)	30(2)
C(111)	-2464(4)	1204(3)	6832(4)	32(2)
C(112)	-2205(4)	1666(3)	7477(4)	33(2)
C(113)	-343(4)	2026(4)	9147(4)	46(2)
C(114)	-275(5)	2358(5)	9860(5)	74(3)
C(115)	-3745(4)	842(4)	5840(4)	50(2)
C(116)	-4653(5)	908(4)	5562(5)	68(3)
C(117)	-1478(4)	-716(3)	7331(4)	37(2)
C(118)	-1145(5)	-1328(3)	7692(4)	48(2)
C(201)	606(4)	3096(3)	5914(4)	29(2)
C(202)	-126(4)	2504(3)	4309(4)	30(2)
C(203)	1079(4)	1963(3)	5092(4)	31(2)
C(204)	1385(4)	4020(3)	5810(4)	39(2)
C(205)	2430(4)	2117(3)	4901(4)	38(2)
C(206)	-17(4)	3242(3)	3314(4)	39(2)
C(207)	1064(4)	3394(3)	5418(4)	30(2)
C(208)	1789(4)	3003(3)	5390(4)	33(2)

Table 2.6. (cont'd) Atomic coordinates ($\times 10^4$) and equivalent isotropic displacement parameters ($\text{\AA}^2 \times 10^3$) for **8**.^a

atom	x	y	z	U(eq)
C(209)	1621(4)	2440(3)	4862(4)	32(2)
C(210)	1204(4)	2684(3)	4091(4)	32(2)
C(211)	405(4)	2985(3)	4085(4)	31(2)
C(212)	547(4)	3529(3)	4642(4)	35(2)
C(213)	769(5)	4506(4)	5844(5)	63(3)
C(214)	1155(6)	5085(4)	6258(6)	75(3)
C(215)	-192(6)	2777(4)	2678(4)	63(3)
C(216)	-580(6)	3051(5)	1930(4)	71(3)
C(217)	2400(4)	1586(3)	4357(4)	45(2)
C(218)	3145(5)	1197(4)	4566(5)	61(2)
C(301)	-559(4)	1513(3)	5513(3)	26(2)
C(302)	-251(4)	1518(3)	4908(4)	28(2)
C(303)	-421(4)	1042(3)	4384(3)	28(2)
C(304)	-895(4)	560(3)	4502(4)	35(2)
C(305)	-1223(4)	537(3)	5100(4)	32(2)
C(306)	-1036(4)	1022(3)	5607(4)	29(2)
C(307)	-111(5)	1053(4)	3721(4)	45(2)
C(308)	-1762(5)	6(3)	5172(4)	44(2)
C(401)	1622(7)	2809(5)	8760(5)	79(3)
C(402)	2383(8)	3206(6)	8935(7)	108(4)
C(403)	2163(10)	3748(8)	8504(9)	151(6)
C(404)	1548(7)	3561(5)	7859(6)	97(4)
C(405)	1311(6)	1067(4)	7425(8)	95(4)
C(406)	1942(7)	735(5)	7274(9)	122(5)
C(407)	2567(7)	1157(5)	7292(10)	147(7)
C(408)	2263(5)	1791(4)	7331(6)	63(3)
C(501)	-572(7)	3715(4)	8012(5)	74(3)
C(502)	-369(9)	4357(5)	8349(6)	113(5)
C(503)	-448(9)	4772(5)	7718(6)	119(5)
C(504)	-732(8)	4403(4)	7053(5)	85(3)
C(505)	-2433(5)	3312(5)	6070(5)	63(3)
C(506)	-3047(7)	3473(6)	5409(6)	96(4)
C(507)	-2661(5)	3737(5)	4869(5)	68(3)
C(508)	-1825(6)	3515(5)	5119(5)	76(3)
C(801)	749(14)	2(12)	9475(14)	159(8)
C(802)	1155(14)	-90(12)	8895(14)	154(8)
C(803)	1305(15)	-537(13)	8458(14)	166(9)
C(804)	1092(14)	-1078(12)	8827(14)	156(8)
O(801)	686(11)	-766(10)	9347(11)	210(7)
B(701)	2139(6)	4503(5)	3988(6)	52(3)

^aNumbers in parentheses are estimated standard deviations of the last significant figure. ^bU(eq) is defined as one third of the trace of the orthogonalized U_{ij} tensor.

Table 2.7. Atomic coordinates ($\times 10^4$) and equivalent isotropic displacement parameters ($\text{\AA}^2 \times 10^3$) for **9**.^a

atom	x	y	z	U(eq)
Cu(1)	4086(1)	6891(1)	1620(1)	38(1)
Zn(1)	3146(1)	7655(1)	1235(1)	35(1)
S(501)	3054(1)	8413(1)	2373(1)	49(1)
F(501)	4008(2)	8431(3)	2829(2)	96(1)
F(502)	3460(2)	7705(2)	3166(2)	114(2)
F(503)	3389(2)	8858(2)	3280(1)	103(2)
O(101)	2888(1)	6677(2)	1355(1)	39(1)
O(102)	3599(1)	6121(2)	1728(1)	37(1)
O(103)	2846(1)	5875(2)	223(1)	34(1)
O(104)	4135(1)	4657(1)	1133(1)	32(1)
O(201)	3698(1)	8306(2)	1001(1)	37(1)
O(202)	4407(1)	7748(2)	1365(1)	39(1)
O(203)	5279(1)	6904(1)	699(1)	32(1)
O(204)	3870(1)	7785(2)	-245(1)	39(1)
O(401)	4866(1)	6390(2)	1862(1)	49(1)
O(501)	3276(2)	7866(2)	2043(1)	54(1)
O(502)	2546(2)	8233(3)	2563(2)	101(2)
O(503)	3119(2)	9145(2)	2201(2)	85(1)
O(504)	2458(1)	8237(2)	1231(1)	50(1)
O(505)	3000(1)	7420(2)	415(1)	50(1)
N(101)	3487(1)	5227(2)	655(1)	25(1)
N(201)	4603(1)	7337(2)	190(1)	26(1)
C(101)	3115(2)	6144(2)	1580(2)	31(1)
C(102)	2953(2)	5393(2)	531(2)	29(1)
C(103)	3667(2)	4739(2)	1052(2)	29(1)
C(104)	2437(2)	5733(2)	2180(2)	42(1)
C(105)	3471(2)	3607(2)	1550(2)	36(1)
C(106)	2054(2)	4848(2)	393(2)	37(1)
C(107)	2748(2)	5495(2)	1702(2)	34(1)
C(108)	3066(2)	4786(2)	1814(2)	35(1)
C(109)	3234(2)	4334(2)	1343(2)	29(1)
C(110)	2755(2)	4211(2)	972(2)	31(1)
C(111)	2519(2)	4946(2)	789(2)	31(1)
C(112)	2324(2)	5374(2)	1260(2)	36(1)
C(113)	2767(2)	5930(3)	2656(2)	58(1)
C(114)	2425(3)	6133(4)	3107(2)	84(2)
C(115)	2182(2)	4417(2)	-87(2)	42(1)
C(116)	1735(2)	4447(3)	-505(2)	51(1)
C(117)	3588(2)	3025(2)	1139(2)	38(1)
C(118)	3899(2)	2387(2)	1369(2)	53(1)
C(201)	4184(2)	8255(2)	1109(2)	34(1)
C(202)	4313(2)	7899(2)	-54(2)	30(1)
C(203)	5082(2)	7427(2)	488(2)	26(1)
C(204)	4437(2)	9539(2)	1279(2)	48(1)
C(205)	5944(2)	8086(2)	581(2)	35(1)
C(206)	4398(2)	9028(2)	-585(2)	42(1)

Table 2.7. (cont'd) Atomic coordinates ($\times 10^4$) and equivalent isotropic displacement parameters ($\text{Å}^2 \times 10^3$) for **9**.^a

atom	x	y	z	U(eq)
C(207)	4544(2)	8877(2)	919(2)	36(1)
C(208)	5139(2)	8664(2)	943(2)	35(1)
C(209)	5339(2)	8186(2)	495(2)	28(1)
C(210)	5187(2)	8569(2)	-18(2)	32(1)
C(211)	4579(2)	8652(2)	-74(2)	32(1)
C(212)	4373(2)	9120(2)	372(2)	39(1)
C(213)	4538(3)	9422(3)	1826(2)	61(2)
C(214)	4345(3)	10109(3)	2135(2)	79(2)
C(215)	4547(2)	8652(3)	-1082(2)	52(1)
C(216)	4277(3)	9022(3)	-1551(2)	69(2)
C(217)	6243(2)	7672(2)	174(2)	35(1)
C(218)	6793(2)	7412(3)	375(2)	52(1)
C(301)	4058(1)	6269(2)	427(1)	22(1)
C(302)	4419(2)	6589(2)	107(2)	25(1)
C(303)	4622(2)	6207(2)	-304(1)	25(1)
C(304)	4456(2)	5485(2)	-378(2)	29(1)
C(305)	4089(2)	5152(2)	-65(2)	26(1)
C(306)	3891(2)	5559(2)	338(1)	24(1)
C(307)	4995(2)	6549(2)	-675(2)	37(1)
C(308)	3902(2)	4379(2)	-177(2)	38(1)
C(401)	5362(2)	6796(3)	1921(2)	52(1)
C(402)	5801(3)	6270(4)	1839(3)	85(2)
C(403)	5556(3)	5536(4)	1870(3)	86(2)
C(404)	4987(3)	5673(3)	1689(2)	66(2)
C(501)	3503(3)	8356(3)	2931(2)	66(2)
C(502)	1938(2)	7930(4)	1320(3)	86(2)
C(503)	1563(3)	8552(6)	1259(6)	202(7)
C(504)	1860(3)	9200(4)	1213(4)	111(3)
C(505)	2415(2)	8999(3)	1083(2)	61(2)
C(601)	5176(5)	3614(7)	2277(4)	163(4)
C(602)	5334(6)	2880(7)	2165(5)	168(5)
O(601)	5000	2409(10)	2500	264(8)

^aNumbers in parentheses are estimated standard deviations of the last significant figure. ^bU(eq) is defined as one third of the trace of the orthogonalized U_{ij} tensor.

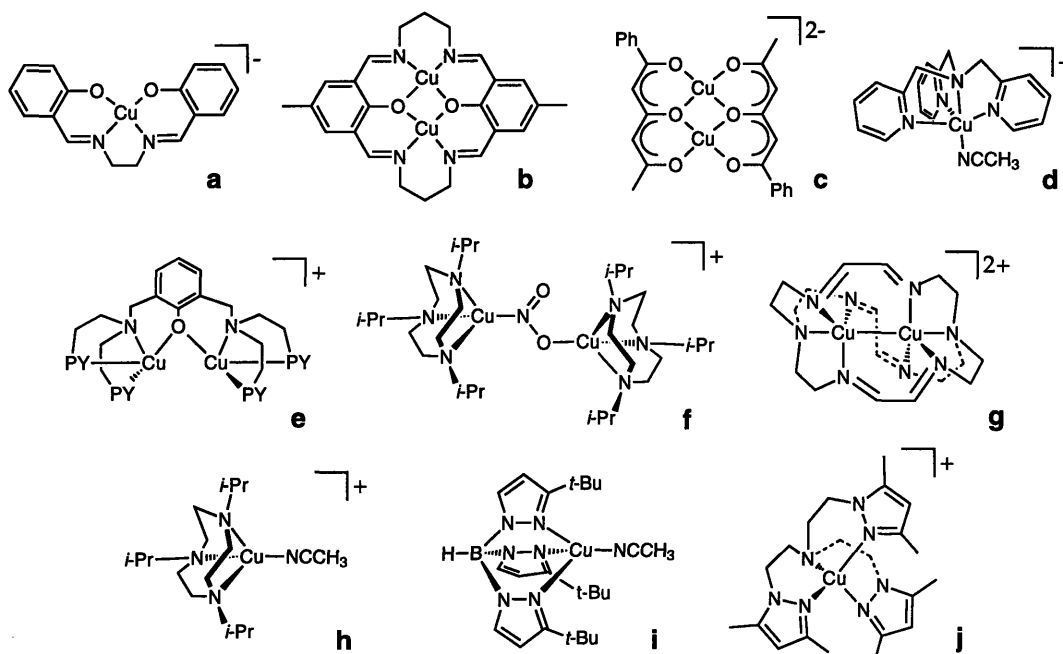
Table 2.8. Atomic coordinates ($\times 10^4$) and equivalent isotropic displacement parameters ($\text{Å}^2 \times 10^3$) for **11**.^a

atom	x	y	z	U(eq)
CU1	930(2)	4667(1)	8648(1)	38(1)
CU1'	1310(2)	4532(1)	8484(1)	42(1)
ZN1	919(1)	4644(1)	6303(1)	29(1)
C(401)	1642(12)	4745(5)	10030(9)	53(3)
C(402)	1166(15)	4208(13)	9850(12)	89(7)
C(403)	2681(11)	4570(7)	10350(12)	64(4)
C(406)	1795(40)	3664(17)	9962(31)	201(25)
C(407)	2593(13)	4047(8)	9801(11)	68(4)
C(41)	2421(8)	4453(6)	9695(8)	54(3)
C(42)	1974(10)	3974(5)	9452(8)	55(3)
C(43)	2223(13)	4696(6)	10484(9)	65(3)
C(44)	1586(21)	3849(7)	10083(15)	73(6)
C(45)	1206(11)	4476(7)	10226(12)	68(4)
C(404)	2829(5)	4328(3)	11318(4)	85(2)
C(405)	2288(6)	3771(3)	11093(5)	93(2)
S(501)	2606(1)	3784(1)	7091(1)	64(1)
F(501)	3120(4)	4298(3)	5959(5)	184(3)
F(502)	4070(4)	4368(3)	7354(6)	175(3)
F(503)	3994(3)	3628(2)	6611(4)	126(2)
O(101)	1206(2)	5388(1)	6708(2)	37(1)
O(102)	1307(2)	5322(1)	8136(2)	40(1)
O(103)	-429(2)	6346(1)	5693(2)	37(1)
O(104)	-66(2)	6162(1)	8630(2)	42(1)
O(201)	-103(2)	4168(1)	6202(2)	36(1)
O(202)	57(2)	4210(1)	7648(2)	40(1)
O(203)	-1785(2)	4584(1)	8004(2)	43(1)
O(204)	-2275(2)	4606(1)	5012(2)	33(1)
O(501)	2108(3)	4272(2)	7160(3)	60(1)
O(502)	3103(4)	3521(2)	7932(4)	113(2)
O(503)	2042(4)	3429(2)	6356(4)	103(2)
O(504)	948(2)	4656(1)	5078(2)	40(1)
N(101)	-283(2)	6303(1)	7162(2)	28(1)
N(201)	-2119(2)	4596(1)	6490(2)	26(1)
C(101)	1444(3)	5563(2)	7518(3)	30(1)
C(102)	1(3)	6493(2)	6481(3)	29(1)
C(103)	215(3)	6379(2)	8111(3)	30(1)
C(104)	3042(3)	5929(2)	7939(3)	37(1)
C(105)	1181(3)	7034(2)	9304(3)	40(1)
C(106)	740(3)	7274(2)	5991(3)	38(1)
C(107)	2009(3)	6104(2)	7747(3)	29(1)
C(108)	1966(3)	6393(2)	8590(3)	32(1)
C(109)	1083(3)	6749(2)	8410(3)	31(1)
C(110)	971(3)	7164(2)	7657(3)	32(1)
C(111)	855(3)	6868(2)	6772(3)	31(1)
C(112)	1713(3)	6497(2)	6926(3)	31(1)
C(113)	3505(3)	5508(2)	8663(4)	49(1)

Table 2.8. (cont'd) Atomic coordinates ($\times 10^4$) and equivalent isotropic displacement parameters ($\text{Å}^2 \times 10^3$) for **11**.^a

atom	x	y	z	U(eq)
C(114)	4522(4)	5422(2)	8800(4)	67(2)
C(115)	-82(4)	7669(2)	5713(4)	52(1)
C(116)	-73(4)	8087(2)	5014(4)	61(2)
C(117)	343(4)	7394(2)	9232(3)	50(1)
C(118)	362(5)	7558(3)	10149(4)	85(2)
C(201)	-252(3)	3997(2)	6883(3)	29(1)
C(202)	-2302(3)	4342(2)	5652(3)	27(1)
C(203)	-2002(3)	4323(2)	7309(3)	30(1)
C(204)	-103(3)	2997(2)	6839(3)	39(1)
C(205)	-2538(3)	3554(2)	8001(3)	40(1)
C(206)	-3225(3)	3588(2)	4600(3)	34(1)
C(207)	-835(3)	3464(2)	6730(3)	30(1)
C(208)	-1261(3)	3392(2)	7445(3)	33(1)
C(209)	-2184(3)	3703(2)	7251(3)	31(1)
C(210)	-2897(3)	3564(2)	6296(3)	31(1)
C(211)	-2520(3)	3725(2)	5583(3)	28(1)
C(212)	-1599(3)	3415(2)	5763(3)	31(1)
C(213)	715(4)	2966(2)	7749(4)	52(1)
C(214)	1403(4)	2511(2)	7755(5)	65(2)
C(215)	-4164(3)	3880(2)	4263(3)	44(1)
C(216)	-4837(3)	3681(2)	3322(3)	52(1)
C(217)	-3478(3)	3807(2)	7893(3)	49(1)
C(218)	-3608(4)	3784(3)	8782(4)	69(2)
C(301)	-1207(3)	5452(1)	6841(3)	27(1)
C(302)	-2066(3)	5191(2)	6519(3)	27(1)
C(303)	-2897(3)	5484(2)	6231(3)	37(1)
C(304)	-2839(3)	6054(2)	6276(4)	45(1)
C(305)	-1989(3)	6333(2)	6586(3)	40(1)
C(306)	-1172(3)	6022(2)	6861(3)	29(1)
C(307)	-3840(3)	5198(2)	5875(4)	55(1)
C(308)	-1951(4)	6956(2)	6630(5)	67(2)
C(501)	3485(6)	4028(3)	6733(7)	93(2)

^aNumbers in parentheses are estimated standard deviations of the last significant figure. ^bU(eq) is defined as one third of the trace of the orthogonalized U_{ij} tensor.

Table 2.9. Selected electrochemical data for a range of copper redox couples.

Entry	Redox Couple	Solvent/Electrolyte	Lit. Ref. Elec.	Lit.	Scaled	ref.
				$E_{1/2}^a$	$E_{1/2}^b$	
a	$\text{Cu}^{\text{II}}/\text{Cu}^{\text{I}}$	$\text{Pr}_4\text{NClO}_4/0.1 \text{ M, DMF}$	SCE	-1210	-1770 ^c	54
b	$(\text{Cu}^{\text{II}}\text{Cu}^{\text{I}})/(\text{Cu}^{\text{I}}\text{Cu}^{\text{I}})$	$\text{Bu}_4\text{NClO}_4/0.1 \text{ M, DMF}$	NHE	-517	-1318 ^d	17
c	$(\text{Cu}^{\text{II}}\text{Cu}^{\text{I}})/(\text{Cu}^{\text{I}}\text{Cu}^{\text{I}})$	$\text{Et}_4\text{NClO}_4/0.1 \text{ M, DMF}$	SCE	-470	-1030 ^c	60
d	$\text{Cu}^{\text{II}}/\text{Cu}^{\text{I}}$	$\text{Bu}_4\text{NPF}_6/0.2 \text{ M, DMF}$	$\text{Cp}_2\text{Fe}^+/Cp_2\text{Fe, DMF}$	-628	-518 ^e	56
e	$(\text{Cu}^{\text{II}}\text{Cu}^{\text{I}})/(\text{Cu}^{\text{I}}\text{Cu}^{\text{I}})$	$\text{Bu}_4\text{NPF}_6/0.2 \text{ M, DMF}$	Ag/AgNO_3	-587	-497 ^f	59
f	$(\text{Cu}^{\text{II}}\text{Cu}^{\text{I}})/(\text{Cu}^{\text{I}}\text{Cu}^{\text{I}})$	$\text{Bu}_4\text{NPF}_6/0.5 \text{ M, CH}_2\text{Cl}_2$	SCE	+70	-490 ^c	52b
7	$(\text{Cu}^{\text{II}}\text{Cu}^{\text{I}})/(\text{Cu}^{\text{I}}\text{Cu}^{\text{I}})$	$\text{Bu}_4\text{NPF}_6/0.5 \text{ M, THF}$	$\text{Cp}_2\text{Fe}^+/Cp_2\text{Fe, THF}$	-218	-218	This Work
g	$(\text{Cu}^{\text{II}}\text{Cu}^{\text{I}})/(\text{Cu}^{\text{I}}\text{Cu}^{\text{I}})$	Not Given/DMF	Ag/AgCl	+310	-206 ^g	24
h	$\text{Cu}^{\text{II}}/\text{Cu}^{\text{I}}$	$\text{Bu}_4\text{NPF}_6/0.5 \text{ M, MeCN}$	SCE	+360	-200 ^c	57
i	$\text{Cu}^{\text{II}}/\text{Cu}^{\text{I}}$	$\text{Bu}_4\text{NOTf}/0.1 \text{ M, CH}_2\text{Cl}_2/\text{MeCN (9:1)}$	SCE	+910	+109 ^c	55
j	$\text{Cu}^{\text{II}}/\text{Cu}^{\text{I}}$	$\text{Bu}_4\text{NBF}_4/0.1 \text{ M, MeCN}$	SCE	+690	+130 ^c	58

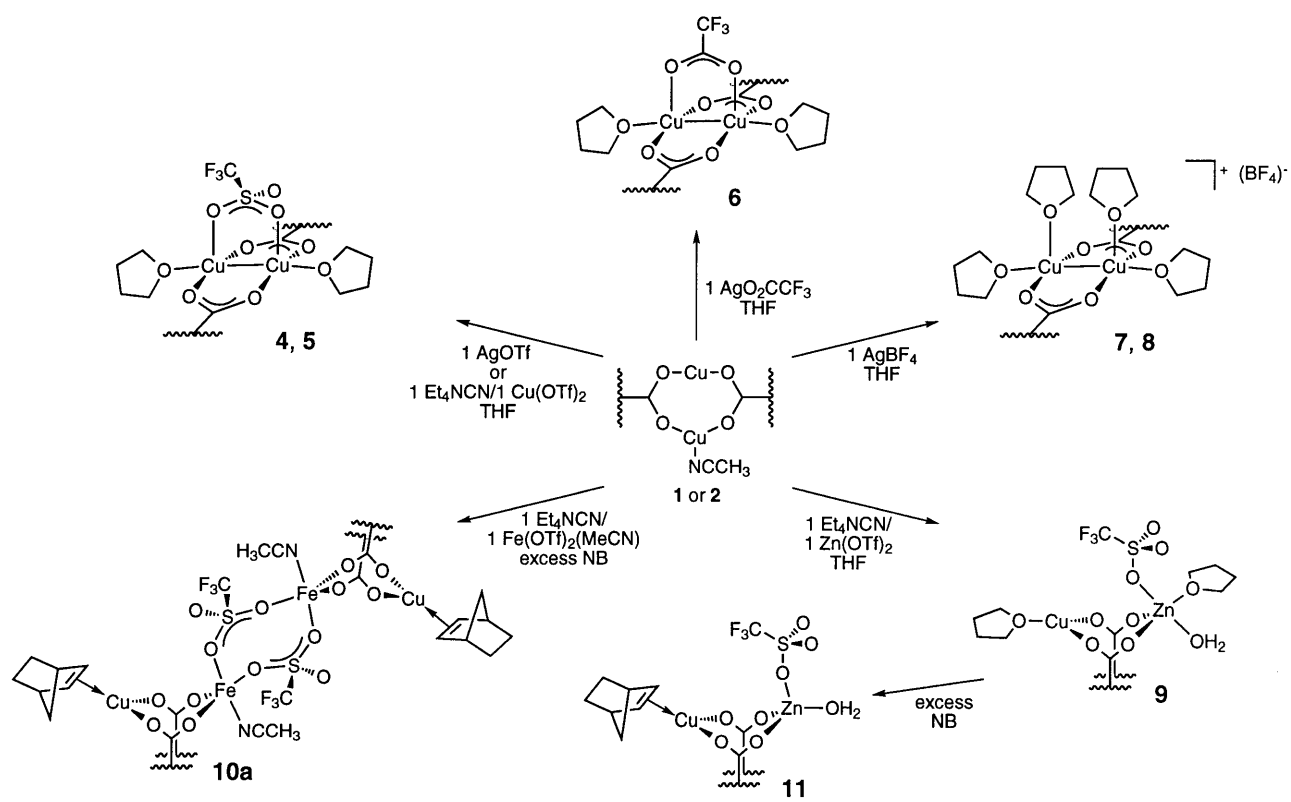
^a $E_{1/2}$ values are listed in mV. ^bAll literature potentials have been scaled to $\text{Cp}_2\text{Fe}^+/\text{Cp}_2\text{Fe}$ in THF.

^c $\text{Cp}_2\text{Fe}^+/\text{Cp}_2\text{Fe} = +560 \text{ mV vs. SCE in THF}$ (see ref. 62). ^dSCE = +241.2 mV vs. NHE (see ref. 61).

^e $\text{Cp}_2\text{Fe}^+/\text{Cp}_2\text{Fe}$ in DMF = -110 mV vs. $\text{Cp}_2\text{Fe}^+/\text{Cp}_2\text{Fe}$ in THF (see ref. 62). ^f $\text{Cp}_2\text{Fe}^+/\text{Cp}_2\text{Fe} = +20 \text{ mV vs. Ag}/\text{AgNO}_3$ (see ref. 56). ^g $\text{Ag}/\text{AgCl} = -44.2 \text{ mV vs. SCE}$ (see ref. 61).

Table 2.10. EPR g values and copper hyperfine coupling constants for **7**, derived from a simulation of the frozen solution X-band spectrum acquired at 77 K.

Compd.	g ₁	g ₂	g ₃	A ₁ ^{Cu} (Hz)	A ₂ ^{Cu} (Hz)	A ₃ ^{Cu} (Hz)
7	2.030	2.158	2.312	20.0	55.0	122.5



Scheme 2.1.

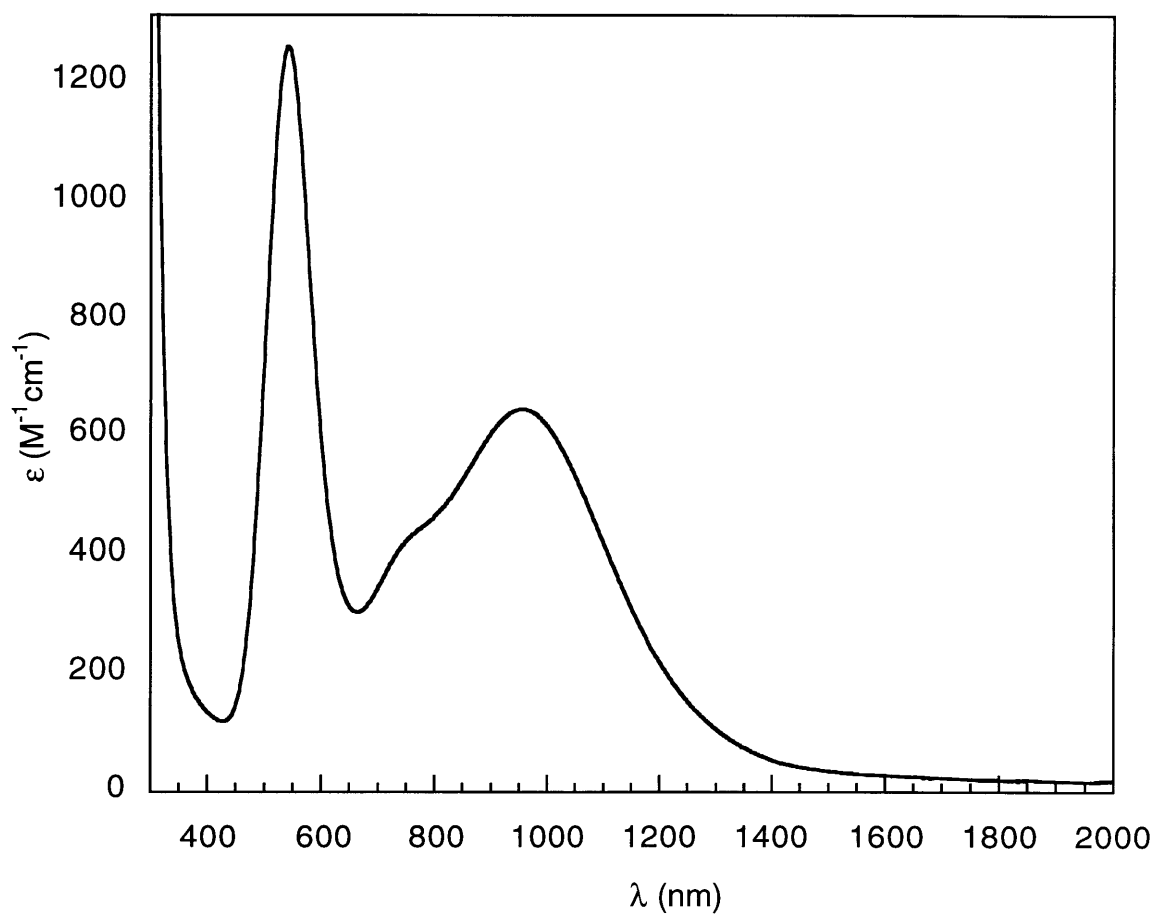


Figure 2.1. Electronic absorption spectrum of [Cu₂(XDK)(μ-OTf)(THF)₂] (**4**), 0.74 mM in THF.

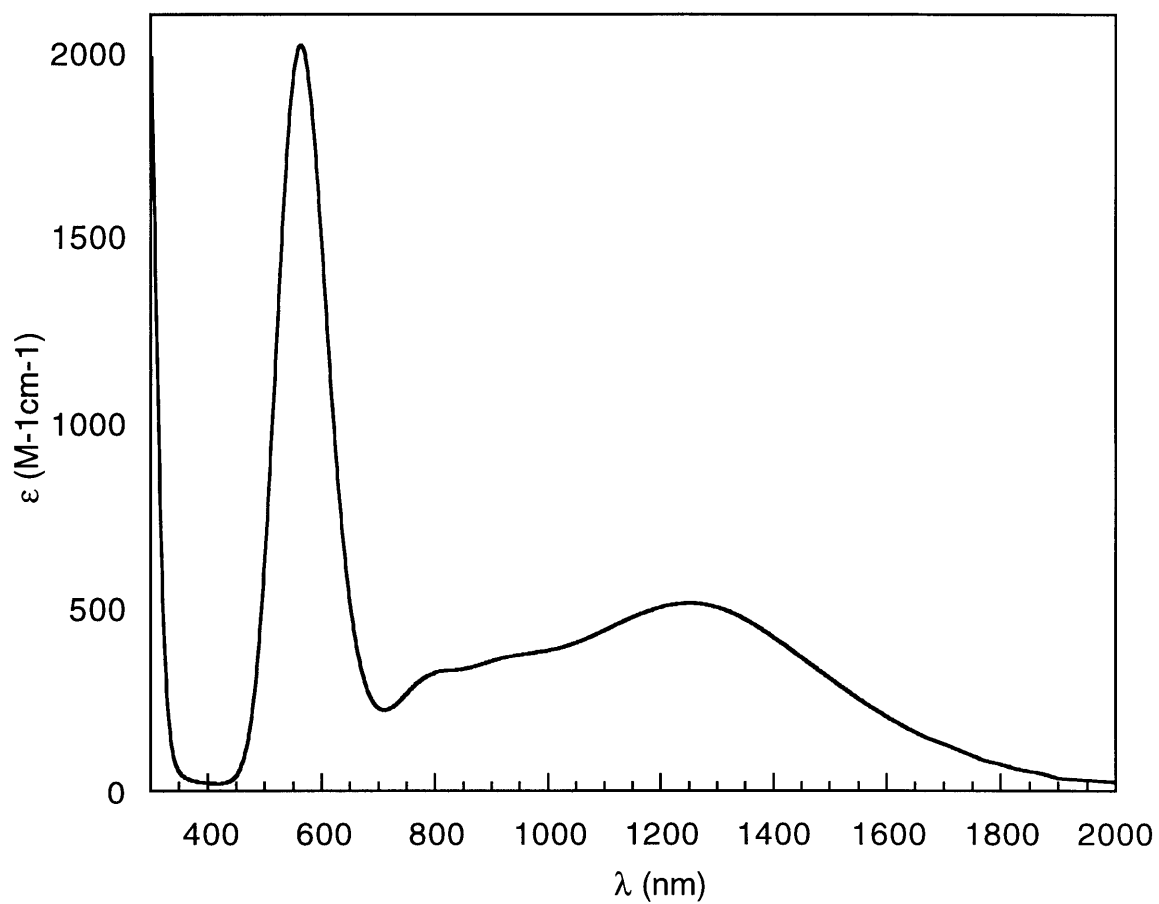


Figure 2.2. Electronic absorption spectrum of [Cu₂(XDK)(μ-O₂CCF₃)(THF)₂] (**6**), 0.74 mM in THF.

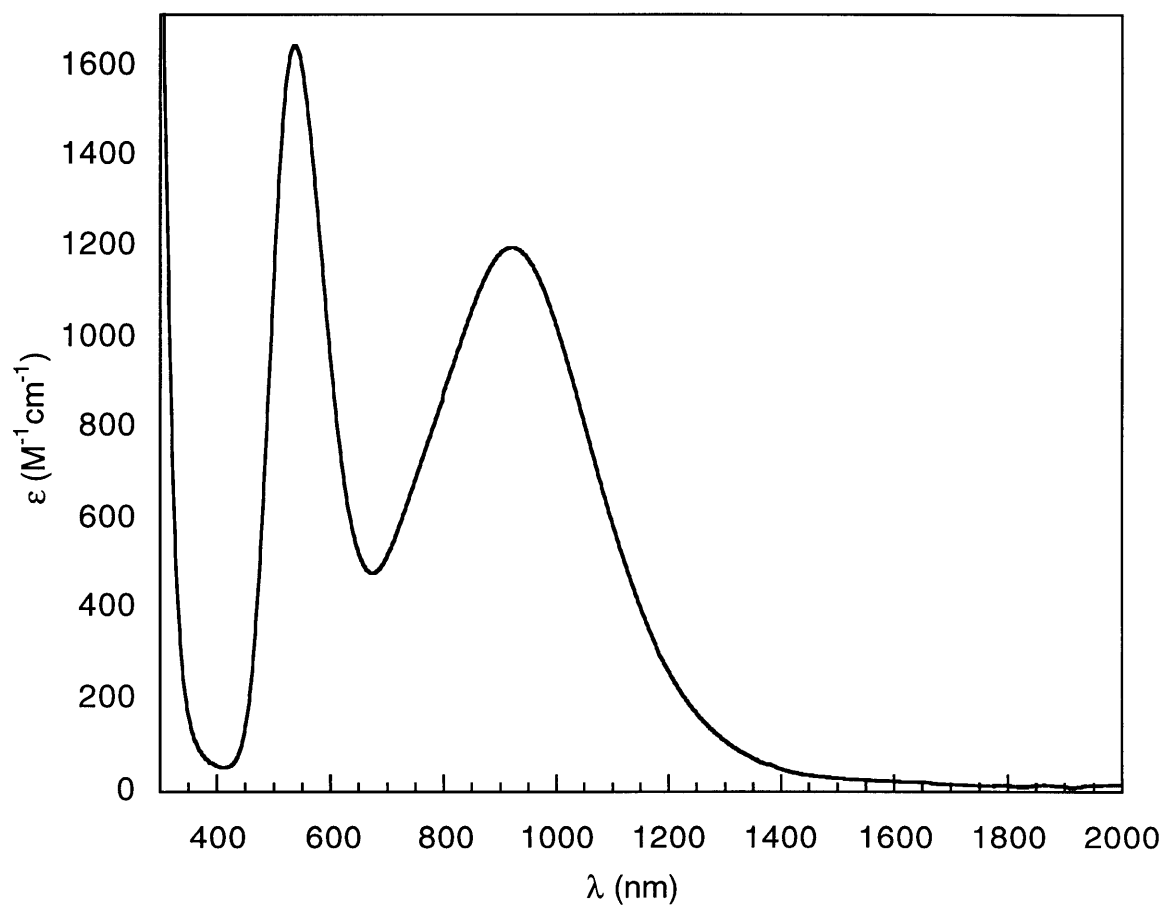


Figure 2.3. Electronic absorption spectrum of [Cu₂(XDK)(THF)₄](BF₄) (7), 0.47 mM in THF.

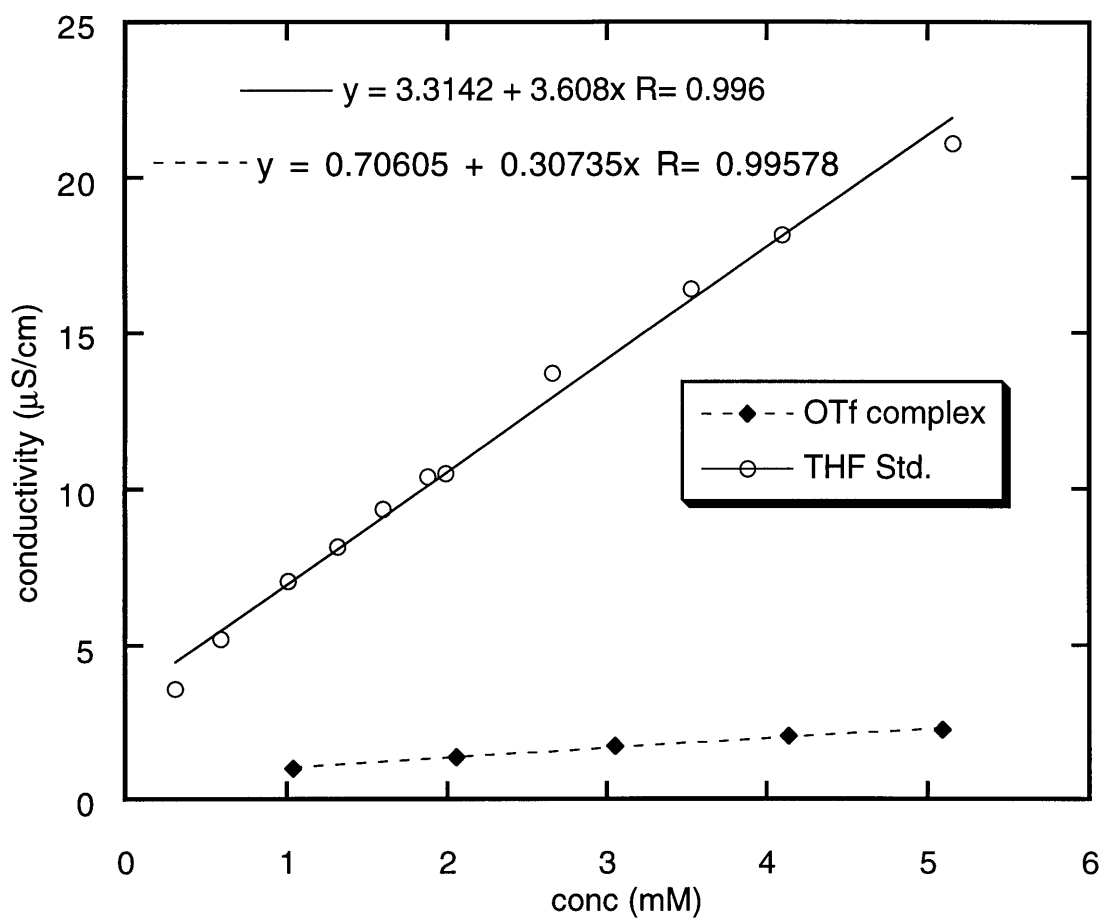


Figure 2.4. Conductivity plots for $[\text{Cu}_2(\text{XDK})(\mu\text{-OTf})(\text{THF})_2]$ (**4**) and Bu_4NPF_6 in THF at 296K.

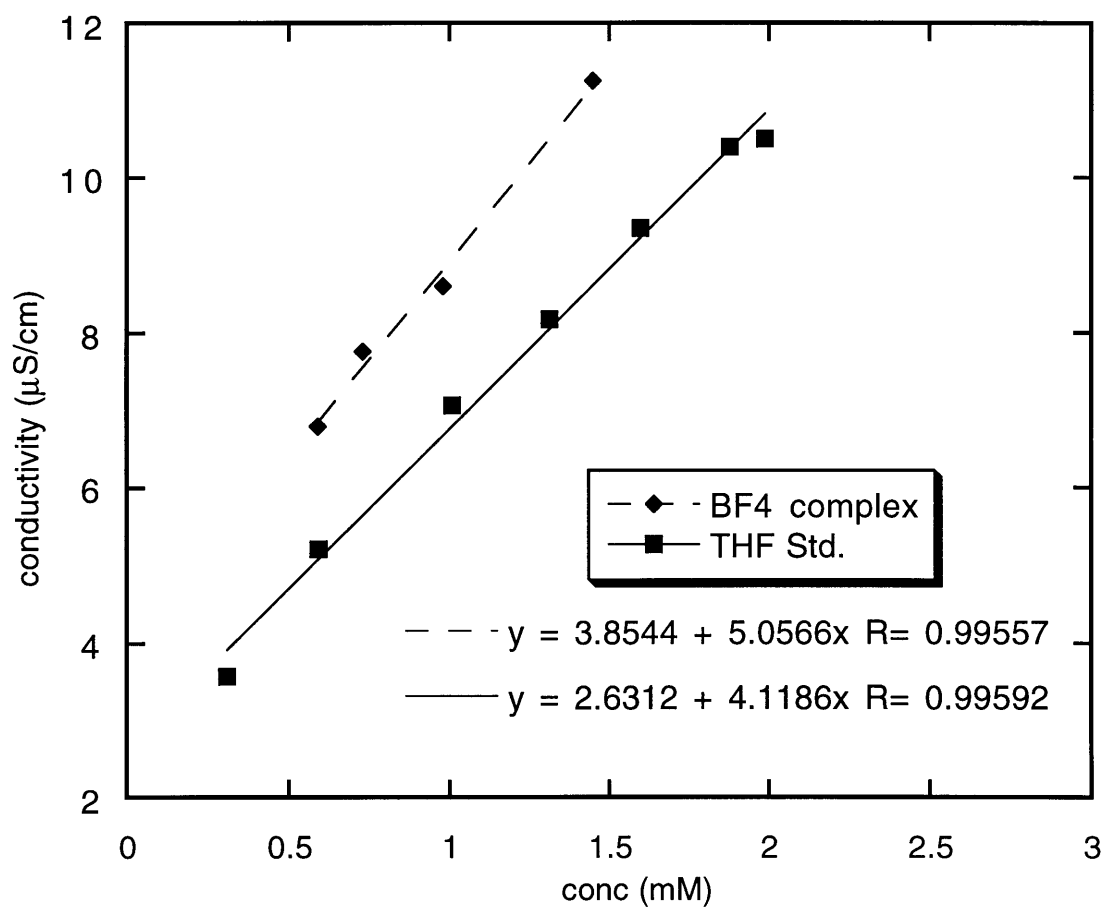


Figure 2.5. Conductivity plots for $[\text{Cu}_2(\text{XDK})(\text{THF})_4](\text{BF}_4)$ (7) in THF and Bu_4NPF_6 in THF at 296 K.

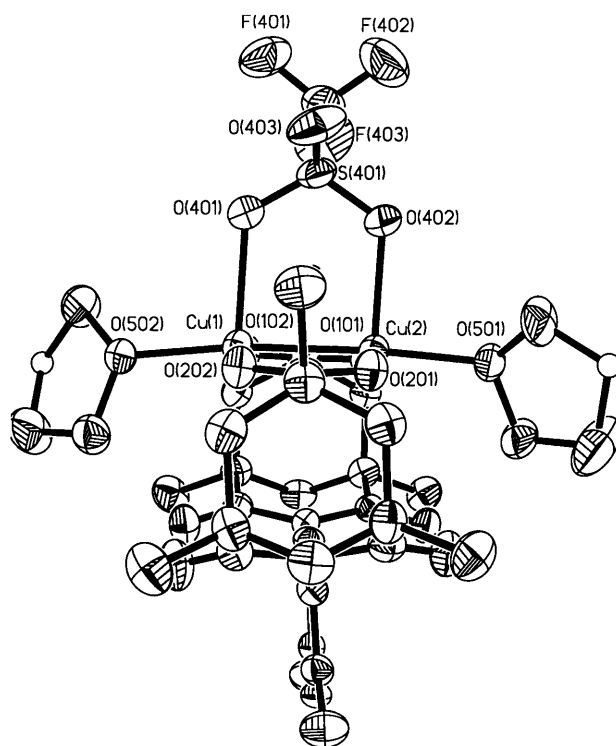


Figure 2.6. ORTEP diagram of [Cu₂(XDK)(μ-OTf)(THF)₂] (4) with 50% thermal ellipsoids. Atoms represented as open circles were refined isotropically.

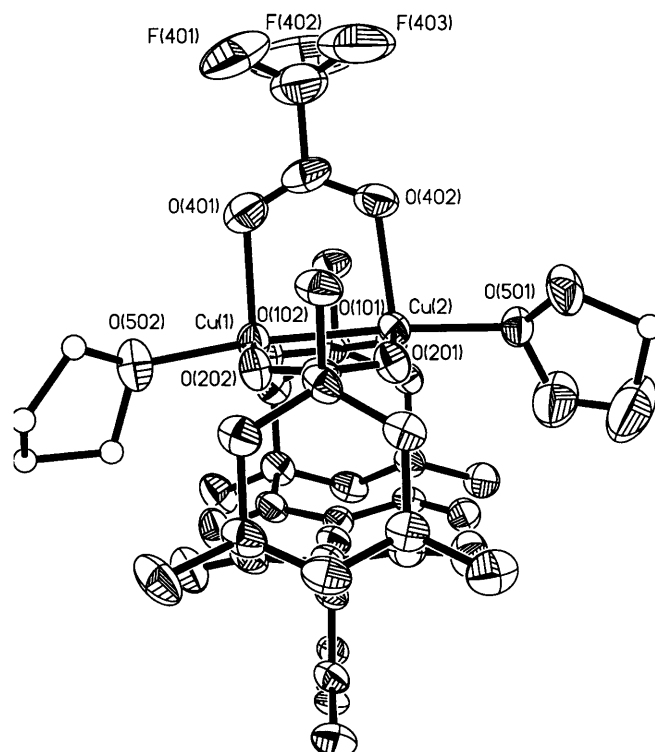


Figure 2.7. ORTEP diagram of $[\text{Cu}_2(\text{XDK})(\mu\text{-O}_2\text{CCF}_3)(\text{THF})_2]$ (**6**) with 50% thermal ellipsoids. Atoms represented as open circles were refined isotropically.

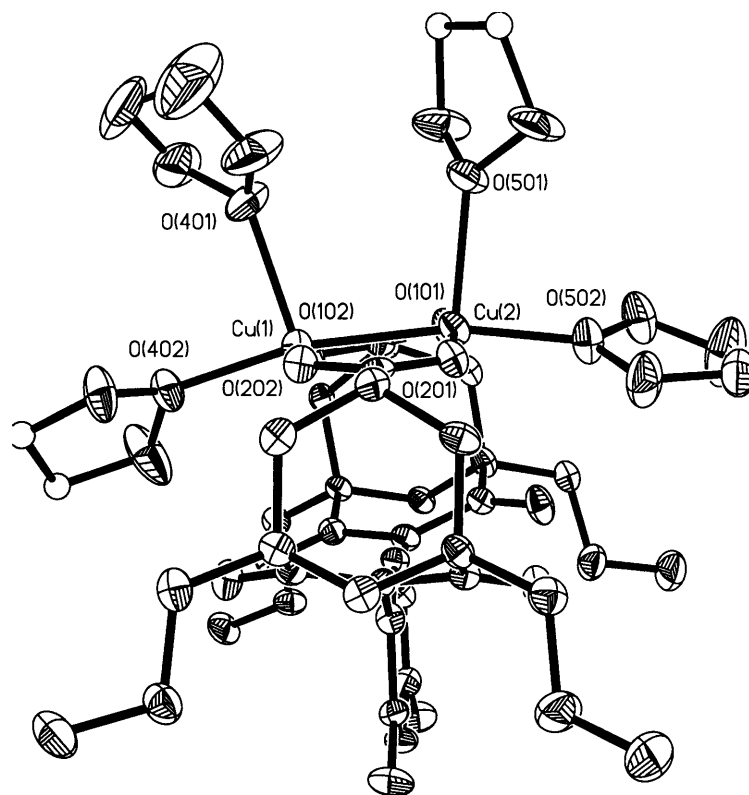


Figure 2.8. ORTEP diagram of [Cu₂(PXDK)(THF)₄](BF₄) (8) with 50% thermal ellipsoids. The PXDK propyl substituents adjacent to the copper coordination spheres have been omitted for clarity, and atoms represented as open circles were refined isotropically.

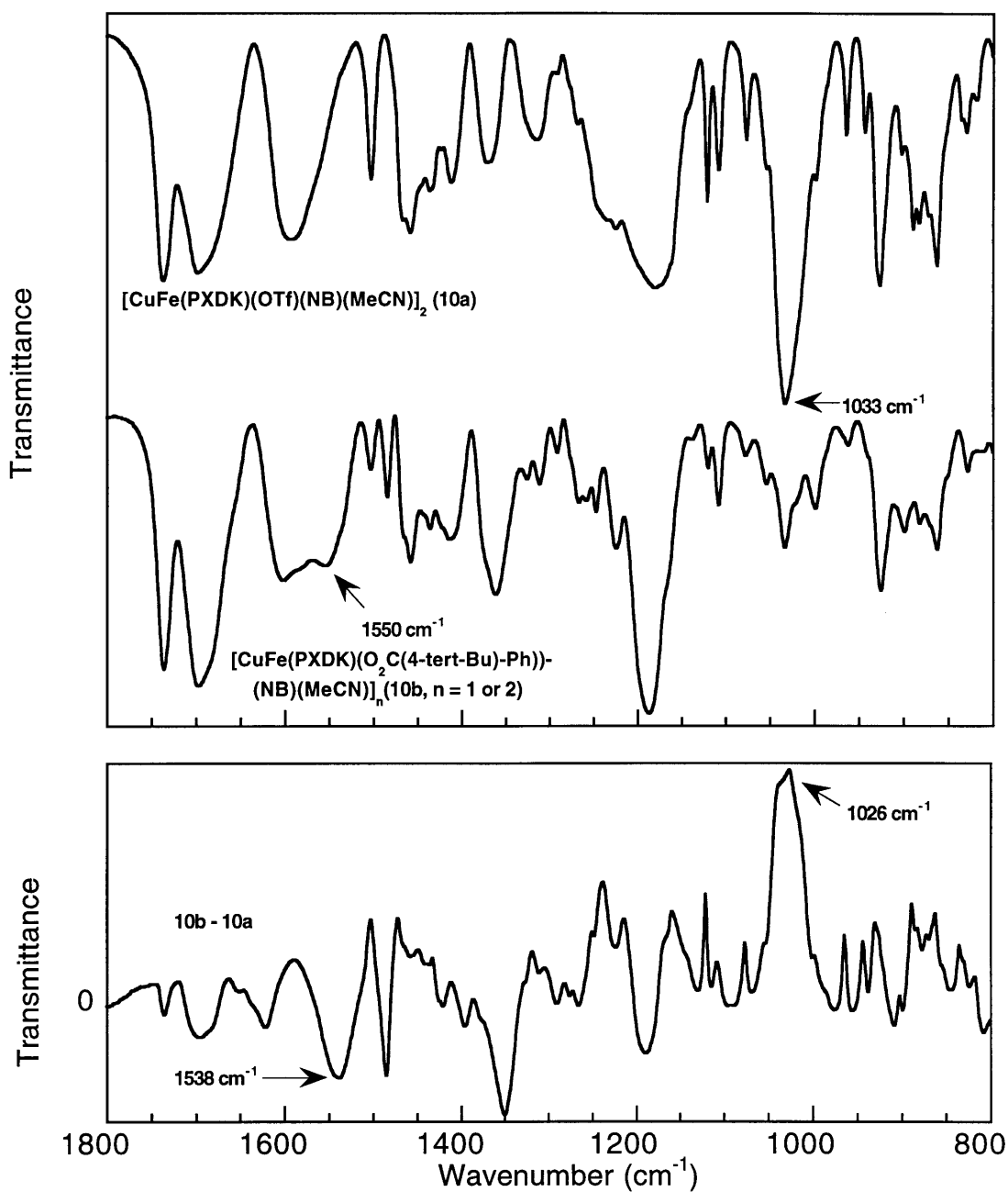


Figure 2.9. (Top) Stacked IR spectra of **10a** and **10b** in the carboxylate- ν_{CO} and the triflate- ν_{SO} regions; (Bottom) Difference IR spectrum of **10b-10a**.

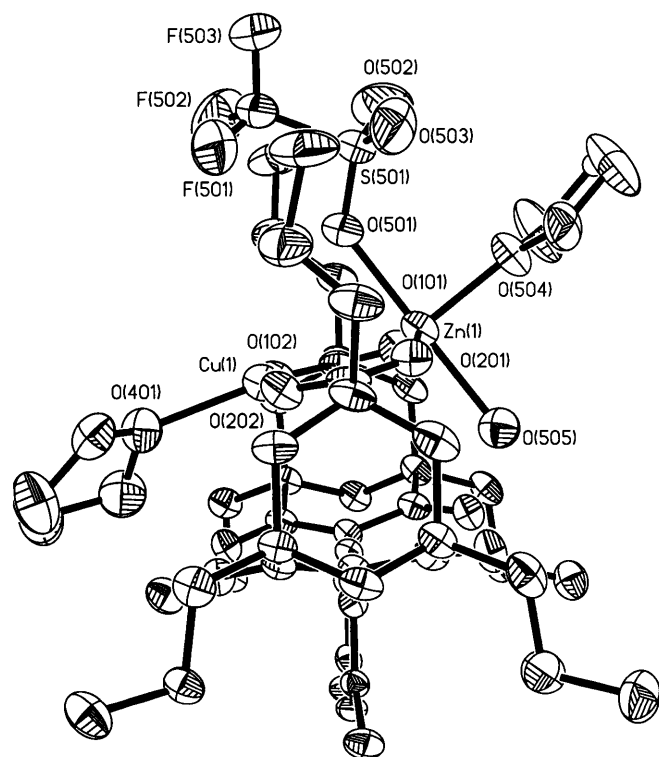


Figure 2.10. ORTEP diagram of $[\text{CuZn}(\text{PXDK})(\text{OTf})(\text{THF})_2(\text{H}_2\text{O})]$ (**9**) with 50% thermal ellipsoids. One of the carbon atoms of the THF ligated to Zn1 was refined isotropically; it is represented as an open circle.

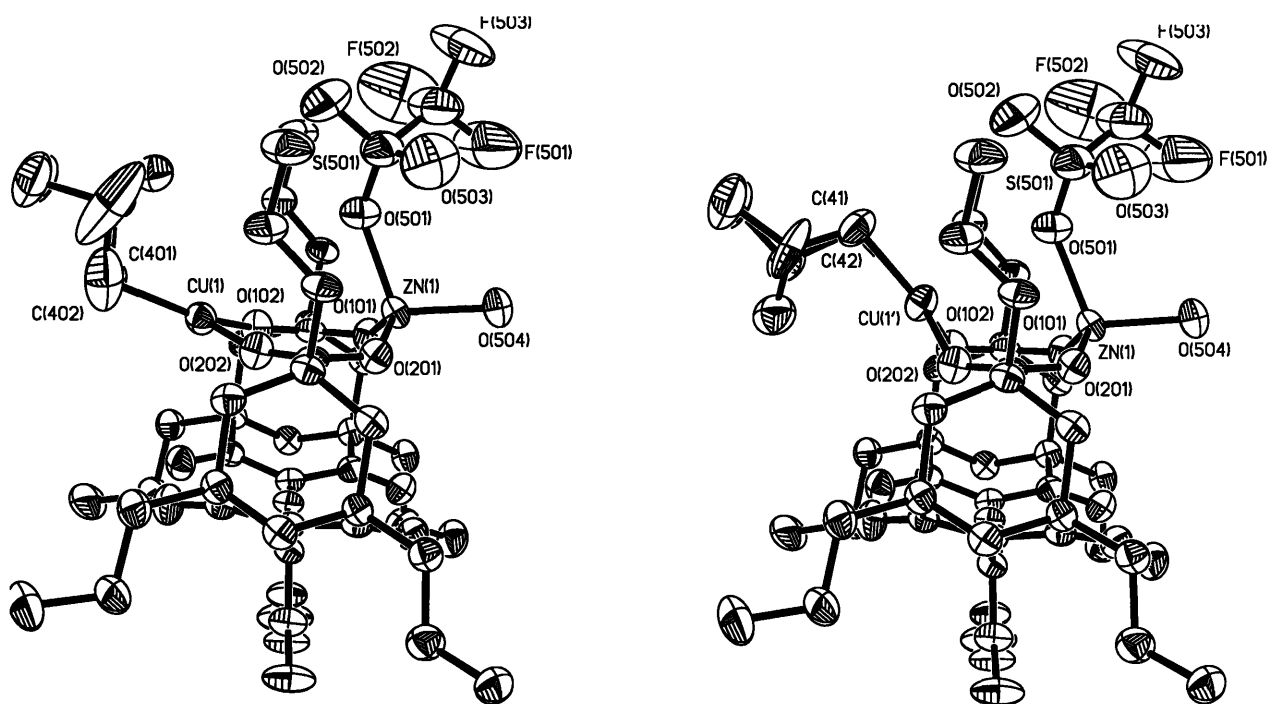


Figure 2.11. ORTEP diagrams of [CuZn(PXDK)(OTf)(NB)(H₂O)] (11) with 50% thermal ellipsoids, showing the two orientations of the copper-norbornene fragment (see the Experimental section for details).

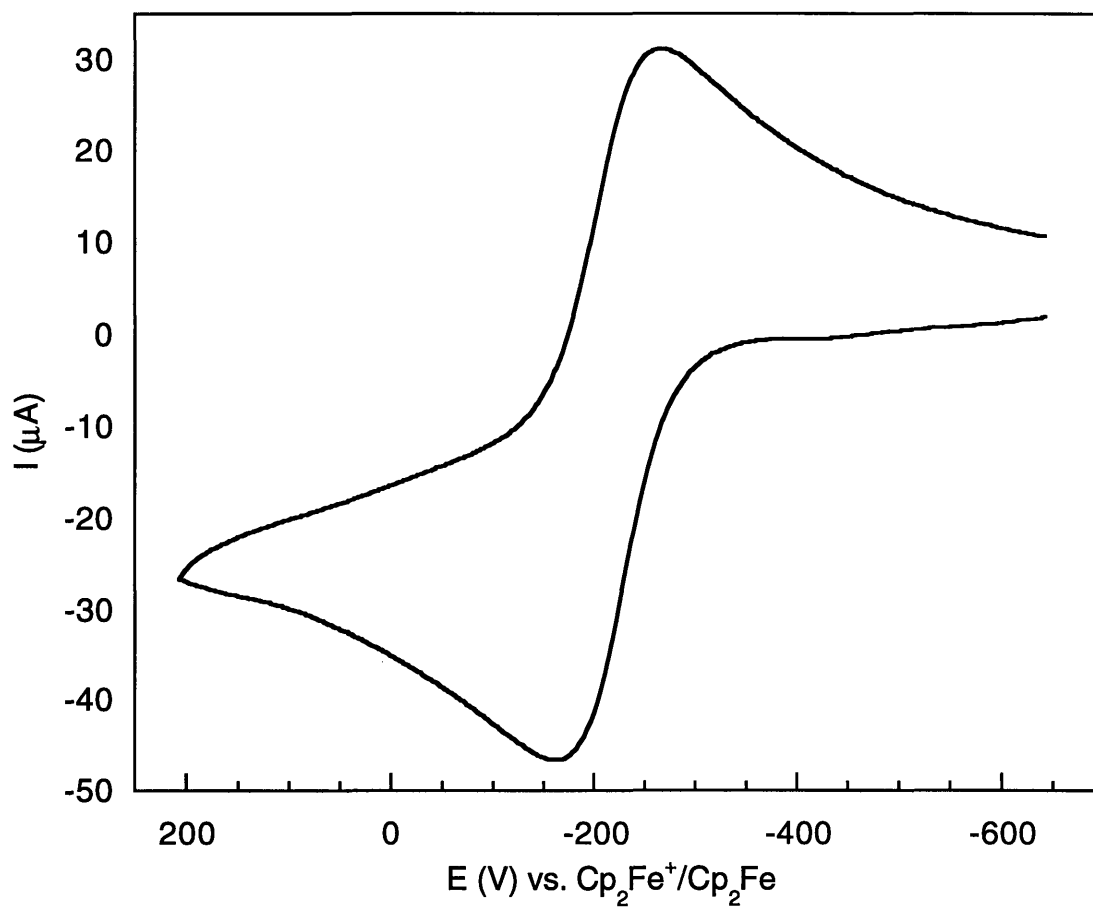


Figure 2.12. Cyclic voltammogram of 10 mM $[\text{Cu}_2(\text{XDK})]$ in THF with 0.5 M $(\text{Bu}_4\text{N})(\text{PF}_6)$ as supporting electrolyte and an anodic scan speed of 50 mV/sec.

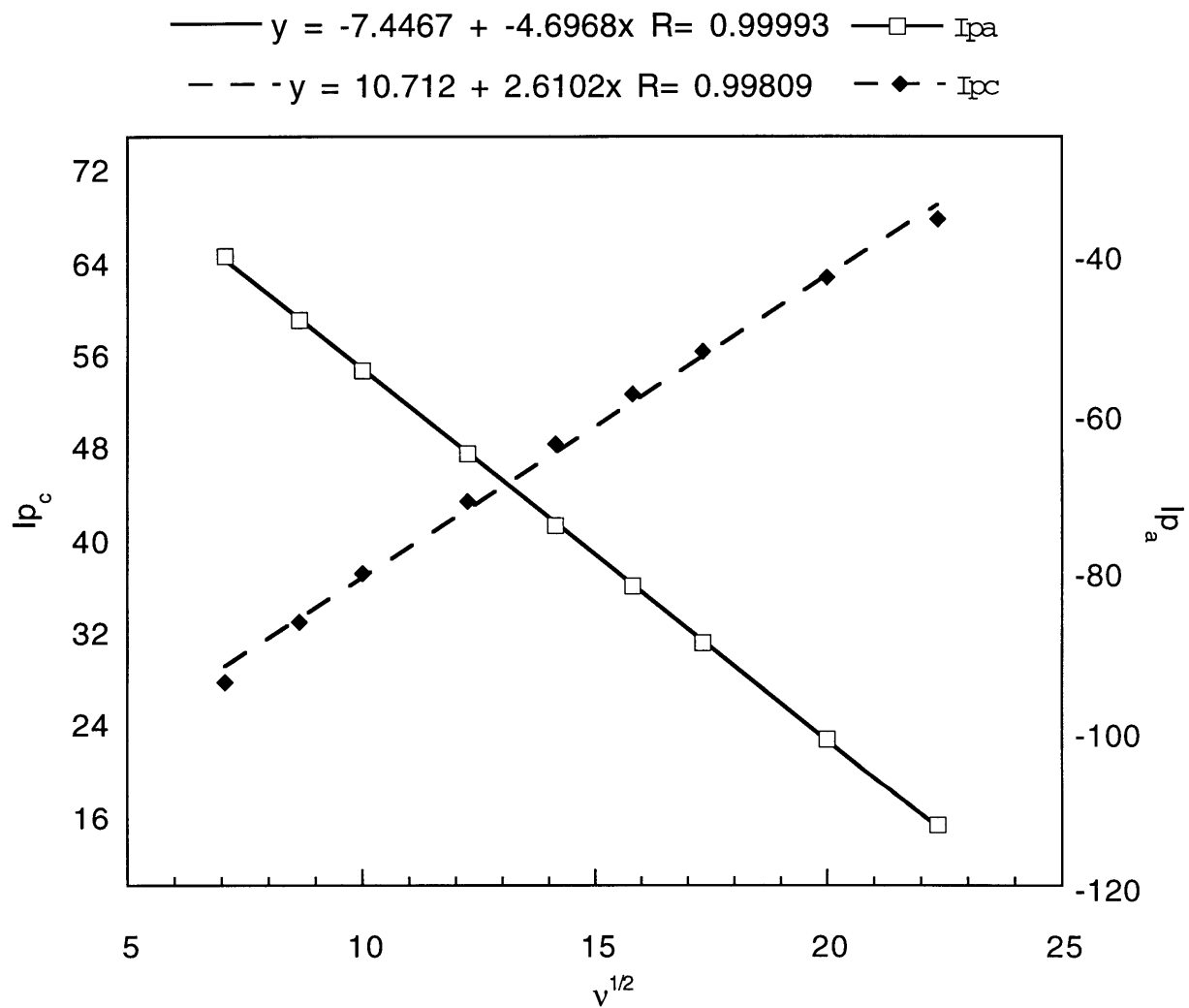


Figure 2.13. Plot of anodic and cathodic currents versus $(\text{scan speed})^{1/2}$ for $[\text{Cu}_2(\text{XDK})]$.

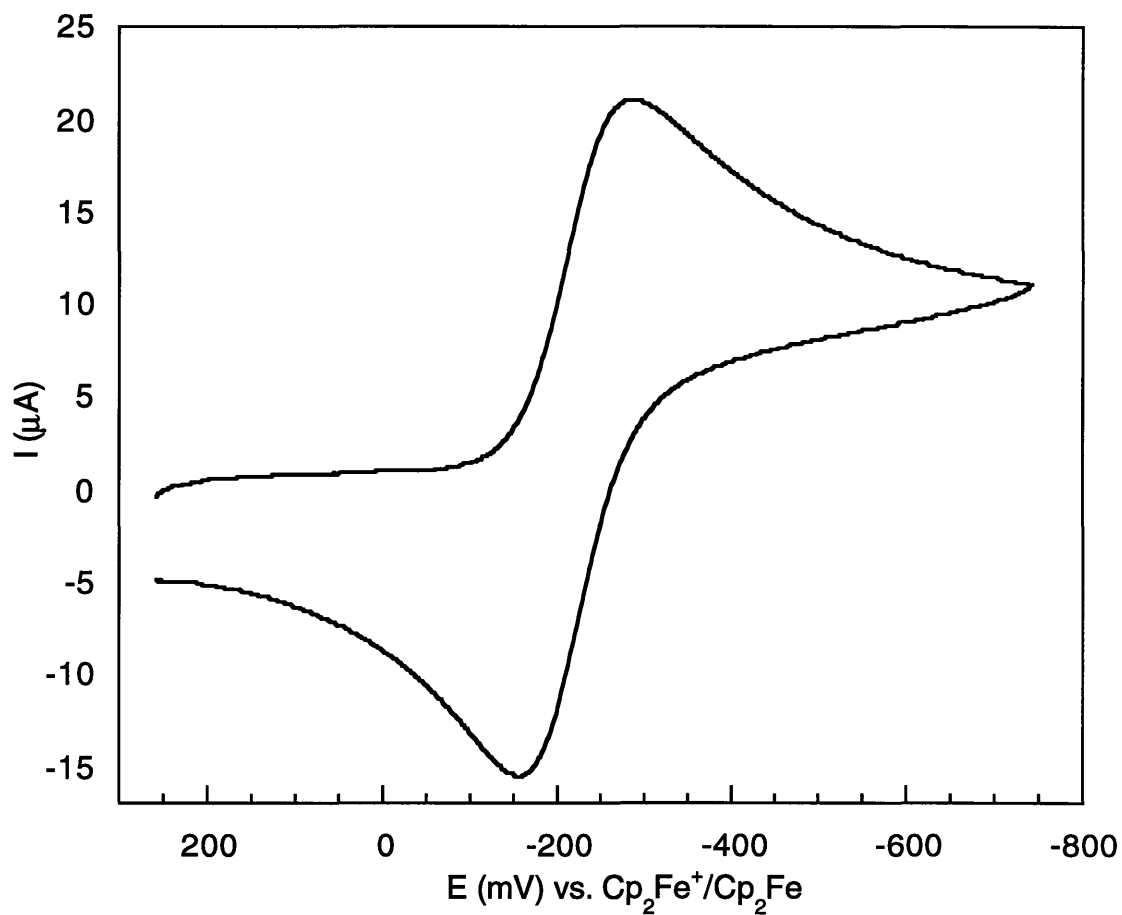


Figure 2.14. Cyclic voltammogram of 10 mM $[\text{Cu}_2(\text{XDK})(\text{THF})_4](\text{BF}_4)$ (7) in THF with 0.5 M $(\text{Bu}_4\text{N})(\text{PF}_6)$ as supporting electrolyte and a cathodic scan speed of 50 mV/sec.

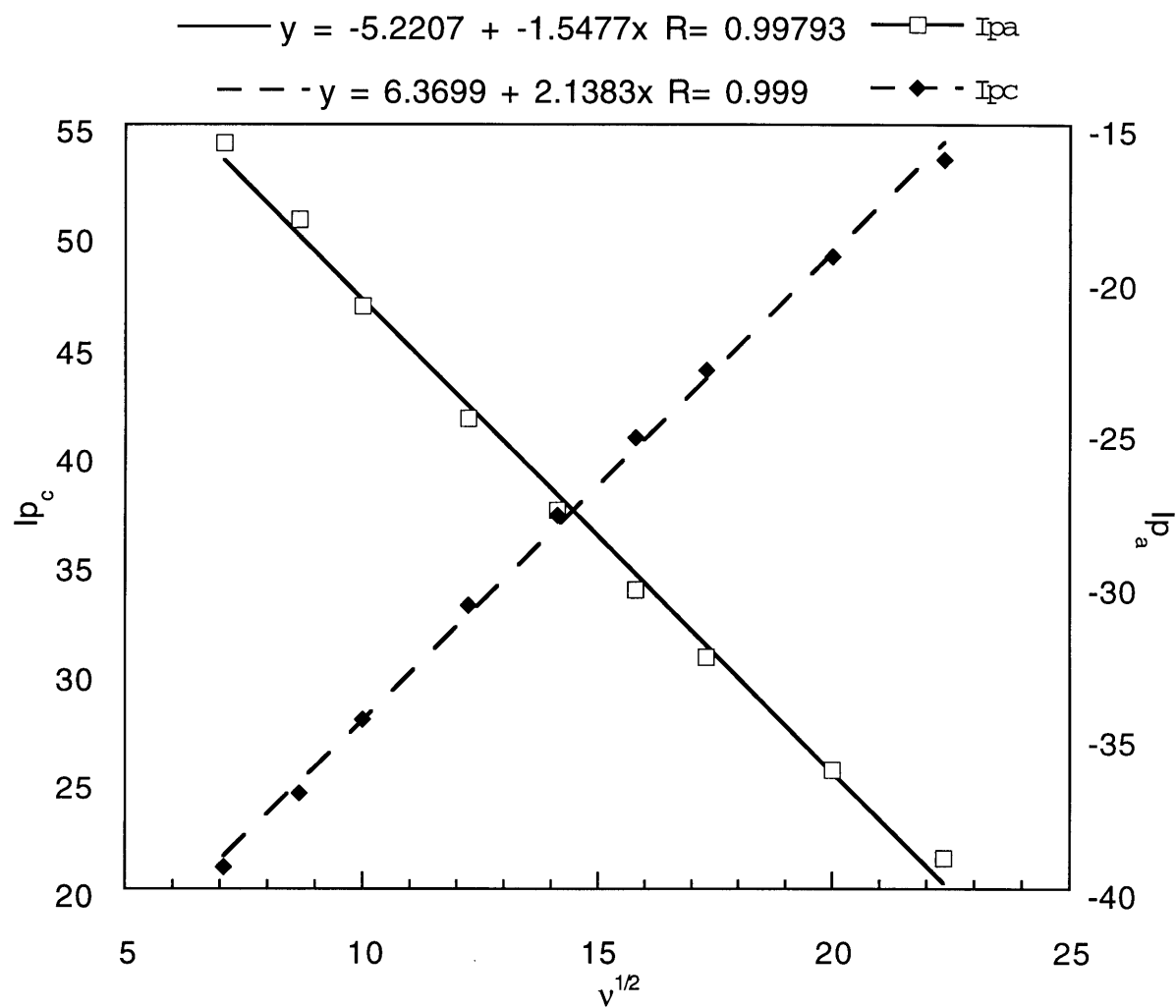


Figure 2.15. Plot of anodic and cathodic currents versus $(\text{scan speed})^{1/2}$ for $[\text{Cu}_2(\text{XDK})(\text{THF})_4](\text{BF}_4)$ (7).

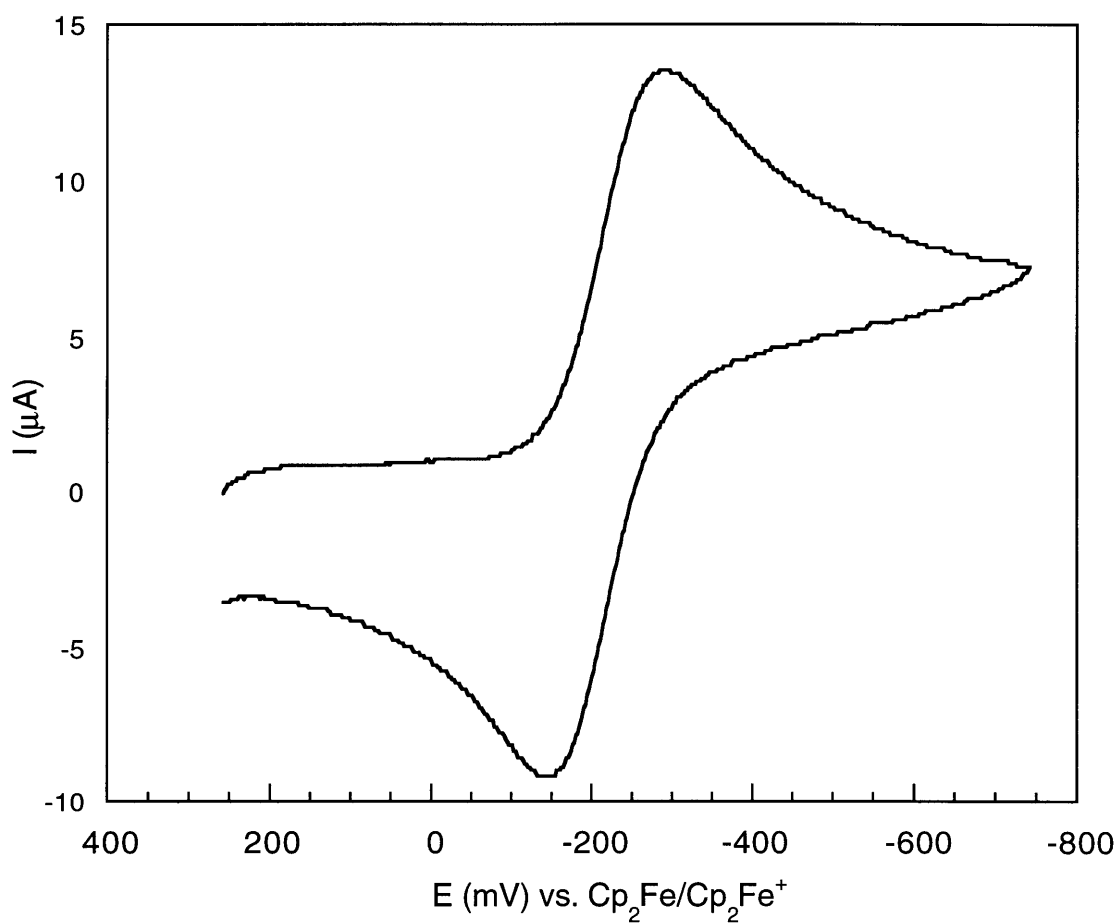


Figure 2.16. Cyclic voltammogram of 10 mM $[\text{Cu}_2(\text{XDK})(\mu\text{-OTf})(\text{THF})_2]$ (**4**) in THF with 0.5 M $(\text{Bu}_4\text{N})(\text{PF}_6)$ as supporting electrolyte and a cathodic scan speed of 50 mV/sec.

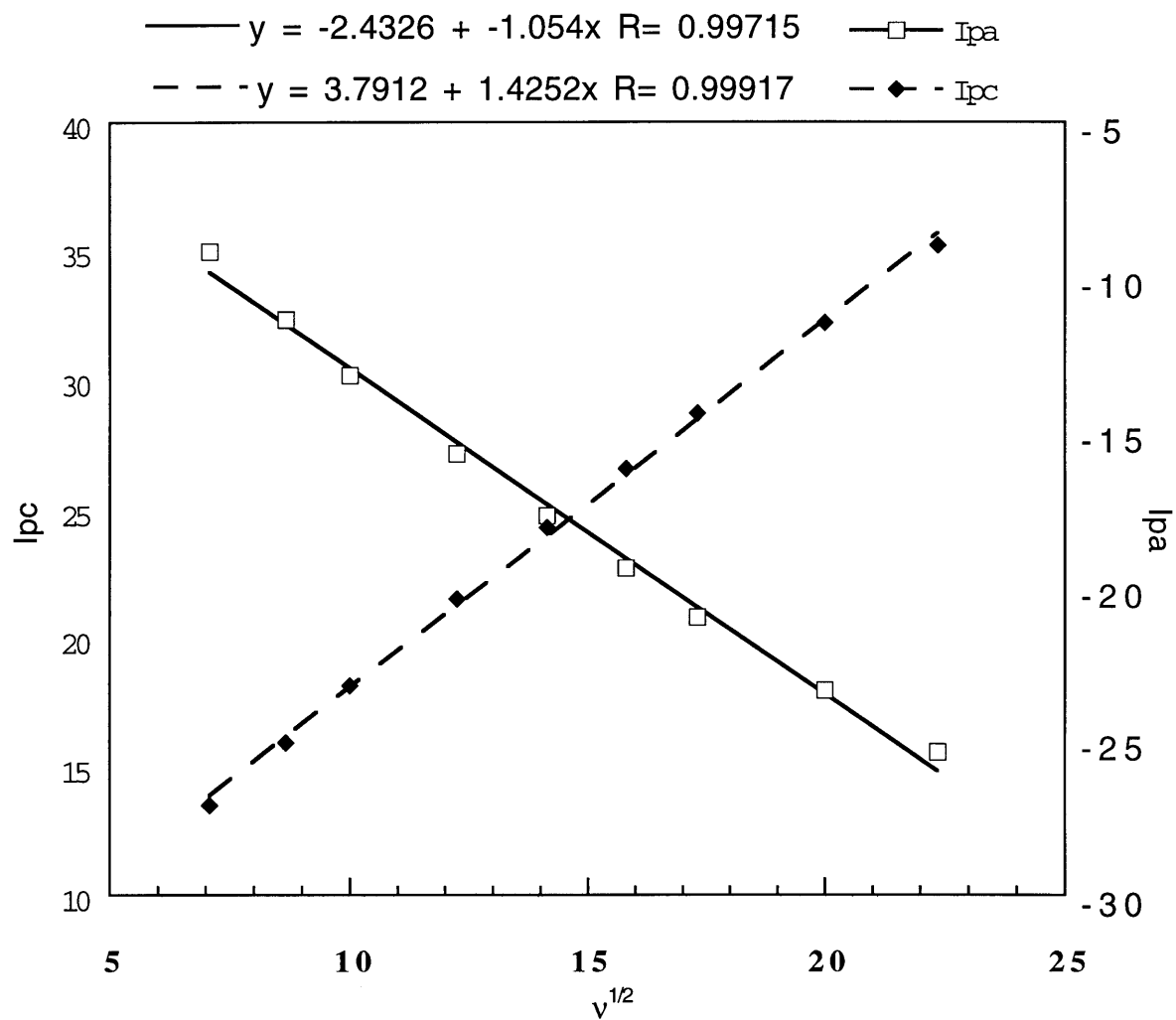


Figure 2.17. Plot of anodic and cathodic currents versus $(\text{scan speed})^{1/2}$ for $[\text{Cu}_2(\text{XDK})(\mu\text{-OTf})(\text{THF})_2]$ (**4**).

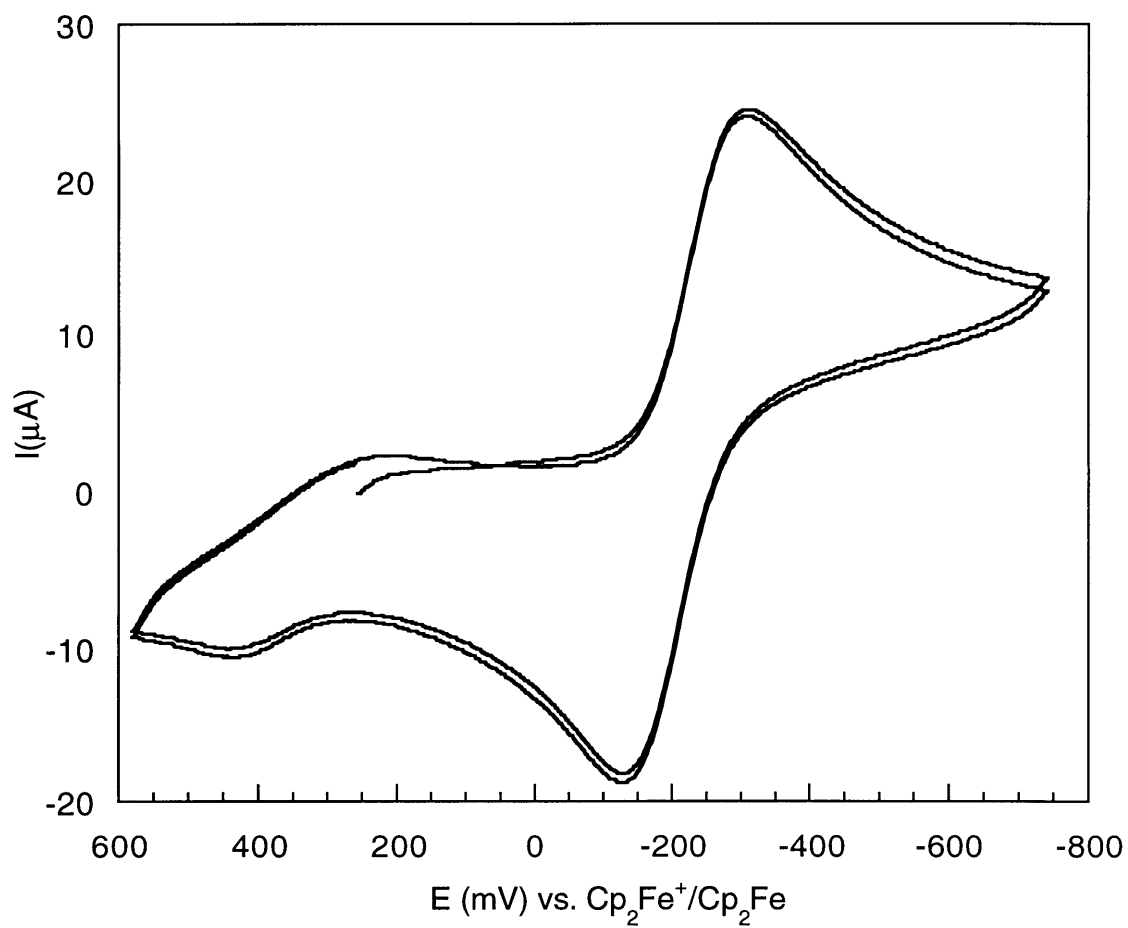


Figure 2.18. Cyclic voltammogram of 10 mM $[\text{Cu}_2(\text{XDK})(\mu\text{-OTf})(\text{THF})_2]$ (**4**) in THF (2 cycles) with 0.5 M $(\text{Bu}_4\text{N})(\text{PF}_6)$ as supporting electrolyte and a cathodic scan speed of 200 mV/sec

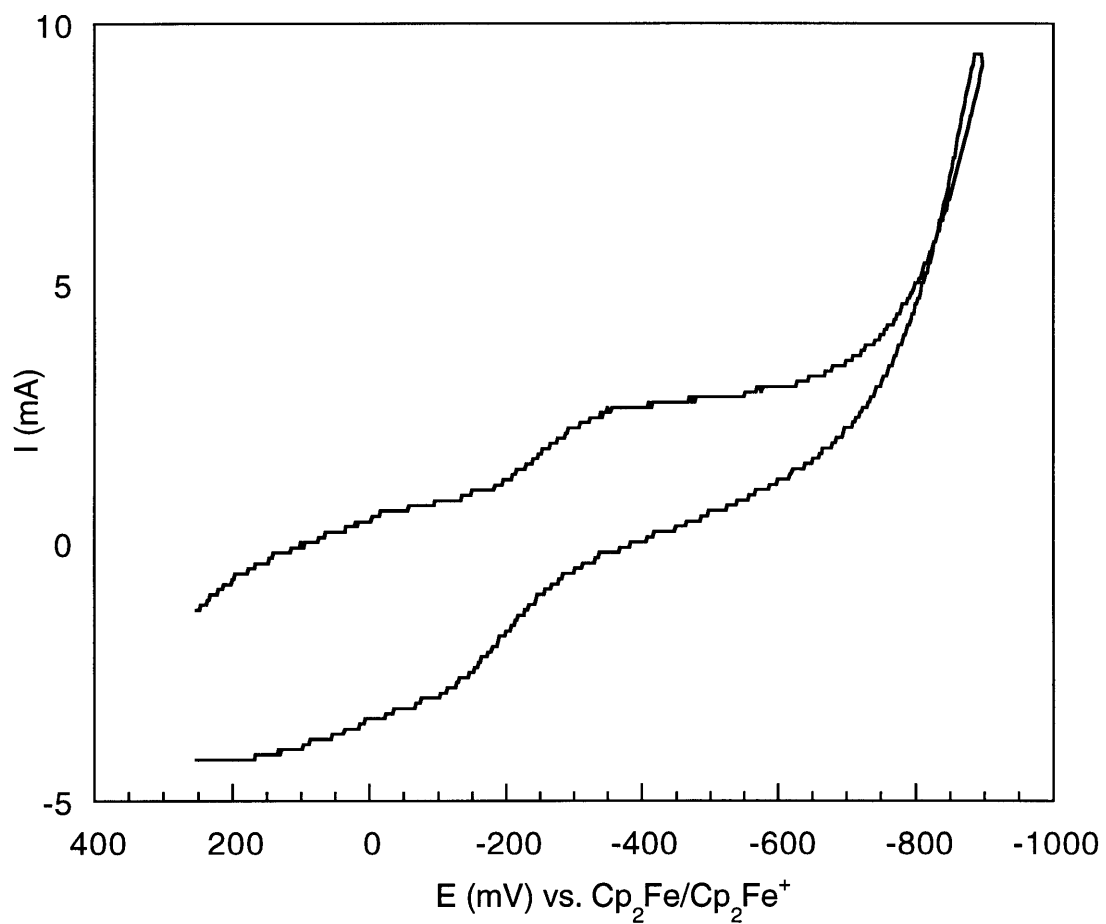


Figure 2.19. Cyclic voltammogram of 10 mM $[\text{Cu}_2(\text{XDK})(\mu\text{-O}_2\text{CCF}_3)(\text{THF})_2]$ (**6**) in THF with 0.5 M $(\text{Bu}_4\text{N})(\text{PF}_6)$ as supporting electrolyte and a cathodic scan speed of 200 mV/sec.

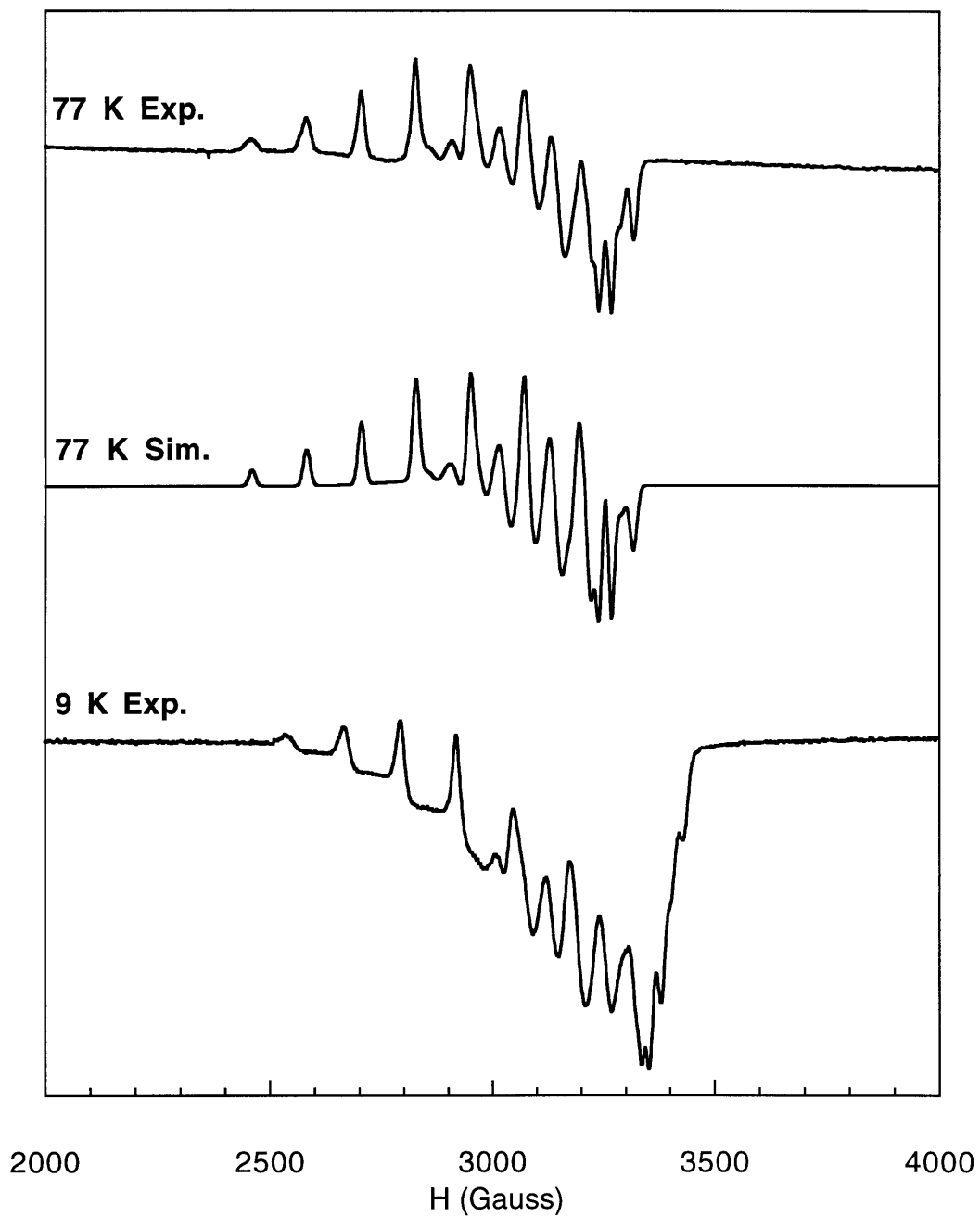


Figure 2.20. X-band EPR spectra of 1 mM $[\text{Cu}_2(\text{XDK})(\text{THF})_4](\text{BF}_4)$ (7) as a frozen solution at 77 and 9 K, along with a simulation of the 77 K data. See Table 2.10 for simulation parameters.

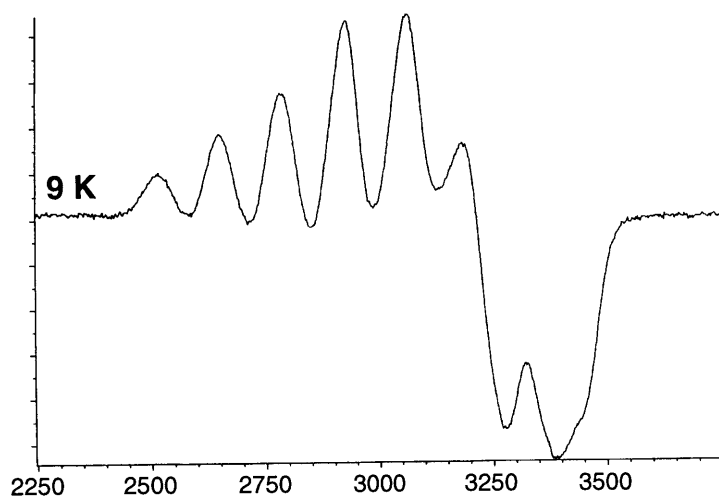
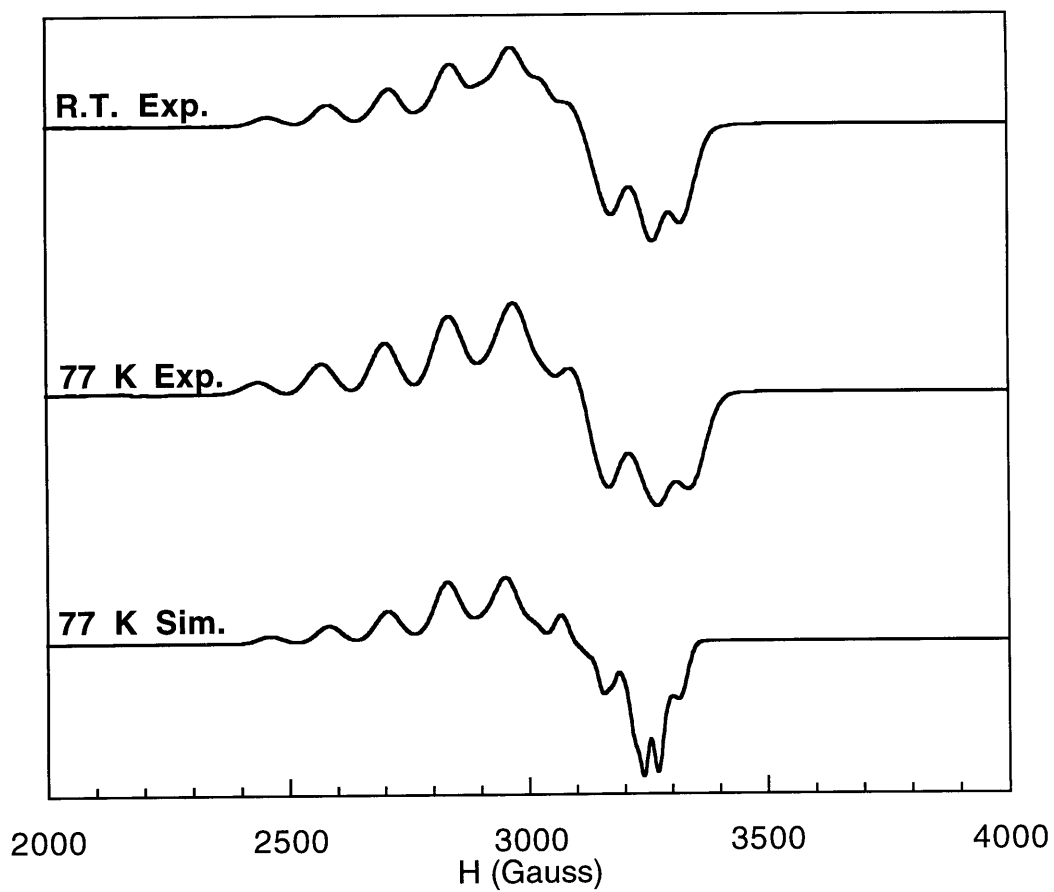


Figure 2.21. X-band EPR spectra of $[\text{Cu}_2(\text{XDK})(\text{THF})_4](\text{BF}_4)$ (7) as a powdered solid at 296, 77, and 9 K, along with a simulation of the 77 K data.



Figure 2.22. Q-band EPR spectrum of $[\text{Cu}_2(\text{XDK})(\text{THF})_4](\text{BF}_4)$ (7) as a frozen solution at 2K.

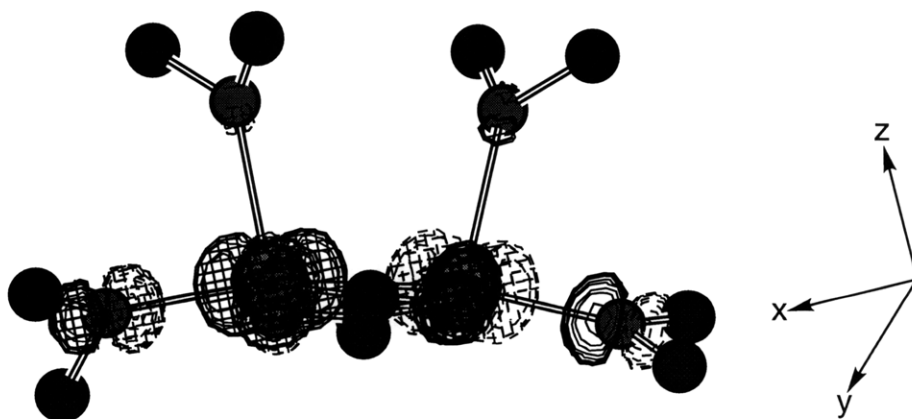
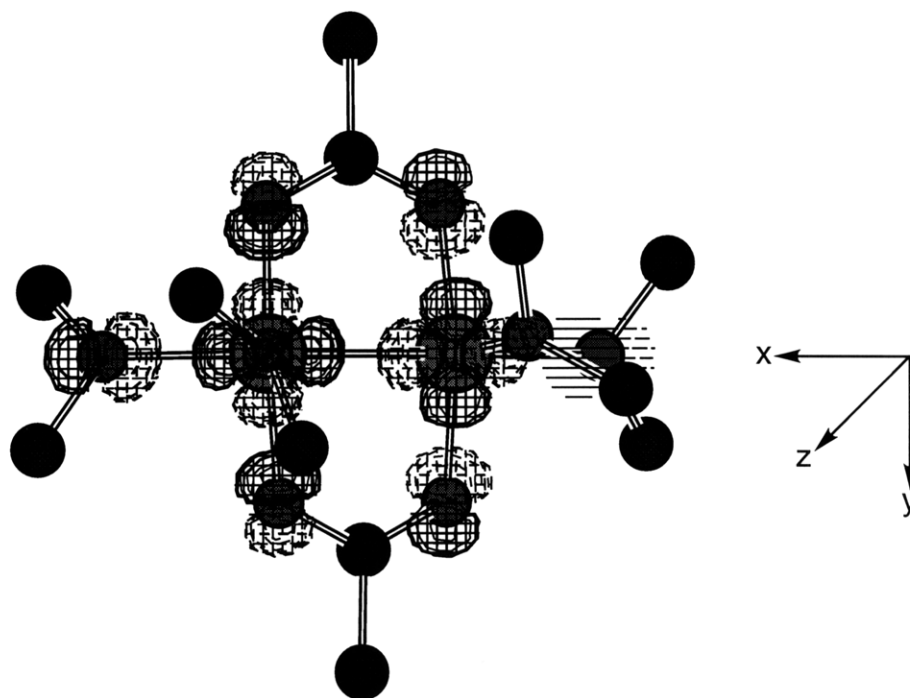


Figure 2.23. Contour plots derived from extended Hückel calculations for the SOMO of $[\text{Cu}_2(\mu\text{-O}_2\text{CCH}_3)_2(\text{OMe}_2)_4]$, a simplified model of 7 and 8.

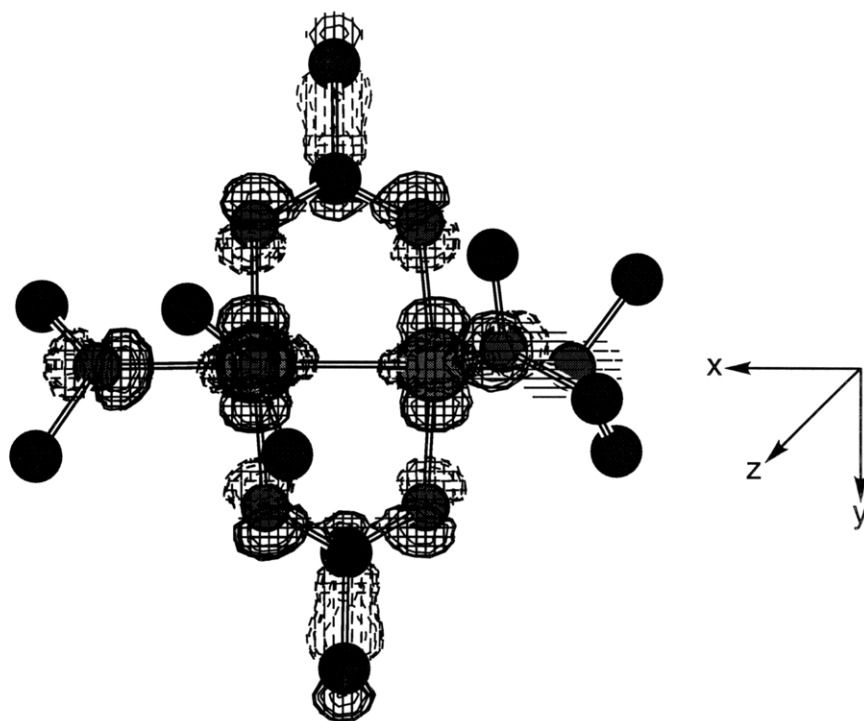


Figure 2.24. Contour plot derived from extended Hückel calculations for the SHOMO of $[\text{Cu}_2(\mu\text{-O}_2\text{CCH}_3)_2(\text{OMe})_4]$.

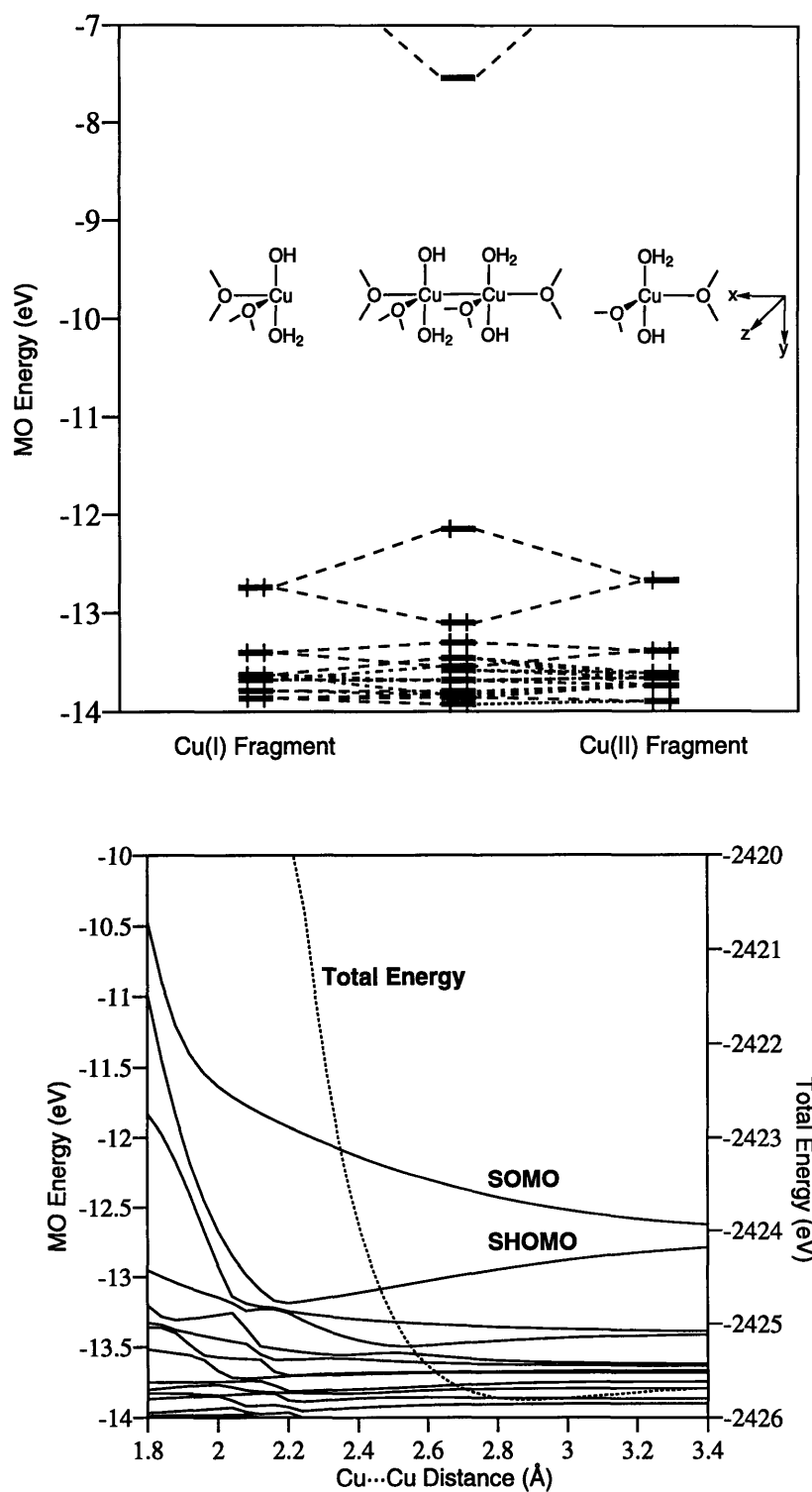


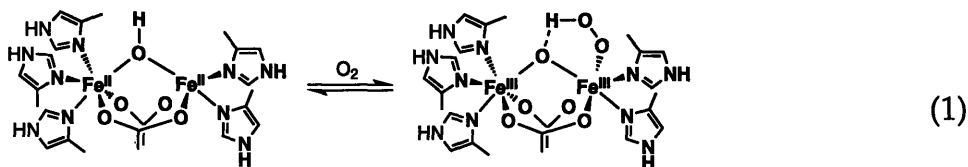
Figure 2.25. Fragment molecular orbital diagram and a Walsh diagram for $[\text{Cu}_2(\text{OH})_2(\text{OH}_2)_2(\text{OMe}_2)_4]$, a simplified model of 7 and 8.

Chapter III

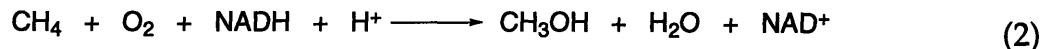
**Modeling the H_{peroxo} Intermediate of Soluble Methane Monooxygenase:
Preparation of Sterically Hindered Diiron(II) Tetracarboxylate Complexes, and Their
Reactivity Toward Dioxygen**

Introduction

Over the last few decades, a class of carboxylate-bridged diiron proteins has been discovered that utilizes dioxygen for a variety of functions, ranging from O₂ transport to the selective catalytic oxidation of organic substrates by hydroxylation, epoxidation, or hydrogen atom abstraction processes.¹⁻⁵ This diversity is aptly represented in three of the most intensively studied of these proteins, hemerythrin, ribonucleotide reductase, and methane monooxygenase. Hemerythrin (Hr) is the dioxygen carrier protein in marine invertebrates. The reduced protein has a [Fe₂(μ-OH)(μ-O₂CR)₂(His)₅]⁺ donor set, and in the oxidized form O₂ is bound as a terminal η¹-hydroperoxide, hydrogen bonded to the oxo bridge (eq 1).



Ribonucleotide reductases are essential for reducing ribonucleotides to deoxyribonucleotides, which are used in DNA biosynthesis. The *E. coli* form of this enzyme houses a diiron active site in the R2 subunit (RNR-R2). Here O₂ is activated and one of its oxidizing equivalents is used to generate a tyrosyl radical, which in turn transfers an electron from the R1 subunit, where the ribonucleotide reduction is catalyzed. Methane monooxygenase (MMO) is used by obligate methanotrophic bacteria to oxidize methane selectively to methanol. These bacteria use methane as their sole source of carbon and energy. This mixed function oxidase incorporates one of the oxygen atoms from dioxygen into methanol and the other into water (eq 2). The soluble form (sMMO) contains a diiron center in the hydroxylase component (MMOH), the site of methane oxidation.



Unlike hemerythrin, the RNR-R2 and MMOH enzymes contain oxygen-rich coordination environments at their diiron active sites. In each protein four carboxylate and two imidazole ligands are distributed about the two iron atoms. The remainder of coordination sites are occupied by a variable number of water, hydroxide, or oxo ligands, depending on the enzyme and its position in the catalytic cycle. Depicted in Figure 3.1 are the active site structures of the diiron(II) forms of RNR-R2 and MMOH, and the oxidized diiron(III) form of MMOH, each deduced from X-ray crystal structural analyses.⁶⁻⁸

A detailed mechanistic picture of the O₂ activation process in RNR-R2^{2,9,10} and sMMO^{2,4,9,10} is emerging as a result of the detection and spectroscopic characterization of transient oxygen intermediates (Figure 3.2). For RNR-R2, the first intermediate forms and decays within 35 milliseconds.¹¹ Based on the similarity of its Mössbauer and UV-vis spectra to those observed for a model complex and an analogous intermediate in MMOH (vide infra), this species has been tentatively assigned as a diiron(III) peroxo complex, the product of O₂ binding to the fully reduced diiron center combined with two-electron reduction. Intermediate X, which forms subsequently after the peroxo, has Mössbauer,¹² Q-band ENDOR,¹³ and EXAFS¹⁴ spectra consistent with an antiferromagnetically coupled Fe(III)Fe(IV) center with at least one oxo bridge and a terminal water or hydroxide ligand. In addition, X has an Fe...Fe separation of 2.5 Å and at least one Fe–O distance of 1.8 Å. The EXAFS parameters are consistent with the presence of two or three single atom bridges. This high-valent intermediate X is the direct precursor to catalytically active RNR-R2 (RR_{act}) and generates the active enzyme possibly by hydrogen atom abstraction from Tyr-122, to afford an oxo-bridged diiron(III) center and the tyrosyl radical. Presumably X is the product of peroxide O–O bond cleavage, but it is not clear whether injection of an extra electron must accompany O–O bond scission or,

alternatively, whether a yet unobserved dioxodiiron(IV) species might be initially generated.¹⁰

For MMOH, a metastable diiron(III) peroxo intermediate (H_{peroxo}) has also been identified as an early product of the O_2 reaction chemistry,¹⁵ but it forms and decays more slowly than its RNR-R2 analog.¹¹ H_{peroxo} converts to a diiron(IV) species termed Q (or MMOH-Q).^{15,16} This intermediate, or a closely related derivative, is believed to be the active substrate oxidant since Q is the last iron-oxygen species detected prior to methane oxidation, and its decomposition is accelerated by the presence of substrate. The structure of Q has been interrogated by EXAFS, which revealed quite similar parameters to those observed for intermediate X in RNR-R2.¹⁷ The EXAFS data do not provide unique structural information about either high-valent intermediate, however, particularly regarding the coordination of the oxygen ligands derived from O_2 .

Recent experiments on RNR-R2 and MMOH reveal that the two systems share common oxygen intermediates, the fate of which is exquisitely regulated according to their different oxidative functions. In one study, an RNR-R2 mutant was prepared in which an aspartate residue in the active site was replaced with glutamate, affording an MMOH-like coordination environment.¹⁸ With this modest change in the flexibility of a single carboxylate ligand, the D84E mutant remarkably afforded a diiron(III) peroxo that formed and decayed at rates comparable to those of MMOH- H_{peroxo} , proceeding to form a stoichiometric amount of a stable tyrosyl radical, most likely via intermediate X. These results lend credence to the assignment of the initial O_2 intermediate in native RNR-R2 as a diiron(III) peroxo species, and reveal that the stability of the peroxo intermediates in RNR-R2 and MMOH can be regulated by tuning the active site ligands.

In the other study, intermediate Q in MMOH was reduced radiolytically at low temperature, while keeping the active site structure conformationally fixed in a

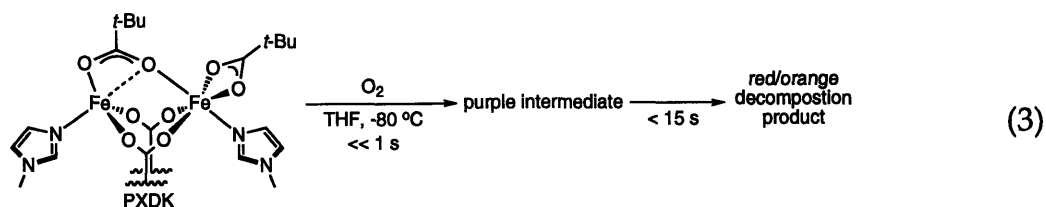
frozen solution.¹⁹ This procedure provided a new spectroscopically distinct species, termed Q_X , having Mössbauer parameters essentially identical to those of R2-X. This result, coupled with the EXAFS studies of Q, suggests that R2-X and Q have very similar structures, and that R2-X is derived from a Q-like analog by reduction with an external electron. In this manner, the extra oxidizing equivalent in a dioxodiiron(IV) intermediate could be quickly sequestered in RNR-R2 by an outer sphere reduction, so that R2-X can generate a tyrosyl radical stable towards further degradation by a metal-based oxidant. In contrast, both oxidizing equivalents of MMOH-Q are retained for methane oxidation.

Considerable effort has been expended to prepare synthetic models for the dioxygen intermediates described above for RNR-R2 and sMMO. The goals have been to mimic their spectroscopic and structural features, and ultimately their oxidation chemistry.^{1,5} The most notable systems reported to date include three well characterized diiron(III) peroxo complexes and an Fe(III)Fe(IV) bis(μ -oxo) species, the properties of which are summarized in Table 3.1. The peroxo complexes were all prepared by exposure of the ferrous precursor to O_2 at low temperature.²⁰⁻²² They have UV-vis spectra characterized by a broad charge-transfer band centered at ~ 600 nm ($\epsilon \sim 2000 \text{ M}^{-1}\text{cm}^{-1}$), and resonance Raman O–O stretches at $\sim 900 \text{ cm}^{-1}$. In addition, X-ray structural studies revealed the peroxide to be bound symmetrically in an eclipsed or gauche μ -1,2 bridging mode for each complex.

The Fe(III)Fe(IV) bis(μ -oxo) model was prepared from hydrogen peroxide and a diiron(III) bis(μ -oxo) "diamond core" precursor, possibly via a diiron(III)(μ -oxo)(μ -peroxo) intermediate.^{23,24} It has an antiferromagnetically coupled, valence localized, $S = 1/2$ ground state and distinct Mössbauer quadrupole doublets for the Fe(III) and Fe(IV) ions. The electronic structure of the metal ions matches well with analogous spectroscopic data accumulated for Q_X and X, but it is not yet clear whether the arrangement of oxo ligands in each system is the same.

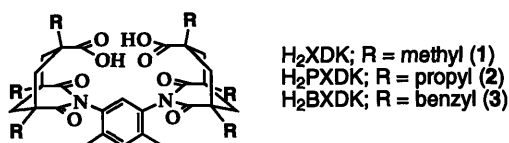
Despite these recent advances, there are many deficiencies in the models for RNR-R2 and sMMO. Most importantly, in no system where a peroxo has been derived from the reaction of an iron(II) precursor with O₂ has conversion to a high valent Q- or X-like species been demonstrated, nor has hydrocarbon oxidation chemistry been achieved. These shortcomings may stem from the fact that the present model systems do not reproduce the ligand composition found at the RNR-R2 and sMMO active sites; their soft, nitrogen-rich coordination environments more closely resemble the active site residues in hemerythrin. The widely different fates of the peroxo ligands in Hr, RNR-R2, and sMMO may be due in part to the ability of the latter two systems, owing to their more basic, oxygen-rich donor sets, to support higher iron oxidation states required for O–O bond cleavage. With this hypothesis in mind, we were interested to investigate a carboxylate-rich model system in the hope that it would more closely mimic the RNR/sMMO systems from the dioxygen binding through O–O bond cleavage and substrate oxidation steps.

Recently, carboxylate-bridged diiron(II) complexes having the xylylenediamine bis(Kemp's triacid imide) (H₂XDK) ligand system were described, and their reactivity towards dioxygen explored in a preliminary manner.²⁵ A family of diferrous tris(carboxylate-bridged) complexes was obtained which matched the composition of amino acid ligands at the MMOH active site. When one of these derivatives was exposed to O₂ at low temperature in THF, the solution flashed deep purple, but quickly decayed to a red-orange color in less than 30 s (eq 3). Monitoring this reaction by stopped-flow UV-vis spectroscopy revealed the build-up and



decay over 10 s of an intermediate with an optical band centered at 650 nm. This species was tentatively assigned as a diiron(III) peroxy, but its inherent instability precluded any further characterization or functional reactivity studies.

In previous investigations from this laboratory, we have focused on the thermal decomposition of well defined diiron(III) peroxy complexes.^{26,27} Kinetic studies revealed the decay to have second order behavior in the peroxy, resulting in the extrusion of 0.5 equivalents of O₂ and cleanly yielding diiron(III) oxo-bridged derivatives. Since bimolecular decay pathways are typically retarded by implementing sterically more hindered ligands, we modified the diiron XDK ligand system with bulkier R groups with the aim of stabilizing the incipient peroxy intermediate. Presented here are the synthesis and characterization of sterically



hindered diiron(II) tetracarboxylate complexes and studies of their reactivity toward O₂ to form stable peroxy adducts. A detailed account of their reactivity toward electrophilic, nucleophilic, and hydrocarbon substrates is in the following chapter.²⁸

Experimental Section

General Considerations. The compounds H₂XDK (1),²⁹ H₂PXDK (2),²⁵, H₂BXDK (3),³⁰ 1-phenylcyclohexanecarboxylic acid,³¹ and [FeTp^{3,5}-iPr₂(O₂CCH₂Ph)]²⁰ were prepared according to literature procedures. The thallium(I) salts of the carboxylic acid ligands were obtained as described in the literature or by analogous procedures,^{30,32} and each was identified by ¹H NMR spectroscopy as the desolvated thallium salt of high purity (>95%). Ligands 1-methylimidazole and 1-butyliimidazole were degassed and stored over 3 Å molecular sieves for several days

prior to use. Dioxygen (99.994%, BOC Gases) was dried by passing the gas stream through a column of Drierite. Labeled dioxygen (50% $^{18}\text{O}_2$ and 95% $^{18}\text{O}_2$) reagents were purchased from Cambridge Isotope Laboratories, Inc., and used without further purification. All other reagents were procured from commercial sources and used as received unless otherwise noted. THF, benzene, toluene, pentane, and Et_2O were distilled from sodium benzophenone ketyl under nitrogen. Dichloromethane, 1,2-dichloroethane, and pyridine were distilled from CaH_2 under nitrogen. The NMR solvent CD_2Cl_2 was degassed, passed through activated basic alumina, and stored over 3 Å molecular sieves prior to use. All air sensitive manipulations were carried out either in a nitrogen filled Vacuum Atmospheres drybox or by standard Schlenk line techniques at room temperature unless otherwise noted.

Synthesis. $[\text{Fe}(\text{XDK})(\text{py})_2]$ (4). To a rapidly stirred suspension of $\text{Ti}_2(\text{XDK})$ (2.00 g, 2.02 mmol) and pyridine (1.64 ml, 20.2 mmol) in THF (15 mL) was added a solution of FeBr_2 (446 mg, 2.02 mmol) in THF (5 mL). After 6 h, the precipitated TiBr was removed by filtration through Celite, and the filtrate was evaporated to dryness. The crude residue was washed with pentane (20 mL) to remove any residual pyridine, isolated by filtration, and dried fully in vacuo to afford **4** as a light yellow powder (1.44 g, 90%). This crude material was used for subsequent reactions without further purification. Recrystallization from $\text{CH}_2\text{Cl}_2/\text{pyridine}/\text{Et}_2\text{O}$ afforded **4** as yellow blocks which appeared suitable for X-ray crystallography: IR (KBr) 3068, 2961, 2929, 1735, 1696, 1602, 1404, 1463, 1358, 1334, 1218, 1195, 1087, 1039, 958, 835, 760, 626 cm^{-1} ; UV-vis (CH_2Cl_2) (λ_{max} , nm (ϵ , $\text{M}^{-1}, \text{cm}^{-1}$)) 364 (580). Anal. Calcd for $\text{C}_{42}\text{H}_{48}\text{N}_4\text{O}_8\text{Fe}_1$: C, 63.64; H, 6.10; N, 7.07. Found: C, 61.33; H, 6.26; N, 6.60.

$[\text{Fe}(\text{BXDK})(\text{py})_2]$ (5). This compound was prepared as a light yellow powder from $\text{Ti}_2(\text{BXDK})$ (2.33 g, 1.61 mmol), pyridine (560 μl , 6.92 mmol), and FeBr_2 (354 mg, 1.61 mmol) by a procedure analogous to that used to prepare **4** (1.55 g, 77%). The crude material was used for all subsequent reactions. Recrystallization from

CH₂Cl₂/Et₂O provided **5** as opaque yellow needles. IR (KBr) 3062, 3027, 2921, 2857, 1734, 1693, 1603, 1495, 1446, 1352, 1191, 1040, 935, 761, 700, 593, 526 cm⁻¹; UV-vis (CH₂Cl₂) (λ_{max}, nm (ε, M⁻¹, cm⁻¹)) 361 (690). Anal. Calcd for C₇₈H₇₂N₄O₈Fe₁: C, 74.97; H, 5.81; N, 4.49. Found: C, 74.45; H, 5.80; N, 4.34.

[Fe₂(BXDK)(μ-O₂Ct-Bu)(O₂Ct-Bu)(py)₂] (**6**). To a stirred solution of TlO₂Ct-Bu (147 mg, 0.480 mmol) and pyridine (116 μl, 1.44 mmol) in THF (3 mL) was added FeBr₂ (53 mg, 0.24 mmol) in THF (1 ml). After 10 min this mixture was added in one portion to a stirred solution of **5** (300 mg, 0.240 mmol) in CH₂Cl₂ (3 mL). The resulting mixture was allowed to stir for 0.5 h, after which time the precipitated TlBr was removed by filtration through Celite, and the volatile components were removed in vacuo. Recrystallization from CH₂Cl₂/Et₂O afforded **6** as yellow blocks (265 mg, 73%) which appeared suitable for X-ray crystallography. IR (KBr) 3062, 3028, 2959, 2923, 2863, 1734, 1693, 1602, 1541, 1486, 1407, 1365, 1221, 1189, 1042, 937, 763, 701, 608, 528 cm⁻¹; UV-vis (CH₂Cl₂) (λ_{max}, nm (ε, M⁻¹, cm⁻¹)) 355 (920). Anal. Calcd for C_{88.5}H₉₁N₄O₁₂Fe₂Cl (6·0.5CH₂Cl₂): C, 68.71; H, 5.90; N, 3.60. Found: C, 68.45; H, 6.06; N, 3.48. One lattice dichloromethane was identified by X-ray crystallography, and apparently it was not removed completely by pumping on the sample in vacuo for one day. When this procedure was repeated with heating, sample decomposition was observed.

[Fe₂(XDK)(μ-O₂CPhCy)(O₂CPhCy)(py)₂] (**7**). This compound was prepared from Tl(O₂CPhCy) (308 mg, 0.757 mmol), pyridine (184 μl, 2.27 mmol), FeBr₂ (83 mg, 0.378 mmol) and **4** (300 mg, 0.378 mmol) as described for **6**. Recrystallization from benzene/pentane afforded **7** as pale yellow blocks which appeared suitable for X-ray crystallography (291 mg, 61%). IR (KBr) 3063, 2960, 2928, 2862, 1737, 1699, 1614, 1448, 1405, 1355, 1221, 1187, 1069, 957, 851, 760, 698, 637 cm⁻¹; UV-vis (CH₂Cl₂) (λ_{max}, nm (ε, M⁻¹, cm⁻¹)) 354 (840). Anal. Calcd for C₆₈H₇₈N₄O₁₂Fe₂: C, 65.08; H, 6.26; N, 4.46. Found: C, 64.09; H, 6.63; N, 4.08.

[Fe₂(XDK)(μ-O₂C*Ar*)(O₂C*Ar*)(py)₂] (8). This compound was prepared from TiO₂C*Ar* (342 mg, 0.757 mmol), pyridine (184 μl, 2.27 mmol), FeBr₂ (83 mg, 0.378 mmol), and **4** (300 mg, 0.378 mmol) as described for **6**. Recrystallization from THF/pentane provided **8** as yellow blocks (285 mg, 56%). IR (KBr) 2960, 2870, 1736, 1699, 1611, 1536, 1464, 1412, 1357, 1220, 1192, 1069, 958, 841, 760, 698, 511 cm⁻¹; UV-vis (CH₂Cl₂) (λ_{max}, nm (ε, M⁻¹, cm⁻¹)) 353 (790). Anal. Calcd for C₇₂H₉₆N₄O₁₂Fe₂: C, 65.45; H, 7.32; N, 4.24. Found: C, 66.17; H, 7.01; N, 3.80.

[Fe₂(XDK)(μ-O₂C*Ar*)(O₂C*Ar*)(3-Fpy)₂] (9). This compound was prepared from TiO₂C*Ar* (342 mg, 0.757 mmol), 3-fluoropyridine (157 μl, 1.82 mmol), FeBr₂ (83 mg, 0.378 mmol), and **4** (300 mg, 0.378 mmol) as described for **6**. Recrystallization from THF/pentane provided **9** as yellow blocks (246 mg, 48%). IR (KBr) 2962, 2931, 2870, 1735, 1697, 1608, 1463, 1409, 1359, 1233, 1197, 1101, 959, 761, 537 cm⁻¹; UV-vis (CH₂Cl₂) (λ_{max}, nm (ε, M⁻¹, cm⁻¹)) 361 (790). Anal. Calcd for C₇₂H₉₆N₄O₁₂Fe₂F₂: C, 63.72; H, 6.98; N, 4.13. Found: C, 63.95; H, 6.96; N, 3.53.

[Fe₂(BXDK)(μ-O₂C*i-Pr*)(O₂C*i-Pr*)(py)₂] (10). This compound was prepared from TiO₂*i-Pr* (70 mg, 0.24 mmol), pyridine (60 μl, 0.72 mmol), FeBr₂ (26 mg, 0.12 mmol), and **5** (150 mg, 0.120 mmol) as described for **6**. Recrystallization from THF/pentane provided **10** as yellow needles (135 mg, 76%). IR (KBr) 3062, 3028, 2965, 2923, 2869, 1733, 1693, 1602, 1546, 1495, 1446, 1364, 1190, 1034, 850, 763, 701, 528 cm⁻¹; UV-vis (CH₂Cl₂) (λ_{max}, nm (ε, M⁻¹, cm⁻¹)) 357 (920). Anal. Calcd for C₈₆H₈₆N₄O₁₂Fe₂: C, 69.82; H, 5.86; N, 3.79. Found: C, 69.34; H, 6.05; N, 3.50.

[Fe₂(BXDK)(μ-O₂CH₂*t-Bu*)(O₂CH₂*t-Bu*)(py)₂] (11). This compound was prepared from TiO₂CH₂*t-Bu* (77 mg, 0.24 mmol), pyridine (60 μl, 0.72 mmol), FeBr₂ (26 mg, 0.12 mmol), and **5** (150 mg, 0.120 mmol) as described for **6**. Recrystallization from THF/pentane provided **11** as yellow blocks (130 mg, 71%). IR (KBr) 3062, 3028, 2952, 2866, 1733, 1693, 1603, 1548, 1447, 1364, 1190, 1041, 936, 744, 701, 528 cm⁻¹; UV-vis

(CH₂Cl₂) (λ_{max} , nm (ϵ , M⁻¹, cm⁻¹)) 358 (960). Anal. Calcd for C₉₀H₉₄N₄O₁₂Fe₂: C, 70.40; H, 6.17; N, 3.65. Found: C, 70.20; H, 6.60; N, 3.26.

[Fe₂(BXDK)(μ -O₂CPh)(O₂CPh)(py)₂] (12). This compound was prepared from TiO₂CPh (78 mg, 0.24 mmol), pyridine (60 μ l, 0.72 mmol), FeBr₂ (26 mg, 0.12 mmol), and **5** (150 mg, 0.120 mmol) as described for **6**. Recrystallization from THF/CH₂Cl₂/pentane provided **12** as yellow blocks (132 mg, 71%) which appeared suitable for X-ray crystallography. IR (KBr) 3061, 3028, 2952, 2920, 2865, 1733, 1694, 1604, 1543, 1495, 1447, 1364, 1189, 1069, 1042, 937, 853, 762, 720, 701, 588, 528 cm⁻¹; UV-vis (CH₂Cl₂) (λ_{max} , nm (ϵ , M⁻¹, cm⁻¹)) 351 (1400). Anal. Calcd for C₉₃H₈₄N₄O₁₂Fe₂Cl₂ (**12**·1CH₂Cl₂): C, 68.43; H, 5.19; N, 3.43. Found: C, 68.84; H, 5.21; N, 3.13.

[Fe₂(BXDK)(μ -O₂CPhCy)(O₂CPhCy)(py)₂] (13). This compound was prepared from TiO₂CPhCy (391 mg, 0.960 mmol), pyridine (233 μ l, 2.88 mmol), FeBr₂ (106 mg, 0.480 mmol), and **5** (600 mg, 0.480 mmol) as described for **6**. Recrystallization from CH₂Cl₂/THF/pentane provided **13** as yellow blocks (623 mg, 76%) which appeared suitable for X-ray crystallography. IR (KBr) 3061, 3028, 2920, 2856, 1735, 1696, 1605, 1494, 1452, 1398, 1366, 1191, 1073, 1042, 864, 762, 699, 526 cm⁻¹; UV-vis (CH₂Cl₂) (λ_{max} , nm (ϵ , M⁻¹, cm⁻¹)) 354 (940). Anal. Calcd for C₁₀₄H₁₀₂N₄O₁₂Fe₂: C, 72.98; H, 6.01; N, 3.27. Found: C, 72.73; H, 6.09; N, 3.02.

[Fe₂(BXDK)(μ -O₂CAr)(O₂CAr)(py)₂] (14). This compound was prepared from TiO₂CAr (108 mg, 0.240 mmol), pyridine (60 μ l, 0.72 mmol), FeBr₂ (26 mg, 0.12 mmol), and **5** (150 mg, 0.120 mmol) as described for **6**. Recrystallization from benzene/pentane provided **14** as yellow blocks (144 mg, 67%) which appeared suitable for X-ray crystallography. IR (KBr) 3068, 3028, 2960, 2928, 2868, 1733, 1693, 1605, 1462, 1406, 1362, 1190, 1070, 937, 762, 701, 730, 528 cm⁻¹; UV-vis (CH₂Cl₂) (λ_{max} , nm (ϵ , M⁻¹, cm⁻¹)) 352 (870). Anal. Calcd for C₁₀₈H₁₂₀N₄O₁₂Fe₂: C, 72.96; H, 6.80; N, 3.15. Found: C, 72.96; H, 7.10; N, 3.03.

[Fe₂(XDK)(μ-O₂CPhCy)(O₂CPhCy)(Me-Im)₂] (15). To a stirred suspension of Tl₂(XDK) (420 mg, 0.425 mmol) and Me-Im (71 μl, 0.89 mmol) in THF (5 mL) was added FeBr₂ (187 mg, 0.851 mmol) in THF (2 mL) followed by TlO₂CPhCy (347 mg, 0.851 mmol) in THF (2 mL). After 12 h the mixture was allowed to settle and the majority of the precipitated TlBr was removed by filtration through Celite. The resulting cloudy filtrate was evaporated to dryness and taken up in benzene. Filtration through Celite afforded a clear filtrate. The Celite/TlBr filter cakes were extracted two additional times with THF (5 mL) to obtain additional product. The combined filtrates were evaporated to dryness to yield a crude white residue. This material was suspended in pentane (10 mL), and the resulting white powder was isolated by filtration. Recrystallization from THF/pentane afforded **15** as colorless needles (386 mg, 72%). IR (KBr) 2959, 2929, 2859, 1734, 1695, 1609, 1535, 1462, 1405, 1357, 1228, 1192, 1087, 958, 852, 762, 697, 628 cm⁻¹. Anal. Calcd for C₆₆H₈₀N₆O₁₂Fe₂: C, 62.86; H, 6.39; N, 6.66. Found: C, 62.66; H, 6.79; N, 6.00.

[Fe₂(PXDK)(μ-O₂CPhCy)(O₂CPhCy)(Bu-Im)₂] (16). This compound was prepared from Tl₂(PXDK) (788 mg, 0.682 mmol), Bu-Im (184 μl, 1.40 mmol), FeBr₂ (300 mg, 1.36 mmol), and TlO₂CPhCy (556 mg, 1.36 mmol) as described for **15**. Recrystallization from Et₂O/pentane at -30 °C provided **16** as colorless needles (737 mg, 71%). Recrystallization from a highly dilute pentane solution over several days at room temperature yielded colorless blocks which appeared suitable for X-ray crystallography. IR (KBr) 3127, 2959, 2872, 1734, 1693, 1612, 1526, 1456, 1371, 1246, 1187, 1109, 948, 828, 763, 697, 660, 574 cm⁻¹. Anal. Calcd for C₈₄H₁₁₆N₆O₁₂Fe₂: C, 66.66; H, 7.72; N, 5.55. Found: C, 65.13; H, 7.81; N, 5.14.

Collection and Reduction of X-ray Data

All crystals were mounted on the tips of quartz fibers with Paratone-N (Exxon), cooled to low temperature (~ -85 °C), and placed on Siemens CCD X-ray diffraction system controlled by a Pentium-based PC running the SMART software

package.³³ The general procedures for data collection and reduction follow those reported previously.³⁴ All structures were solved by use of the direct methods programs SIR-92³⁵ or XS, part of the TEXSAN³⁶ and SHELXTL³⁷ program packages, respectively. Structure refinements were carried out with XL, part of the SHELXTL program package.³⁷ All remaining non-hydrogen atoms were located and their positions refined by a series of least-squares cycles and Fourier syntheses. Hydrogen atoms were assigned idealized positions and given a thermal parameter 1.2 times the thermal parameter of the carbon atom to which each was attached. Empirical absorption corrections were calculated and applied for each structure using SADABS, part of the SHELXTL program package.³⁷

The structure of **7** contains a lattice benzene molecule which was refined at partial occupancy. Two of the three lattice benzene molecules in the structure of **13** have large thermal parameters. The structure of **12** contains a lattice THF molecule disordered over two positions, where an inversion center passes through the center of a carbon-carbon bond. It was refined as a cyclopentane molecule with one of the carbon atoms at full occupancy, and the occupancy of the other three carbon atoms was distributed over two positions per atom and refined. The butyl group of one of the Bu-Im ligands in the structure of **16** is disordered. The occupancy of the carbon atom β to the imidazole nitrogen was distributed over two positions and refined. The other carbon atoms of the butyl group were refined at full occupancy.

Pertinent crystallographic information for each complex including refinement residuals is available in Table 3.2. Selected bond distances and angles, as well as atomic coordinates and equivalent isotropic displacement parameters, are provided Tables 3.3 and 3.4-3.8, respectively.

Physical Measurements. NMR spectra were recorded on a Varian Unity-300 NMR spectrometer. ¹H NMR chemical shifts are reported versus tetramethylsilane and referenced to the residual solvent peak. FTIR spectra were recorded on a BioRad

FTS-135 FTIR spectrometer. Room-temperature UV-vis spectra were recorded on a Cary 1E spectrophotometer. Low-temperature spectra were recorded on a HP8452A diode array spectrophotometer using a custom manufactured immersion dewar, equipped with a 3 mL cell (1 cm pathlength) with quartz windows connected to a 14/20 female joint via a 10 cm long glass tube. A temperature of $-77\text{ }^{\circ}\text{C}$ was maintained with a dry ice/acetone bath and monitored with a Sensortek Model BAT-12 thermocouple thermometer. Conductivity measurements were carried out in THF or CH_2Cl_2 with a Fisher Scientific conductivity bridge, model 9-326, outfitted with a platinum black electrode. Manometric experiments were carried out according to literature procedure,³⁸ using Vaska's complex or $[\text{Fe}(\text{Tp}^{3,5}\text{-iPr}_2)_2(\text{O}_2\text{CCH}_2\text{Ph})]^{20}$ as authentic standards, which form 1:1 and 2:1 complex:dioxygen adducts, respectively. Elemental analyses were performed by Microlytics, South Deerfield, MA.

EPR Spectroscopy. Spectra were recorded at 4.5 K on a Bruker Model 300 ESP X-band spectrometer operating at 9.47 GHz. Liquid helium temperatures were maintained with an Oxford Instruments EPR 900 cryostat. For all measurements 1 mM frozen solutions were prepared in 2-methyltetrahydrofuran, a solvent in which the samples glassed well.

Resonance Raman Spectroscopy. Raman data were acquired by using a Coherent Innova 90 argon laser with an excitation wavelength of 647.1 nm and 65 mW of power. A 0.6-m single monochromator (1200 grooves/nm grating), with an entrance slit of 100 μm , and a liquid nitrogen cooled-CCD detector (Princeton Instruments, Inc.) were used in a standard backscattering configuration. A holographic notch filter (Kaiser Optical Systems) was used to attenuate Rayleigh scattering. Spectra of all samples were collected in toluene or CH_2Cl_2 solution at $-77\text{ }^{\circ}\text{C}$ with the same custom-manufactured dewar used to acquire low-temperature UV-vis spectra. Solute concentrations were made as high as possible depending on

the solubility of the reduced sample, ~20 mM in the best cases, to ensure an optimal signal to noise ratio. A total of 1000 scans each with a three second exposure time were collected for each sample. Raman shifts were calibrated with toluene or CH_2Cl_2 as an internal standard. The data were processed by using CSMA software (Princeton Instruments, Inc. Version 2.4A) on a Gateway 2000 computer, and the resulting ASCII files were processed with Kaleidagraph (Abelbeck Software). Spectra are displayed in Figures 3.13-3.15, and O–O and Fe–O stretching frequencies are listed in Table 3.11.

Mössbauer Spectroscopy. Solid samples were prepared by suspending ~0.04 mol of powdered material in Apiezon N grease, and then packing the mixture into a nylon sample holder. Frozen solution samples of diferrous complexes **13** or **15** were prepared in THF in a drybox. In each case 1 mL of the ~40 mM solution was syringed into a nylon sample holder, that was then sealed with Apiezon N grease, brought out of the drybox, and rapidly cooled to 77 K. Peroxo sample **13**-O₂ was prepared in a round bottom flask at -77 °C by exposing 1 mL of a THF solution of **13** (40 mM) to excess O₂ (1 atm) for 2 h. The sample was quickly transferred (< 5 s) to a nylon sample holder, immersed in liquid nitrogen, by means of a glass syringe equipped with a 4 cm stainless steel needle, and precooled to -77 °C. All data were collected at 77 K with a ⁵⁷Co source in a Rh matrix at room temperature and fit to Lorentzian line shapes. Spectra are illustrated in Figures 3.16-3.18, and parameters derived from fits are listed in Table 3.12.

UV-Vis Kinetics. Experiments were carried out by using the custom dewar mentioned above. Reduced samples in freshly distilled THF solution, typically 0.5 mM, were loaded in a drybox and the dewar was fitted with a rubber septum. The apparatus was brought out, placed under a positive N₂ pressure, and cooled to -77 °C with a dry ice acetone bath. The samples were subjected to an O₂ purge at atmospheric pressure for 5.0 min at a flow rate of 10 standard cubic centimeters per

minute (SCCM), maintained with a Matheson Dyna-Blender Model 8280 oxygen/nitrogen constant flow mixing system. Purging for this time length and at this flow rate resulted in highly reproducible rate constants, thus assuring that the entire sample solution and vessel headspace were completely purged with the desired gas mixture. For dioxygen dependent kinetic studies, the mole fraction of O₂ was controlled by diluting pure O₂ with dinitrogen, while retaining a total flow rate of 10 SCCM. Oxygen concentrations were calculated using eq 4, where X = mole fraction of O₂, L = Ostwald coefficient (0.245 for THF), P_(g) = partial pressure, and V^o_(l) = molar volume.³⁹ All experiments were carried out under pseudo -first -order oxygen concentrations, ranging from 3.07-15.4 mM, while keeping the initial

$$X = \left(\frac{RT}{P_{(g)}LV^o_{(l)}} + 1 \right)^{-1} \quad (4)$$

concentration of diferrous complex constant for each run. Scans were acquired at 600 nm and points were taken every 2-10 sec, depending on the rate at which the reaction proceeded. Reactions were followed to at least four half lives in all cases. Data were analyzed with Kaleidagraph (Abelbeck Software) and fit to model-dependent equations by using nonlinear least squares regression. In all cases the data were fit unambiguously to a first order exponential buildup, defined in eq 5, where A_t is the absorbance at time t, ΔA is the change in absorbance during the reaction,

$$A_t = A_\infty + (\Delta A)(1 - \exp(-k_{obs}t)) \quad (5)$$

$$\text{rate} = k[\text{Fe}_2^{2+}][\text{O}_2] \quad (6)$$

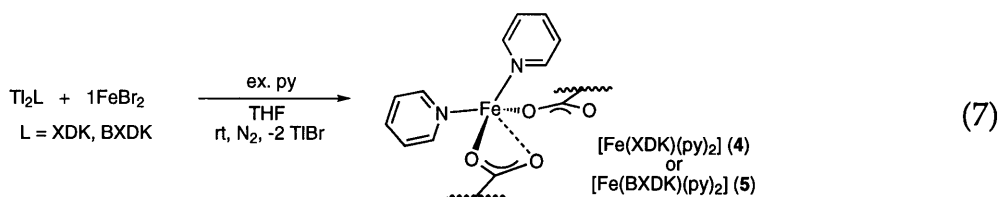
A_∞ is the absorbance at infinite time, and k_{obs} (≡ k_ψ) is the observed psuedo first order rate constant. All plots of ln(k_{obs}) vs ln([O₂]) were linear with a slope close to 1.0, implying that an overall second order rate law applies, eq 6. Second order rate constants, tabulated in Table 3.13, were derived from the slopes of k_{obs} vs. [O₂] plots.

Standard errors in these rates are based on linear regression analyses of the slopes, and are reported at the 95% confidence level. Plots of A_{600} vs. time, k_{ψ} vs. $[O_2]$, and $\ln(k_{\psi})$ vs. $\ln([O_2])$ for complexes **6**, **7**, **13**, and **14** are illustrated in Figures 3.19-3.22.

Results and Discussion

Preparation and Characterization of $[Fe(XDK)(py)_2]$ (**4**) and $[Fe(BXDK)(py)_2]$ (**5**).

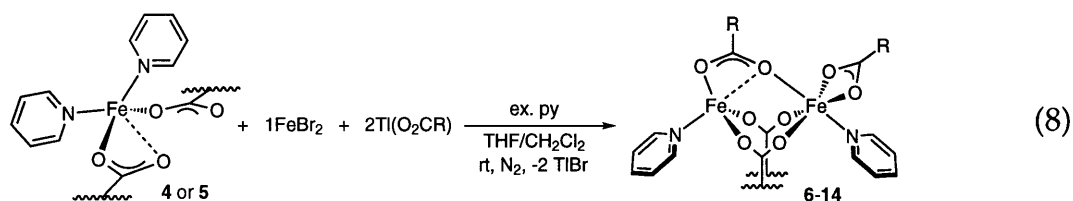
In order to develop an efficient route to a family of diiron(II) complexes incorporating the XDK ligand system and ancillary carboxylates of variable steric properties, the synthesis of pure mononuclear precursors in large quantities was desired. Treatment of $Tl_2(XDK)$ or $Tl_2(BXDK)$ with 1 equiv of iron(II) bromide and excess pyridine provided yellow bis(pyridine) adducts **4** and **5**, respectively, in multigram quantities and high yield (eq 7). An X-ray structural analysis on the XDK



derivative revealed the iron atom to be coordinated by three XDK oxygen and two pyridine nitrogen atoms.⁴⁰ The structure is essentially identical to that determined for the Zn(II) analog,⁴¹ with one long XDK Fe–O interaction at 2.326(5) Å and the other two at an average distance of 2.080(3) Å. In contrast, the analogous reaction with 1-methyl- or 1-butylimidazole led to a mixture of intractable products, even when exactly two equivalents were used.

Preparation and Characterization of Dinuclear $[Fe_2(BXDK)(\mu-O_2Ct-Bu)(O_2Ct-Bu)(py)_2]$ (6**), $[Fe_2(XDK)(\mu-O_2CPhCy)(O_2CPhCy)(py)_2]$ (**7**), $[Fe_2(XDK)(\mu-O_2CAr)(O_2CAr)(py)_2]$ (**8**), $[Fe_2(XDK)(\mu-O_2CAr)(O_2CAr)(3-Fpy)_2]$ (**9**), $[Fe_2(BXDK)(\mu-O_2Ci-Pr)(O_2Ci-Pr)(py)_2]$ (**10**), $[Fe_2(BXDK)(\mu-O_2CH_2t-Bu)(O_2CH_2t-Bu)(py)_2]$ (**11**),**

[Fe₂(BXDK)(μ-O₂CPh)(O₂CPh)(py)₂] (12), [Fe₂(BXDK)(μ-O₂CPhCy)(O₂CPhCy)(py)₂] (13), [Fe₂(BXDK)(μ-O₂CAR)(O₂CAR)(py)₂] (14), [Fe₂(XDK)(μ-O₂CPhCy)(O₂CPhCy)(Me-Im)₂] (15), and [Fe₂(PXDK)(μ-O₂CPhCy)(O₂CPhCy)(Bu-Im)₂] (16). The diferrous bis(pyridine) complexes 7-14 were conveniently prepared from 4 or 5 and “[Fe(O₂CR)(py)_n]”, the latter being generated in situ from iron(II) bromide, the



appropriate ancillary carboxylate, and excess pyridine (eq 8). The 3-fluoropyridine derivative 9 and imidazole adducts 15-16 were prepared in one-pot reactions from the thallium carboxylic acid reagents, two equiv of iron(II) bromide, and two equiv of 3-fluoropyridine or 1-alkylimidazole. In the preparation of 15 and 16, removal of the TlBr precipitate was aided by allowing the reaction mixtures to stand overnight prior to filtration through Celite. Additional extractions of the resulting Celite/TlBr filter cake were required to recover substantial quantities of additional product. All complexes were obtained in high yield and purity following recrystallization at room temperature. Despite repeated attempts in each case, elemental analysis samples of 4, 7, 8 and 16 deviated 1-2% from calculated carbon values. It is unclear whether these complexes have poor combustion properties and/or they contain minor impurities, but other closely related derivatives have analyzed correctly. Schematic representations of all complexes 4-16 are provided in Scheme 3.1.

The IR spectra of complexes 7-16 displayed a new C–O stretch at 1605-1615 cm⁻¹, and another centered at 1693 cm⁻¹ was more intense and broadened compared to the dithallium(I) and/or mononuclear iron(II) precursors. Both of these differences are attributed to the two additional carboxylate ligands in the products.

The UV-vis spectra of the pyridine adducts **5-14** all exhibited an absorbance at 350-360 nm ($\epsilon = 500-1000 \text{ cm}^{-1}$), tentatively assigned as a metal-to-ligand charge transfer, which was absent in the colorless 1-alkylimidazole derivatives. Complexes **4-16** are all non-electrolytes, so most are soluble in solvents as non-polar as THF. Where aliphatic groups have been incorporated into the XDK and 1-alkylimidazole ligands, for example **16**, complexes are readily soluble in diethyl ether and cyclopentane.

Because **6, 7, 12-13**, and **16** represent the spectrum of steric hindrance and electronic differences within this series of complexes, X-ray structures were acquired to ascertain how each ligand component might influence the iron coordination geometries and dioxygen reactivity. ORTEP and space-filling diagrams are displayed in Figures 3.3-3.10, and selected bond distances and angles are listed in Table 2.3. Each structure consists of a four- or five-coordinate iron atom (Fe1) ligated by two *syn-syn* bidentate bridging XDK oxygen atoms and one or two monodentate bridging ancillary carboxylate oxygen atoms.⁴² The number of latter donor atoms depends on the choice of N-donor ligand and the steric properties of the XDK and ancillary carboxylate substituents. The Fe2 atoms in **6** and **12** are best described as distorted trigonal bipyramidal, whereas those in **7, 13**, and **16** are distorted tetrahedral. The other iron atom (Fe1) has a coordinatively saturated octahedral geometry in all cases, and it is ligated by two *syn-syn* bidentate bridging XDK carboxylate oxygen atoms, two symmetric chelating ancillary carboxylate atoms, and a N-donor nitrogen atom.

The most significant difference in these structures is the orientation of the bridging ancillary carboxylate ligand relative to the rest of the complex framework. Five metrical parameters change significantly within the series: Fe2-O402, Fe2-O401, Fe1-O402-Fe2, Fe1-O402-C401, Fe2-O401-C401, and Fe2-O402-C401. These changes are all related to the tilt angle, τ , of this monodentate bridging carboxylate ligand toward the center of the complex, as defined in Figure 3.11.⁴² Within the

subset of pyridine complexes **6**, **7**, and **12-13**, a repulsive interaction between the two ancillary carboxylate substituents decreases τ . In complexes **12** and **13**, τ is also affected in the same sense by a steric interaction between the bridging ancillary carboxylate and the XDK benzyl substituents. As the Fe2–O402 distance (**B**) lengthens the Fe2–O401 distance (**D**) shortens, resulting in no change in the Fe1–O402 distance (**A**) across the series. Similarly, an increase in the Fe2–O401–C401 angle (γ) is accompanied by a decrease in the Fe1–O402–Fe2 (Θ), Fe1–O402–C401 (α), and Fe2–O402–C401 (β) angles. Based on these parameters, the order of increasing steric repulsion between the carboxylate substituents for this subset of pyridine complexes is: **12** < **6** < **7** < **13**, corresponding to $\Delta\tau = -7^\circ$, proceeding from **12** \rightarrow **13**. By contrast, τ is much smaller for the butyl-imidazole adduct **16** compared to all the pyridine adducts, apparently due to the more basic character of the 1-alkylimidazole donor compared to pyridine which increases the electron density at Fe2, thereby disrupting the Fe2–O402 interaction entirely. Hence, for **16** these steric and electronic factors have the combined effect of nearly inducing a complete carboxylate shift⁴² from the monodentate bridging observed for the pyridine adducts to *syn syn* bidentate bridging.

Reactions of the Diferrous Complexes Toward Dioxygen. UV-Vis and Manometry. As mentioned in the introduction, previous studies revealed the presence of a short-lived intermediate generated when $[\text{Fe}_2(\text{PXDK})(\mu\text{-O}_2\text{Ctert-Bu})(\text{O}_2\text{Ctert-Bu})(\text{Me-Im})_2]$ was exposed to excess O_2 at -77°C in THF solution. As an initial approach toward stabilizing this species, we implemented the more sterically demanding BXDK ligand, while holding the other steric properties constant, and changed the N-donor ligand to pyridine. Space-filling diagrams of the previously reported complex and **6** are displayed in Figure 3.4. From these representations, it is apparent that the BXDK benzyl substituents proximal to its carboxylate oxygen donor atoms shroud the iron coordination sites to a greater extent than do PXDK propyl

groups. Furthermore, the benzyl substituents appear to enforce a single approach for O₂ to the unsaturated metal center along the Fe–Fe vector.

Exposure of **6** to O₂ under identical conditions to those previously reported resulted in a much slower color change to deep midnight blue over the course of 2-3 h. The buildup of this species was monitored by UV-vis spectroscopy, revealing a broad absorption centered at ~580 nm ($\epsilon \sim 1200 \text{ M}^{-1}\text{cm}^{-1}$, Figure 3.12A). This feature is characteristic of an iron(III)-peroxo ligand-to-metal charge transfer band,^{1,5} and it immediately suggested that a family of peroxo complexes having steric and electronic properties similar to **6** could be accessed. The oxygenation is irreversible, since application of high vacuum/Ar purge cycles to the solution at -77 °C resulted in no diminution of the charge transfer band. Warming above -65 °C under excess O₂ or Ar, or under high vacuum, caused rapid peroxo decomposition within five minutes, as judged by a color change to light brown. A similar decomposition was noted if the peroxo solution is allowed to stand at -77 °C for 12-24 h.

The other diiron(II) tetracarboxylate complexes were then screened for their ability to form stable peroxo complexes, the results of which are summarized in Table 3.9. The O₂ reactions either resulted in rapid decomposition to form room-temperature stable Fe(III) products, or afforded an intermediate very similar to that observed for **6**. For BXDK derivatives with pyridine, ancillary carboxylate ligands smaller than pivolate (**10-12**) reacted with O₂ at a similar rate, but none of these reactions resulted in the buildup of the 580 nm charge-transfer band. The less sterically encumbering XDK ligand formed stable peroxo adducts when significantly more hindered ancillary carboxylates were implemented, such as 1-phenylcyclohexyl- (PhCy) or 2,4,6-triisopropyl (Ar) carboxylic acid (**7-8**, Figure 3.12B). Similarly, these hindered carboxylates afforded stable peroxo adducts with 3-fluoropyridine or 1-alkylimidazole donors (**9**, **15-16**, Figure 3.12C). The rate of peroxo formation is considerably faster for the 1-alkylimidazole complexes compared to all

the pyridine analogs, however, with 15-16 reacting with O₂ to completion within seconds versus 0.25-2 h for 6-14, as judged by UV-vis spectroscopy. The energy and intensity of the peroxo-to-iron(III) charge transfer band in these derivatives were the same as for the pyridine analogs. This result is not surprising because other diiron(III) peroxo complexes with widely varying ligand sets possess essentially an identical transition.^{1,5} Furthermore, equivalent irreversible O₂ binding and thermal stability behavior was noted for all peroxo derivatives irrespective of their steric and electronic properties.

Oxygen uptake experiments were carried out on pyridine adduct 13 in CH₂Cl₂, and 1-butylimidazole adduct 16 in THF and Et₂O (Table 3.10). Vaska's complex and [FeTp^{3,5-iPr2}(O₂CCH₂Ph)]²⁰ were used as authentic O₂ uptake standards in CH₂Cl₂ and the ethereal solvents, respectively. Complexes 13 and 16 consumed 1.0 ± 0.1 equivalents of dioxygen, consistent with a discrete diiron(III) peroxide formulation for each. When the peroxo adducts were allowed to decay by warming to room temperature, additional O₂ consumption was observed for those manometric experiments carried out in CH₂Cl₂ or THF, whereas no further uptake was noted for the diethyl ether trials. All of this decay behavior is in stark contrast to that noted for another diiron(III) peroxo system,²⁷ where 0.5 equivalents of O₂ was *released* upon peroxo decay, and suggests that the peroxide ligand is retained in the decomposition products and/or ligand or solvent oxidation is occurring concomitant with peroxo decay. A detailed analysis of this chemistry will be discussed elsewhere.²⁸

The oxygen adducts exhibited the greatest stability toward decomposition in the least polar solvents, such as THF and toluene. By contrast, dichloromethane could be utilized with the more sterically demanding pyridine derivatives 7-8 and 13-14, but the peroxo adducts derived from less hindered 6 or the 1-alkylimidazole derivatives 15-16 were observed to decompose in this solvent within seconds. The higher dielectric constant⁴³ of CH₂Cl₂ (9.08) compared to THF (7.58) and toluene

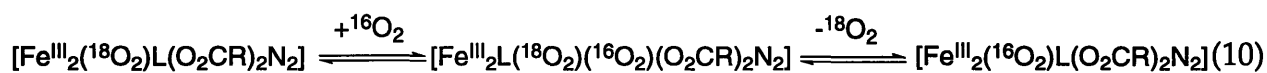
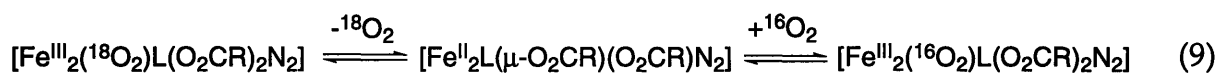
(2.379) may lead to fluxional ligand exchange processes in the chlorinated solvent, possibly involving a carboxylate shift⁴² of the ancillary donors, which could result in dissociation of a carboxylate oxygen ligand. The preference for mondentate over chelating carboxylate ligation is accentuated in increasingly polar media,^{41,44} and such a process here could compromise the steric pocket surrounding the peroxide, leading to bimolecular decay. The highly sterically demanding R substituents in **7-9** and **13-14** may shroud the peroxide sufficiently to prevent decay by this mechanism. Rapid degradation of the peroxos derived from complexes **15-16** may be due to the greater basicity of the 1-alkylimidazole ligand compared to pyridine, which may render the carboxylate donors even more labile. Alternatively, decay of the peroxo adducts may occur by direct reaction with CH₂Cl₂, since 1,2-dichloroethane is detected by GC-MS in the solvent mixture upon warming.²⁸ Taken together, this survey of steric, electronic, and solvent polarity studies demonstrates that oxygen adducts can be stabilized with this ligand system provided the carboxylate substituents form a sufficiently hindered array about the peroxide ligand.

EPR and ¹H NMR Studies. The peroxo adducts are EPR silent at 4.5 K, a feature which is consistent with an antiferromagnetically coupled, S = 0 ground state. Similar to other diiron(III) peroxides, including the sMMO H_{peroxo} intermediate,¹⁵ this coupling is most likely mediated by a bridging peroxide.^{45,46} A ¹H NMR spectrum for the peroxo adducts formed in this study was not observed at -80 °C, however, suggesting low lying paramagnetic excited states are accessed thermally at higher temperatures, inducing fast relaxation of the ligand protons. By contrast, a paramagnetically shifted but reasonably sharp ¹H NMR spectrum was observed for a diiron (III) peroxo complex with a hindered hydrotris(pyrazolyl)borate ligand.⁴⁵

Resonance Raman Studies of the Peroxo Adducts. Raman spectra were acquired for peroxo adducts derived from complexes **6-8**, **13-14**, and **16** in fluid

solution at -77 °C. The results of these experiments are summarized in Table 3.11, and the spectra acquired for 16·O₂ are displayed in Figures 3.13-3.14. The pyridine and 1-butylimidazole derivatives all give rise to a ν(¹⁶O–¹⁶O) band at 864 cm⁻¹ in toluene solution. When ¹⁸O₂ was used to prepare 16·O₂ this band shifts to 818 cm⁻¹, in good agreement with the theoretically predicted shift of 50 cm⁻¹ for a diatomic O–O harmonic oscillator. The peak shifts slightly to 861 cm⁻¹ for 13·¹⁶O₂ in CH₂Cl₂ solution. A ν(Fe–O) band was detected at 484 cm⁻¹ for 13·O₂ in CH₂Cl₂, but a negligible shift was noted for this feature upon ¹⁸O₂ substitution. The band was obscured entirely in toluene solution due to the intense solvent background peaks in this spectral region. The observed ν(O–O) frequencies of 861–864 cm⁻¹ are typical of diiron(μ-1,2-peroxo) complexes. Although these values are 15–40 cm⁻¹ lower than other complexes with this ligating motif,^{1,5} they are 50–60 cm⁻¹ higher in energy than those reported for mononuclear iron(III) η²-peroxo adducts.¹ We therefore tentatively assign μ-1,2-peroxo coordination mode for 13·O₂ and 16·O₂.

Raman spectroscopy was also used to measure the exchange of peroxide with free O₂. Such an exchange process could either be a dissociative (eq 9), implying



reversible O₂ binding, or associative, mediated by a bis(O₂) intermediate (eq 10). The former mechanism is unlikely because O₂ is not liberated when a solution of the peroxo adduct is placed under a dynamic vacuum. A sample of 16·¹⁸O₂ was prepared by exposing a 20 mM solution of 16 in toluene to ~0.25 atm of excess ¹⁸O₂ for 1 h, and Raman spectra were recorded prior to and following a vigorous, five-minute ¹⁶O₂ purge. The ν(¹⁶O–¹⁶O) feature appeared in the spectrum immediately following the purge, but not at the expense of the intensity of the ν(¹⁸O–¹⁸O) band. Moreover, the

$\nu(^{16}\text{O}-^{16}\text{O})$ peak continued to grow in intensity when the solution was allowed to stir under 1 atm of $^{16}\text{O}_2$ over two hours, but again the $\nu(^{18}\text{O}-^{18}\text{O})$ band did not diminish. These results suggest that oxygenation of the reduced complex is slow under the concentrated conditions of the Raman experiment, and that peroxide does not exchange with free O_2 by any mechanism, at least over several hours.

We attempted to obtain structural information about the orientation of peroxide binding by carrying out a labeling experiment with a 1:2:1 statistical mixture of $^{18}\text{O}_2$, $^{16}\text{O}^{18}\text{O}$, and $^{16}\text{O}_2$ (Figure 3.15). If the peroxide oxygen atoms are distributed asymmetrically about the Fe(III) ions, then two $^{16}\text{O}^{18}\text{O}$ peroxide peaks should be observed, with a 1:1:1:1 relative intensity ratio for the $^{18}\text{O}_2$, $^{16}\text{O}^{18}\text{O}$, $^{18}\text{O}^{16}\text{O}$, and $^{16}\text{O}_2$ isotopomers. Alternatively, equivalent $^{16}\text{O}^{18}\text{O}$ and $^{18}\text{O}^{16}\text{O}$ peroxide stretching frequencies would give rise to three peaks in a 1:2:1 ratio. Interpretation of resulting Raman spectrum proved to be difficult, however, because of the difficulty of resolving the $^{16}\text{O}^{18}\text{O}$ peroxide peak(s) and the fact that their intensity relative to the $^{18}\text{O}_2$ and $^{16}\text{O}_2$ bands were obscured by a coincidental toluene peak, even after considerable effort was expended to subtract the solvent background.

Mössbauer Spectroscopy. Zero-field Mössbauer studies were carried out to gain additional information concerning the iron environments in the reduced and peroxo complexes. The results of these experiments are summarized in Table 3.12, and spectra with overlaid fits are illustrated in Figures 3.16-3.18. Spectra were recorded for **13** in the solid state, and for **13** and **15** in frozen THF solution. Each spectrum consists of two overlapping quadrupole doublets of equal intensity, indicating inequivalent iron sites. Pairing of the four peaks derived from a fitting protocol is ambiguous, so both combinations for each complex are listed in Table 3.12. Consistent with our previous assignments in similar complexes,²⁵ we tentatively attribute the doublet with the higher quadrupole splitting parameter (ΔE_Q) to the four-coordinate iron(II) center, since it has a more asymmetric

coordination environment compared to the octahedral metal ion. The iron(II) isomer shifts (δ) and ΔE_Q values for **13** are slightly different in the solid state and solution, in contrast to the previous study where a less hindered analog exhibited the nearly identical parameters in the two different phases.²⁵ In the present system it is neither known how the solid and solution structures differ nor what magnitude of change would be required to yield slightly altered Mössbauer spectra. Nevertheless, the equal integrated intensity of the two quadrupole doublets is consistent with the dinuclear structure remaining intact in solution.

A Mössbauer spectrum of **13**·O₂ in THF is displayed in Figure 3.18. A modest amount (20%) of the diiron(II) starting material is apparent in this sample, as judged by the identical isomer shift of the most positive feature compared to that observed for **13** (Figure 3.18, Top). This result is consistent with the Raman experiment mentioned above, where it was determined that oxygenation of extremely concentrated diiron(II) samples (20 mM) is slow relative to the rate in more dilute solutions, such as that used for the UV-vis protocol. It is difficult to know a priori how long to permit the reduced complexes to react with O₂ before quenching the sample in liquid nitrogen. Given the thermal instability of the peroxo complexes, which decompose significantly within 12-24 h at -77 °C, and the fact that the spectroscopic properties of the reduced complexes are well known, we chose not to allow any of these concentrated reactions to proceed beyond ~2 h. The bottom portion of Figure 3.18 displays the experimental data with the diiron(II) component subtracted out, together with a fit of the peroxo spectrum.

Like the iron(II) complexes, the peroxo consists of two overlapping quadrupole doublets of equal integrated intensity. Both possible pairings of the four simulated peaks are listed in Table 3.12, along with the Mössbauer parameters for oxyhemerythrin⁴⁷ and MMO-H_{peroxo}.¹⁵ The isomer shifts and ΔE_Q values are both in the range typical of high spin Fe(III),⁴⁸ and these parameters bear considerable

resemblance to those determined for the phenoxo-bridged peroxo complex in Table 3.1.²¹ These results indicate either that the peroxo sample is composed of one dinuclear complex with inequivalent iron centers, or of two different dinuclear peroxo complexes with equivalent iron centers within the same molecule. Since a 1:1 ratio of two different peroxo isomers is highly improbable, we conclude the former alternative best describes the makeup of $13 \cdot O_2$.

Kinetic Studies of the Reaction of the Diferrous Complexes With O_2 and a Proposed Mechanism for Peroxo Formation. The UV-vis, manometric, EPR, resonance Raman, and Mössbauer spectroscopic data collectively point to the formation of a discrete (μ -1,2-peroxo) diiron(III) complex with inequivalent metal centers. With these results in hand, we decided to investigate the mechanism of peroxo formation by time-resolved UV-vis kinetic studies to determine the reaction order with respect to the diferrous complex and O_2 . Moreover, X-ray structural investigations demonstrated that the coordination number of one of the starting diiron(II) centers could be modulated as a function of intramolecular steric repulsions (*vide supra*), and we were interested to determine whether this effect might play a role in the kinetics of oxygenation.

Kinetic runs were carried out at $-77^\circ C$ on pyridine adducts **6**, **7**, **13**, and **14** using a custom-made immersion dewar. All experiments were performed under pseudo-first-order conditions, with the iron complex as the limiting reagent. Dioxygen concentrations were varied over a range of 3.1-15.4 mM. The buildup of the peroxo charge transfer band was monitored at 600 nm as a function of time (Figures 3.19-3.22, Top). These plots could be fit to a first order exponential buildup for each complex. Plots of $\ln(k_{\psi})$ vs. the $\ln[O_2]$ afforded straight lines with slopes near 1.0, indicating that the oxygenation reaction is first order in this reagent (Figures 3.19-3.22, Bottom). Second order rate constants were obtained for the four iron complexes from the slopes derived from plots of k_{ψ} vs. the $[O_2]$ (Figures 3.19-

3.22, Middle). These rate constants are provided in Table 3.13 along with metrical data from the crystal structures of **6**, **7**, and **13** describing the orientation of each bridging ancillary carboxylate. Activation parameters could not be obtained because the peroxo adducts decompose quite rapidly above $-65\text{ }^{\circ}\text{C}$, thus limiting the temperature for acquisition to only a 15° range.

The first-order dependence in each reagent indicates that the rate limiting step in these oxygenation reactions is a bimolecular collision between the diiron(II) complex and dioxygen. Within the series, the rate constants increase modestly over a four-fold range as the steric demands of the carboxylate substituents are enhanced. This kinetic trend correlates well with lengthening of the Fe₂-O₄₀₂ bond and decrease in τ as a function of the same steric parameters and may indicate that, in the transition state, cleavage of this bond is required to open a coordination site for O₂ binding to Fe₂. This event corresponds to a rate limiting carboxylate shift from monodentate bridging to *syn syn* bidentate bridging. Such structural/kinetic comparisons must be viewed with caution, however, since the Mössbauer studies on the diiron(II) complexes showed that the solid and solution structures may not be identical. Nevertheless, the trend does suggest that bond cleavage is involved in the rate limiting step and argues against a mechanism where passage of the O₂ molecule to an iron center is impeded by the sterically encumbering carboxylate substituents. The latter mechanism was observed for the oxygenation of a series of iron(II) hydrotris(pyrazolyl)borate-carboxylate complexes, where exceedingly bulky carboxylate substituents shut down the reaction entirely.⁴⁵ By contrast, space-filling models of **6-16** show that the pathway to the four- or five-coordinate iron center is unobstructed, regardless of the carboxylate substituents (Figures 3.4 and 3.6, for example).

The 1-alkylimidazole adducts **15** and **16** react to completion with O₂ in the time of mixing of the two reagents ($< 1\text{ s}$), much more rapidly than the oxygenation

rates observed for the pyridine complexes. Neither could be studied by these conventional kinetics methods. The less hindered analog $[\text{Fe}_2(\text{PXDK})(\mu\text{-O}_2\text{Ctert-Bu})(\text{O}_2\text{Ctert-Bu})(\text{Me-Im})_2]$, was previously analyzed by stopped-flow UV-vis spectroscopy under very similar experimental conditions: $[\text{Fe}_2^{2+}] = 0.8 \text{ mM}$ (after mixing) in THF, $T = -76 \text{ }^\circ\text{C}$, excess O_2 .²⁵ These studies revealed a pseudo-first-order rate constant of 300 s^{-1} , a value $> 10^5$ faster than the pseudo-first-order rate constants observed for the pyridine adducts. The dramatically enhanced rates could be due in part to the minimal bonding interaction between the Fe_2 and O_4O_2 in this complex. Because changes in this parameter have only a modest effect on the rate constants, however, we attribute most of the rate difference instead to the greater basicity of the 1-alkylimidazole ligand compared with pyridine. This electronic factor should lead to a significantly more negative midpoint potential for the diiron(II)/diron(III) couple with 1-alkylimidazole, thereby enhancing the thermodynamic driving force for the O_2 reaction, and consequently accelerating the rate.

A mechanism for peroxo formation is presented in Scheme 3.2. Although peroxo buildup exhibits clean first order dependence in each reaction component, the kinetics do not reveal if the rate limiting event leads to peroxo formation directly. Alternatively, very fast electron transfer and/or ligand rearrangement steps may occur *after* O_2 binding, thereby preceding final peroxo assembly. Consequently, if the final peroxo formation event is beyond the rate limiting step, then prior intermediates could involve a diiron(II)- O_2 adduct, an Fe(II)Fe(III) superoxide complex, and/or several plausible isomers based on the arrangement of the carboxylate and nitrogen donors. Two likely possibilities are structures **a** and **b** in Scheme 3.2. For the final structure, the spectroscopic data are consistent with a bridged peroxo arrangement with inequivalent iron sites. To accommodate the latter feature, the mirror plane and rotational symmetry of the diiron-XDK framework must be removed. Structures **c-e** incorporate these properties through

the orientation of the peroxide (c) or the other ligands (d and e). We consider these or closely related isomers as viable candidates for the structures of the peroxo complexes presented here.

Conclusions

A family of diferric peroxo-bridged complexes has been prepared which matches exactly the combination of carboxylate and imidazole donors of the H_{peroxo} intermediate in sMMO. A variety of methods including UV-Vis, EPR, Resonance Raman, and Mössbauer spectroscopies have been employed to elucidate their structures. These adducts have inequivalent iron coordination environments, a feature which is attributed either to an asymmetric peroxide bridge, a disproportionate arrangement of the ancillary carboxylate and nitrogen donor ligands about each iron center, or a combination of two. Kinetic studies revealed that the rate of peroxo formation is first order in diiron(II) complex and O_2 , implicating a rate-determining bimolecular collision between the reaction components. Moreover, the rate of peroxo formation tracks inversely with the steric demands of the carboxylate substituents, implying that a carboxylate shift is associated with the rate-determining step. The oxygenation rate is affected much more dramatically by the basicity of the N-donor ligand, however, with a difference of $>10^5 \text{ s}^{-1}$ noted for the pseudo-first-order rate constants with 1-alkylimidazole versus pyridine ligation. In sum, these studies have spawned the most accurate compositional models of the H_{peroxo} intermediate reported to date, and their steric and electronic tunability have allowed us to explain many factors which affect their formation, structure, and stability.

Acknowledgement. This work was supported by a grant from the National Science Foundation and AKZO Corp. DDL thanks Ann Valentine and Dietrich

Steinhuebel of the Lippard group at MIT for experimental assistance and many helpful discussions.

References and Notes

- (1) Feig, A. L.; Lippard, S. J. *Chem. Rev.* **1994**, *94*, 759-805.
- (2) Wallar, B. J.; Lipscomb, J. D. *Chem. Rev.* **1996**, *96*, 2625-2657.
- (3) Liu, K. E.; Lippard, S. J. In *Adv. Inorg. Chem.*; A. G. Sykes, Ed.; Academic Press, Inc.: San Diego, CA, 1995; Vol. 42; pp 263-289.
- (4) Valentine, A. M.; Lippard, S. J. *J. Chem. Soc., Dalton Trans.* **1997**, 3925-3931.
- (5) Que, L., Jr. *J. Chem. Soc., Dalton Trans.* **1997**, 3933-3940.
- (6) Rosenzweig, A. C.; Brandstetter, H.; Whittington, D. A.; Nordlund, P.; Lippard, S. J.; Frederick, C. A. *Proteins* **1997**, *29*, 141-152.
- (7) Rosenzweig, A. C.; Nordlund, P.; Takahara, P. M.; Frederick, C. A.; Lippard, S. *J. Chem. Biol.* **1995**, *2*, 409-418.
- (8) Nordlund, P.; Eklund, H. *Current Opinion in Structural Biology* **1995**, *5*, 758-766.
- (9) Kurtz, D. M. J. *JBIC* **1997**, *2*, 159-167.
- (10) Edmundson, D. E.; Huynh, B. H. *Inorg. Chim. Acta* **1996**, *252*, 399-404.
- (11) Burdi, D.; Riggs-Gelasco, P.; Tong, W.; Willems, J.-P.; Lee, H.-I.; Doan, P. E.; Sturgeon, B.; Shu, L.; Que, L., Jr.; Hoffmann, B. M.; Stubbe, J. *Stenbock Symposium Proceedings: Biosynthesis and Function of Metal Clusters For Enzymes* **1997**, *25*, 85-95.
- (12) Sturgeon, B. E.; Burdi, D.; Chen, S.; Huynh, B. H.; Edmondson, D. E.; Stubbe, J. *J. Am. Chem. Soc.* **1997**, *118*, 7551-7557.
- (13) Willems, J.-P.; Lee, H.-I.; Burdi, D.; Doan, P. E.; Stubbe, J. *J. Am. Chem. Soc.* **1997**, *119*, 9816-9824.
- (14) Riggs-Gelasco, P.; Shu, L.; Chen, S.; Burdi, D.; Huynh, B. H.; Que, L., Jr.; Stubbe, J. *J. Am. Chem. Soc.* **1998**, *120*, In Press.
- (15) Liu, K. E.; Valentine, A. M.; Wang, D.; Huynh, B. H.; Edmondson, D. E.; Salifoglou, A.; Lippard, S. J. *J. Am. Chem. Soc.* **1995**, *117*, 10174-10185.

- (16) Lee, S.-K.; Nesheim, J. C.; Lipscomb, J. D. *J. Biol. Chem.* **1993**, *268*, 21569-21577.
- (17) Shu, L.; Nesheim, J. C.; Kauffmann, K.; Munck, E.; Lipscomb, J. D.; Que, L., Jr. *Science* **1997**, *275*, 515-518.
- (18) Bollinger, J. M. J.; Krebs, C.; Vicol, A.; Chen, S.; Ley, B. A.; Edmondson, D. E.; Huynh, B. H. *J. Am. Chem. Soc.* **1998**, *120*, In Press.
- (19) Valentine, A. M.; Tavares, P.; Pereira, A. S.; Davydov, R.; Krebs, C.; Hoffman, B. M.; Edmondson, D. E.; Huynh, B. H.; Lippard, S. J. *J. Am. Chem. Soc.* **1998**, *120*, In Press.
- (20) Kim, K.; Lippard, S. J. *J. Am. Chem. Soc.* **1996**, *118*, 4914-4915.
- (21) Ookubo, T.; Sugimoto, H.; Nagayama, T.; Masuda, H.; Sato, T.; Tanaka, K.; Maeda, Y.; Okawa, H.; Hayashi, Y.; Uehara, A.; Suzuki, M. *J. Am. Chem. Soc.* **1996**, *118*, 701-702.
- (22) Dong, Y.; Yan, S.; V.G. Young, J.; Que, L., Jr. *Angew. Chem. Int. Ed. Engl.* **1996**, *35*, 618-620.
- (23) Dong, Y.; Zang, Y. Z.; Shu, L.; Wilkinson, E. C.; Que, L., Jr. *J. Am. Chem. Soc.* **1997**, *119*, 12683-12684.
- (24) Que, L., Jr.; Dong, Y. *Acc. Chem. Res.* **1996**, *29*, 190-196.
- (25) Herold, S. H.; Lippard, S. J. *J. Am. Chem. Soc.* **1997**, *119*, 145-156.
- (26) Feig, A. L.; Masschelein, A.; Bakac, A.; Lippard, S. J. *J. Am. Chem. Soc.* **1997**, *119*, 334-342.
- (27) Feig, A. L.; Becker, M.; Schindler, S.; von Eldik, R.; Lippard, S. J. *Inorg. Chem.* **1996**, *35*, 2590-2601.
- (28) LeCloux, D. D. Chapter 4.
- (29) Rebek, J., Jr.; Marshall, L.; Wolak, R.; Parris, K.; Killoran, M.; Askew, B.; Nemeth, D.; Islam, N. *J. Am. Chem. Soc.* **1985**, *107*, 7476-7481.
- (30) LeCloux, D. D.; Lippard, S. J. *Inorg. Chem.* **1997**, *36*, 4035-4046.

- (31) Calderon, S. N.; Newman, A. H.; Tortella, F. C. *J. Med. Chem.* **1991**, *34*, 3159-3164.
- (32) Doyle, G.; Erikson, K. A.; Modrick, M.; Ansell, G. *Organometallics* **1982**, *1*, 1613-1618.
- (33) SMART. 4.0; Siemens Industrial Automation, Inc.: Madison, WI, 1994.
- (34) Feig, A. L.; Bautista, M. T.; Lippard, S. J. *Inorg. Chem.* **1996**, *35*, 6892-6898.
- (35) Burla, M. C.; Camalli, M.; Cascarano, G.; Giacovazzo, C.; Polidori, G.; Spagna, R.; Viterbo, D. *J. Appl. Crystallogr.* **1989**, *22*, 389-393.
- (36) TEXSAN: *Single Crystal Structure Analysis Software. 1.6c*; Molecular Structure Corporation: The Woodlands, TX, 1995.
- (37) SHELXTL: *Structure Analysis Program. 5.0*; Siemens Industrial Automation, Inc.: Madison, WI, 1995.
- (38) Mahapatra, S.; Halfen, J. A.; Wilkinson, E. C.; Pan, G.; Wang, X.; Jr., Young, V.G., Jr.; Cramer, C. J.; Que, L., Jr.; Tolman, W. B. *J. Am. Chem. Soc.* **1996**, *118*, 11555-11574.
- (39) *Oxygen and Ozone*; R. Battino, Ed.; Pergamon Press: Oxford, U.K., 1981; Vol. 7.
- (40). X-ray data for 4 crystallized from CH₂Cl₂/Et₂O: P2₁/n, a = 12.3185(2) Å, b = 16.2489(2) Å, c = 20.4920 (1) Å, β = 103.77(1)°, V = 3983.92(8) Å³, Z = 4, T = 188 K, R = 6.77%, wR² = 13.72%. This structure is not described in further detail here because it is nearly identical to that of the Zn(II) analog; see reference 41.
- (41) Tanase, T.; Yun, J. W.; Lippard, S. J. *Inorg. Chem.* **1995**, *34*, 4220-4229.
- (42) Rardin, R. L.; Tolman, W. B.; Lippard, S. J. *New J. Chem.* **1991**, *15*, 417-430.
- (43) *Handbook of Chemistry and Physics, 68th Edition*; R. C. Weast, Ed.; CRC Press, Inc.: Boca Raton, FL, 1988.
- (44) Connolly, J. A.; Kim, J. H.; Banaszcyk, M.; Drouin, M.; Chin, J. *Inorg. Chem.* **1995**, *34*, 1094.

- (45) Kitajima, N.; Tamura, N.; Amagai, H.; Fukui, H.; Moro-oka, Y.; Mizutani, Y.; Kitagawa, T.; Mathur, R.; Heerwegh, K.; Reed, C. A.; Randall, C. R.; Que, L., Jr.; Tatsumi, K. *J. Am. Chem. Soc.* **1994**, *116*, 9071-9085.
- (46) Dong, Y.; Menage, S.; Brennan, B. A.; Elgren, T. E.; Jang, H. G.; Pearce, L. L.; Que, L., Jr. *J. Am. Chem. Soc.* **1993**, *115*, 1851-1859.
- (47) Clark, P. E.; Webb, J. *Biochemistry* **1981**, *20*, 4628-4632.
- (48) Dickson, D. P. E.; Berry, F. J. In *Mössbauer Spectroscopy* Cambridge University Press: Cambridge, U.K., 1986.

Table 3.1. Summary of data acquired for notable RR and sMMO model complexes.

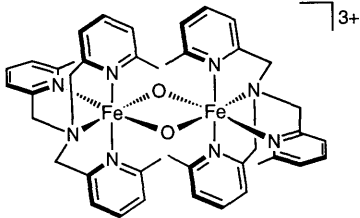
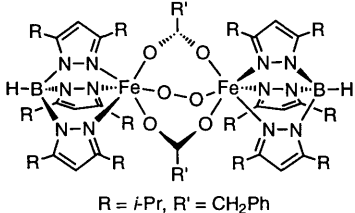
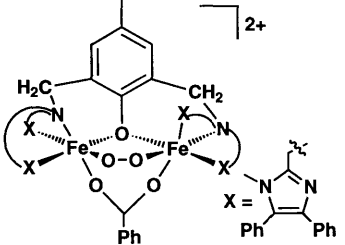
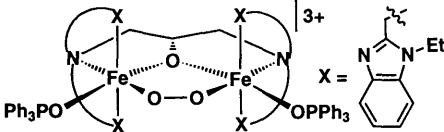
	UV-Vis (λ_{\max} , nm (ϵ , $M^{-1}cm^{-1}$))	Resonance Raman (cm^{-1})		X-ray (\AA)		Mossbauer (mm/s)		ref.
		ν_{O-O}	ν_{Fe-O}	Fe...Fe	O-O	δ	ΔE_Q	
	350(8000)	Not Reported		Not Reported		0.48, 0.08	1.6, 0.5	
 <p>R = <i>i</i>Pr, R' = CH₂Ph</p>	694 (2650)	888	415	4.007(4)	1.406(8)	0.66	1.40	
	500-800 (1700)	Not Detected	Not Detected	3.327(2)	1.426(6)	0.58, 0.65	0.74, 1.70	
	694 (2650)	900	Not Reported	3.462(2)	1.416(7)	Not Reported		

Table 3.2. Summary of X-ray Crystallographic Data.

	6-CH ₂ Cl ₂	7-2.5PhH	12-2CH ₂ Cl ₂ 0.5THF	13-3PhH	16
formula	C ₈₉ H ₉₂ N ₄ O ₁₂ Fe ₂ Cl ₂	C ₈₃ H ₉₃ N ₄ O ₁₂ Fe ₂	C ₉₆ H ₉₀ N ₄ O _{12.5} Fe ₂ Cl ₄	C ₁₂₂ H ₁₂₀ N ₄ O ₁₂ Fe ₂	C ₈₄ H ₁₁₆ N ₆ O ₁₂ Fe ₂
fw	1592.27	1450.38	1753.22	1945.92	1513.53
space group	<i>P</i> 1	<i>P</i> 1	<i>P</i> 1	<i>P</i> 2 ₁ / <i>n</i>	<i>P</i> 1
a, Å	13.1316(2)	14.7993(3)	14.0207(2)	21.1197(11)	13.2699(2)
b, Å	17.1922(1)	15.5674(3)	16.78920(10)	17.9106(9)	14.09470(10)
c, Å	19.0528(1)	18.0666(3)	19.3547(3)	27.8373(14)	23.0607(4)
α, deg	96.764(1)	88.8330(10)	96.1947(9)		97.1800(10)
β, deg	104.042(1)	81.5630(10)	102.8972(8)	103.6300(10)	97.3300(10)
γ, deg	96.712(1)	70.7380(10)	96.2151(9)		106.4840(10)
V, Å ³	4096.30(7)	3885.02(13)	4373.79(10)	10233.4(9)	4042.74(10)
Z	2	2	2	4	2
ρ _{calcd} , g/cm ³	1.291	1.266	1.331	1.263	1.243
T, °C	-85	-85	-85	-85	-85
μ(Mo Kα), mm ⁻¹	0.483	0.437	0.518	0.349	0.422
transmission coeff	0.857-1.000	0.788-1.000	0.858-1.000	0.791-1.000	0.871-1.000
2θ limits, deg	3-46	3-57	3-57	3-57	3-57
total no. of data	17736	22684	25335	40431	25104
no. of unique data	11368	16152	17952	14536	17409
observed data ^a	9221	13216	13809	9120	12887
no. of parameters	982	897	1025	1231	937
R(%) ^b	4.48	4.59	8.81	7.52	5.18
wR ₂ (%) ^c	10.95	12.94	25.18	15.56	12.99
max, min peaks, e/Å ³	0.656, -0.506	1.046, -0.385	1.247, -1.533	0.752, -0.361	1.056, -0.597

^aObservation criterion: $I > 2\sigma(I)$. ^b $R = \sum ||F_O| - |F_C|| / \sum |F_O|$. ^c $wR^2 = \{\sum [w(F_O^2 - F_C^2)^2] / \sum [w(F_O^2)^2]\}^{1/2}$.

Table 3.3. Selected Bond Distances and Angles.^a

		Distances (Å)		Angles (deg)	
6	Fe1...Fe2	3.5110(6)	O101-Fe1-O201	103.67(9)	
	Fe1-O101	2.091(2)	O101-Fe1-O501	163.63(9)	
	Fe1-O201	2.077(2)	O101-Fe1-N501	91.90(10)	
	Fe1-O402	2.172(2)	O402-Fe1-N501	174.12(10)	
	Fe1-O502	2.193(2)	O501-Fe1-O502	60.10(9)	
	Fe1-N501	2.191(3)	O102-Fe2-O202	133.33(9)	
	Fe2-O102	1.992(2)	O102-Fe2-O401	118.34(9)	
	Fe2-O202	2.017(2)	O401-Fe2-N401	105.20(9)	
	Fe2-O401	2.062(2)	Fe1-O402-Fe2	102.13(9)	
	Fe2-N401	2.096(2)	Fe1-O402-C401	170.6(2)	
	Fe2-O402	2.340(2)	Fe2-O401-C401	97.5(2)	
				Fe2-O402-C401	84.5(2)
7	Fe1...Fe2	3.5932(4)	O101-Fe1-O201	104.50(7)	
	Fe1-O101	2.064(2)	O101-Fe1-O501	161.68(7)	
	Fe1-O201	2.095(2)	O101-Fe1-N501	84.89(7)	
	Fe1-O402	2.217(2)	O402-Fe1-N501	170.97(7)	
	Fe1-O502	2.221(2)	O501-Fe1-O502	60.18(6)	
	Fe1-N501	2.182(2)	O102-Fe2-O202	135.53(7)	
	Fe2-O102	2.000(2)	O102-Fe2-O401	104.81(7)	
	Fe2-O202	1.979(2)	O401-Fe2-N401	108.02(6)	
	Fe2-O401	2.050(2)	Fe1-O402-Fe2	100.47(6)	
	Fe2-N401	2.115(2)	Fe1-O402-C401	171.5(2)	
	Fe2...O402	2.454(2)	Fe2-O401-C401	100.15(13)	
				Fe2-O402-C401	81.84(12)
12	Fe1...Fe2	3.5121(8)	O101-Fe1-O201	109.65(13)	
	Fe1-O101	2.091(3)	O101-Fe1-O501	149.96(13)	
	Fe1-O201	2.070(3)	O101-Fe1-N501	90.39(12)	
	Fe1-O402	2.184(3)	O402-Fe1-N501	174.99(14)	
	Fe1-O502	2.104(4)	O501-Fe1-O502	59.43(13)	
	Fe1-N501	2.145(3)	O102-Fe2-O202	123.72(14)	

Table 3.3. (cont ' d) Selected Bond Distances and Angles.^a

	<u>Distances</u>		<u>Angles</u>	
	Fe2-O102	2.006(3)	O102-Fe2-O401	102.5(2)
	Fe2-O202	1.990(3)	O401-Fe2-N401	97.1(2)
	Fe2-O401	2.047(4)	Fe1-O402-Fe2	102.55(12)
	Fe2-N401	2.093(3)	Fe1-O402-C401	168.9(3)
	Fe2-O402	2.317(3)	Fe2-O401-C401	96.3(3)
			Fe2-O402-C401	84.6(3)
13	Fe1...Fe2	3.5649(10)	O101-Fe1-O201	105.84(13)
	Fe1-O101	2.077(3)	O101-Fe1-O501	161.74(14)
	Fe1-O201	2.110(3)	O101-Fe1-N501	83.06(14)
	Fe1-O402	2.194(4)	O402-Fe1-N501	170.47(14)
	Fe1-O502	2.203(3)	O501-Fe1-O502	60.24(13)
	Fe1-N501	2.174(4)	O102-Fe2-O202	133.4(2)
	Fe2-O102	1.970(3)	O102-Fe2-O401	107.5(2)
	Fe2-O202	1.986(3)	O401-Fe2-N401	106.0(2)
	Fe2-O401	2.017(4)	Fe1-O402-Fe2	98.96(13)
	Fe2-N401	2.089(4)	Fe1-O402-C401	168.0(3)
	Fe2...O402	2.489(4)	Fe2-O401-C401	101.5(3)
			Fe2-O402-C401	80.3(3)
16	Fe1...Fe2	3.6671(5)	O101-Fe1-O201	92.72(8)
	Fe1-O101	2.064(2)	O101-Fe1-O501	156.53(8)
	Fe1-O201	2.117(2)	O101-Fe1-N501	86.82(8)
	Fe1-O402	2.154(2)	O402-Fe1-N501	174.34(8)
	Fe1-O502	2.305(2)	O501-Fe1-O502	59.45(7)
	Fe1-N501	2.148(2)	O102-Fe2-O202	146.36(7)
	Fe2-O102	2.026(2)	O102-Fe2-O401	100.01(8)
	Fe2-O202	1.974(2)	O401-Fe2-N401	106.03(8)
	Fe2-O401	2.006(4)	Fe1-O402-Fe2	87.72(6)
	Fe2-N401	2.072(2)	Fe1-O402-C401	152.6(2)
	Fe2...O402	3.055(2)	Fe2-O401-C401	116.6(2)

Table 3.3. (cont 'd) Selected Bond Distances and Angles.^a

<u>Distances</u>	<u>Angles</u>
Fe2-O402-C401	67.46(15)

^aNumbers in parentheses are estimated standard deviations of the last significant figure. Atoms are labeled as indicated in Figures 3.3-3.10.

Table 3.4. Atomic coordinates ($\times 10^4$) and equivalent isotropic displacement parameters ($\text{\AA}^2 \times 10^3$) for **6**.^a

atom	x	y	z	U(eq)
Fe(2)	1548(1)	1050(1)	7589(1)	26(1)
Fe(1)	818(1)	2144(1)	9015(1)	29(1)
O(101)	-16(2)	991(1)	8745(1)	33(1)
O(102)	455(2)	303(1)	7836(1)	29(1)
O(103)	-2847(2)	815(1)	7813(1)	34(1)
O(104)	-1246(2)	-603(1)	6356(1)	30(1)
O(201)	614(2)	2550(1)	8013(1)	35(1)
O(202)	1540(2)	2119(1)	7253(1)	35(1)
O(203)	-71(2)	2167(1)	5611(1)	31(1)
O(204)	-1656(2)	3105(1)	7333(1)	37(1)
O(401)	3116(2)	1096(1)	8144(1)	41(1)
O(402)	2189(2)	1657(1)	8809(1)	38(1)
O(501)	1764(2)	3265(1)	9613(1)	50(1)
O(502)	1364(2)	2309(1)	10213(1)	48(1)
N(101)	-2089(2)	84(1)	7073(1)	24(1)
N(201)	-903(2)	2663(1)	6438(1)	24(1)
N(401)	1405(2)	439(1)	6542(1)	28(1)
N(501)	-615(2)	2643(2)	9103(2)	41(1)
C(101)	13(2)	356(2)	8359(2)	25(1)
C(102)	-2513(2)	202(2)	7680(2)	26(1)
C(103)	-1625(2)	-580(2)	6874(2)	23(1)
C(104)	375(2)	-567(2)	9265(2)	32(1)
C(105)	-1692(2)	-2047(2)	6845(2)	31(1)
C(106)	-3504(2)	-461(2)	8469(2)	33(1)
C(107)	-466(2)	-422(2)	8561(2)	25(1)
C(108)	-630(2)	-1141(2)	7959(2)	25(1)
C(109)	-1650(2)	-1247(2)	7334(2)	25(1)
C(110)	-2606(2)	-1244(2)	7647(2)	27(1)
C(111)	-2529(2)	-462(2)	8137(2)	25(1)
C(112)	-1513(2)	-343(2)	8774(2)	27(1)
C(113)	1274(2)	-976(2)	9116(2)	34(1)
C(114)	1237(3)	-1786(2)	9152(2)	51(1)
C(115)	2015(4)	-2188(3)	8980(3)	71(1)
C(116)	2829(4)	-1803(3)	8766(3)	72(1)
C(117)	2896(3)	-1006(3)	8740(2)	65(1)
C(118)	2118(3)	-594(2)	8922(2)	47(1)
C(119)	-2646(3)	-2305(2)	6195(2)	36(1)
C(120)	-2567(3)	-2225(2)	5490(2)	45(1)
C(121)	-3425(4)	-2473(2)	4891(2)	62(1)
C(122)	-4380(4)	-2798(3)	4982(3)	69(1)
C(123)	-4483(3)	-2893(2)	5673(3)	62(1)
C(124)	-3612(3)	-2647(2)	6279(2)	47(1)
C(125)	-4564(2)	-741(2)	7920(2)	34(1)
C(126)	-5147(3)	-224(2)	7552(2)	44(1)
C(127)	-6096(3)	-503(3)	7021(2)	57(1)
C(128)	-6464(3)	-1298(3)	6854(2)	60(1)

Table 3.4. (cont'd) Atomic coordinates ($\times 10^4$) and equivalent isotropic displacement parameters ($\text{Å}^2 \times 10^3$) for **6**.^a

atom	x	y	z	U(eq)
C(129)	-5911(3)	-1821(2)	7214(2)	57(1)
C(130)	-4976(3)	-1546(2)	7749(2)	44(1)
C(201)	1174(2)	2663(2)	7579(2)	30(1)
C(202)	-1012(2)	3249(2)	6991(2)	28(1)
C(203)	-164(2)	2731(2)	6023(2)	25(1)
C(204)	2642(3)	3732(2)	8008(2)	39(1)
C(205)	748(2)	3659(2)	5368(2)	29(1)
C(206)	-879(3)	4706(2)	7395(2)	38(1)
C(207)	1503(2)	3515(2)	7463(2)	31(1)
C(208)	1576(2)	3566(2)	6679(2)	29(1)
C(209)	501(2)	3543(2)	6109(2)	27(1)
C(210)	-88(2)	4183(2)	6373(2)	29(1)
C(211)	-304(2)	4049(2)	7101(2)	30(1)
C(212)	763(3)	4072(2)	7675(2)	35(1)
C(213)	3169(3)	4571(2)	8087(2)	47(1)
C(214)	3049(3)	5141(3)	8639(3)	73(1)
C(215)	3511(5)	5929(3)	8704(4)	102(2)
C(216)	4097(5)	6144(3)	8240(5)	107(3)
C(217)	4234(4)	5594(3)	7707(4)	93(2)
C(218)	3778(3)	4804(2)	7631(3)	61(1)
C(219)	-160(2)	3559(2)	4685(2)	33(1)
C(220)	-891(3)	4090(2)	4573(2)	40(1)
C(221)	-1675(3)	3998(2)	3913(2)	49(1)
C(222)	-1725(3)	3393(2)	3358(2)	54(1)
C(223)	-1015(3)	2865(2)	3469(2)	55(1)
C(224)	-245(3)	2946(2)	4122(2)	43(1)
C(225)	-1854(3)	4873(2)	6864(2)	41(1)
C(226)	-1770(3)	5423(2)	6395(2)	55(1)
C(227)	-2660(5)	5570(3)	5897(3)	80(2)
C(228)	-3653(5)	5181(3)	5877(3)	98(2)
C(229)	-3750(4)	4646(3)	6352(4)	91(2)
C(230)	-2852(3)	4491(2)	6843(3)	63(1)
C(301)	-1492(2)	1365(2)	6741(2)	24(1)
C(302)	-1643(2)	1928(2)	6277(2)	24(1)
C(303)	-2494(2)	1812(2)	5659(2)	27(1)
C(304)	-3183(2)	1102(2)	5511(2)	32(1)
C(305)	-3059(2)	515(2)	5960(2)	29(1)
C(306)	-2209(2)	670(2)	6580(2)	25(1)
C(307)	-2667(3)	2434(2)	5159(2)	40(1)
C(308)	-3836(2)	-244(2)	5786(2)	41(1)
C(401)	3076(2)	1482(2)	8739(2)	33(1)
C(402)	4069(3)	1725(2)	9365(2)	42(1)
C(403)	4973(4)	1320(4)	9201(3)	100(2)
C(404)	3845(4)	1545(4)	10053(2)	97(2)
C(405)	4384(4)	2611(3)	9410(3)	106(2)
C(406)	1665(3)	818(2)	6019(2)	40(1)

Table 3.4. (cont'd) Atomic coordinates ($\times 10^4$) and equivalent isotropic displacement parameters ($\text{Å}^2 \times 10^3$) for **6**.^a

atom	x	y	z	U(eq)
C(407)	1600(3)	440(2)	5330(2)	47(1)
C(408)	1241(3)	-358(2)	5158(2)	39(1)
C(409)	989(3)	-754(2)	5688(2)	40(1)
C(410)	1082(2)	-341(2)	6369(2)	34(1)
C(501)	1772(3)	3012(2)	10209(2)	45(1)
C(502)	2230(4)	3577(2)	10932(2)	56(1)
C(503)	1314(6)	3804(5)	11190(5)	194(5)
C(504)	2911(5)	4309(3)	10826(3)	95(2)
C(505)	2923(6)	3169(3)	11469(3)	125(3)
C(506)	-601(4)	3425(2)	9237(3)	67(1)
C(507)	-1482(5)	3769(3)	9279(3)	90(2)
C(508)	-2435(4)	3298(4)	9168(3)	87(2)
C(509)	-2465(4)	2507(3)	9023(3)	94(2)
C(510)	-1529(3)	2205(3)	8996(3)	64(1)
C(601)	-4194(4)	2146(3)	7030(4)	104(2)
Cl(1)	-5214(1)	1421(1)	6505(1)	109(1)
Cl(2)	-4667(1)	2961(1)	7422(1)	113(1)

^aNumbers in parentheses are estimated standard deviations of the last significant figure. ^bU(eq) is defined as one third of the trace of the orthogonalized U_{ij} tensor.

Table 3.5. Atomic coordinates ($\times 10^4$) and equivalent isotropic displacement parameters ($\text{\AA}^2 \times 10^3$) for **7**.^a

atom	x	y	z	U(eq)
Fe(1)	-2350(1)	6383(1)	13121(1)	25(1)
Fe(2)	-2689(1)	5997(1)	11243(1)	26(1)
O(101)	-2162(1)	5061(1)	12806(1)	36(1)
O(102)	-2176(1)	4733(1)	11612(1)	33(1)
O(103)	-3811(1)	4196(1)	13830(1)	46(1)
O(104)	-3650(1)	3501(1)	11383(1)	40(1)
O(201)	-3696(1)	7147(1)	12827(1)	34(1)
O(202)	-3769(1)	7117(1)	11601(1)	34(1)
O(203)	-5805(1)	6929(1)	11264(1)	43(1)
O(204)	-6048(1)	7131(1)	13784(1)	48(1)
O(401)	-1487(1)	6284(1)	10750(1)	35(1)
O(402)	-1675(1)	6515(1)	11965(1)	33(1)
O(501)	-2101(1)	7551(1)	13558(1)	41(1)
O(502)	-1033(1)	6198(1)	13644(1)	35(1)
N(101)	-3710(1)	3850(1)	12602(1)	31(1)
N(201)	-5820(1)	7035(1)	12516(1)	33(1)
N(401)	-3346(1)	5644(1)	10386(1)	31(1)
N(501)	-3022(1)	6049(2)	14196(1)	34(1)
C(101)	-1959(1)	4518(2)	12264(1)	28(1)
C(102)	-3362(2)	3707(2)	13300(1)	34(1)
C(103)	-3270(2)	3330(2)	11944(1)	32(1)
C(104)	-292(2)	3546(2)	12222(2)	43(1)
C(105)	-2253(2)	1809(2)	11392(2)	55(1)
C(106)	-2496(2)	2543(2)	14138(2)	58(1)
C(107)	-1342(2)	3526(2)	12368(1)	32(1)
C(108)	-1439(2)	2858(2)	11794(1)	37(1)
C(109)	-2337(2)	2542(2)	11977(2)	39(1)
C(110)	-2362(2)	2167(2)	12765(2)	46(1)
C(111)	-2442(2)	2903(2)	13342(1)	39(1)
C(112)	-1543(2)	3217(2)	13174(1)	37(1)
C(201)	-4002(1)	7504(2)	12245(1)	29(1)
C(202)	-6040(2)	7533(2)	13202(1)	38(1)
C(203)	-5919(2)	7422(2)	11803(1)	37(1)
C(204)	-3927(2)	9029(2)	12194(2)	52(1)
C(205)	-6726(2)	8757(2)	11085(2)	61(1)
C(206)	-6885(2)	9011(2)	13901(2)	63(1)
C(207)	-4661(2)	8508(2)	12290(1)	37(1)
C(208)	-5267(2)	8735(2)	11649(2)	43(1)
C(209)	-6187(2)	8453(2)	11761(2)	44(1)
C(210)	-6811(2)	8893(2)	12495(2)	50(1)
C(211)	-6268(2)	8556(2)	13158(2)	45(1)
C(212)	-5314(2)	8786(2)	13053(2)	43(1)
C(301)	-4767(2)	5438(2)	12552(1)	31(1)
C(302)	-5684(2)	6072(2)	12561(1)	31(1)
C(303)	-6505(2)	5799(2)	12618(1)	37(1)
C(304)	-6368(2)	4880(2)	12669(1)	41(1)

Table 3.5. (cont'd) Atomic coordinates ($\times 10^4$) and equivalent isotropic displacement parameters ($\text{\AA}^2 \times 10^3$) for **7**.^a

atom	x	y	z	U(eq)
C(305)	-5463(2)	4223(2)	12668(1)	37(1)
C(306)	-4661(2)	4526(2)	12598(1)	30(1)
C(307)	-7499(2)	6497(2)	12618(2)	53(1)
C(308)	-5358(2)	3234(2)	12755(2)	53(1)
C(401)	-1192(2)	6485(2)	11326(1)	27(1)
C(402)	-251(2)	6725(2)	11212(1)	28(1)
C(403)	188(2)	6622(2)	11949(1)	30(1)
C(404)	546(2)	5636(2)	12190(1)	34(1)
C(405)	1257(2)	5002(2)	11568(1)	41(1)
C(406)	812(2)	5093(2)	10848(1)	40(1)
C(407)	486(2)	6074(2)	10605(1)	35(1)
C(408)	-545(2)	7720(2)	10986(1)	33(1)
C(409)	-1270(2)	8385(2)	11447(2)	42(1)
C(410)	-1576(2)	9289(2)	11245(2)	56(1)
C(411)	-1157(3)	9553(2)	10574(2)	58(1)
C(412)	-425(3)	8906(2)	10129(2)	57(1)
C(413)	-127(2)	8003(2)	10323(1)	45(1)
C(414)	-3982(2)	6286(2)	10039(1)	40(1)
C(415)	-4432(2)	6075(2)	9481(1)	46(1)
C(416)	-4226(2)	5177(2)	9272(1)	45(1)
C(417)	-3564(2)	4515(2)	9620(1)	42(1)
C(418)	-3143(2)	4774(2)	10172(1)	35(1)
C(501)	-1352(2)	7040(2)	13798(1)	32(1)
C(502)	-839(2)	7441(2)	14314(1)	34(1)
C(503)	266(2)	7067(2)	14048(1)	40(1)
C(504)	821(2)	7480(2)	14515(2)	51(1)
C(505)	481(2)	8511(2)	14473(2)	58(1)
C(506)	-611(2)	8917(2)	14709(2)	58(1)
C(507)	-1158(2)	8483(2)	14258(2)	44(1)
C(508)	-1117(2)	7124(2)	15103(1)	38(1)
C(509)	-1955(2)	7624(2)	15559(2)	56(1)
C(510)	-2221(3)	7308(3)	16265(2)	73(1)
C(511)	-1651(3)	6487(3)	16511(2)	68(1)
C(512)	-826(3)	5979(3)	16063(2)	61(1)
C(513)	-565(2)	6295(2)	15365(2)	49(1)
C(514)	-2490(2)	5457(2)	14645(1)	44(1)
C(515)	-2895(2)	5085(2)	15256(2)	54(1)
C(516)	-3891(2)	5325(2)	15411(1)	53(1)
C(517)	-4442(2)	5943(2)	14968(1)	52(1)
C(518)	-3985(2)	6288(2)	14369(1)	43(1)
C(601)	116(3)	10039(3)	12662(3)	94(1)
C(602)	327(3)	10546(3)	13218(2)	80(1)
C(603)	899(3)	11065(3)	13030(3)	84(1)
C(604)	1287(3)	11119(3)	12309(3)	85(1)
C(605)	1107(3)	10650(3)	11753(2)	84(1)
C(606)	532(3)	10087(3)	11890(3)	90(1)

Table 3.5. (cont'd) Atomic coordinates ($\times 10^4$) and equivalent isotropic displacement parameters ($\text{\AA}^2 \times 10^3$) for **7**.^a

atom	x	y	z	U(eq)
C(607)	-2637(3)	8175(3)	9755(2)	75(1)
C(608)	-3510(4)	8859(3)	9825(2)	86(1)
C(609)	-4156(3)	8913(3)	9320(3)	87(1)
C(610)	-3916(4)	8301(3)	8749(3)	90(1)
C(611)	-3024(4)	7594(3)	8680(3)	95(1)
C(612)	-2385(3)	7535(3)	9195(3)	81(1)
C(613)	-4730(11)	8994(10)	15185(9)	208(5)
C(614)	-4334(7)	9498(7)	14670(5)	133(3)
C(615)	-4302(10)	10320(10)	14304(8)	206(5)

^aNumbers in parentheses are estimated standard deviations of the last significant figure. ^bU(eq) is defined as one third of the trace of the orthogonalized U_{ij} tensor.

Table 3.6. Atomic coordinates ($\times 10^4$) and equivalent isotropic displacement parameters ($\text{\AA}^2 \times 10^3$) for **12**.^a

atom	x	y	z	U(eq)
Fe(1)	4521(1)	2895(1)	6088(1)	34(1)
Fe(2)	3725(1)	3963(1)	7469(1)	33(1)
Cl(1)	9398(3)	1821(2)	7584(3)	174(2)
Cl(2)	10020(2)	3436(2)	8244(2)	143(1)
Cl(3)	4173(3)	10020(3)	5607(2)	166(2)
Cl(4)	4353(4)	8644(2)	6399(3)	177(2)
O(101)	4739(2)	2369(2)	7033(2)	41(1)
O(102)	3976(3)	2909(2)	7826(2)	43(1)
O(103)	6857(2)	1788(2)	7845(2)	41(1)
O(104)	5297(2)	2977(2)	9409(2)	39(1)
O(201)	5150(2)	4096(2)	6309(2)	38(1)
O(202)	4765(2)	4739(2)	7258(2)	38(1)
O(203)	6442(2)	5585(2)	8687(2)	39(1)
O(204)	7803(2)	4217(2)	7091(2)	42(1)
O(401)	2250(3)	3752(3)	6985(2)	69(1)
O(402)	3179(2)	3303(2)	6309(2)	42(1)
O(501)	3967(3)	2774(2)	4853(2)	54(1)
O(502)	3706(3)	1812(2)	5503(2)	55(1)
N(101)	6118(2)	2356(2)	8666(2)	29(1)
N(201)	7209(2)	4941(2)	7918(2)	30(1)
N(401)	3596(3)	4534(2)	8454(2)	38(1)
N(501)	5909(2)	2592(2)	5925(2)	47(1)
C(101)	4257(3)	2316(3)	7504(2)	34(1)
C(102)	6241(3)	1702(2)	8186(2)	31(1)
C(103)	5389(3)	2357(2)	9063(2)	30(1)
C(104)	2888(4)	1248(3)	7120(3)	48(1)
C(105)	4445(3)	1520(3)	9756(2)	37(1)
C(106)	6138(3)	191(3)	7950(2)	41(1)
C(107)	3917(3)	1473(2)	7673(2)	36(1)
C(108)	3781(3)	1503(3)	8443(2)	35(1)
C(109)	4742(3)	1556(2)	9029(2)	31(1)
C(110)	5305(3)	855(2)	8858(2)	33(1)
C(111)	5568(3)	905(2)	8134(2)	33(1)
C(112)	4617(3)	853(3)	7545(2)	38(1)
C(113)	2246(5)	482(4)	7200(4)	78(2)
C(114)	1667(12)	321(11)	7495(9)	62(4)
C(115)	1037(17)	-439(18)	7543(13)	89(6)
C(116)	1308(18)	-941(12)	7141(12)	74(5)
C(117)	1927(17)	-1022(14)	6627(13)	97(7)
C(118)	2529(11)	-256(8)	6630(8)	56(4)
C(4)	1517(7)	620(7)	7701(6)	51(3)
C(5)	893(10)	-41(9)	7799(8)	76(4)
C(6)	975(13)	-837(12)	7407(10)	86(5)
C(7)	1588(11)	-996(8)	6957(8)	68(4)
C(8)	2230(7)	-258(6)	6927(5)	50(3)
C(119)	5265(3)	1658(3)	10429(2)	40(1)

Table 3.6. (cont'd) Atomic coordinates ($\times 10^4$) and equivalent isotropic displacement parameters ($\text{Å}^2 \times 10^3$) for **12**.^a

atom	x	y	z	U(eq)
C(120)	5423(4)	2377(3)	10896(3)	51(1)
C(121)	6128(5)	2501(4)	11531(3)	64(2)
C(122)	6709(4)	1903(4)	11725(3)	63(2)
C(123)	6582(4)	1195(4)	11266(3)	58(1)
C(124)	5850(4)	1064(3)	10626(3)	47(1)
C(125)	6995(3)	63(2)	8538(2)	38(1)
C(126)	7926(3)	511(3)	8642(3)	47(1)
C(127)	8701(4)	400(3)	9204(4)	60(1)
C(128)	8555(4)	-154(4)	9657(3)	64(2)
C(129)	7646(4)	-611(4)	9552(3)	59(1)
C(130)	6875(4)	-507(3)	8989(3)	50(1)
C(201)	5146(3)	4718(3)	6721(2)	32(1)
C(202)	7525(3)	4847(2)	7278(2)	32(1)
C(203)	6767(3)	5601(2)	8158(2)	32(1)
C(204)	4792(3)	5732(3)	5888(2)	38(1)
C(205)	6800(3)	7101(3)	8256(2)	39(1)
C(206)	8387(3)	5587(3)	6477(2)	41(1)
C(207)	5578(3)	5537(2)	6543(2)	32(1)
C(208)	5752(3)	6231(2)	7170(2)	32(1)
C(209)	6737(3)	6317(2)	7733(2)	32(1)
C(210)	7597(3)	6343(2)	7370(2)	34(1)
C(211)	7508(3)	5569(3)	6859(2)	34(1)
C(212)	6535(3)	5471(3)	6272(2)	36(1)
C(213)	3765(3)	5788(3)	5992(2)	44(1)
C(214)	3005(4)	5151(4)	5671(3)	60(1)
C(215)	2041(5)	5184(5)	5717(5)	85(2)
C(216)	1822(5)	5859(6)	6119(4)	87(2)
C(217)	2544(5)	6475(5)	6442(3)	81(2)
C(218)	3515(5)	6446(4)	6366(3)	67(2)
C(219)	7712(4)	7308(3)	8872(3)	45(1)
C(220)	8611(4)	7672(3)	8782(3)	55(1)
C(221)	9440(4)	7848(4)	9348(4)	68(2)
C(222)	9385(5)	7678(4)	10025(4)	75(2)
C(223)	8493(5)	7332(4)	10125(3)	71(2)
C(224)	7665(4)	7143(3)	9553(3)	54(1)
C(225)	9404(4)	5757(3)	6974(3)	48(1)
C(226)	9848(4)	6544(4)	7260(3)	61(1)
C(227)	10770(5)	6700(6)	7738(4)	87(2)
C(228)	11266(5)	6061(7)	7939(4)	92(3)
C(229)	10849(5)	5274(6)	7634(5)	90(3)
C(230)	9924(4)	5128(4)	7170(4)	62(2)
C(301)	6678(3)	3644(2)	8294(2)	29(1)
C(302)	7365(3)	4330(2)	8392(2)	30(1)
C(303)	8207(3)	4464(3)	8952(2)	38(1)
C(304)	8324(3)	3884(3)	9423(2)	39(1)
C(305)	7645(3)	3196(2)	9350(2)	33(1)

Table 3.6. (cont'd) Atomic coordinates ($\times 10^4$) and equivalent isotropic displacement parameters ($\text{\AA}^2 \times 10^3$) for **12**.^a

atom	x	y	z	U(eq)
C(306)	6826(3)	3083(2)	8769(2)	29(1)
C(307)	8968(4)	5207(3)	9058(3)	52(1)
C(308)	7783(3)	2599(3)	9885(3)	45(1)
C(401)	2342(4)	3398(3)	6393(3)	50(1)
C(402)	1452(4)	3157(5)	5787(4)	79(2)
C(403)	568(6)	3414(8)	5830(7)	142(5)
C(404)	-232(8)	3259(10)	5268(9)	186(8)
C(405)	-186(8)	2835(8)	4653(8)	156(6)
C(406)	663(7)	2541(7)	4608(5)	121(4)
C(407)	1499(5)	2757(4)	5157(4)	77(2)
C(408)	2847(4)	4260(4)	8739(3)	60(1)
C(409)	2755(5)	4585(4)	9402(3)	71(2)
C(410)	3459(5)	5222(4)	9795(3)	59(1)
C(411)	4188(5)	5498(4)	9491(4)	75(2)
C(412)	4221(5)	5150(4)	8820(3)	63(2)
C(501)	3598(4)	2073(3)	4899(3)	48(1)
C(502)	2995(4)	1527(3)	4248(3)	48(1)
C(503)	3019(4)	1700(3)	3575(3)	56(1)
C(504)	2460(5)	1196(4)	2968(3)	66(2)
C(505)	1867(5)	520(4)	3054(3)	68(2)
C(506)	1834(6)	341(4)	3714(4)	85(2)
C(507)	2404(5)	842(4)	4312(3)	73(2)
C(508)	6375(3)	3014(3)	5485(2)	66(2)
C(509)	7246(4)	2795(4)	5342(3)	112(3)
C(510)	7652(4)	2154(4)	5638(4)	155(5)
C(511)	7186(4)	1731(4)	6077(4)	134(4)
C(512)	6314(4)	1950(3)	6221(3)	91(3)
C(601)	-363(17)	-778(14)	4320(12)	117(6)
C(602)	552(17)	-952(14)	4487(13)	120(6)
C(603)	884(26)	-597(22)	5201(19)	177(11)
C(605)	420(13)	89(13)	5332(10)	191(7)
C(606)	4732(10)	9242(8)	5748(7)	137(4)
C(607)	9024(7)	2733(6)	7786(7)	116(3)

^aNumbers in parentheses are estimated standard deviations of the last significant figure. ^bU(eq) is defined as one third of the trace of the orthogonalized U_{ij} tensor.

Table 3.7. Atomic coordinates ($\times 10^4$) and equivalent isotropic displacement parameters ($\text{\AA}^2 \times 10^3$) for **13.a**

atom	x	y	z	U(eq)
Fe(1)	6571(1)	6895(1)	727(1)	25(1)
Fe(2)	6604(1)	8845(1)	989(1)	26(1)
O(101)	5927(2)	7245(2)	1141(1)	35(1)
O(102)	5947(2)	8454(2)	1322(1)	37(1)
O(103)	6593(2)	6612(2)	2354(1)	35(1)
O(104)	6378(2)	9109(2)	2401(1)	32(1)
O(201)	7479(2)	7373(2)	1067(1)	25(1)
O(202)	7538(2)	8612(2)	1043(1)	29(1)
O(203)	8639(2)	9214(2)	2023(1)	32(1)
O(204)	8668(2)	6684(2)	2067(1)	37(1)
O(401)	6137(2)	9129(2)	295(1)	46(1)
O(402)	6348(2)	7929(2)	298(1)	38(1)
O(501)	6996(2)	6278(2)	214(1)	40(1)
O(502)	5953(2)	6161(2)	174(1)	37(1)
N(101)	6490(2)	7853(2)	2450(1)	24(1)
N(201)	8616(2)	7945(2)	2008(1)	22(1)
N(401)	6742(2)	9839(2)	1393(1)	29(1)
N(501)	6724(2)	5964(2)	1243(2)	28(1)
C(101)	5718(2)	7803(3)	1318(2)	27(1)
C(102)	6236(3)	7124(3)	2381(2)	27(1)
C(103)	6112(2)	8508(3)	2400(2)	26(1)
C(104)	4557(2)	7639(3)	1030(2)	34(1)
C(105)	5154(3)	9097(3)	2627(2)	34(1)
C(106)	5446(3)	6276(3)	2632(2)	39(1)
C(107)	5100(2)	7709(3)	1522(2)	26(1)
C(108)	4986(2)	8388(3)	1826(2)	27(1)
C(109)	5389(2)	8413(3)	2368(2)	26(1)
C(110)	5280(2)	7687(3)	2621(2)	30(1)
C(111)	5508(2)	7030(3)	2364(2)	28(1)
C(112)	5117(2)	6991(3)	1821(2)	28(1)
C(113)	3862(3)	7608(3)	1077(2)	39(1)
C(114)	3587(3)	6972(4)	1201(2)	45(2)
C(115)	2947(4)	6949(5)	1252(3)	70(2)
C(116)	2571(4)	7576(6)	1149(4)	92(3)
C(117)	2822(4)	8210(5)	1001(4)	106(4)
C(118)	3463(3)	8232(4)	970(3)	72(2)
C(119)	5481(3)	9207(3)	3163(2)	34(1)
C(120)	6002(3)	9690(3)	3315(2)	41(2)
C(121)	6306(3)	9789(3)	3808(2)	48(2)
C(122)	6089(3)	9394(4)	4162(2)	54(2)
C(123)	5572(3)	8916(4)	4026(2)	62(2)
C(124)	5264(3)	8821(4)	3530(2)	49(2)
C(125)	4763(3)	6078(3)	2655(2)	43(2)
C(126)	4504(3)	6323(4)	3042(2)	57(2)
C(127)	3874(4)	6164(4)	3063(3)	76(2)
C(128)	3487(4)	5758(5)	2694(4)	82(3)

Table 3.7. (cont'd) Atomic coordinates ($\times 10^4$) and equivalent isotropic displacement parameters ($\text{Å}^2 \times 10^3$) for **13**.^a

atom	x	y	z	U(eq)
C(129)	3732(4)	5487(4)	2307(3)	68(2)
C(130)	4366(3)	5651(3)	2291(2)	52(2)
C(201)	7760(2)	7962(3)	997(2)	24(1)
C(202)	8825(2)	7243(3)	1882(2)	26(1)
C(203)	8808(2)	8644(3)	1854(2)	26(1)
C(204)	8082(2)	7907(3)	237(2)	32(1)
C(205)	9651(2)	9364(3)	1572(2)	32(1)
C(206)	9669(3)	6522(3)	1564(2)	32(1)
C(207)	8383(2)	7924(3)	813(2)	25(1)
C(208)	8811(2)	8624(3)	948(2)	27(1)
C(209)	9238(2)	8636(3)	1483(2)	26(1)
C(210)	9655(2)	7940(3)	1561(2)	29(1)
C(211)	9243(2)	7240(3)	1499(2)	26(1)
C(212)	8787(2)	7223(3)	972(2)	27(1)
C(213)	8554(3)	7796(3)	-92(2)	33(1)
C(214)	8633(3)	7089(3)	-275(2)	44(2)
C(215)	9040(4)	6987(4)	-598(2)	61(2)
C(216)	9351(3)	7581(5)	-747(2)	65(2)
C(217)	9271(3)	8285(4)	-577(2)	56(2)
C(218)	8867(3)	8386(3)	-252(2)	43(2)
C(219)	10203(2)	9382(3)	1315(2)	37(1)
C(220)	10110(3)	9609(3)	829(2)	50(2)
C(221)	10624(3)	9599(4)	596(3)	68(2)
C(222)	11230(3)	9371(5)	840(3)	76(2)
C(223)	11331(3)	9157(5)	1325(3)	76(2)
C(224)	10820(3)	9160(4)	1556(2)	53(2)
C(225)	10291(3)	6554(3)	1964(2)	42(2)
C(226)	10866(3)	6745(4)	1847(3)	60(2)
C(227)	11453(4)	6804(5)	2195(3)	90(3)
C(228)	11451(5)	6684(5)	2661(4)	100(3)
C(229)	10913(5)	6484(5)	2825(3)	93(3)
C(230)	10292(4)	6408(4)	2453(2)	81(3)
C(301)	7556(2)	7917(3)	2231(2)	26(1)
C(302)	8229(2)	7954(3)	2378(2)	25(1)
C(303)	8550(2)	7998(3)	2875(2)	27(1)
C(304)	8167(3)	8006(3)	3222(2)	29(1)
C(305)	7496(3)	7972(3)	3089(2)	29(1)
C(306)	7195(2)	7925(3)	2588(2)	24(1)
C(307)	9282(3)	8038(4)	3034(2)	44(2)
C(308)	7110(3)	7973(4)	3483(2)	43(2)
C(401)	6107(2)	8505(3)	74(2)	31(1)
C(402)	5791(3)	8499(3)	-483(2)	36(1)
C(403)	5227(3)	9052(3)	-597(2)	50(2)
C(404)	4656(3)	8811(4)	-379(3)	61(2)
C(405)	4402(3)	8039(4)	-557(3)	67(2)
C(406)	4959(3)	7471(4)	-447(2)	54(2)

Table 3.7. (cont'd) Atomic coordinates ($\times 10^4$) and equivalent isotropic displacement parameters ($\text{\AA}^2 \times 10^3$) for **13**.^a

atom	x	y	z	U(eq)
C(407)	5537(3)	7705(3)	-653(2)	43(2)
C(408)	6355(3)	8724(3)	-720(2)	40(2)
C(409)	6790(3)	8222(4)	-814(2)	53(2)
C(410)	7303(3)	8438(5)	-1016(2)	63(2)
C(411)	7389(4)	9143(5)	-1125(3)	83(3)
C(412)	6953(6)	9655(5)	-1047(4)	135(5)
C(413)	6434(5)	9444(4)	-845(3)	106(3)
C(414)	7340(3)	10124(3)	1553(2)	38(1)
C(415)	7464(3)	10738(3)	1849(2)	51(2)
C(416)	6965(3)	11094(3)	1989(2)	44(2)
C(417)	6342(3)	10814(3)	1824(2)	42(2)
C(418)	6254(3)	10187(3)	1530(2)	33(1)
C(501)	6455(3)	5964(3)	39(2)	32(1)
C(502)	6416(3)	5338(3)	-353(2)	34(1)
C(503)	5793(3)	4880(3)	-405(2)	43(2)
C(504)	5778(3)	4406(3)	42(2)	54(2)
C(505)	6360(3)	3901(4)	186(3)	59(2)
C(506)	6984(3)	4356(4)	267(2)	54(2)
C(507)	7008(3)	4813(3)	-187(2)	45(2)
C(508)	6448(3)	5740(3)	-835(2)	41(2)
C(509)	7029(4)	6017(5)	-901(3)	89(3)
C(510)	7079(5)	6376(6)	-1335(3)	105(3)
C(511)	6549(5)	6479(4)	-1701(3)	81(2)
C(512)	5963(4)	6227(6)	-1646(3)	89(3)
C(513)	5917(4)	5848(5)	-1213(3)	75(2)
C(514)	6212(3)	5555(3)	1295(2)	36(1)
C(515)	6257(3)	5011(3)	1649(2)	47(2)
C(516)	6855(4)	4866(3)	1964(2)	49(2)
C(517)	7377(3)	5266(3)	1903(2)	43(2)
C(518)	7301(3)	5809(3)	1547(2)	33(1)
C(601)	10405(4)	6630(6)	356(3)	84(3)
C(602)	11049(5)	6739(6)	401(3)	92(3)
C(603)	11474(4)	6153(8)	520(4)	103(4)
C(604)	11240(6)	5468(7)	614(4)	114(4)
C(605)	10578(6)	5383(6)	562(3)	98(3)
C(606)	10172(4)	5960(6)	437(3)	82(3)
C(607)	8259(6)	5431(9)	-2594(6)	130(4)
C(608)	8407(7)	5298(7)	-2101(5)	142(5)
C(609)	8497(8)	5927(9)	-1822(5)	163(5)
C(610)	8422(7)	6677(8)	-2014(5)	143(4)
C(611)	8234(6)	6817(9)	-2483(6)	151(6)
C(612)	8168(7)	6149(13)	-2780(6)	176(7)
C(613)	6854(8)	6964(9)	4581(5)	177(5)
C(614)	6398(9)	6383(12)	4401(6)	212(7)
C(615)	6677(8)	5737(10)	4588(6)	185(6)
C(616)	7399(8)	5392(9)	4712(5)	174(5)

Table 3.7. (cont'd) Atomic coordinates ($\times 10^4$) and equivalent isotropic displacement parameters ($\text{Å}^2 \times 10^3$) for **13**.^a

atom	x	y	z	U(eq)
C(617)	7784(7)	5981(9)	4666(5)	160(5)
C(618)	7521(8)	6674(10)	4648(6)	187(6)

^aNumbers in parentheses are estimated standard deviations of the last significant figure. ^bU(eq) is defined as one third of the trace of the orthogonalized Uij tensor.

Table 3.8. Atomic coordinates ($\times 10^4$) and equivalent isotropic displacement parameters ($\text{Å}^2 \times 10^3$) for **16**.^a

atom	x	y	z	U(eq)
Fe(1)	5968(1)	7038(1)	8216(1)	21(1)
Fe(2)	5554(1)	6659(1)	6590(1)	23(1)
O(101)	4980(2)	5883(1)	7572(1)	36(1)
O(102)	4774(1)	5217(1)	6638(1)	27(1)
O(103)	2126(2)	5572(1)	7614(1)	31(1)
O(104)	2648(1)	4324(1)	5805(1)	27(1)
O(201)	5488(1)	8144(1)	7810(1)	27(1)
O(202)	5741(1)	8090(1)	6871(1)	27(1)
O(203)	4107(1)	8529(1)	5896(1)	29(1)
O(204)	2963(1)	8551(1)	7661(1)	29(1)
O(401)	7068(1)	6638(2)	6755(1)	35(1)
O(402)	7248(1)	7274(1)	7710(1)	32(1)
O(501)	7068(2)	7699(1)	9001(1)	33(1)
O(502)	6523(2)	6054(1)	8835(1)	33(1)
N(101)	2351(2)	4925(1)	6706(1)	22(1)
N(201)	3514(2)	8569(1)	6775(1)	21(1)
N(401)	5160(2)	6491(2)	5677(1)	27(1)
N(402)	4120(2)	5955(2)	4806(1)	31(1)
N(501)	4625(2)	6889(2)	8666(1)	27(1)
N(502)	3101(2)	7033(2)	8872(1)	37(1)
C(101)	4696(2)	5134(2)	7171(1)	22(1)
C(102)	2264(2)	4879(2)	7311(1)	24(1)
C(103)	2550(2)	4186(2)	6306(1)	23(1)
C(104)	5291(2)	3888(2)	7659(1)	30(1)
C(105)	2193(2)	2349(2)	6003(1)	32(1)
C(106)	1701(2)	3775(2)	8044(1)	33(1)
C(107)	4293(2)	4095(2)	7336(1)	23(1)
C(108)	3759(2)	3292(2)	6784(1)	24(1)
C(109)	2601(2)	3224(2)	6529(1)	24(1)
C(110)	1928(2)	3048(2)	7020(1)	27(1)
C(111)	2342(2)	3927(2)	7534(1)	25(1)
C(112)	3521(2)	4061(2)	7786(1)	26(1)
C(113)	6178(2)	3892(3)	7305(1)	42(1)
C(114)	7106(3)	3672(3)	7661(2)	58(1)
C(115)	495(2)	3539(2)	7876(1)	40(1)
C(116)	-31(3)	3554(4)	8423(2)	74(1)
C(117)	1072(2)	2137(2)	5675(2)	45(1)
C(118)	742(4)	1238(3)	5203(2)	109(2)
C(201)	5728(2)	8554(2)	7377(1)	23(1)
C(202)	3527(2)	9019(2)	7356(1)	23(1)
C(203)	4158(2)	9008(2)	6376(1)	22(1)
C(204)	7243(2)	10100(2)	7768(1)	36(1)
C(205)	4992(2)	10615(2)	6031(1)	30(1)
C(206)	3762(2)	10618(2)	8028(1)	29(1)
C(207)	6045(2)	9705(2)	7464(1)	25(1)
C(208)	5981(2)	10104(2)	6872(1)	27(1)

Table 3.8. (con't) Atomic coordinates ($\times 10^4$) and equivalent isotropic displacement parameters ($\text{\AA}^2 \times 10^3$) for **16**.^a

atom	x	y	z	U(eq)
C(209)	4862(2)	10090(2)	6575(1)	24(1)
C(210)	4368(2)	10624(2)	7025(1)	26(1)
C(211)	4250(2)	10098(2)	7562(1)	24(1)
C(212)	5369(2)	10109(2)	7866(1)	27(1)
C(213)	7551(3)	9806(3)	8347(2)	50(1)
C(214)	8652(3)	10464(3)	8677(2)	69(1)
C(215)	2666(2)	10715(2)	7830(1)	35(1)
C(216)	2230(3)	11130(3)	8352(1)	45(1)
C(217)	3984(2)	10586(2)	5630(1)	40(1)
C(218)	4206(3)	11263(2)	5170(1)	47(1)
C(301)	2935(2)	6736(2)	6715(1)	21(1)
C(302)	2746(2)	7590(2)	6549(1)	22(1)
C(303)	1821(2)	7535(2)	6169(1)	24(1)
C(304)	1112(2)	6585(2)	5944(1)	26(1)
C(305)	1275(2)	5712(2)	6097(1)	24(1)
C(306)	2195(2)	5808(2)	6492(1)	20(1)
C(307)	1572(2)	8460(2)	6017(1)	39(1)
C(308)	445(2)	4712(2)	5847(1)	33(1)
C(401)	7622(2)	7122(2)	7255(1)	28(1)
C(402)	8829(2)	7582(2)	7265(1)	29(1)
C(403)	9235(2)	6888(2)	6847(1)	43(1)
C(404)	9135(3)	5887(3)	7050(2)	54(1)
C(405)	9705(3)	6014(3)	7678(2)	57(1)
C(406)	9323(2)	6699(2)	8099(2)	43(1)
C(407)	9435(2)	7705(2)	7898(1)	33(1)
C(408)	8970(2)	8584(2)	7038(1)	34(1)
C(409)	8376(3)	8641(3)	6509(1)	48(1)
C(410)	8491(3)	9539(3)	6302(2)	61(1)
C(411)	9224(3)	10408(3)	6610(2)	65(1)
C(412)	9832(3)	10376(3)	7129(2)	64(1)
C(413)	9709(2)	9476(2)	7345(2)	48(1)
C(414)	5777(2)	6370(2)	5247(1)	30(1)
C(415)	5140(2)	6035(2)	4714(1)	33(1)
C(416)	4172(2)	6232(2)	5391(1)	29(1)
C(417)	3144(3)	5603(2)	4361(1)	44(1)
C(418)	2814(3)	6441(2)	4117(1)	42(1)
C(419)	2476(3)	7124(2)	4557(1)	42(1)
C(420)	2035(3)	7866(3)	4264(2)	59(1)
C(501)	7003(2)	6871(2)	9176(1)	28(1)
C(502)	7443(2)	6878(2)	9829(1)	33(1)
C(503)	7738(2)	5914(2)	9892(1)	41(1)
C(504)	8689(3)	5855(3)	9593(2)	54(1)
C(505)	9654(3)	6769(3)	9825(2)	62(1)
C(506)	9380(3)	7731(3)	9762(2)	55(1)
C(507)	8429(2)	7792(3)	10064(1)	44(1)
C(508)	6525(2)	6955(2)	10161(1)	32(1)

Table 3.8. (con't) Atomic coordinates ($\times 10^4$) and equivalent isotropic displacement parameters ($\text{Å}^2 \times 10^3$) for **16**.^a

atom	x	y	z	U(eq)
C(509)	6180(2)	7798(2)	10171(1)	37(1)
C(510)	5350(3)	7884(3)	10456(1)	44(1)
C(511)	4830(3)	7124(3)	10734(1)	46(1)
C(512)	5152(2)	6272(3)	10728(1)	43(1)
C(513)	5997(2)	6197(2)	10448(1)	37(1)
C(514)	4282(2)	6262(2)	9061(1)	30(1)
C(515)	3340(2)	6347(2)	9191(1)	37(1)
C(516)	3898(2)	7339(2)	8567(1)	34(1)
C(517)	2165(3)	7395(4)	8870(2)	65(1)
C(518)	2352(5)	8172(4)	9516(3)	55(2)
C(51D)	2248(9)	8266(9)	9105(6)	52(4)
C(519)	3233(6)	8992(5)	9631(2)	120(2)
C(520)	3378(6)	9630(4)	10219(3)	120(2)

^aNumbers in parentheses are estimated standard deviations of the last significant figure. ^bU(eq) is defined as one third of the trace of the orthogonalized U_{ij} tensor.

Table 3.9. Effect of ligand steric and electronic properties and solvent on stable peroxy adduct formation.

$$\text{Fe}_2\text{L}(\text{O}_2\text{CR})_2(\text{N})_2 + \text{ex. O}_2 \xrightarrow[\text{THF, toluene, or CH}_2\text{Cl}_2]{-80\text{ }^\circ\text{C}} \text{midnight blue solution: } \lambda_{\text{max}} = 580 \text{ (1200-1300) or decomposition}$$

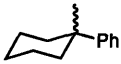
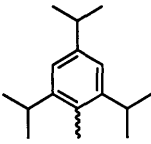
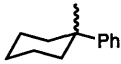
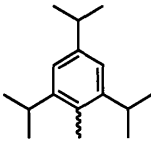
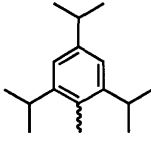
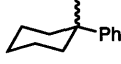
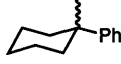
Complex	L	N	R	Compatible Solvents For Stable Peroxo Formation
10-12	BXDK	py	<i>i</i> -Pr, Ph or CH ₂ C(CH ₃) ₃	None
6			<i>tert</i> -Bu	THF or PhCH ₃
13				THF, PhCH ₃ , or CH ₂ Cl ₂
14				THF, PhCH ₃ , or CH ₂ Cl ₂
7	XDK			THF, PhCH ₃ , or CH ₂ Cl ₂
8				THF, PhCH ₃ , or CH ₂ Cl ₂
9		3-F-py		THF, PhCH ₃ , or CH ₂ Cl ₂
15		Me-Im		THF
16	PXDK	Bu-Im		THF or PhCH ₃

Table 3.10. Manometric studies of the dioxygen uptake for **13**, **16**, and [Fe(Tp^{3,5}-iPr₂)(O₂CH₂Ph)] vs. equimolar Vaska's complex.^a

Compound	Solvent	O ₂ Uptake, Peroxo Formation (equiv)	O ₂ Uptake, Peroxo Decay (equiv)
IrCl(CO)(PPh ₃) ₂	CH ₂ Cl ₂	1.0	-
(13)	CH ₂ Cl ₂	1.0 ± 0.1	0.7 ± 0.1
[Fe(Tp ^{3,5} -iPr ₂)(O ₂ CH ₂ Ph)]	THF	0.55 ± 0.1	0.3 ± 0.1
[Fe(Tp ^{3,5} -iPr ₂)(O ₂ CH ₂ Ph)]	Et ₂ O	0.45 ± 0.1	0
16	THF	0.9 ± 0.1	1.0 ± 0.1
16	Et ₂ O	1.0 ± 0.1	0

^aAll O₂ uptake values are in equivalents based on the amount of O₂ uptake by equimolar Vaska's complex under identical conditions. T = -77 °C for the formation and 22 °C for the decay. In each case following decay, the system was brought back to equilibrium at -77 °C for the final pressure reading.

Table 3.11. A summary of resonance Raman data obtained for the peroxo adducts.

Compound	solvent	$\nu(\text{Fe}-^{16}\text{O}) (^{18}\text{O})$	$\nu(^{16}\text{O}-^{16}\text{O}) (^{18}\text{O}_2)$
[Fe ₂ (O ₂)(BXDK)(μ -O ₂ Ct-Bu)- (O ₂ Ct-Bu)(py) ₂] (6·O ₂)	toluene	Not Observed ^a	864
[Fe ₂ (O ₂)(XDK)(μ -O ₂ CPhCy)- (O ₂ CPhCy)(py) ₂] (7·O ₂)	toluene	Not Observed	864
[Fe ₂ (O ₂)(XDK)(μ -O ₂ CAr)- (O ₂ CAr)(py) ₂] (8·O ₂)	toluene	Not Observed	864
[Fe ₂ (O ₂)(BXDK)(μ -O ₂ CPhCy)- (O ₂ CPhCy)(py) ₂] (13·O ₂)	toluene	Not Observed	864
(13·O ₂)	CH ₂ Cl ₂	484 (484)	861 (811)
[Fe ₂ (O ₂)(BXDK)(μ -O ₂ CAr)- (O ₂ CAr)(py) ₂] (14·O ₂)	toluene	Not Observed	864
[Fe ₂ (O ₂)(PXDK)(μ -O ₂ CPhCy)- (O ₂ CPhCy)(Bu-Im) ₂] (16·O ₂)	toluene	Not Observed	864(818)

^aFe-O stretches were not observed for the toluene samples. These features were likely obscured by the large solvent background in this region, overwhelming even with solvent subtraction.

Table 3.12. Mössbauer parameters for $[\text{Fe}_2(\text{BXDK})(\mu\text{-O}_2\text{CPhCy})(\text{O}_2\text{CPhCy})(\text{py})_2]$ (**13**), $[\text{Fe}_2(\text{XDK})(\mu\text{-O}_2\text{CPhCy})(\text{O}_2\text{CPhCy})(\text{Me-Im})_2]$ (**15**), and $[\text{Fe}_2(\text{O}_2)(\text{BXDK})(\text{O}_2\text{CPhCy})_2(\text{py})_2]$ (**13**·**O**₂).

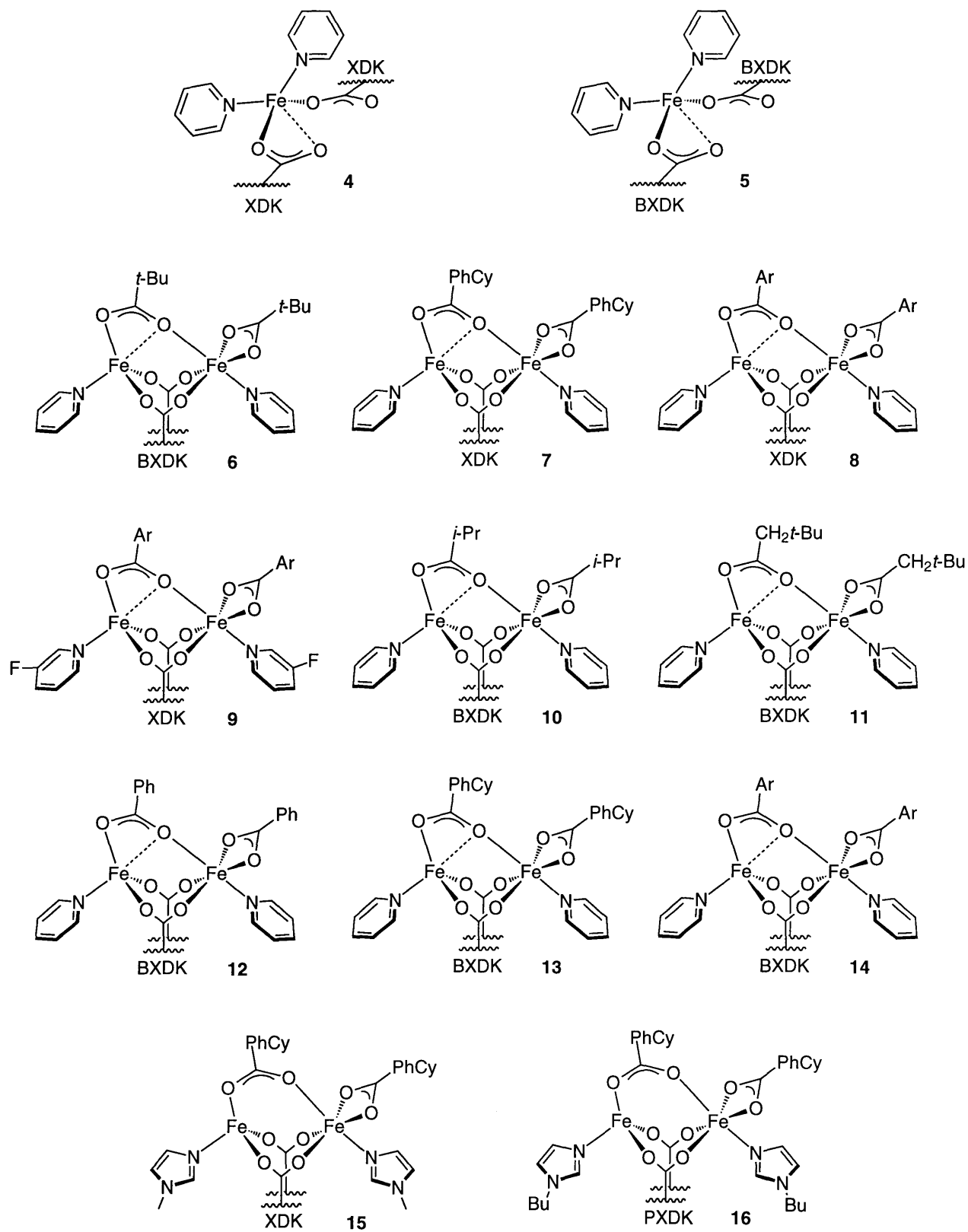
Complex	δ (mm/s)	ΔE_Q (mm/s)	$\Gamma_{1/2}$ (mm/s)	ref
13 (solid)	1.27	3.03	0.39	<i>a</i>
	1.07	2.54	0.37	
	or	or	or	
	1.29	2.98	0.38	
	1.05	2.58	0.38	
13 (THF soln.)	1.23	3.10	0.47	<i>a</i>
	1.22	2.61	0.50	
	or	or	or	
	1.34	2.87	0.50	
	1.10	2.85	0.47	
15 (THF soln)	1.24	3.19	0.43	<i>a</i>
	1.26	2.73	0.44	
	or	or	or	
	1.36	2.94	0.44	
	1.14	2.98	0.43	
13 · O ₂	0.62	1.22	0.42	<i>a</i>
	0.48	0.86	0.42	
	or	or	or	
	0.64	1.18	0.41	
	0.46	0.89	0.42	
Oxyhemerythrin	0.51	1.96	0.30	47
	0.52	0.95	0.36	
MMOH _{peroxo}	0.66	1.51	0.27	15

^aThis work.

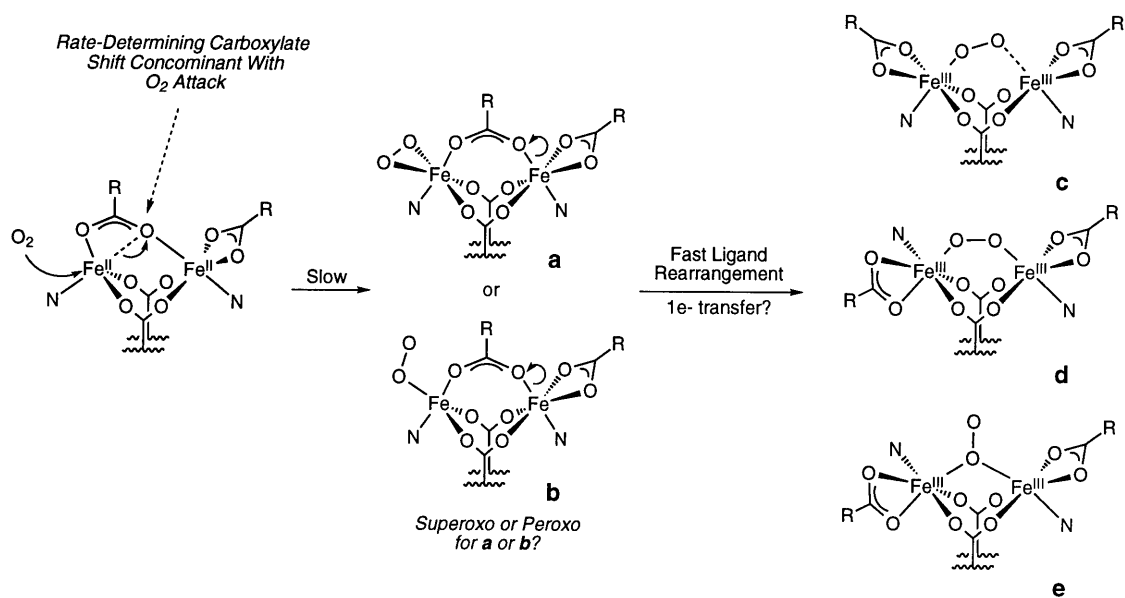
Table 3.13. Summary of kinetic data for the reaction of the diferrous complexes with oxygen at -77 °C, and a correlation with selected solid state metrical parameters.

Parameter	6	7	13	14
k (M ⁻¹ s ⁻¹)	0.0398 ± 0.0009	0.045 ± 0.003	0.16 ± 0.01	0.115 ± 0.005
Fe2-O402	2.340(2)	2.454(2)	2.489(4)	
Fe2-O401	2.062(2)	2.050(2)	2.017(4)	
Fe1-O402	2.172(2)	2.217(2)	2.194(4)	
Fe1-O402-Fe2	102.13(9)	100.47(6)	98.96(13)	Not
Fe1-O402-C401	170.6(2)	171.5(2)	168.0(3)	Available ^a
Fe2-O401-C401	97.5(2)	100.15(13)	101.5(3)	
Fe2-O402-C401	84.5(2)	81.84(12)	80.3(3)	
τ^b	73	71	66	

^aAn X-ray structure was acquired for **14**, but it was of insufficient quality for an accurate determination of bond distances and angles. ^bSee Figure 3.11 for a complete definition of τ .



Scheme 3.1.



Scheme 3.2.

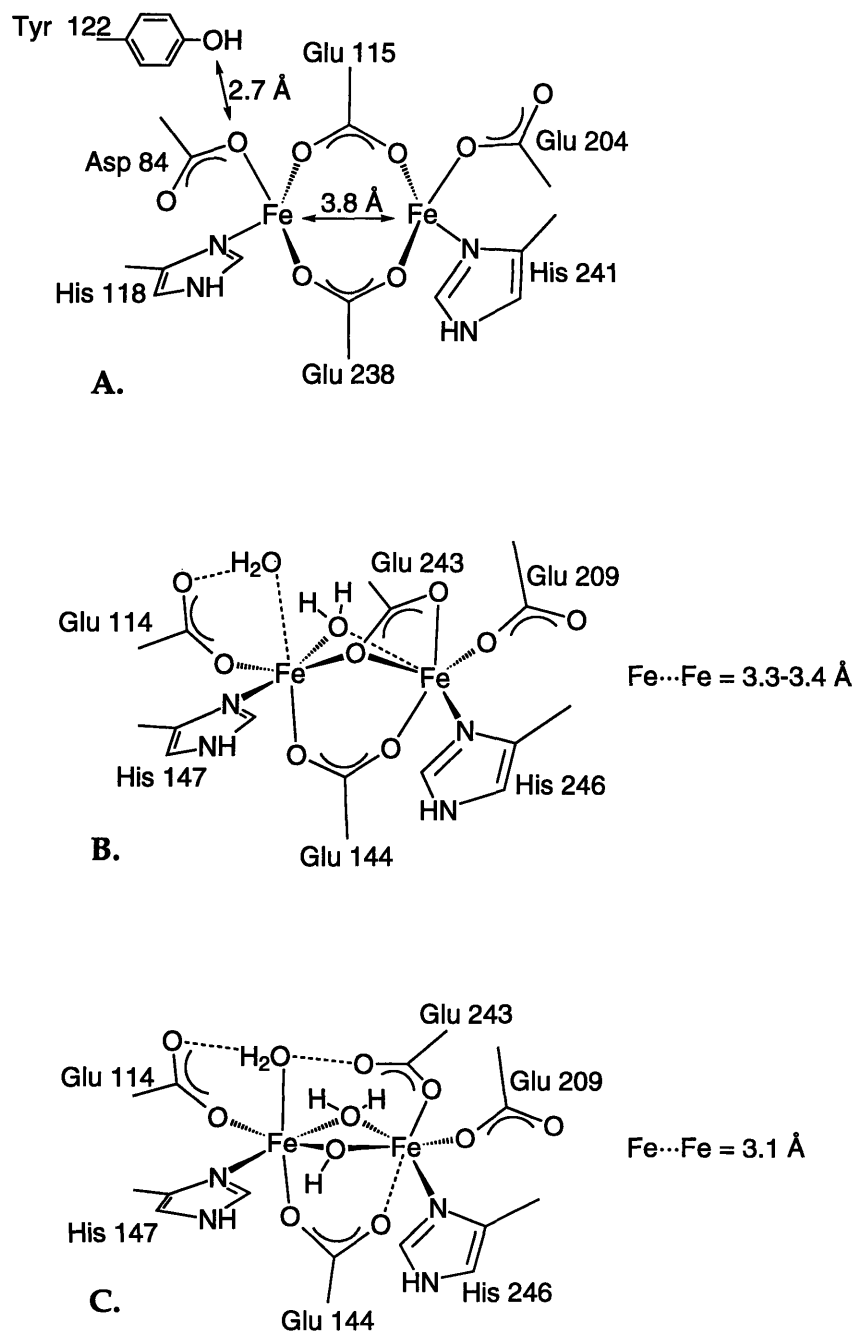
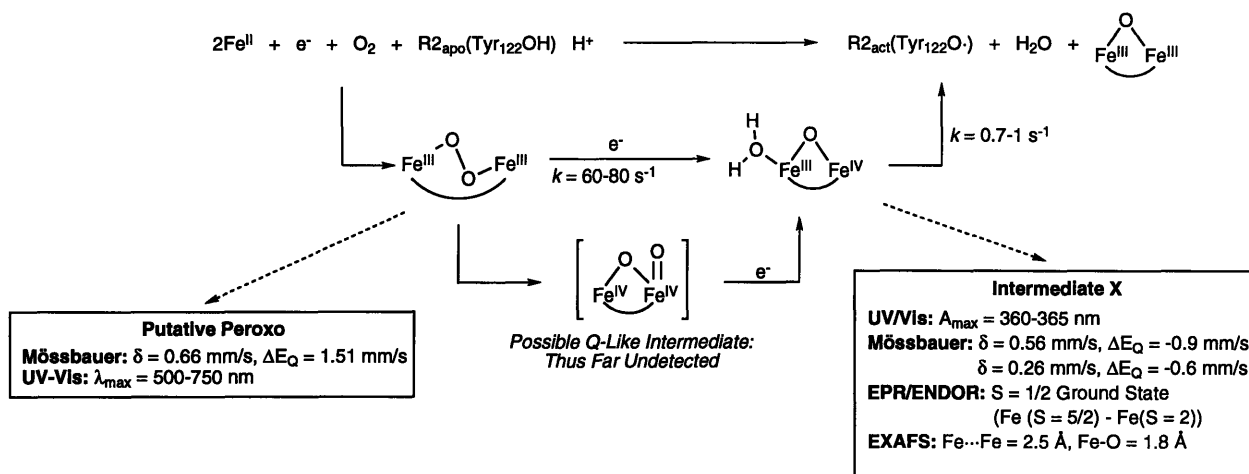


Figure 3.1. Chemdraw representations of the active site structures of: (A) reduced R2, (B) reduced MMOH (H_{red}), and (C) oxidized MMOH (H_{ox}).

Ribonucleotide Reductase



Soluble Methane Monooxygenase

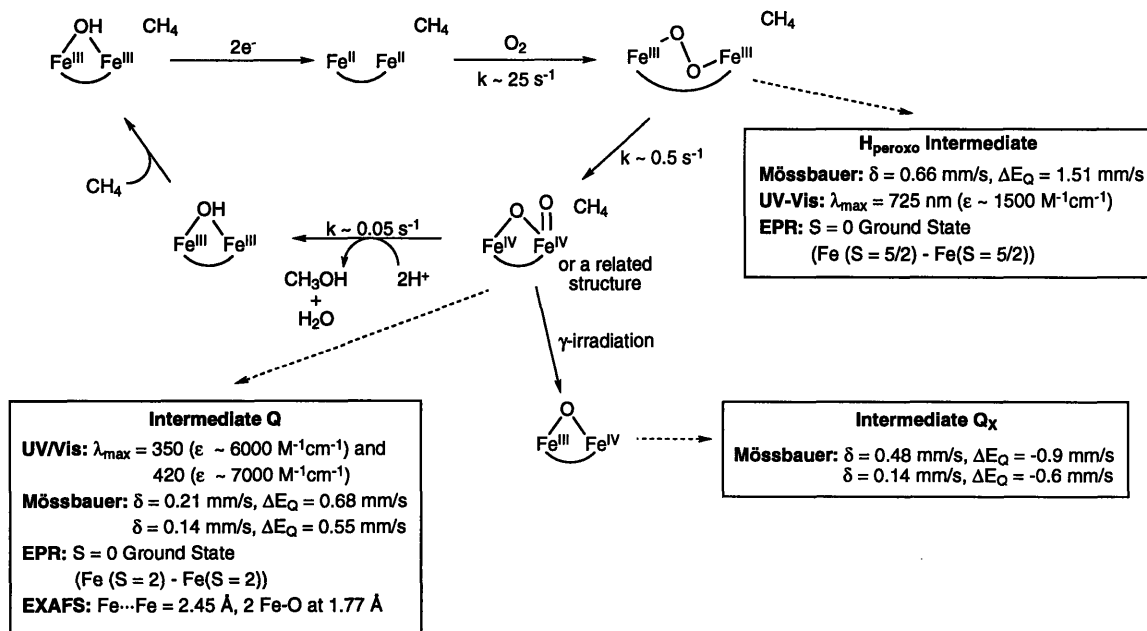


Figure 3.2. A summary of mechanisms elucidated for tyrosyl radical generation in the R2 subunit of ribonucleotide reductase, and for the catalytic oxidation of methane in sMMO.

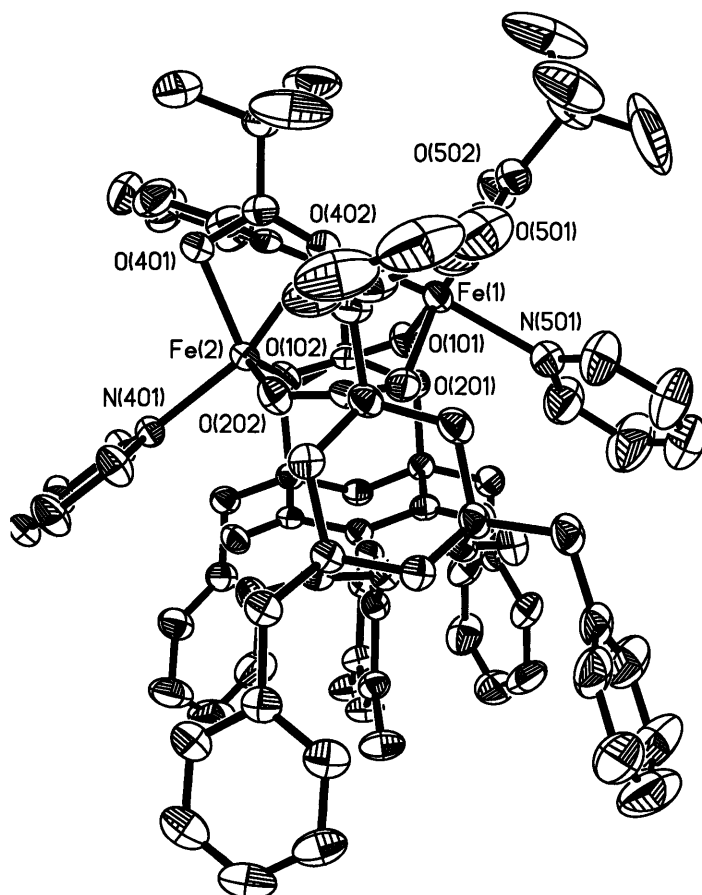


Figure 3.3. ORTEP diagram of [Fe₂(BXDK)(μ-O₂Ctert-Bu)(O₂Ctert-Bu)(py)₂] (6) with 50% thermal ellipsoids.

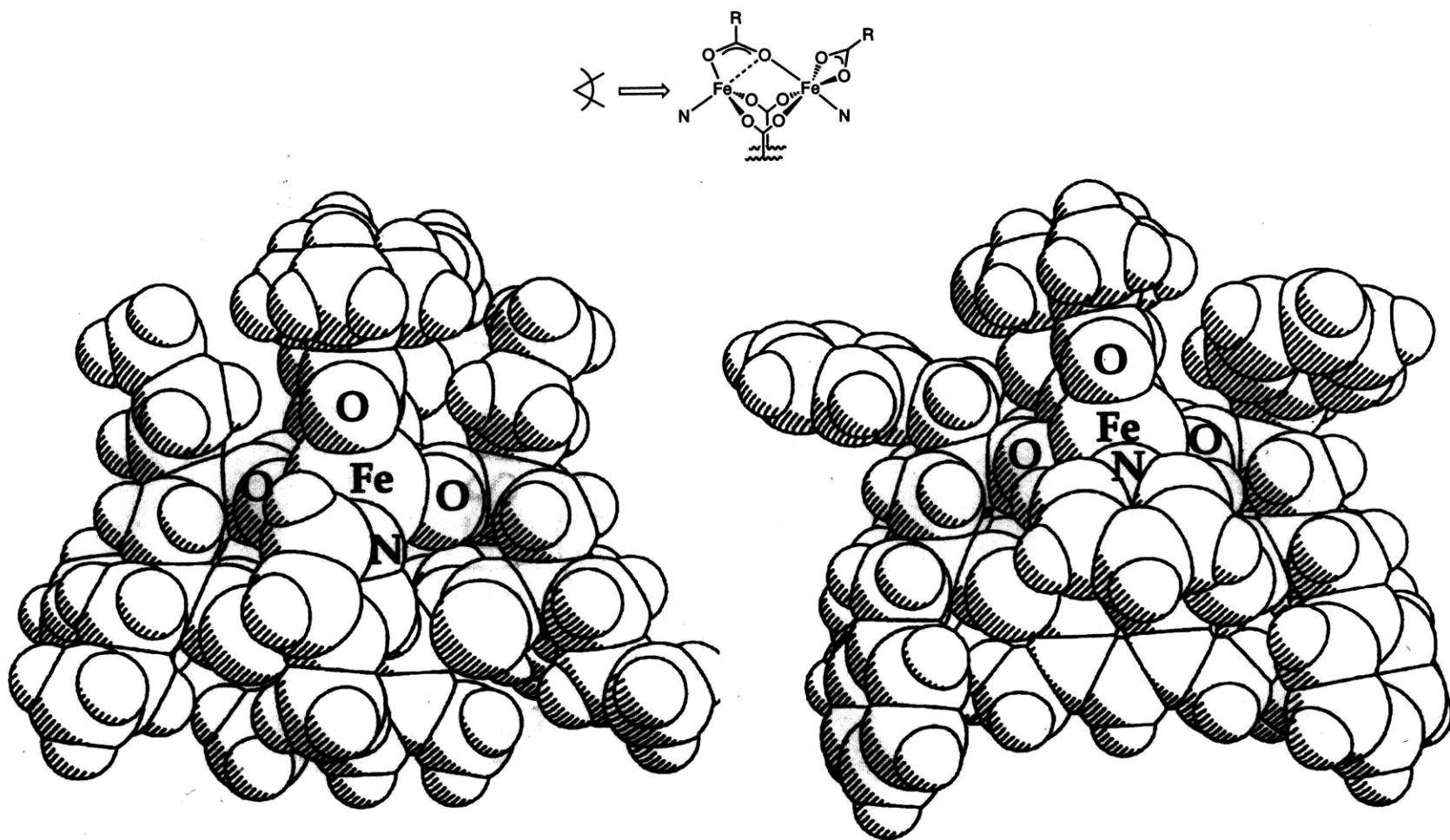


Figure 3.4. Space-filling representations of $[\text{Fe}_2(\text{PXDK})(\text{O}_2\text{Ct-Bu})(\mu\text{-O}_2\text{Ct-Bu})(\text{Me-lm})_2]$ from ref. 25 and $[\text{Fe}_2(\text{BXDK})(\text{O}_2\text{Ct-Bu})(\mu\text{-O}_2\text{Ct-Bu})(\text{py})_2]$ (6), looking down the Fe...Fe vector.

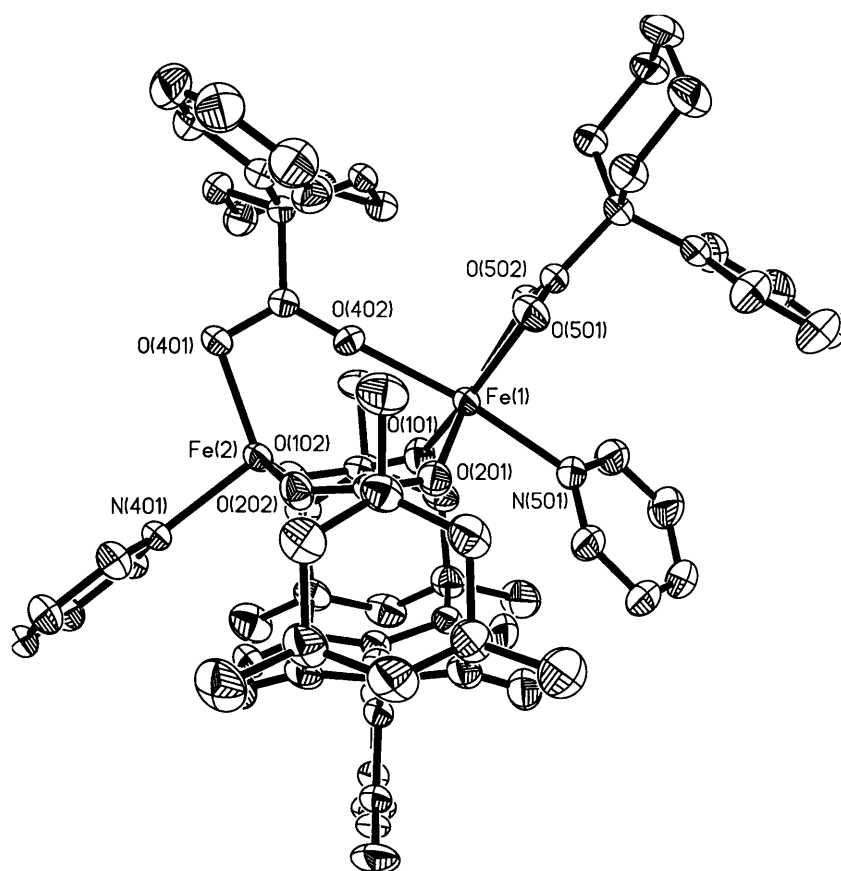


Figure 3.5. ORTEP diagram of $[\text{Fe}_2(\text{XDK})(\mu\text{-O}_2\text{CPhCy})(\text{O}_2\text{CPhCy})(\text{py})_2]$ (**7**) with 50% thermal ellipsoids.

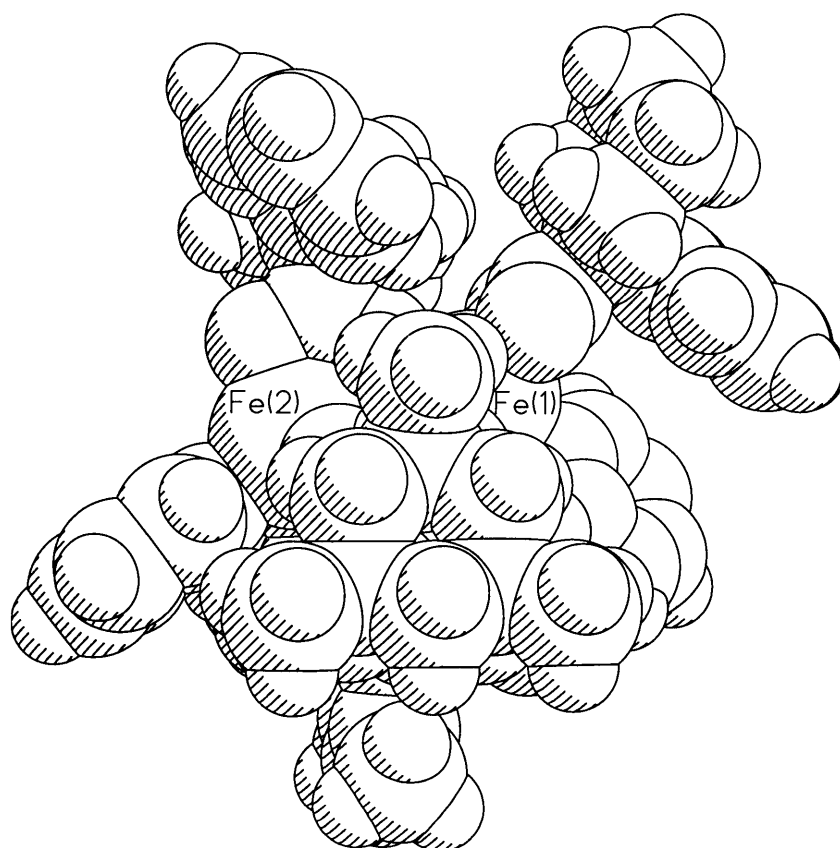


Figure 3.6. Space-filling representation of $[\text{Fe}_2(\text{XDK})(\mu\text{-O}_2\text{CPhCy})(\text{O}_2\text{CPhCy})(\text{py})_2]$ (7).

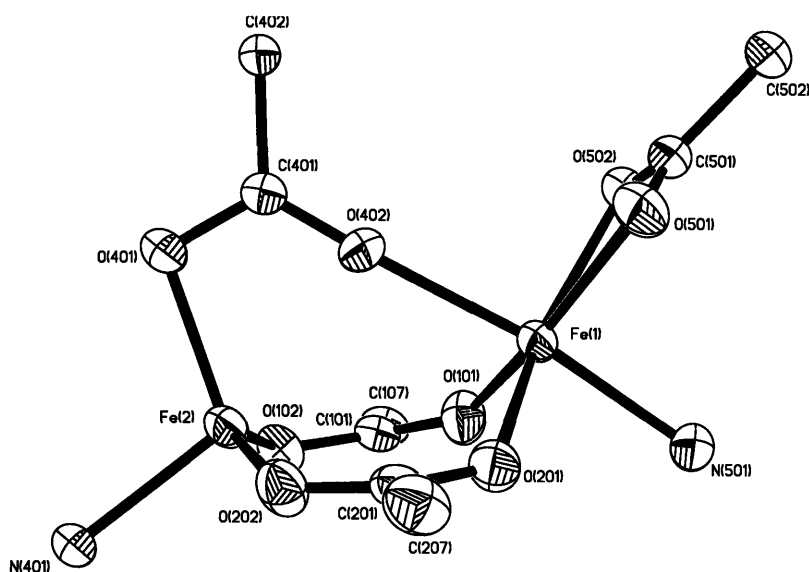


Figure 3.7. ORTEP diagram of $[\text{Fe}_2(\text{XDK})(\mu\text{-O}_2\text{CPhCy})(\text{O}_2\text{CPhCy})(\text{py})_2]$ (7) with 50% thermal ellipsoids, highlighting the iron coordination spheres. All other ORTEP and space-filling diagrams in Figures 3.3 and 3.5-3.10 are presented with identical orientations and numbering schemes.

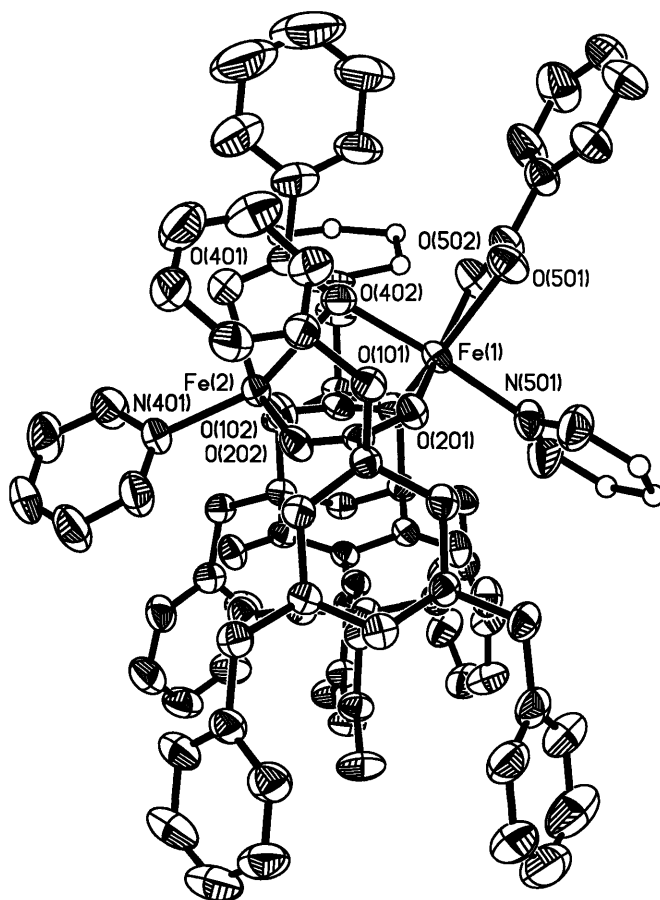


Figure 3.8. ORTEP diagram of $[\text{Fe}_2(\text{BXDK})(\mu\text{-O}_2\text{CPh})(\text{O}_2\text{CPh})(\text{py})_2]$ (**12**) with 50% thermal ellipsoids. Atoms represented as open circles were refined isotropically.

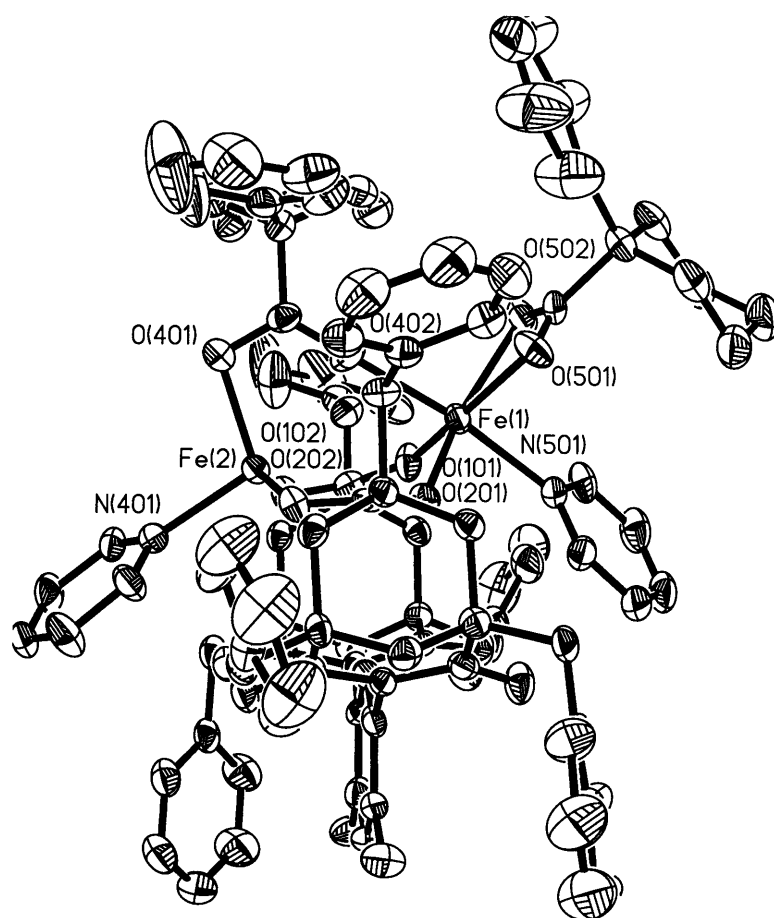


Figure 3.9. ORTEP diagram of [Fe₂(BXDK)(μ-O₂CPhCy)(O₂CPhCy)(py)₂] (**13**) with 50% thermal ellipsoids.

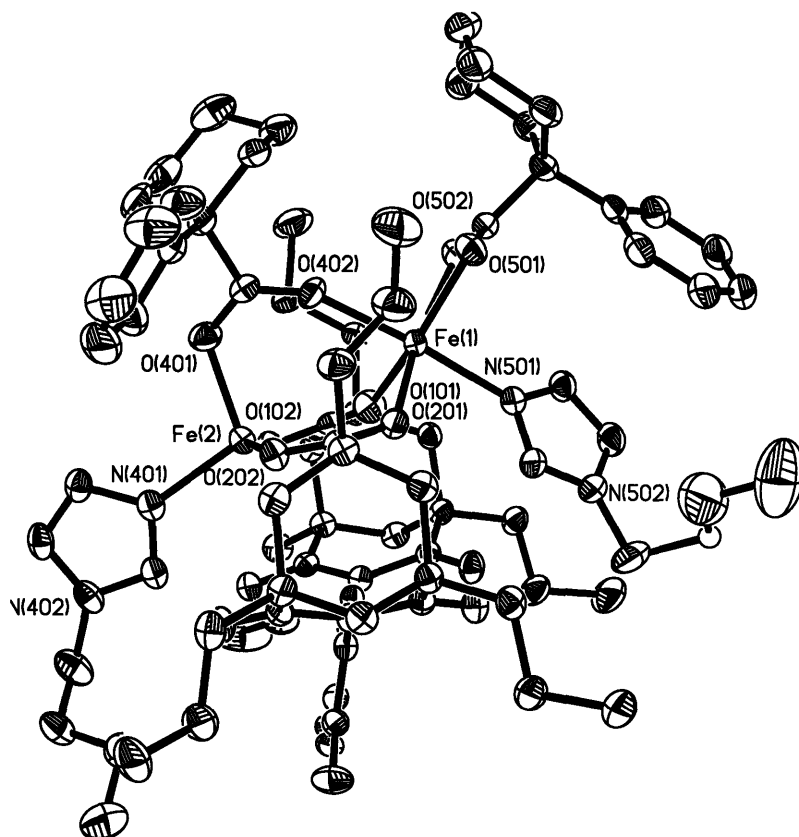
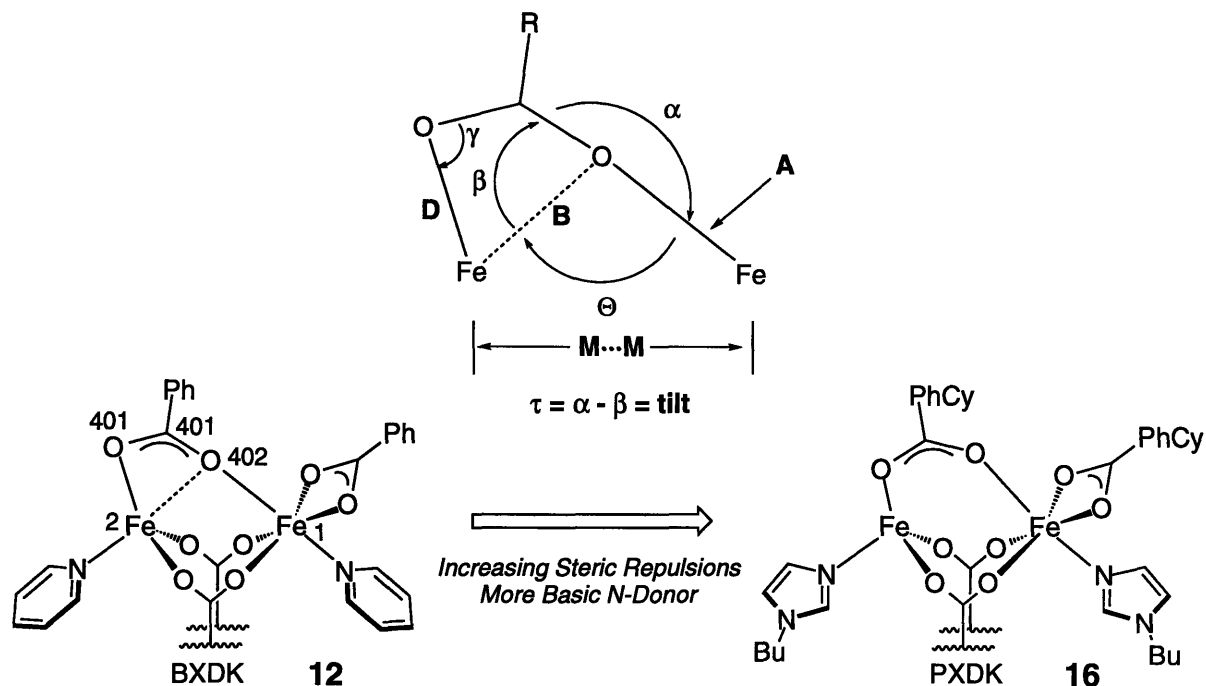


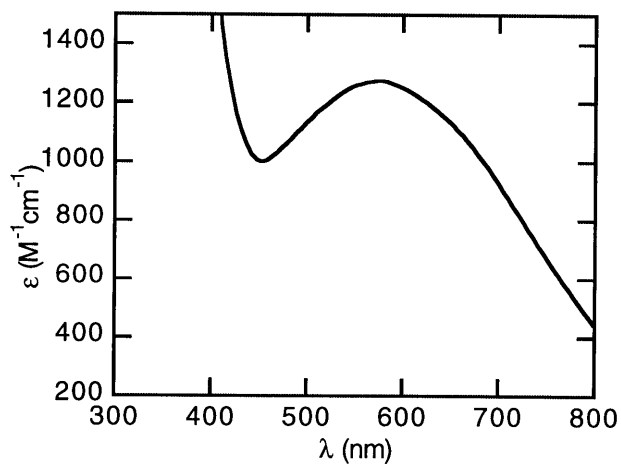
Figure 3.10. ORTEP diagram of $[\text{Fe}_2(\text{PXDK})(\mu\text{-O}_2\text{PhCy})(\text{O}_2\text{PhCy})(\text{Bu-Im})_2]$ (**16**) with 50% thermal ellipsoids. The PXDK carbon atom represented as an open circle was refined isotropically.



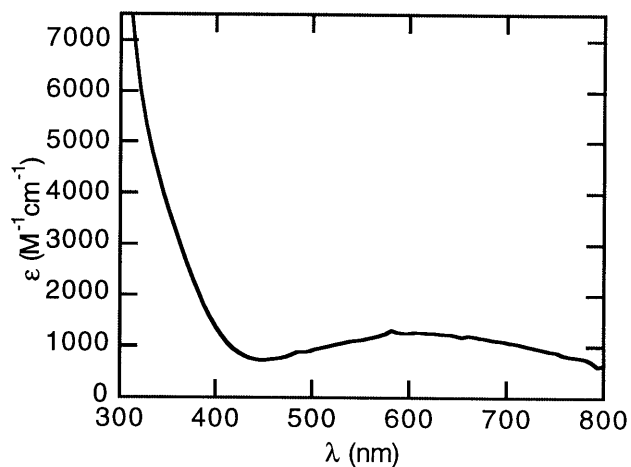
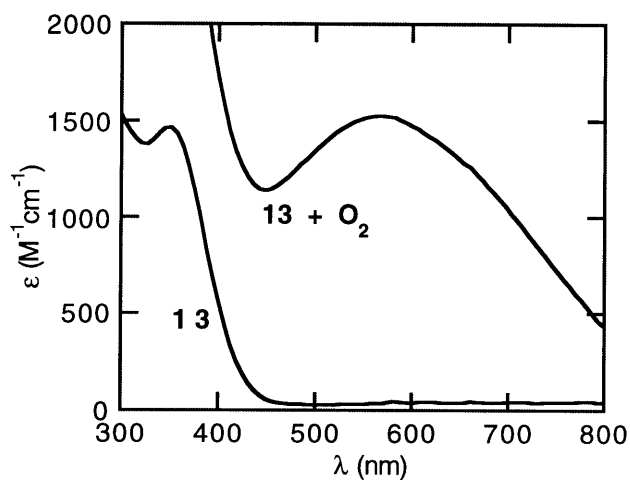
	12	6	7	13	16
XDK Deriv.	BXDK	BXDK	XDK	BXDK	PXDK
Ancil. Carbox.	Ph	<i>tert</i> -Bu	PhCy	PhCy	PhCy
N-Donor	py	py	py	py	Bu-Im
B = Fe2-O402	2.317(3)	2.340(2)	2.454(2)	2.489(4)	3.055(2)
D = Fe2-O401	2.047(4)	2.062(2)	2.050(2)	2.017(4)	2.006(4)
A = Fe1-O402	2.184(3)	2.172(2)	2.217(2)	2.194(4)	2.154(2)
$\Theta = \text{Fe1-O402-Fe2}$	102.55(12)	102.13(9)	100.47(6)	98.96(13)	87.72(6)
$\alpha = \text{Fe1-O402-C401}$	168.9(3)	170.6(2)	171.5(2)	168.0(3)	152.6(2)
$\gamma = \text{Fe2-O401-C401}$	96.3(3)	97.5(2)	100.15(13)	101.5(3)	116.6(2)
$\beta = \text{Fe2-O402-C401}$	84.6(3)	84.5(2)	81.84(12)	80.3(3)	67.46(15)
$\tau = \alpha - \beta$	73	73	71	66	36

Figure 3.11. A schematic illustration of the effect of ligand substituent steric repulsion on the orientation of the bridging ancillary carboxylate, including the relevant metrical parameters which account for this effect.

A.



B.



C.

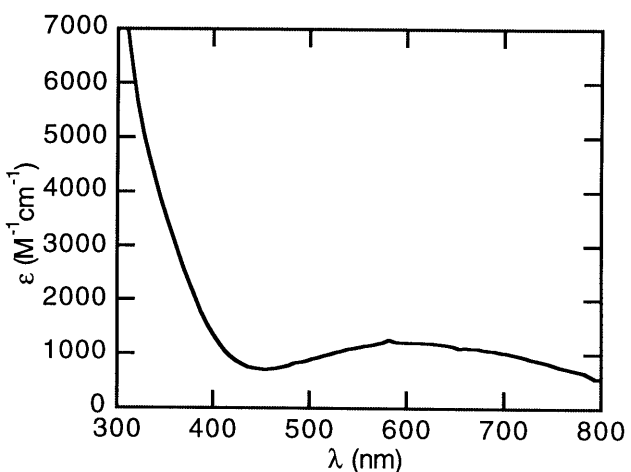
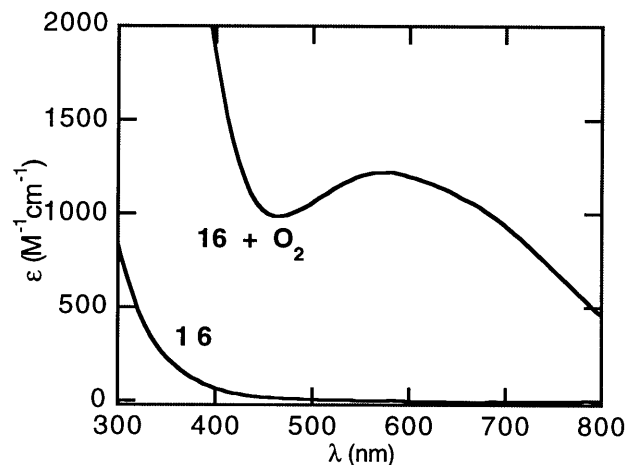
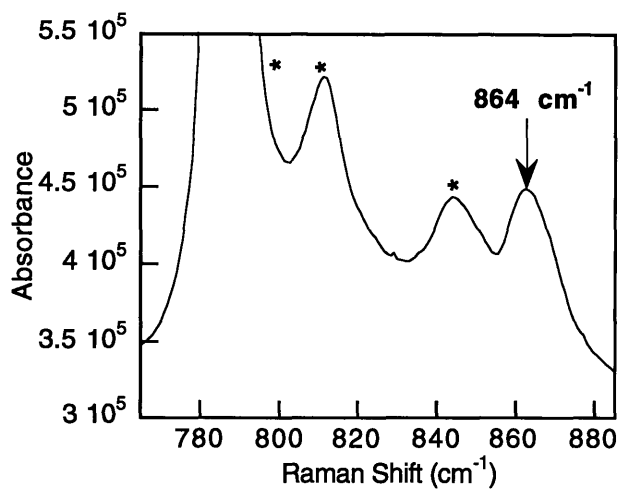
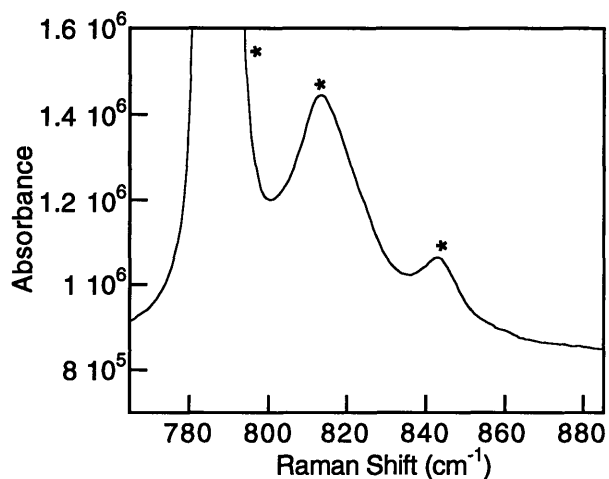


Figure 3.12. Representative UV-Vis spectra for the reaction of diferrous complexes **6-15** with O_2 at $-80^\circ C$: (A) $[Fe_2(BXDK)(\mu-O_2Ct-Bu)(O_2Ct-Bu)(py)_2]$ (**6**), $[Fe_2(BXDK)(\mu-O_2CPhCy)(O_2CPhCy)(py)_2]$ (**13**), and $[Fe_2(PXDK)(\mu-O_2CPhCy)(O_2CPhCy)(Bu-Im)_2]$ (**16**).

A.



B.



C.

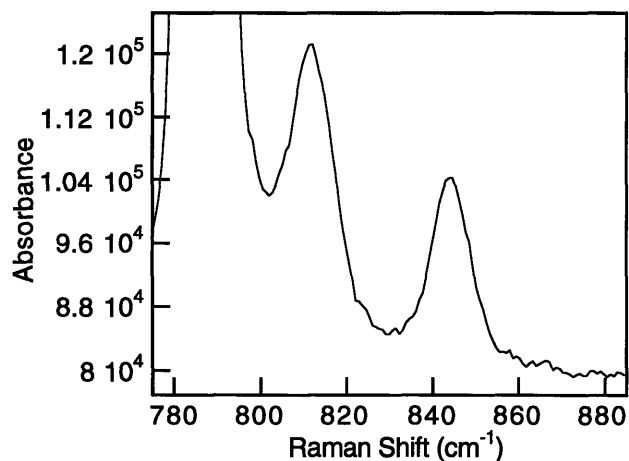
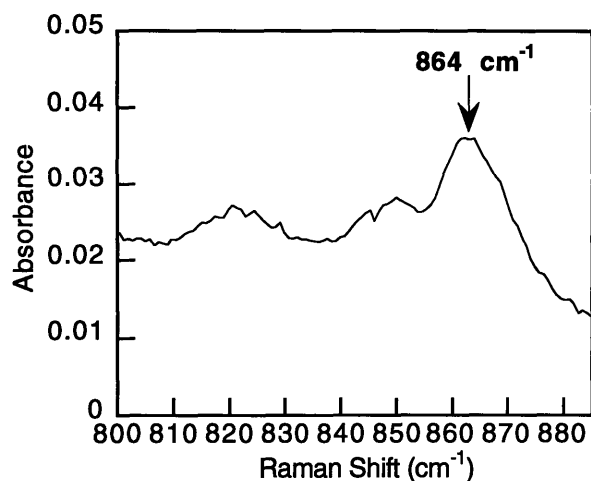
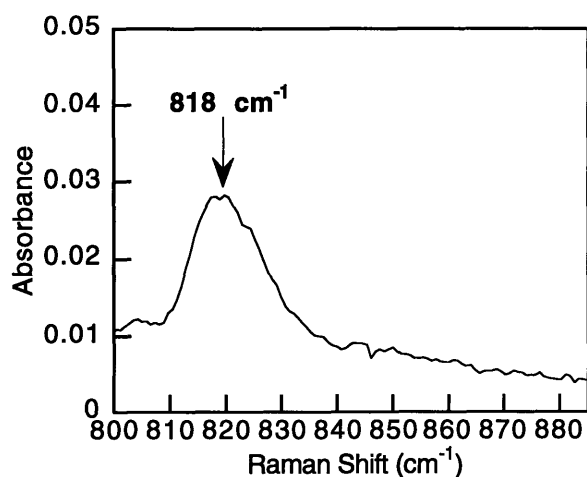


Figure 3.13. Resonance Raman spectra obtained with 647 nm excitation on fluid toluene solutions (-80 °C) of: (A) [Fe₂(¹⁶O₂)(PXDK)(O₂CPhCy)₂(Bu-Im)₂] (16.¹⁶O₂), (B) [Fe₂(¹⁸O₂)(PXDK)(O₂CPhCy)₂(Bu-Im)₂] (16.¹⁸O₂), and toluene. Peaks marked with an asterisk in A and B are due to toluene.

A.



B.



C.

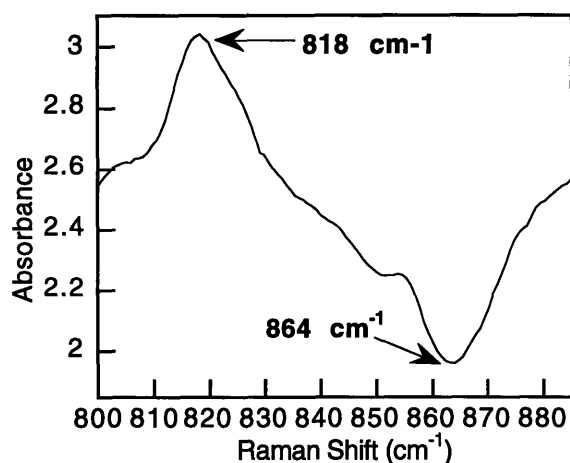
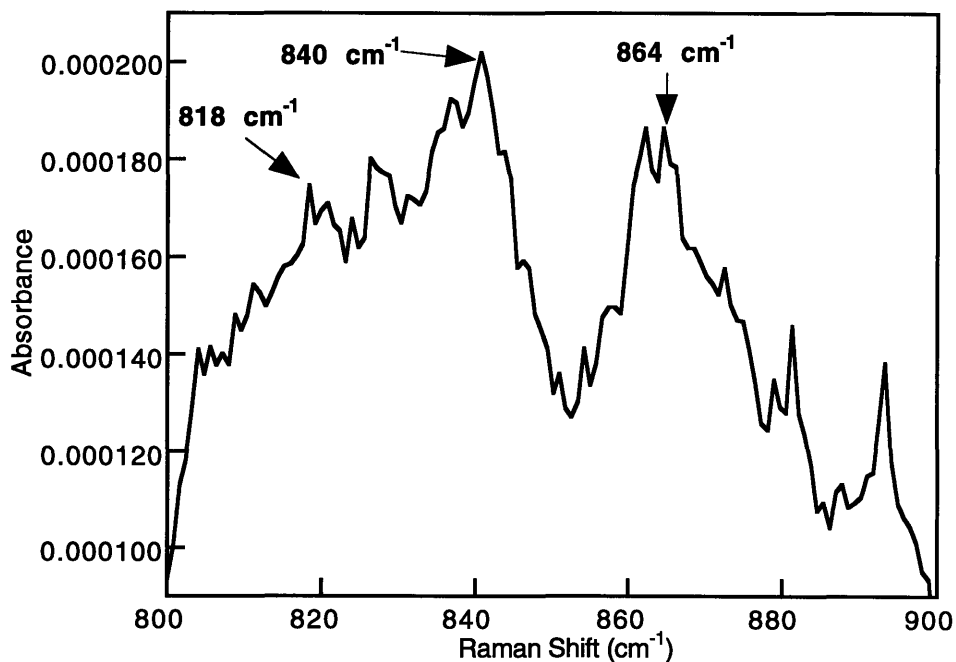
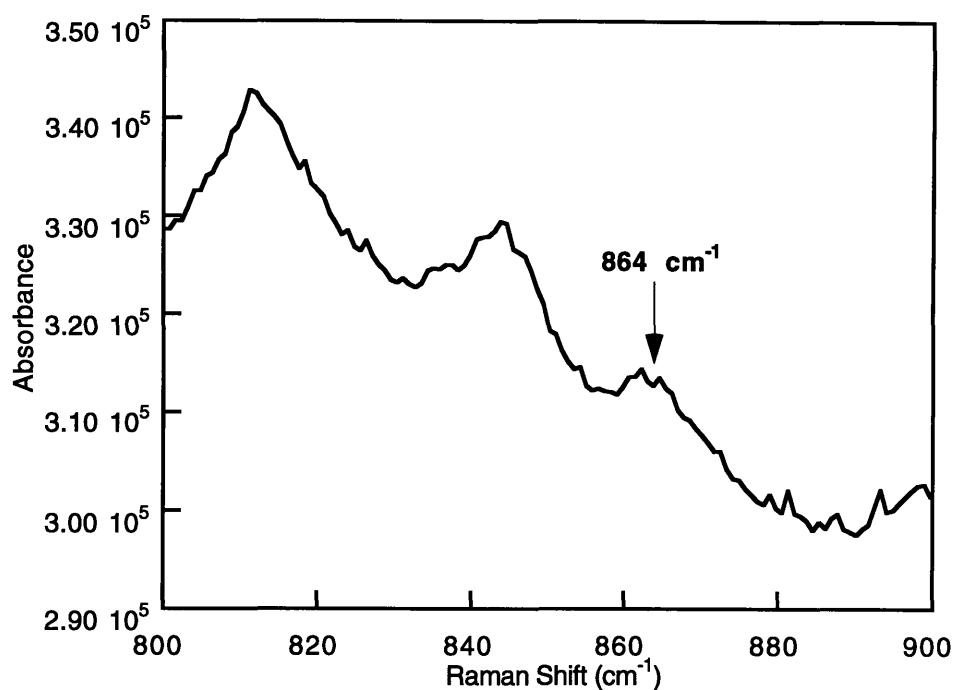


Figure 3.14. Solvent subtracted resonance Raman spectra for: (A) $[\text{Fe}_2(^{16}\text{O}_2)(\text{PXDK})(\text{O}_2\text{CPhCy})_2(\text{Bu-Im})_2]$ ($^{16}\text{O}_2$, normalized to the 788 cm^{-1} toluene peak), (B) $[\text{Fe}_2(^{18}\text{O}_2)(\text{PXDK})(\text{O}_2\text{CPhCy})_2(\text{Bu-Im})_2]$ ($^{18}\text{O}_2$, normalized as above), and (C) $^{16}\text{O}_2$ minus $^{18}\text{O}_2$ (scaled prior to subtraction).

A.



B.

Figure 3.15. (A) Resonance Raman spectrum obtained with 647 nm excitation on a fluid toluene solution ($-80\text{ }^{\circ}\text{C}$) of $[\text{Fe}_2(\text{O}_2)(\text{PXDK})(\text{O}_2\text{CPhCy})_2(\text{Bu-Im})_2]$ ($16\cdot\text{O}_2$), prepared from **16** and a 1:2:1 mixture of $^{16}\text{O}_2$, $^{16}\text{O}^{18}\text{O}$, and $^{18}\text{O}_2$. (B) Toluene solvent background subtracted from the spectrum in A (normalized to the 788 cm^{-1} toluene peak).

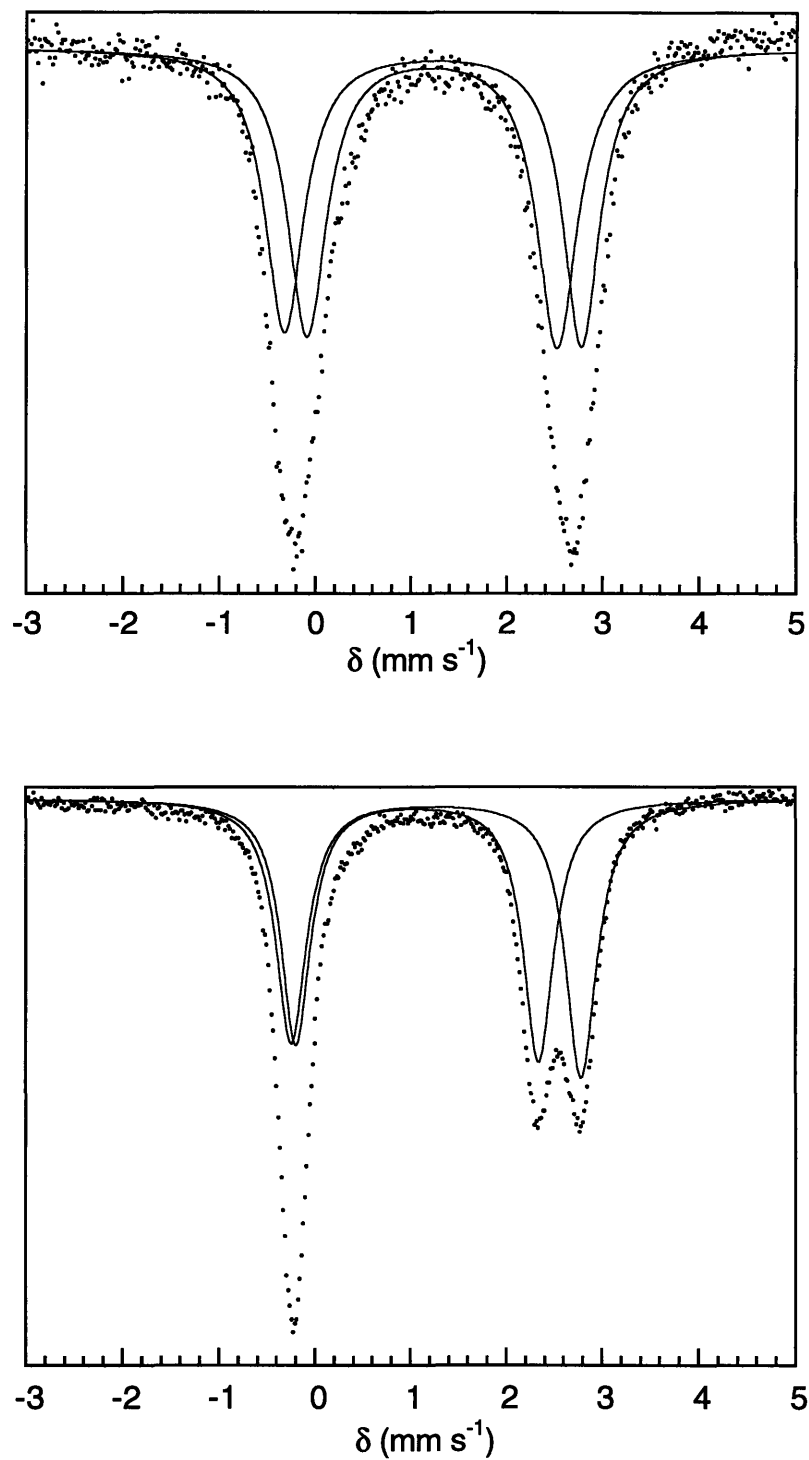


Figure 3.16. Mössbauer spectra (experimental data (\bullet), calculated fit (-)) of $[\text{Fe}_2(\text{BXDK})(\mu\text{-O}_2\text{CPhCy})(\text{O}_2\text{CPhCy})(\text{py})_2]$ (**13**), recorded in THF solution (Top) and in the solid state (Bottom), at 77 K.

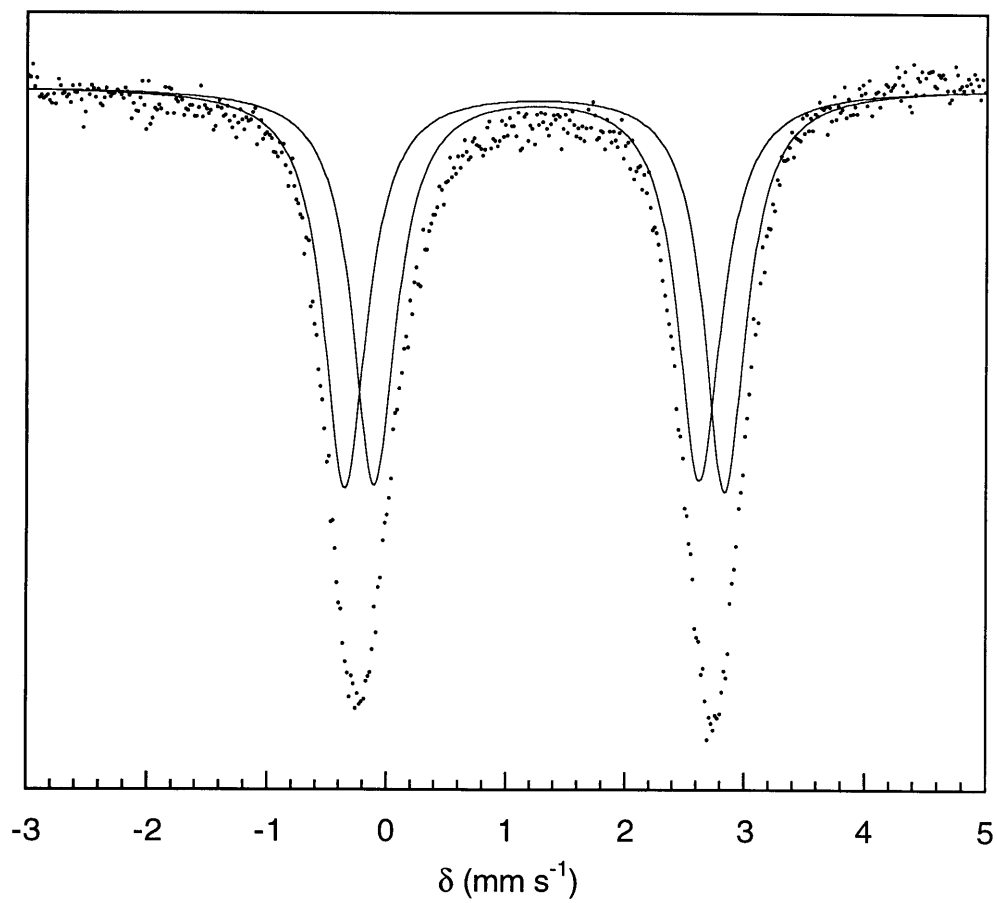


Figure 3.17. Mössbauer spectrum (experimental data (•), calculated fit (-)) of $[\text{Fe}_2(\text{XDK})(\mu\text{-O}_2\text{CPhCy})(\text{O}_2\text{CPhCy})(\text{Me-Im})_2]$ (**15**), recorded in THF solution at 77 K.

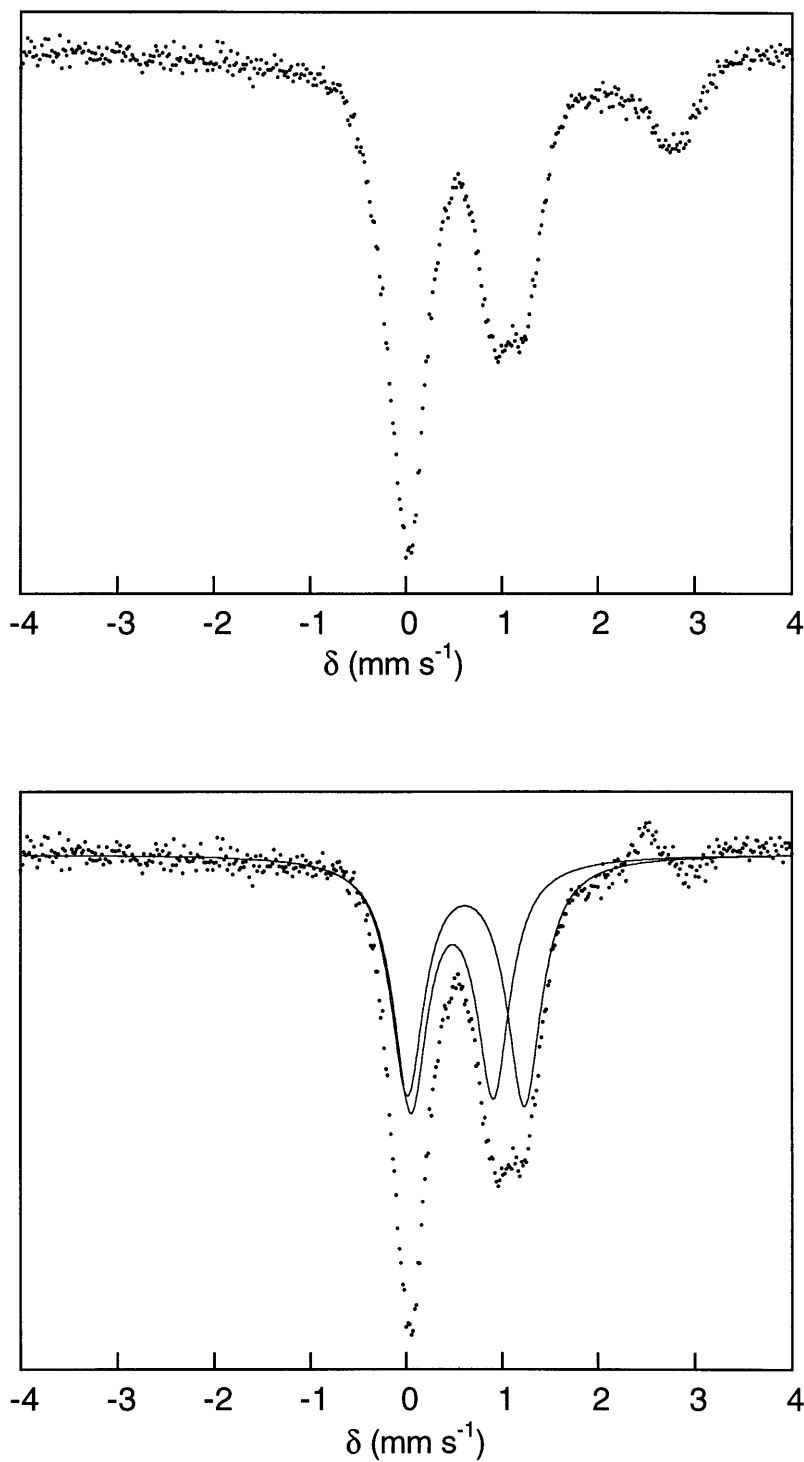


Figure 3.18. Mössbauer spectrum of $^{13}\text{O}_2$ recorded in THF solution at 77 K: (Top) experimental data, and (Bottom) experimental data (\bullet) with the diferrous component removed by subtraction and a calculated fit ($-$) to these data.

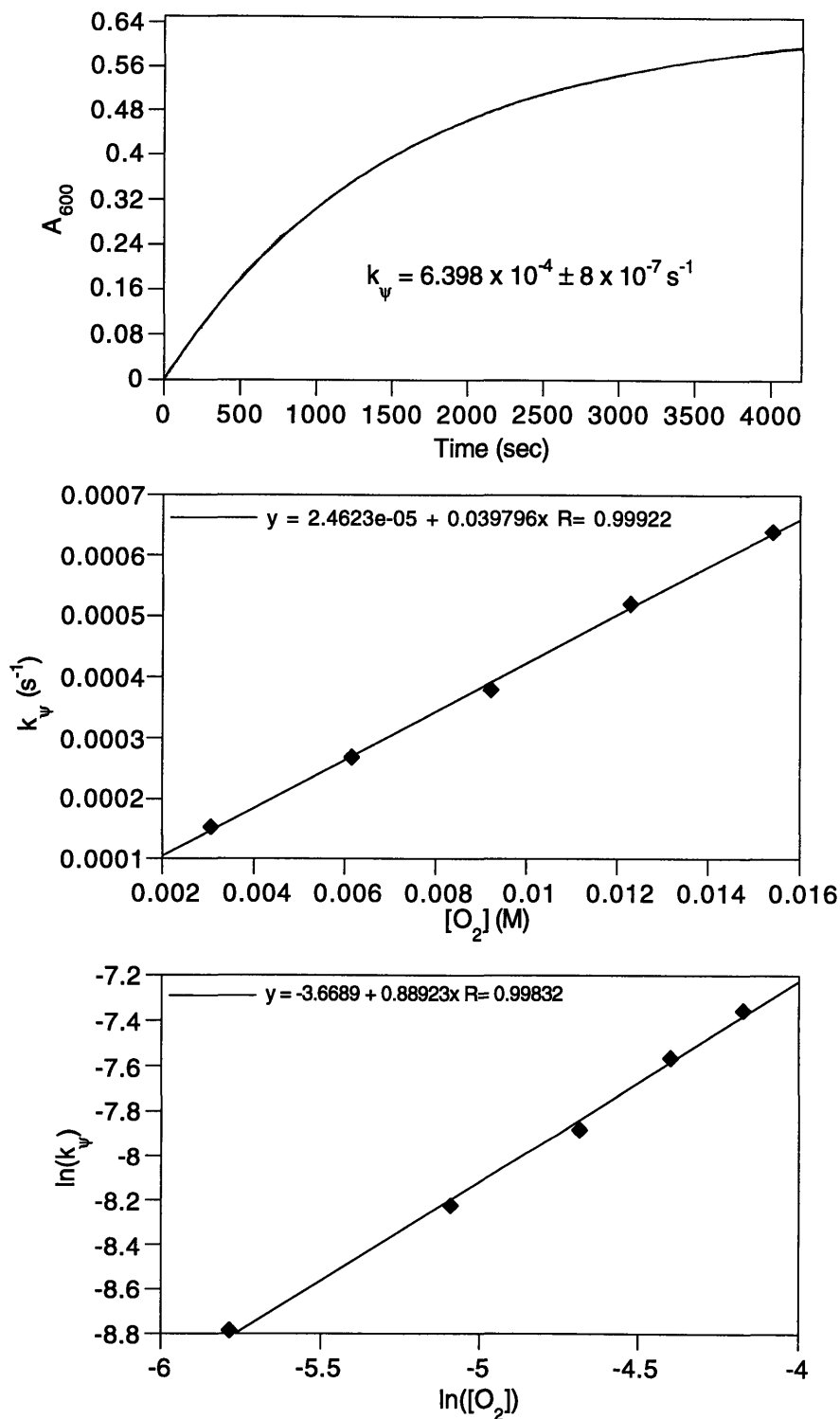


Figure 3.19. Kinetic data for the reaction of $[\text{Fe}_2(\text{BXDK})(\mu\text{-O}_2\text{Ct-Bu})(\text{O}_2\text{Ct-Bu})(\text{py})_2]$ (6) with O_2 in THF at -77°C : (Top) plot of A_{600} vs. time with $[\text{6}]_0 = 0.73 \text{ mM}$ and $[\text{O}_2] = 15.4 \text{ mM}$ and a fit to a first order exponential buildup, (Middle) plot of k_ψ vs. $[\text{O}_2]$, and (Bottom) plot of $\ln(k_\psi)$ vs. $\ln([\text{O}_2])$.

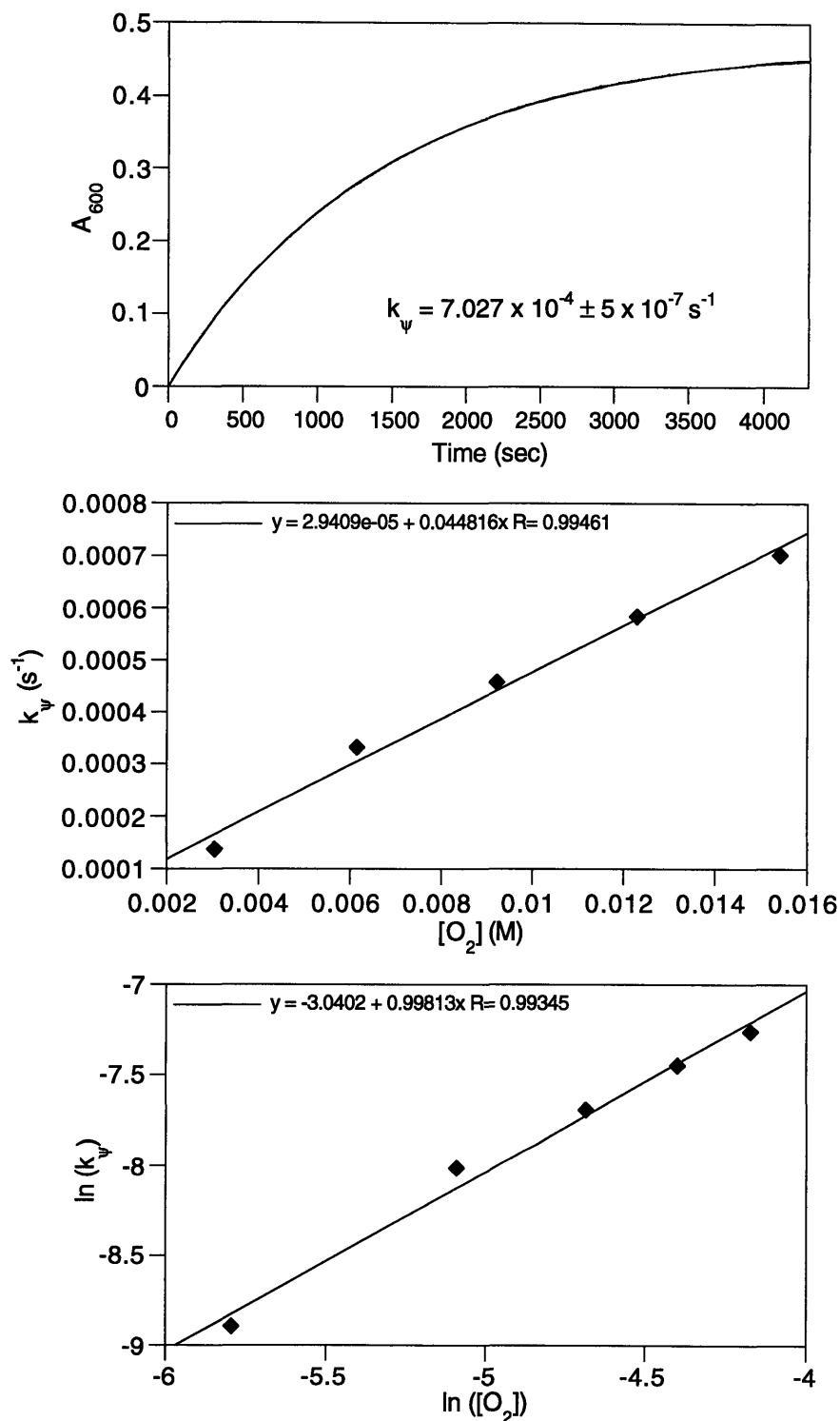


Figure 3.20. Kinetic data for the reaction of $[\text{Fe}_2(\text{XDK})(\mu\text{-O}_2\text{CPhCy})(\text{O}_2\text{CPhCy})(\text{py})_2]$ (7) with O_2 in THF at -77°C : (Top) plot of A_{600} vs. time with $[7]_0 = 0.56 \text{ mM}$ and $[\text{O}_2] = 15.4 \text{ mM}$ and a fit to a first order exponential buildup, (Middle) plot of k_ψ vs. $[\text{O}_2]$, and (Bottom) plot of $\ln(k_\psi)$ vs. $\ln([\text{O}_2])$.

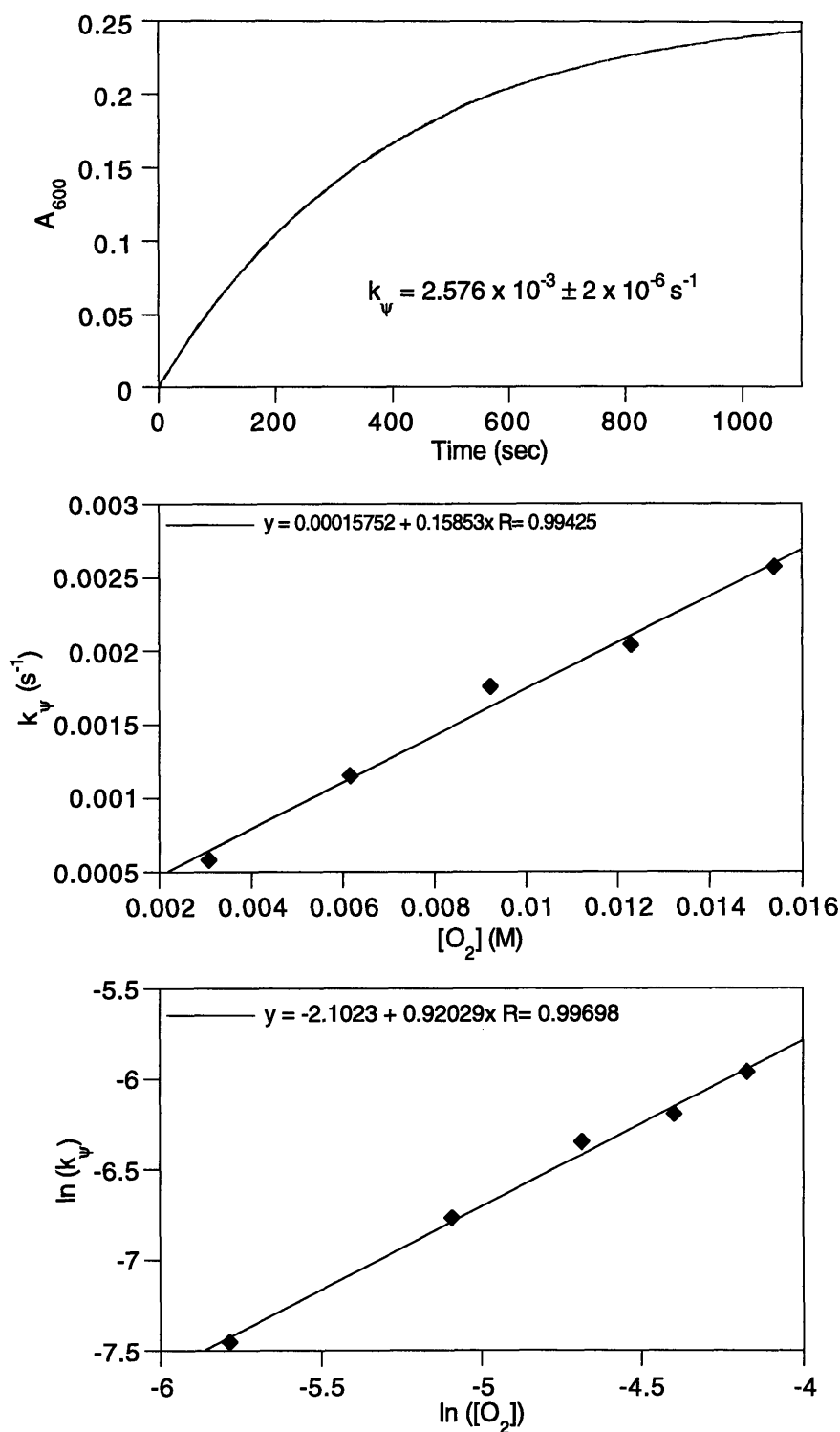


Figure 3.21. Kinetic data for the reaction of $[\text{Fe}_2(\text{BXDK})(\mu\text{-O}_2\text{CPhCy})(\text{O}_2\text{CPhCy})(\text{py})_2]$ (13) with O_2 in THF at -77°C : (Top) plot of A_{600} vs. time with $[\mathbf{13}]_0 = 0.41 \text{ mM}$ and $[\text{O}_2] = 15.4 \text{ mM}$ and a fit to a first order exponential buildup, (Middle) plot of k_ψ vs. $[\text{O}_2]$, and (Bottom) plot of $\ln(k_\psi)$ vs. $\ln([\text{O}_2])$.

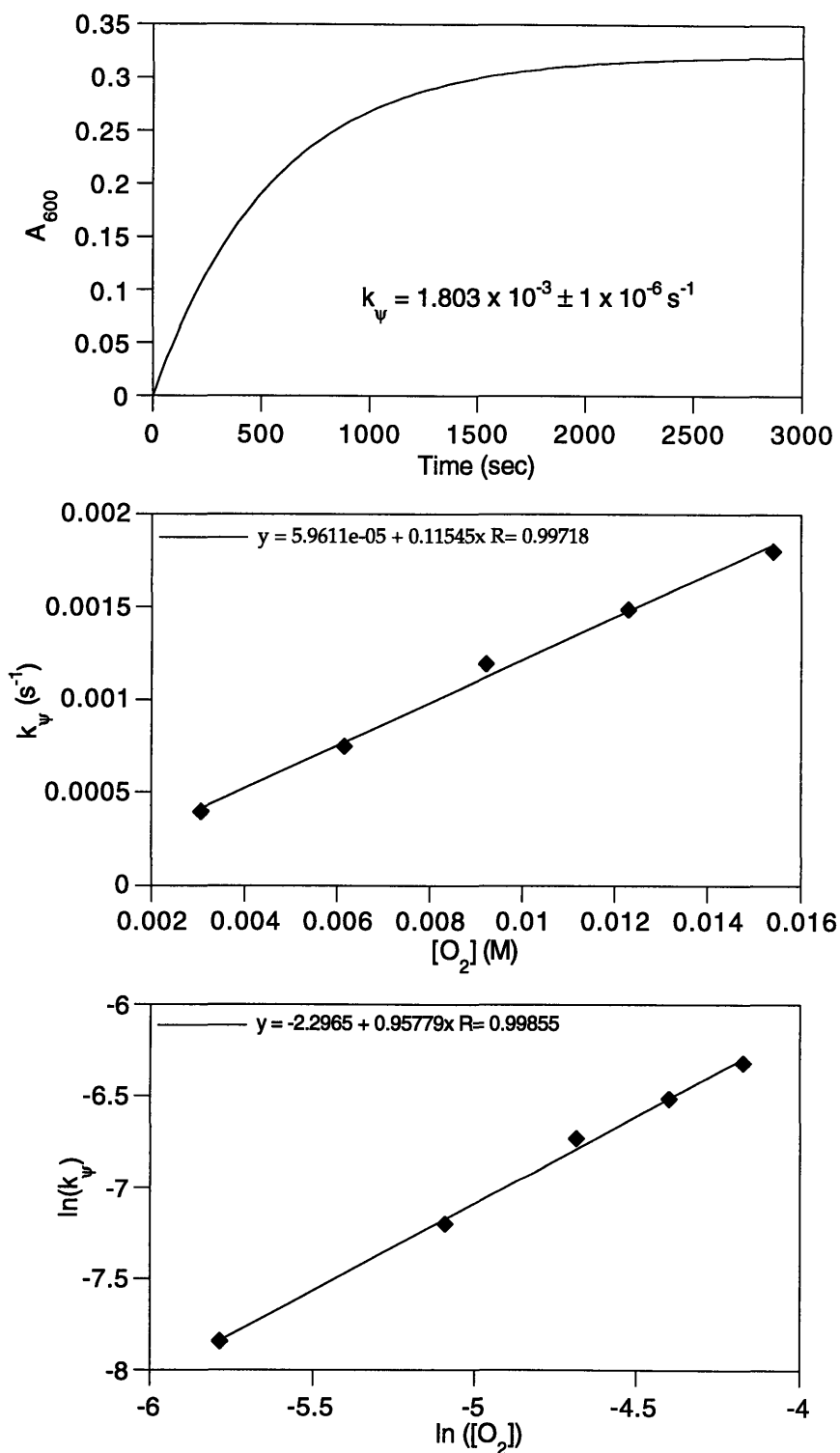


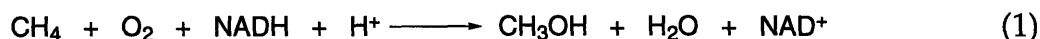
Figure 3.22. Kinetic data for the reaction of $[\text{Fe}_2(\text{BXDK})(\mu\text{-O}_2\text{CAr})(\text{O}_2\text{CAr})(\text{py})_2]$ (14) with O_2 in THF at -77°C : (Top) plot of A_{600} vs. time with $[\mathbf{14}]_0 = 0.39 \text{ mM}$ and $[\text{O}_2] = 15.4 \text{ mM}$ and a fit to a first order exponential buildup, (Middle) plot of k_ψ vs. $[\text{O}_2]$, and (Bottom) plot of $\ln(k_\psi)$ vs. $\ln([\text{O}_2])$.

Chapter IV

The Reactivity of Well Defined Diiron(III) Peroxo Complexes Towards Substrates: Addition to Electrophiles and Hydrocarbon Oxidation

Introduction

The selective and efficient catalytic oxidation of hydrocarbon substrates under mild conditions continues to be a formidable goal for the synthetic chemist.^{1,2} In Nature, obligate methanotrophic bacteria carry out one of the most challenging types of these reactions, the conversion of methane to methanol under ambient conditions (eq 1), utilizing a soluble³⁻⁵ or particulate^{6,7} methane monooxygenase



(sMMO or pMMO). The soluble form houses a diiron center in its hydroxylase component (MMOH), the site of methane oxidation. This protein is a member of a class of non-heme diiron enzymes which carry out a variety of selective hydrocarbon oxidative processes.^{3,5} A closely related enzyme is ribonucleotide reductase, which uses O₂ at a diiron center in its R2 subunit (RNR-R2) to generate a tyrosyl radical which in turn assists in the catalytic reduction of ribonucleotides. We seek to prepare functional synthetic models of these systems, with the goals of aiding in the elucidation of the biological O₂-activation mechanisms, and to develop practical hydrocarbon oxidation catalysts.

The current state of knowledge regarding these systems, including their structural, spectroscopic, and mechanistic ties, was described in detail in Chapter 3; therefore, only a brief review will be provided here. Metal-oxygen intermediates have been characterized for sMMO^{4,8,9} and RNR-R2¹⁰⁻¹² by coupling stopped-flow and rapid freeze quench methods to a variety of spectroscopies. Both proteins react with O₂ in their diferrous forms to afford a diiron(III) peroxo complex as the first detected intermediate. For sMMO, this species converts to a diiron(IV) species, Q, which is believed to be the active substrate oxidant. In RNR-R2, the peroxo converts to a diiron(III)(IV) complex, X, possibly through a diiron(IV) intermediate like

sMMO-Q. Intermediate X reacts with an adjacent tryrosine, formally by hydrogen atom abstraction, to yield a catalytically viable tyrosyl radical.

Much effort has been expended to mimic the oxidation chemistry of non-heme enzymes with iron(III) complexes with either hydrogen peroxide¹³⁻¹⁶ or *tert*-butylhydro peroxide¹⁷⁻¹⁹ as the oxidant. By contrast, the reactivity of discrete, well defined diiron(III) peroxo complexes derived from iron(II) precursors and O₂ is essentially unexplored. Given that sMMO utilizes a reductive O₂ activation pathway, it is desirable to track an oxidation reaction in a model system from the dioxygen binding step, to formation of a high valent oxidant, and finally through the substrate oxidation event. Such a study would provide invaluable insight into the enzymatic mechanism, and as well as spawn the development of practical oxidation catalysts. Here we provide a complete analysis of the reactivity of diiron(III) peroxo complexes derived from the *m*-xylylenediamine bis(kemp's triacid)imide (H₂XDK) ligand system.²⁰

Experimental Section

General Considerations. The complexes [Fe₂(μ-O₂)(PXDK)(μ-O₂CPhCy)(O₂CPhCy)(Bu-Im)₂] (1) and [Fe₂(μ-O₂)(BXDK)(μ-O₂CPhCy)(O₂CPhCy)(py)₂] (2) were prepared from O₂ and the diiron(II) precursors at -77 °C according to an established procedure.²⁰ Authentic samples of 3,3',5,5'-tetra-*tert*-butyl-1,1'-bi-2,2'-phenol,²¹ cyclopentylhydroperoxide,²² and 2-hydroxytetrahydrofuran,²³ were synthesized according to the literature methods, and their purity was confirmed by ¹H NMR and/or GC and GC/MS analyses. Dioxygen (99.994%, BOC Gases) was dried by passing the gas stream through a column of Drierite. Labeled dioxygen (95% ¹⁸O₂) toluene, and THF reagents were purchased from Cambridge Isotope Laboratories, Inc. The solvents were vacuum transferred from Na/benzophenone ketyl. All other reagents were procured from commercial sources and used as received unless otherwise noted. THF, cyclopentane, toluene, pentane, and Et₂O were distilled from

sodium benzophenone ketyl under nitrogen. Pentane, cyclopentane, isopentane, 1-hexene, and cyclohexene were distilled from sodium under nitrogen. Dichloromethane, 1,2-dichloroethane, and pyridine were distilled from CaH_2 under nitrogen. All air sensitive manipulations were carried out either in a nitrogen filled Vacuum Atmospheres drybox or by standard Schlenk line techniques at room temperature unless otherwise noted.

Physical Measurements. NMR spectra were recorded on a Bruker AC-250 or Varian XL-300 spectrometer. ^1H NMR chemical shifts are reported versus tetramethylsilane and referenced to the residual solvent peak. FTIR spectra were recorded on a BioRad FTS-135 FTIR spectrometer.

GC and GC/MS. Analyses were carried out on a HP-5970 gas chromatograph connected to a HP-5971 mass analyzer. Alltech Econo-cap EC-WAX capillary columns of dimensions (15 m x 0.53 mm x 1.2 μm) and (30 m x 0.25 mm x 0.25 μm) were used for GC and GC/MS studies, respectively, except for triphenylphosphine and triphenylphosphine oxide, which were assayed with a HP-101 (12 m x 0.2 mm x 0.2 mm) capillary column. The following method was used to effect nearly all separations: initial temperature = 50 $^\circ\text{C}$, initial time = 10 min, and a temperature ramp of 50-200 $^\circ\text{C}$ at 10 deg/min. The products were identified by comparing their retention times and mass spectral patterns to those of authentic standards. Integrations were acquired by FID detection run in parallel to mass spectrometry by using an HP-3393 integrator. FID response calibration constants were measured by running calibration curves with authentic samples and an internal standard, either cyclopentanone or cyclohexanone.

For kinetic isotope or $^{18}\text{O}_2$ labeling studies, the ratio of isotopomers was determined by mass spectral integration of each parent ion. The integration response was assumed to be identical for the isotopomers.

Low-Temperature UV-vis Spectroscopy. Spectra were recorded on a HP8452A diode array spectrophotometer by using a custom manufactured immersion dewar, equipped with a 3 mL cell (1 cm pathlength) with quartz windows connected to a 14/20 female joint via a 10 cm long glass tube. A temperature of $-77\text{ }^{\circ}\text{C}$ was maintained with a dry ice/acetone bath and monitored with a Sensortek Model BAT-12 thermocouple thermometer.

Resonance Raman Spectroscopy. Raman data were acquired by using a Coherent Innova 90 argon laser with an excitation wavelength of 647.1 nm and 65 mW of power. A 0.6-m single monochromator (1200 grooves/nm grating), with an entrance slit of 100 μm , and a liquid nitrogen cooled-CCD detector (Princeton Instruments, Inc.) were used in a standard backscattering configuration. A holographic notch filter (Kaiser Optical Systems) was used to attenuate Rayleigh scattering. Spectra of all samples were collected in toluene solution at $-77\text{ }^{\circ}\text{C}$ with the same custom-manufactured dewar used to acquire low-temperature UV-vis spectra. Solute concentrations were made as high as possible depending on the solubility of the reduced sample, $\sim 20\text{ mM}$ in the best cases, to ensure an optimal signal-to-noise ratio. High vacuum line techniques were used to transfer $^{18}\text{O}_2$ and to manipulate the resulting samples. A total of 1000 scans each with a three second exposure time were collected for each sample. Raman shifts were calibrated with toluene as an internal standard. The data were processed by using CSMA software (Princeton Instruments, Inc. Version 2.4A) on a Gateway 2000 computer, and the resulting ASCII files were processed with Kaleidagraph (Abelbeck Software).

Synthetic Methods. General Procedures for Stoichiometric Reactions of 1 or 2 at $-77\text{ }^{\circ}\text{C}$. All reactions were monitored by low-temperature UV-vis spectroscopy. The dewar was equipped with a stir bar and loaded in the drybox with 5.0 mL of a 0.50-1.0 mM solution of the diiron(II) precursors of 1 or 2. The apparatus was topped with a rubber septum, brought out of the box, placed under a positive N_2 pressure,

and cooled to $-77\text{ }^{\circ}\text{C}$ with a dry ice acetone bath. A spectrum was recorded, and then the sample was subjected to a gentle purge of O_2 at atmospheric pressure for 15 s, after which time the peroxy complex 1 or 2 had formed to completion, as judged by the blue color which had developed. Excess O_2 was removed with a 5 min Ar purge of the solution. Another spectrum was recorded, and then 200 μl of the test reagent solution was added dropwise to a stirred solution of the peroxy complex, taking care not to allow the peroxy solution to warm above $-77\text{ }^{\circ}\text{C}$. For the CO_2 reactions, the gas was bubbled gently through the solution of the peroxy complex over ~ 30 s. **Note: Owing to the low temperature, this procedure introduces a large excess of CO_2 to the solution, and therefore considerable caution should be taken when venting the solution upon warming so as to not build up a dangerous pressure level.** The resulting mixture was allowed to stir for 15-30 s, by which time a homogenous solution had formed. Additional spectra were recorded, and the reaction was monitored to completion, as judged by the complete decay of the peroxy charge transfer band. The quantities of reagents and solvent used for each reaction are listed in Table 4.1. UV-vis spectra are displayed in Figures 4.1-4.5 and 4.8-4.4.12.

General Procedures for Solvent Oxidation Studies. Samples were prepared in the immersion dewar described above or in a round bottom flask sealed with a rubber septum. All sample volumes were 5.0 mL. Peroxy complex 1 was generated in the usual manner at $-77\text{ }^{\circ}\text{C}$. It was stable for at least several hours at this temperature, as judged by UV-vis spectroscopy, which afforded identical traces in all the solvents. For thermolysis reactions carried out under argon, the peroxy solution was degassed by carrying out three vacuum/Ar purge cycles and three freeze-pump-thaw cycles with liquid nitrogen, and then backfilled with 1 atm of Ar prior to warming. Warming to room temperature over five min was accomplished by removing the dry ice/acetone bath from the stirred solution. Warming over 2 h was carried out by removing the excess dry ice while keeping the flask or UV-vis cell in

contact with the bath. Solutions incubated at low temperature for longer time periods were placed in a -85 °C refrigerator. After addition of an internal standard, the crude reaction mixtures were examined directly by GC and GC/MS analyses.

Intermolecular Kinetic Isotope Measurements. Peroxo complex samples (1.0 mM) were prepared in equimolar quantities of perdeutero or protio solvents, to a total volume of 5.0 mL. Thermolyses were carried out over 5 min as described above, and the crude reaction mixtures were analyzed by GC/MS.

Results and Discussion

Reactions of Peroxide Complexes 1 and 2 with Various Reagents at -77 °C. The electronic spectra of the 1-alkylimidazole and pyridine complexes 1 and 2 were used to monitor their reactivity toward three classes of substrates: oxygen-atom acceptors, electrophiles/acids, and weak H-atom donors. Such a comparative analysis has been used previously to characterize transition metal peroxo complexes, where the reactivity pattern of the peroxide ligand depends on the Lewis acidity of the metal ion and the mode of peroxo coordination.²⁴⁻²⁶ In general, early transition metal ions in high oxidation states render coordinated peroxide ligands electron deficient such that they typically undergo oxygen-atom transfer reactions to acceptors such as phosphines and olefins. These reactions become more favored thermodynamically as the substituents bound to the reacting substrate functionality are more electron releasing. By contrast, low-valent, late-metal peroxo adducts usually behave as nucleophiles, undergoing addition reactions to electrophiles such as CO₂, acyl chlorides, or electron-deficient olefins. In addition, these electron rich peroxo adducts will react with acids to afford hydroperoxo complexes or they may react with an additional acid equivalent to liberate H₂O₂. Peroxo complexes may also display radical character and react with weak hydrogen atom donors such as isopropyl C-H^{27,28} and phenolic O-H^{24,25} bonds. Peroxo O-O bond cleavage may occur prior to

hydrogen atom abstraction in these reactions, as has been demonstrated in a related bis(μ -oxo)dicopper system.²⁹⁻³¹ Moreover, the distinction between nucleophilic/basic versus radical peroxy character can be probed with phenols since deprotonation usually leads to phenoxide coordination,²⁶ whereas hydrogen atom abstraction provides a phenoxyl radical. With the appropriate aryl substitution, such a species can be identified as the 2,2'-biphenol-coupled product.^{24,32}

Stoichiometric reactions were conducted by generating peroxy complex 1 or 2 in solution at -77 °C, followed by thorough removal of excess O₂ with Ar purge/dynamic vacuum cycles and then addition of the reagent. Reactions were monitored by UV-vis spectroscopy. These studies are summarized in Scheme 4.1. No reaction was observed for peroxy adducts 1 or 2 with triphenylphosphine or 2-cyclohexen-1-one, an outcome which suggests that this class of peroxy complexes has no electrophilic character, even toward electron-poor olefins. Similarly, exposure of either peroxy complex to the weak H-atom donor dimethylbenzylamine afforded no reaction.

Treatment of the 1-butylimidazole peroxy complex 1 with 1.0 equiv of 2,4-di-*tert*-butylphenol resulted in a color change from purple to deep royal blue within 30 s. By contrast, peroxy 2 did not react with the phenol under similar conditions. UV-vis spectral studies of both of these reactions were carried out, the results of which are displayed in Figure 4.1-4.2. The product spectrum for 1 + phenol persists for > 2 h at -77 °C, but decays rapidly upon warming to room temperature. No 2,2'-biphenol coupled product was detected by GC/MS, as judged by comparison of the product chromatogram to that of pure 2,2'-biphenol, but H₂O₂ was detected qualitatively. These facts, coupled with the metastable nature of the product and the resemblance of its UV-vis spectrum to that of 1 suggested that a diiron(III) phenoxide-hydroperoxide complex might have been formed through deprotonation of the phenol with the diiron(III)-bound peroxide. The resulting charge transfer band at

620 nm ($\epsilon = 1400 \text{ M}^{-1}\text{cm}^{-1}$) is considerably blue-shifted from those of known hydroperoxo complexes, however, $[\text{Fe}^{\text{III}}(\text{N4Py})(\text{OOH})(\text{MeCN})](\text{ClO}_4)_2$ ($\lambda_{\text{max}} = 458 \text{ nm}$, $\epsilon = 1100 \text{ M}^{-1}\text{cm}^{-1}$)³³ and $[\text{Fe}(\text{TPA})(\text{OOH})](\text{ClO}_4)_2$ ($\lambda_{\text{max}} = 538 \text{ nm}$).¹³ Moreover, reactions with less electron-rich phenols such as the parent compound and pentafluorophenol exhibited UV-vis bands blue shifted of that obtained for the 2,4-di-*tert*-butylphenol product (Figures 4.3-4.4). Both of these facts make it more likely that the product UV-vis feature is due to a phenoxide-to-iron(III) charge transfer.

Resonance Raman studies were conducted to probe further the fate of the peroxide complex **1** upon treatment with 2,4-di-*tert*-butylphenol. Peroxo species were prepared with $^{16}\text{O}_2$ or $^{18}\text{O}_2$, and each was treated with 1.1 equiv of the phenol. Spectra before and after the reaction are displayed in Figures 4.5 and 4.6. For the $^{16}\text{O}_2$ sample, the $\nu(^{16}\text{O}-^{16}\text{O})$ band at 864 cm^{-1} disappears almost entirely upon addition of the phenol, and two new bands appear at 750 and 913 cm^{-1} . The $\nu(^{18}\text{O}-^{18}\text{O})$ band also diminishes when phenol is added, as judged by the narrowing and shifting of the peak at $\sim 825 \text{ cm}^{-1}$, which is composed of the peroxo band and one assigned to toluene (see Chapter 3, Figures 3.13-3.14). The same two new peaks that were observed when phenol was added to the $^{16}\text{O}_2$ sample also appear in the $^{18}\text{O}_2$ spectrum, indicating that neither can be ascribed to a hydroperoxide or peroxide species. These features are therefore assigned to phenol vibrations which are resonance enhanced by the phenoxide-to-iron charge transfer band. A new $\nu(\text{O}-\text{O})$ band may be obscured by the toluene peaks, but none was observed after carrying out solvent subtraction routines.

Irrespective of the identity of the products, this set of experiments shows that **1** behaves as a basic, as opposed to a hydrogen atom abstracting, peroxo species. The fact that **2** does not react at all with 2,4-di-*tert*-butylphenol further supports this conclusion. Compared to pyridine, the more basic 1-alkylimidazole groups impart additional electron density to the iron centers, which is in turn transmitted to the

peroxide. The large discrepancy in the pK_a values for 1-butylimidazole (~ 6.8) compared to phenol (~ 10.0)³⁴ makes proton transfer to the 1-alkylimidazole ligand highly improbable.

Two other proton donors were investigated to probe further the character of the peroxide ligands in **1** and **2**. Treatment of **1** with 1.1 equiv of 2,4,6-tri-*tert*-butylphenol provided no reaction, as judged by UV-vis spectroscopy (Figure 4.7). Apparently proton transfer does not occur in this case because the sterically encumbered phenol blocks access to the peroxide ligand. Alternatively, the deprotonated phenol may be too hindered to bind to the iron center(s). A carboxylic acid was used to determine whether a hydroperoxo complex could be stabilized by an additional hindered carboxylate ligand and to see if the less basic pyridine peroxo complex **2** could be protonated. Treatment of peroxo complex **1** with 1.1 equiv of 1-phenylcyclohexylacetic acid was accompanied by decomposition at $-77\text{ }^\circ\text{C}$ within 15–30 s (Figure 4.8), yielding intractable products following workup at room temperature. Like all the phenol reactions, H_2O_2 was detected qualitatively in the crude decomposed mixtures. Peroxo **2** was completely unreactive toward the carboxylic acid, an outcome which further illustrates the vastly different electronic properties that are imparted to the two peroxo ligands solely by the choice of N-donor ligand.

Electrophilic reagents were examined to probe the nucleophilicity of the peroxo complexes. Exposure of **1** $-77\text{ }^\circ\text{C}$ to a large excess of CO_2 resulted in decay of the peroxide-to-iron charge transfer band at within 15 s (Figure 4.9). As with other peroxo complexes that react with CO_2 , this reaction probably generates a peroxycarbonate species which decomposes to an iron(III) carbonate complex(es), although nothing tractable was isolated from the reaction mixture. Consistent with the protonolysis studies, **2** was unreactive toward CO_2 over the course of 2 h of monitoring the reaction by UV-vis spectroscopy (Figure 4.10).

Finally, the behavior of **1** toward reductants was examined to obtain an estimate of its reduction potential. No reaction was observed with ferrocene or pentamethylferrocene (Figure 4.11), but treatment with cobaltocene induced a rapid decay of the peroxy UV-vis band (Figure 4.12). The cobaltocenium cationic product could not be identified because intense features in the higher energy visible region dominated the spectrum. Assuming this compound donates an electron to the peroxy complex in a 1:1 stoichiometry, then the reduction potential of **1** is estimated to be between that of Cp₂*Fe and cobaltocene, -0.59 and -1.33 mV, respectively vs. Cp₂Fe⁺/Cp₂Fe.³⁵ This value attests to the stability of the diiron(III) peroxy species toward hydrogen atom donors and dioxygen dissociation, since both processes would require reduction of one or both Fe(III) ions. In particular, it provides at least a partial explanation as to why peroxy species **1** deprotonates 2,4-di-*tert*-butylphenol instead of abstracting a hydrogen atom from this reagent.

Thermolysis Reactions Leading to Solvent Oxidation. Solutions of peroxy complexes **1** or **2** rapidly decay when warmed above ~ 65 °C, changing from purple and midnight blue, respectively, to an orange brown color which is characteristic of μ-oxodiiron(III) complexes. Several mechanisms could account for this decay. The most well documented of such a reaction in diiron(III) peroxy chemistry is a bimolecular decomposition accompanied by extrusion of 0.5 equiv of O₂ per diiron complex, affording oxo-bridged Fe(III) products.^{36,37} This process could not account for the entire decomposition of **1** or **2** because manometric studies indicated either that O₂ was not released during decay or that in solvents such as THF and CH₂Cl₂, up to an additional equiv of dioxygen was consumed.²⁰ Such a result might be explained a priori by ligand oxidation, but a thorough ¹H NMR and GC/MS analysis of the organic components revealed no oxidized ligands following acid dissociation and extraction of the decomposition products. Instead, solvent oxidation products were identified in the reaction mixtures for several different solvents. A detailed

analysis of those reactions for **1** was undertaken because its butyl and propyl groups make it soluble in a wide variety of hydrocarbons. Table 4.2 summarizes the results of this initial survey.

These studies defined the scope of the oxidation process. Substrates with particularly weak C–H bonds³⁴ such as THF (92 kcal/mol), cyclohexene (allylic C–H = 85 kcal/mol), and toluene (85 kcal/mol) afforded γ -butyrolactone and 2-hydroxytetrahydrofuran, 2-cyclohexen-1-ol, 2-cyclohexen-1-one, and cyclohexene oxide, and benzaldehyde, respectively, in modest yields based on **1**. Dichloroethane, identified qualitatively as a product of peroxy decay in CH₂Cl₂ solutions, was formed by C–Cl bond homolysis. Solvents with high C–H bond strengths such as isopentane (95 kcal/mol), and pentane (98 kcal/mol) were completely unreactive. Cyclopentane, with an intermediate C–H bond strength (94.5 kcal/mol), provided a small amount of product.

A key to understanding this chemistry is provided by the product distribution for each substrate. For cyclohexene, only allylic oxidation products were produced in appreciable quantities. This result contrasts with that for sMMO, early transition metal peroxy complexes, and many terminal oxo complexes, which all afford the epoxide as the major or exclusive product. For oxidations at saturated C–H bonds, ketones are favored over alcohol products, whereas sMMO affords alcohols exclusively.

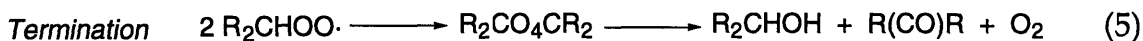
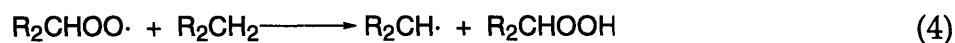
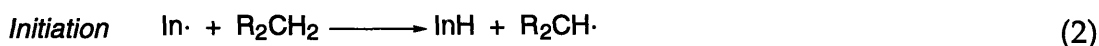
To investigate the mechanism in more detail, we chose to focus on cyclopentane oxidation. This solvent is readily purified and not susceptible to autoxidation in air for months at room temperature. Cyclohexene and THF, on the other hand, autoxidize after ~12 h in air, judging by GC/MS. From a practical standpoint its higher C–H bond strength makes cyclopentane a more attractive target.

Table 4.3 lists a series of conditions designed to probe the oxidation mechanism of cyclopentane. Entries 1-3 reveal that yields of ketone and alcohol are unaffected by the warming rate, or reaction atmosphere, or peroxy concentration, providing in each case the same small quantities of ketone and alcohol in a 2.5:1 ratio. When decomposed reaction mixtures were allowed to stand in air for extended periods of time (entries 6-8), however, a slow but steady production of additional product resulted, as determined by analyzing aliquots of the reaction mixture by GC/MS on a daily basis. After three weeks the total yield of oxidized products based on the original [1] was 250%, but the ketone:alcohol ratio remained invariant over this time period. The latter observation suggests that the entire oxidation process proceeds through a common mechanism, from the initial warming of the peroxy solution and throughout prolonged incubation in air at room temperature. An aliquot of the long-term reaction was removed after 1 day (entry 8) and treated with a 50-fold excess of 2,4,6-*tert*-butylphenol, which completely quenched product formation. Moreover, when solutions of 1 were warmed in the presence 1.0 equiv of this phenol, with which it does not react at -77 °C (*vide supra*), no oxidized products were observed either immediately after the reaction or upon standing in air for several days.

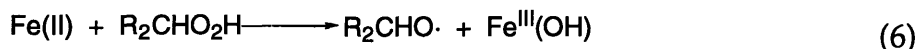
An intermolecular kinetic isotope effect (KIE) was not measured for cyclopentane oxidation because the perdeutero isotopomer is prohibitively expensive. Alternatively, we carried out measurements using THF and toluene as solvents, which afforded $k_{\text{H}}/k_{\text{D}}$ values of 6.2 and 7.8, respectively (Figures 4.15-4.16). These values may be compared to the intramolecular KIE values of 2-3 for Gif cyclohexane and adamantane oxidations,³⁸ and 1.0 for sMMO.³⁹

The ability of phenol to quench product formation indicates that a free radical, non-metal based autoxidation mechanism is most likely occurring for this system. An example of such a mechanism is illustrated by eqs 2-5 for oxidation at a

secondary carbon atom. ²⁶ This well known hydrocarbon oxidation



process is initiated by hydrogen atom abstraction to generate an alkyl radical, which is trapped with dioxygen. The resulting alkyl peroxy radical then reacts with another equivalent of substrate, and the chain is propagated. Chain termination occurs when two alkyl peroxy radicals combine, and this resulting species then rearranges to afford dioxygen, ketone, and alcohol. Decomposition of the resulting alkyl hydroperoxide to ketone and alcohol can be catalyzed by iron salts via the Haber-Weiss cycle (eqs 6-7).^{40,41} The resulting alkoxy radical reacts with substrate to yield alcohol (eq 8), and the alkyl peroxy radical can decompose as indicated in eq 5.



The reaction mixtures were analyzed by ¹H NMR and GC/MS to determine whether a significant concentration of cyclopentylhydroperoxide builds up over the course of the extended reactions. No ¹H NMR resonances or GC/MS peaks attributable to this species were identified upon comparing the data to that obtained for a pure sample prepared independently. A peroxo sample was also warmed in the presence of 10 equiv of PPh₃ to trap any intermediate cyclopentylhydroperoxide, which would afford triphenylphosphine oxide and alcohol. This procedure neither changed the overall yield nor altered the ketone:alcohol ratio, suggesting that if the hydroperoxide is formed it decomposes exceedingly rapidly.

warming, and the resulting reducing equivalents are then used at a diiron(III) peroxide to effect Fenton chemistry, perhaps with trace water serving as a proton source to generate a hydroxyl radical (eq 12).

An important conclusion to be drawn from the cyclopentane oxidation studies is that we have not accessed the manifold of reactivity used by the diiron centers in sMMO in terms of substrate scope, product selectivity, or the oxidation mechanism. Studies of the enzyme with radical clock substrate probes and chiral ethane have provided evidence against a discrete radical intermediate, having a lifetime greater than $\sim 10^{-13}$ s.^{42,43} For a functional model system to duplicate the enzymatic chemistry, metal-based oxidants which formally abstract a hydrogen atom from a substrate molecule must be avoided. Not only might such a reaction lead to undesired radical chain autooxidation chemistry, but also because it would simply that the model has not matched the composition and structure of the key enzymatic oxidant.

Recent X-ray studies of resting state MMOH and EXAFS studies on intermediate Q provide some insight into why the diiron XDK system may not be able to mimic the enzymatic chemistry and suggest new design strategies for improved functional models. In the resting enzyme, only one carboxylate ligand bridges the diiron center. The short Fe...Fe distance of 2.5 Å observed for intermediate Q cannot be accommodated by a *syn syn* bidentate bis(carboxylate)bridged core, and it is unlikely that the rigid XDK ligand system possesses the flexibility to undergo the carboxylate shift⁴⁴ required to convert peroxo adducts 1 or 2 into Q-like diiron(IV) complexes. Alternatively, ligands which provide a single *syn syn* bidentate carboxylate bridge while maintaining a rigid dinucleating framework may provide ideal balance for converting a peroxo adduct into a Q-like species. Efforts to prepare such complexes are currently underway in this laboratory.

Conclusions

The reactivity properties of diiron(III) peroxo complexes **1** and **2** have been fully elucidated. These adducts behave as nucleophilic/basic peroxides, exhibiting no propensity to serve as oxygen atom donors, even for potent acceptors such as triphenylphosphine. The 1-butylimidazole ligands in **1** enhance the nucleophilicity/basicity of the peroxo compared to the pyridine analog, probably because the former ligand is a superior σ -donor. This feature imparts more electron density to the iron centers, which in turn is transmitted to the peroxo ligand. Thermolysis of the peroxo adducts in a variety of media results in solvent oxidation, providing ketone and alcohol products in modest yield based on the complex. A detailed analysis of cyclopentane oxidation provided evidence for a radical chain autoxidation mechanism, a reactivity manifold which does not mimic the hydrocarbon oxidation chemistry of sMMO. Future efforts are aimed at preparing diiron(III) peroxo complexes with mono(carboxylate)-bridged structures, a design aspect which may facilitate conversion to a Q-mimic and allow access to the enzymatic hydroxylation pathway.

References and Notes

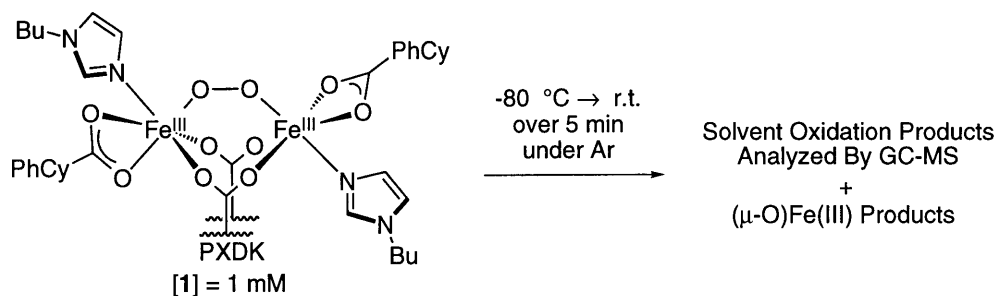
- (1) Shilov, A. E.; Shul'pin, G. B. *Chem. Rev.* **1997**, *97*, 2879-2932.
- (2) Arndsten, B. A.; Bergman, R. G.; Mobley, T. A.; Peterson, T. H. *Acc. Chem. Res.* **1995**, *28*, 154-162.
- (3) Wallar, B. J.; Lipscomb, J. D. *Chem. Rev.* **1996**, *96*, 2625-2657.
- (4) Liu, K. E.; Lippard, S. J. In *Adv. Inorg. Chem.*; A. G. Sykes, Ed.; Academic Press, Inc.: San Diego, CA, 1995; Vol. 42; pp 263-289.
- (5) Feig, A. L.; Lippard, S. J. *Chem. Rev.* **1994**, *94*, 759-805.
- (6) Solomon, E. I.; Sundaram, U. M.; Machonkin, T. E. *Chem. Rev.* **1996**, *96*, 2563-2605.
- (7) Semrau, J. D.; Zolanz, D.; Lidstrom, M. E.; Chan, S. I. *J. Inorg. Biochem.* **1995**, *58*, 235-244.
- (8) Valentine, A. M.; Lippard, S. J. *J. Chem. Soc., Dalton Trans.* **1997**, 3925-3931.
- (9) Valentine, A. M.; Tavares, P.; Pereira, A. S.; Davydov, R.; Krebs, C.; Hoffman, B. M.; Edmondson, D. E.; Huynh, B. H.; Lippard, S. J. *J. Am. Chem. Soc.* **1998**, *120*, In Press.
- (10) Sturgeon, B. E.; Burdi, D.; Chen, S.; Huynh, B. H.; Edmondson, D. E.; Stubbe, J. *J. Am. Chem. Soc.* **1997**, *118*, 7551-7557.
- (11) Willems, J.-P.; Lee, H.-I.; Burdi, D.; Doan, P. E.; Stubbe, J. *J. Am. Chem. Soc.* **1997**, *119*, 9816-9824.
- (12) Burdi, D.; Riggs-Gelasco, P.; Tong, W.; Willems, J.-P.; Lee, H.-I.; Doan, P. E.; Sturgeon, B.; Shu, L.; Que, L. J.; Hoffmann, B. M.; Stubbe, J. *Stenbock Symposium Proceedings: Biosynthesis and Function of Metal Clusters For Enzymes* **1997**, *25*, 85-95.
- (13) Kim, C.; Chen, K.; Kim, J.; Que, L., Jr. *J. Am. Chem. Soc.* **1997**, *119*, 5964-5965.
- (14) Barton, D. H. R.; Doller, D. *Acc. Chem. Res.* **1992**, *25*, 504-512.

- (15) Fish, R. H.; Konings, M. S.; Oberhausen, K. J.; Fong, R. H.; Yu, W. M.; Christou, G.; Vincent, J. B.; Coggin, D. K.; Buchanan, R. M. *Inorg. Chem.* **1991**, *30*, 3002-3006.
- (16) Newcomb, M.; Simakov, P. A.; Park, S.-U. *Tet. Lett.* **1996**, *37*, 819-822.
- (17) MacFaul, P. A.; Ingold, K. U.; Wayner, D. D. M.; Que, L., Jr. *J. Am. Chem. Soc.* **1997**, *119*, 10594-10598.
- (18) Rabion, A.; Chen, S.; Wang, J.; Buchanan, R. M.; Seris, J.-J. *J. Am. Chem. Soc.* **1995**, *117*, 12356-12357.
- (19) MacFaul, P. A.; Arends, I. W. C. E.; Ingold, K. U.; Wayner, D. D. M. *J. Chem. Soc., Perkin Trans. 2* **1997**, 135-145.
- (20) LeCloux, D. D. Chapter 3.
- (21) van der Linden, A.; Schaverien, C. J.; Meijboom, N.; Ganter, C.; Orpen, A. G. *J. Am. Chem. Soc.* **1995**, *117*, 3008-3021.
- (22) Walling, C.; Buckler, S. A. *J. Am. Chem. Soc.* **1955**, *77*, 6032-6038.
- (23) Bates, H. A.; Farina, J. *J. Org. Chem.* **1985**, *50*, 3843-3845.
- (24) Paul, P. P.; Tyeklár, Z.; Jacobsen, R. R.; Karlin, K. D. *J. Am. Chem. Soc.* **1991**, *113*, 5322-5332.
- (25) Tyeklár, Z.; Karlin, K. D. In *Bioinorganic Chemistry of Copper*; K. D. Karlin and Z. Tyeklár, Ed.; Chapman and Hall: New York, 1993; pp 277-291.
- (26) Sheldon, R. A.; Kochi, J. K. In *Metal-Catalyzed Oxidations of Organic Compounds* Academic Press: New York, 1981.
- (27) Reinnaud, O. M.; Theopold, K. H. *J. Am. Chem. Soc.* **1994**, *116*, 6979-6980.
- (28) Hikichi, S.; Komatsuzaki, H.; Kitajima, N.; Akita, M.; Mukai, M.; Kitagawa, T.; Moro-oka, Y. *Inorg. Chem.* **1997**, *266-267*, 266-267.
- (29) Tolman, W. B. *Acc. Chem. Res.* **1997**, *30*, 227-237.
- (30) Mahapatra, S.; Halfen, J. A.; Tolman, W. B. *J. Am. Chem. Soc.* **1996**, *118*, 11575-11586.

- (31) Mahapatra, S.; Halfen, J. A.; Wilkinson, E. C.; Pan, G.; Wang, X.; Jr., Young, V. G., Jr.; Cramer, C. J.; Jr., L. Q.; Tolman, W. B. *J. Am. Chem. Soc.* **1996**, *118*, 11555-11574.
- (32) Kim, C.; Dong, Y.; Que, L., Jr. *J. Am. Chem. Soc.* **1997**, *119*, 3635-3636.
- (33) Lubben, M.; Meetsma, A.; Wilkinson, E. C.; Feringa, B.; Que, L., Jr. *Angew. Chem.* **1991**, *107*, 1610-1612.
- (34) *Handbook of Chemistry and Physics, 68th Edition*; R. C. Weast, Ed.; CRC Press, Inc.: Boca Raton, FL, 1988.
- (35) Connelly, N. G.; Geiger, W. E. *Chem. Rev.* **1996**, *96*, 877-910.
- (36) Feig, A. L.; Becker, M.; Schindler, S.; van Eldik, R.; Lippard, S. J. *Inorg. Chem.* **1996**, *35*, 2590-2601.
- (37) Feig, A. L.; Masschelein, A.; Bakac, A.; Lippard, S. J. *J. Am. Chem. Soc.* **1997**, *119*, 334-342.
- (38) Singh, B.; Long, J. R.; deBiani, F. F.; Gatteschi, D.; Stavropoulos, P. *J. Am. Chem. Society* **1997**, *119*, 7030-7047.
- (39) K.E, L.; Johnson, C. C.; Newcomb, M.; Lippard, S. J. *J. Am. Chem. Soc.* **1993**, *115*, 939-947.
- (40) Sheldon, R. A.; Kochi, J. K. *Advan. Catal.* **1976**, *25*, 272.
- (41) Walling, C. *Acc. Chem. Res.* **1975**, *8*, 125-131.
- (42) Liu, K. E.; Johnson, C. C.; Newcomb, M.; Lippard, S. J. *J. Am. Chem. Soc.* **1993**, *115*, 939-947.
- (43) Valentine, A. M.; Wilkinson, B.; Liu, K. E.; Komar-Panicucci, S.; Priestly, N. D.; Williams, P. G.; Morimoto, H.; Floss, H. G.; Lippard, S. J. *J. Am. Chem. Soc.* **1996**, *119*, 1818-1827.
- (44) Rardin, R. L.; Tolman, W. B.; Lippard, S. J. *New J. Chem.* **1991**, *15*, 417-430.

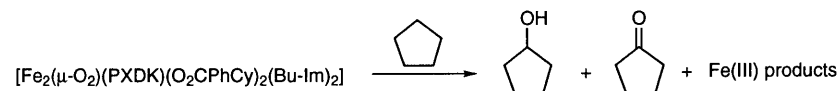
Table 4.1. A summary of reagents and solvents used for the stoichiometric reactions.

Reagent	Reagent Quantity	Peroxo	Quantity of Diiron(II) Precursor (mg, μmol)	Solvent (5.0 mL)
Triphenylphosphine	6.0 mg, 23 μmol	1	5.0, 3.3	THF
2-Cyclohexen-1-one	6.0 mg, 23 μmol	1	6.5, 4.3	THF
Dimethylbenzylamine	10 μl , 66 μmol	1	10, 6.6	Et ₂ O
2,4-Di- <i>tert</i> -Butylphenol	1.0 mg, 4.9 μmol	1	7.4, 4.9	THF
2,4-Di- <i>tert</i> -Butylphenol	1.0 mg, 4.9 μmol	2	7.0, 4.1	CH ₂ Cl ₂
Phenol	0.5 mg, 5.3 μmol	1	6.8, 4.5	THF
Pentafluorophenol	0.7 mg, 3.5 μmol	1	4.8, 3.2	THF
2,4,6-Tri- <i>tert</i> -Butylphenol	5 μl , 5 μmol	1	6.4, 4.2	Cyclopentane
1-Phenylcyclohexylcarboxylic Acid	1.0 mg, 4.7 μmol	1	6.5, 4.3	Toluene
CO ₂	excess	1	7.4, 4.9	Et ₂ O
CO ₂	excess	2	7.0, 4.1	CH ₂ Cl ₂
Pentamethylferrocene	1.4 mg, 4.4 μmol	1	6.0, 4.0	THF
Cobaltocene	0.8 mg, 4.4 μmol	1	6.0, 4.0	THF

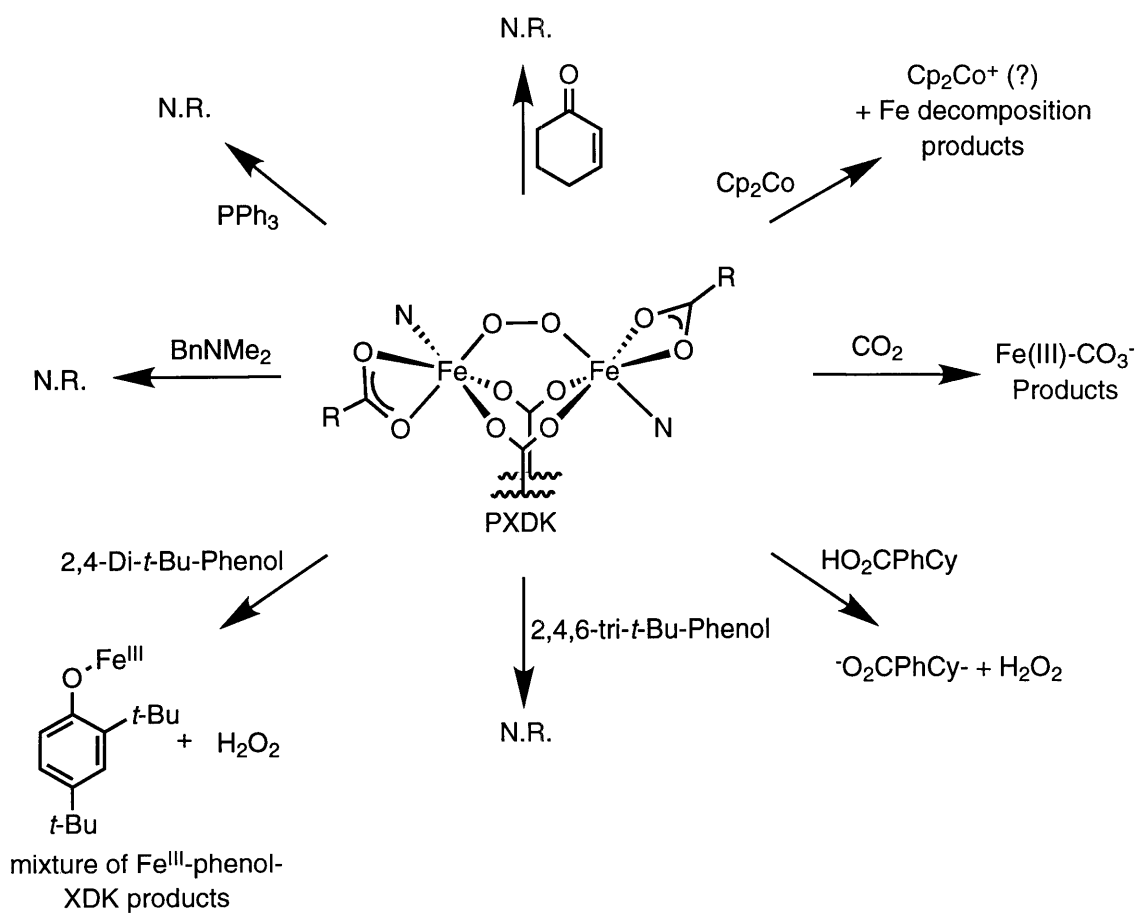
Table 4.2. A survey of solvent oxidation reactions mediated by peroxo **1**.

Solvent	Products (%Yield Based on 1)
	 (5) + (20)
CH_2Cl_2	 (Yield Not Determined)
	 (20)
	 (2) + (5)
	 (14) + (29) + (< 1)
	No Reaction
	No Reaction
	No Reaction

Table 4.3. Cyclopentane oxidation reactions carried out with peroxo **1** under a set of experimental conditions designed to probe the mechanism.



Entry	Atmosphere	Temp (°C)/Heating Rate	Conc. (mM)	Additives (Equiv)	Yield (%)	
					-one	-ol
1	Ar or O ₂	-77 → r.t. over 5 min	1.2	None	5	2
2		-77 → r.t. over 2 h	1.2		5	2
3		-85 for 3 days	1.2		5	2
4		-77 → r.t. over 5 min	0.12		5	2
5		-77 → r.t. over 5 min	11.2		5	2
6	Ar or O ₂ , then air	-77 → r.t. over 5 min then r.t., 24 h	1.2		10	4
7		-77 → r.t. over 5 min then r.t., 3 weeks			170	80
8		-77 → r.t. over 5 min then r.t., 3 weeks		2,4,6- <i>t</i> -Bu-Phenol (10) after 24 h	10	4
9	Ar or O ₂	-77 → r.t. over 5 min		2,4,6- <i>t</i> -Bu-Phenol (10)	0	0
10		-77 → r.t. over 5 min		PPh ₃ (1.0)	5	2
11		-77 → r.t. over 5 min		HO ₂ CPhCy (10) or H ₂ O (10)	5	2



Scheme 4.1.

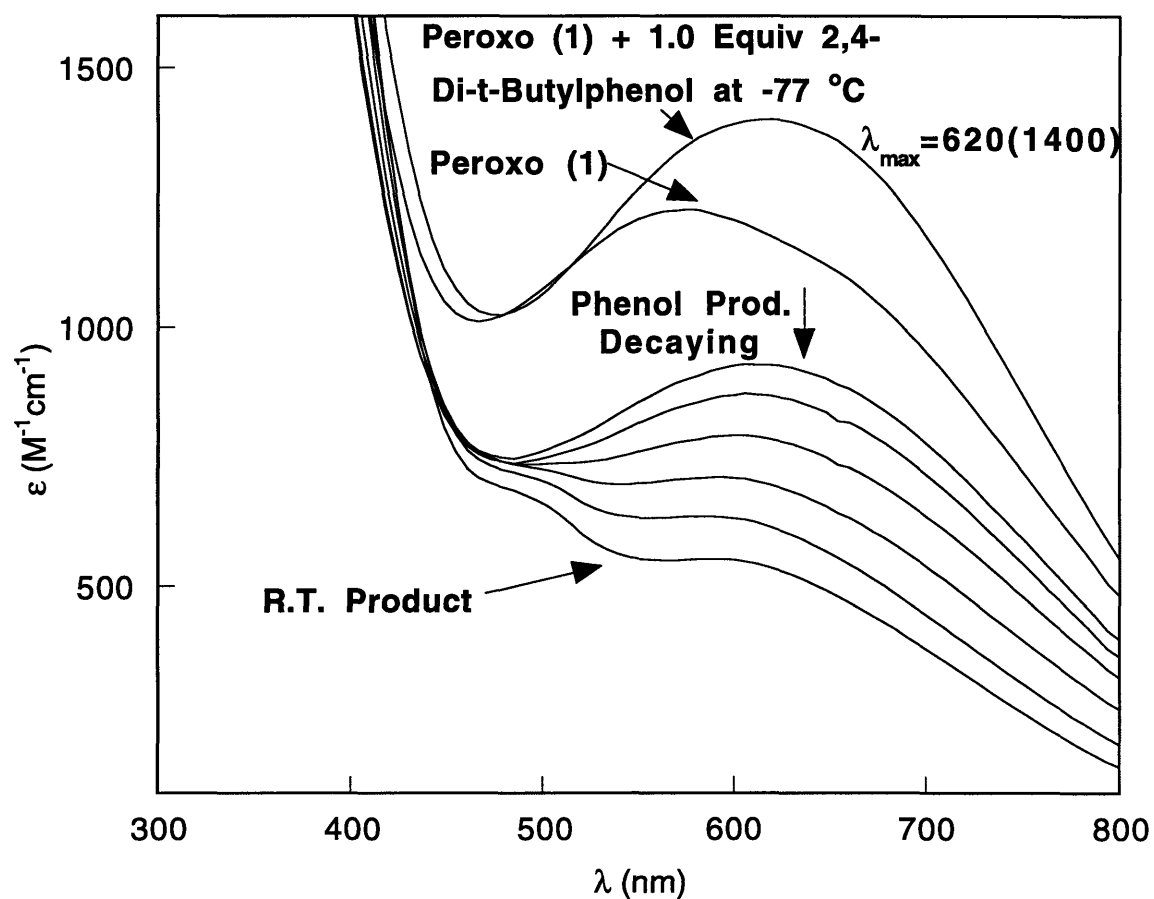


Figure 4.1. Electronic absorption spectrum of 1 in THF at -77 °C (0.98 mM), 1.0 equiv of 2,4-di-*t*-butylphenol added, and six traces qualitatively tracking the decay of the phenol product upon thermolysis from -77 °C to room temperature.

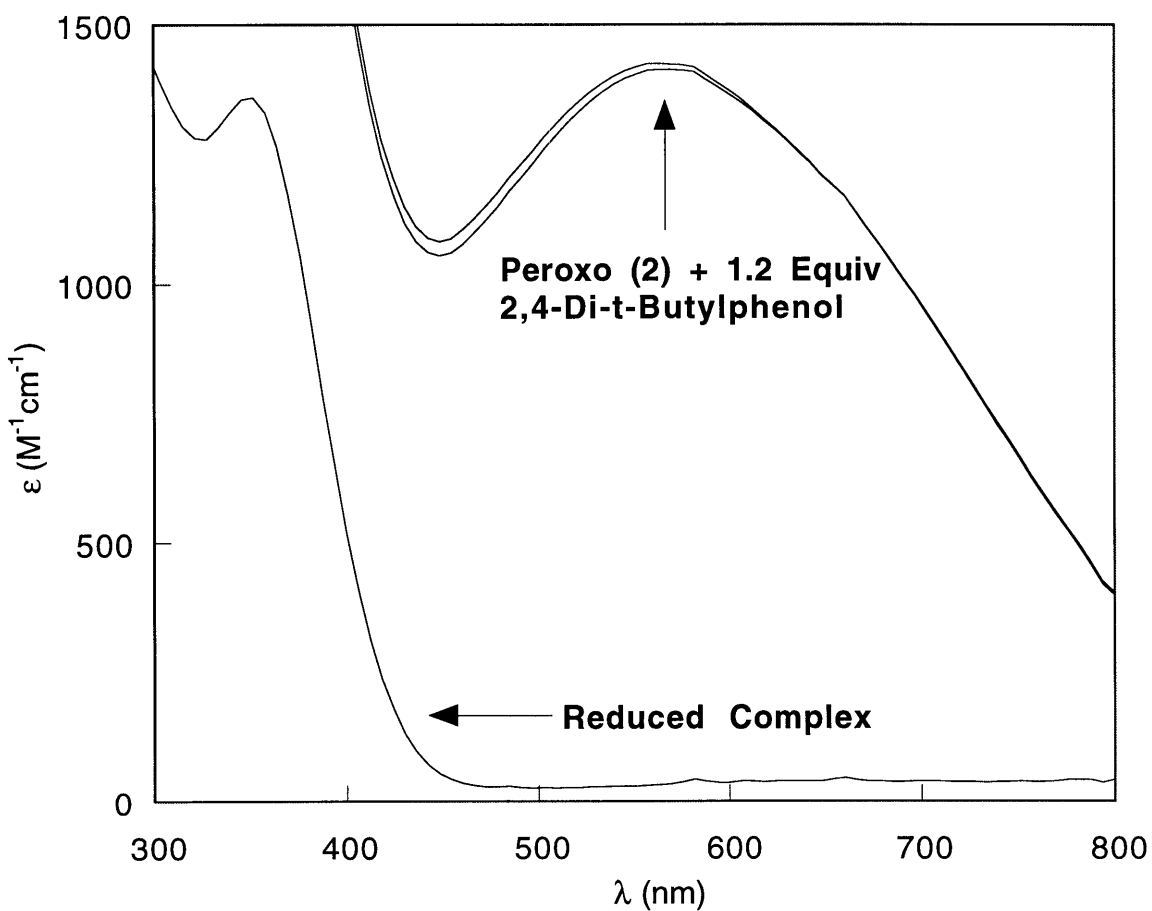


Figure 4.2. Electronic absorption spectrum of 2 in CH_2Cl_2 at -77°C (0.82 mM), 1.2 equiv of 2,4-di-*t*-butylphenol added, and an additional trace monitoring this reaction.

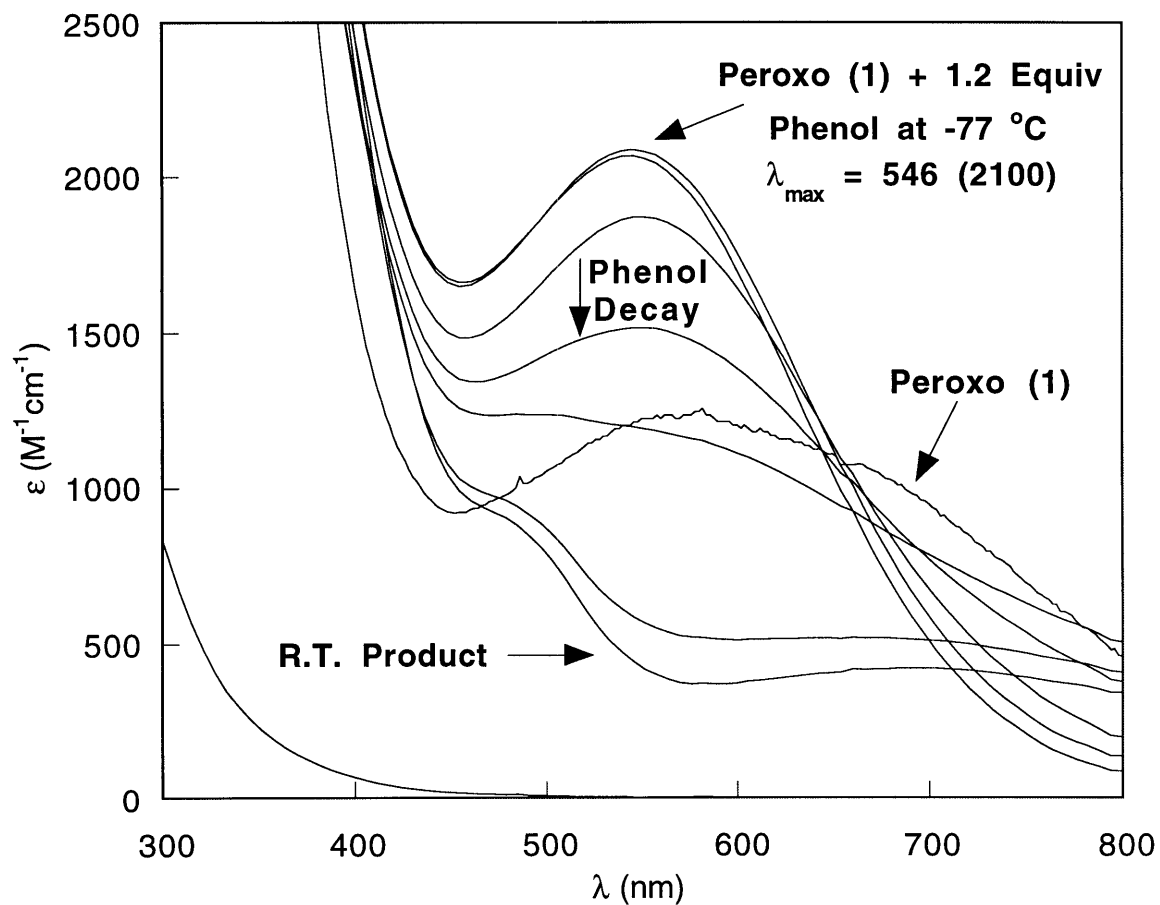


Figure 4.3. Electronic absorption spectrum of 1 in THF at -77 °C (0.90 mM), 1.2 equiv of phenol added, and six traces qualitatively tracking the decay of the phenol product upon thermolysis from -77 °C to room temperature.

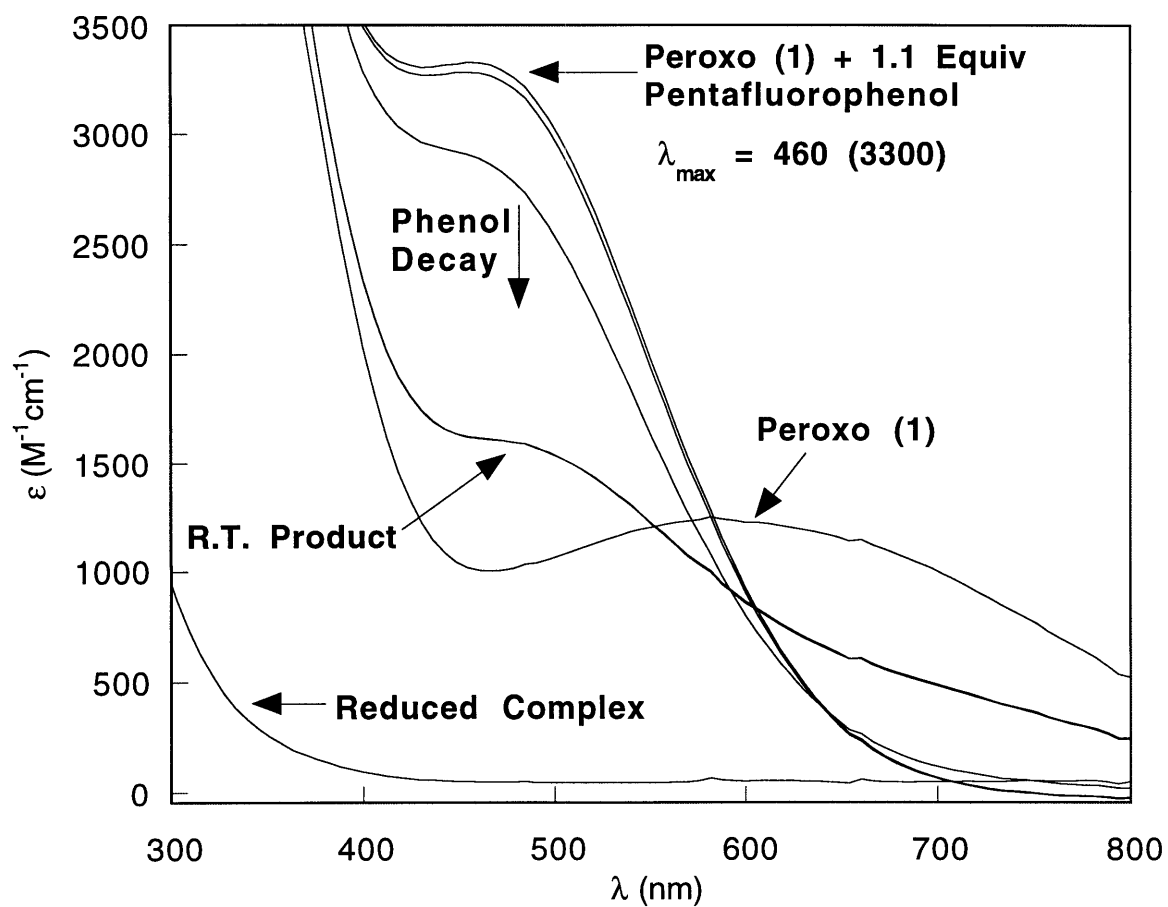
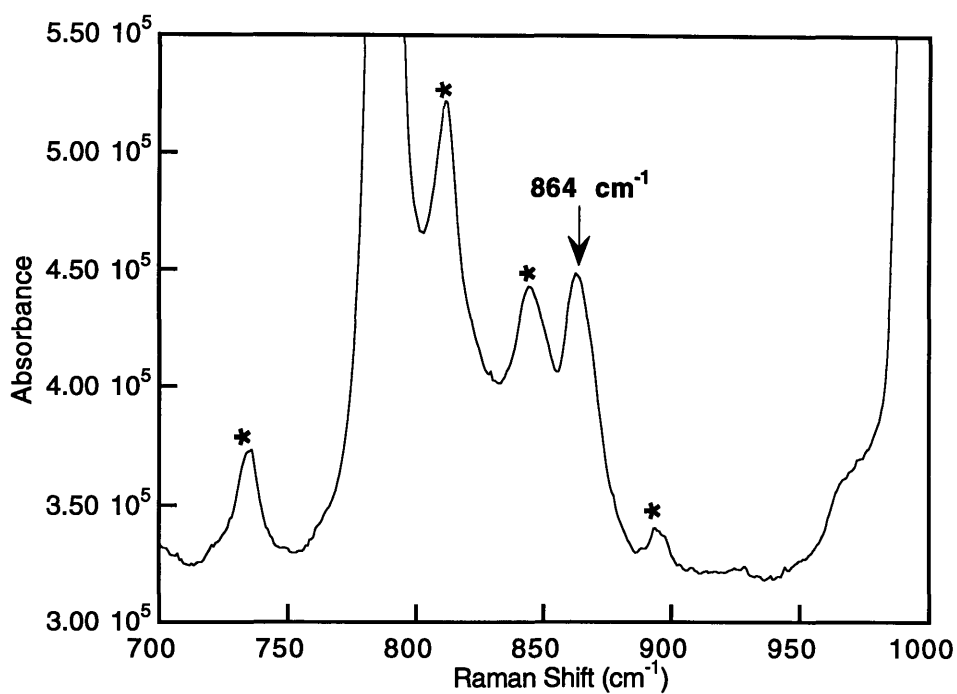


Figure 4.4. Electronic absorption spectrum of **1** in THF at -77 °C (0.63 mM), 1.1 equiv of pentafluorophenol added, and three additional traces tracking the decay of the phenol product upon thermolysis from -77 °C to room temperature.

A.



B.

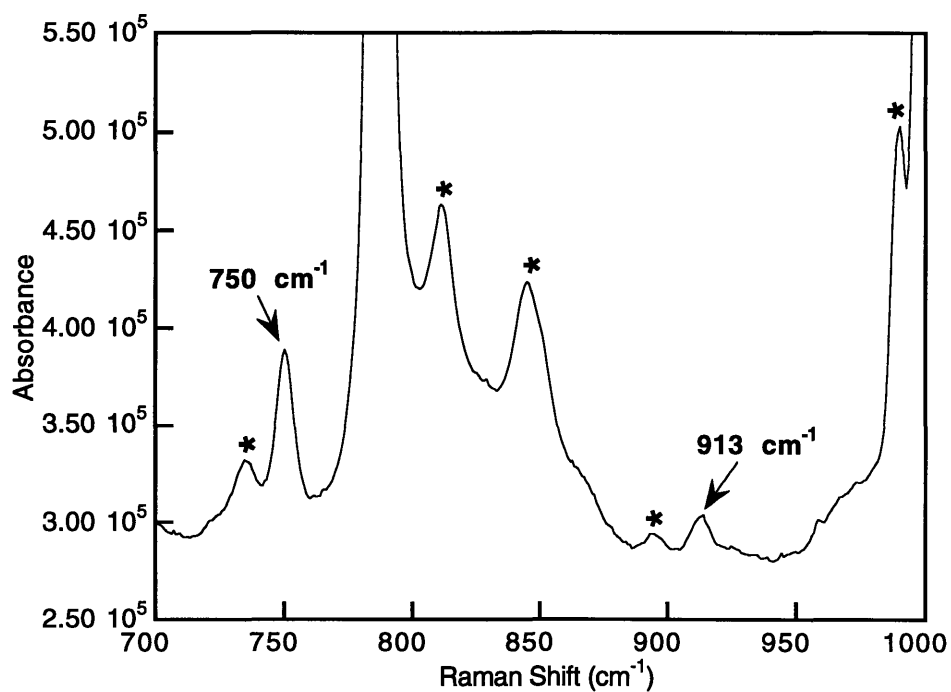
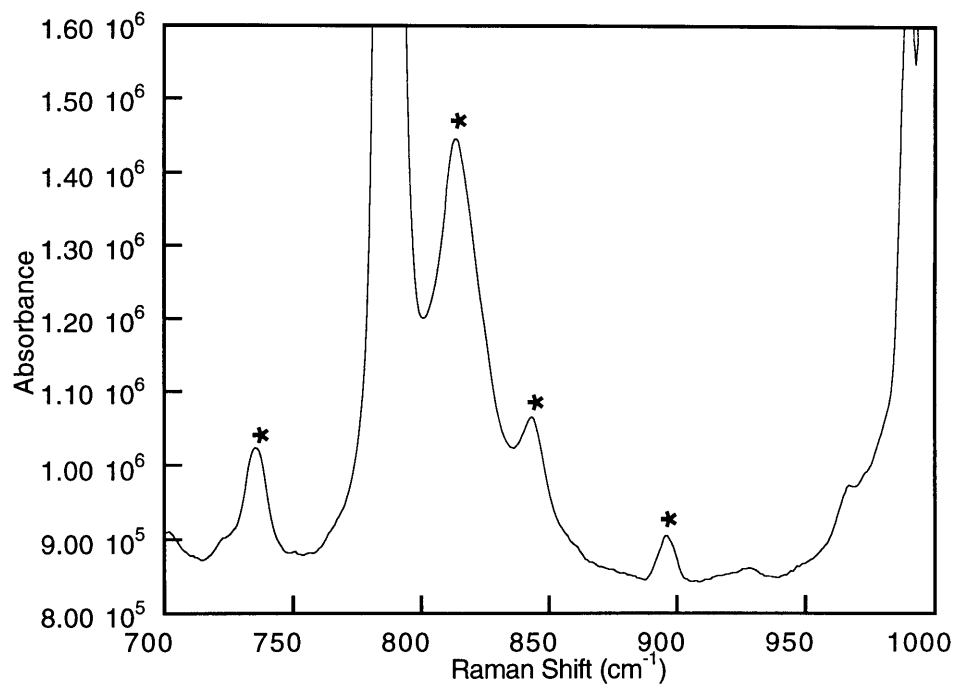


Figure 4.5. Resonance Raman spectra obtained with 647 nm excitation on fluid toluene solutions (-80 °C) of: (A) [Fe₂(¹⁶O₂)(PXDK)(O₂CPhCy)₂(Bu-Im)₂] (1-¹⁶O₂), (B) 1-¹⁶O₂ + 1.1 equiv of 2,4-di-*tert*-butylphenol. Peaks marked with an asterisk and those off scale are due to toluene.

A.



B.

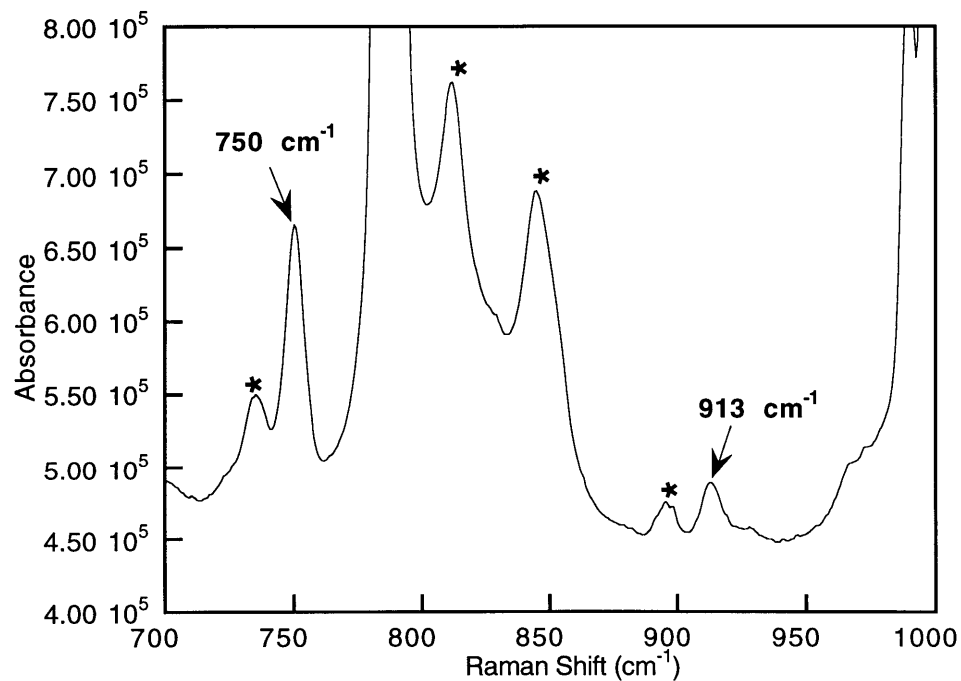


Figure 4.6. Resonance Raman spectra obtained with 647 nm excitation on fluid toluene solutions ($-80 \text{ }^\circ\text{C}$) of: (A) $[\text{Fe}_2(^{18}\text{O}_2)(\text{PXDK})(\text{O}_2\text{CPhCy})_2(\text{Bu-Im})_2]$ ($1\text{-}^{18}\text{O}_2$) and (B) $1\text{-}^{18}\text{O}_2$ + 1.1 equiv of 2,4-di-*tert*-butylphenol. Peaks marked with an asterisk and those off scale are due to toluene.

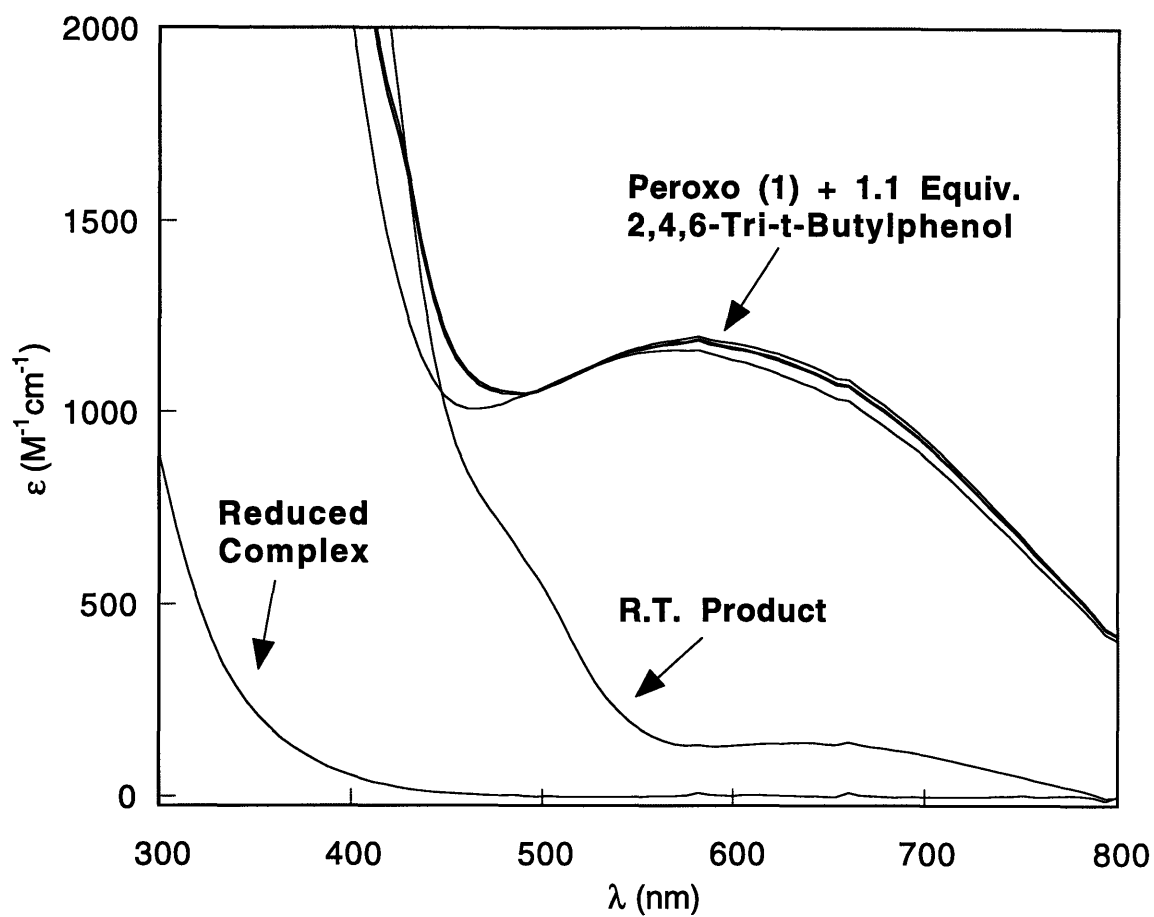


Figure 4.7. Electronic absorption spectrum of 1 in cyclopentane at $-77\text{ }^{\circ}\text{C}$ (0.84 mM), 2 equiv of 2,4,6-tri-*tert*-butylphenol added, and one additional trace showing the decomposition product obtained upon thermolysis from $-77\text{ }^{\circ}\text{C}$ to room temperature.

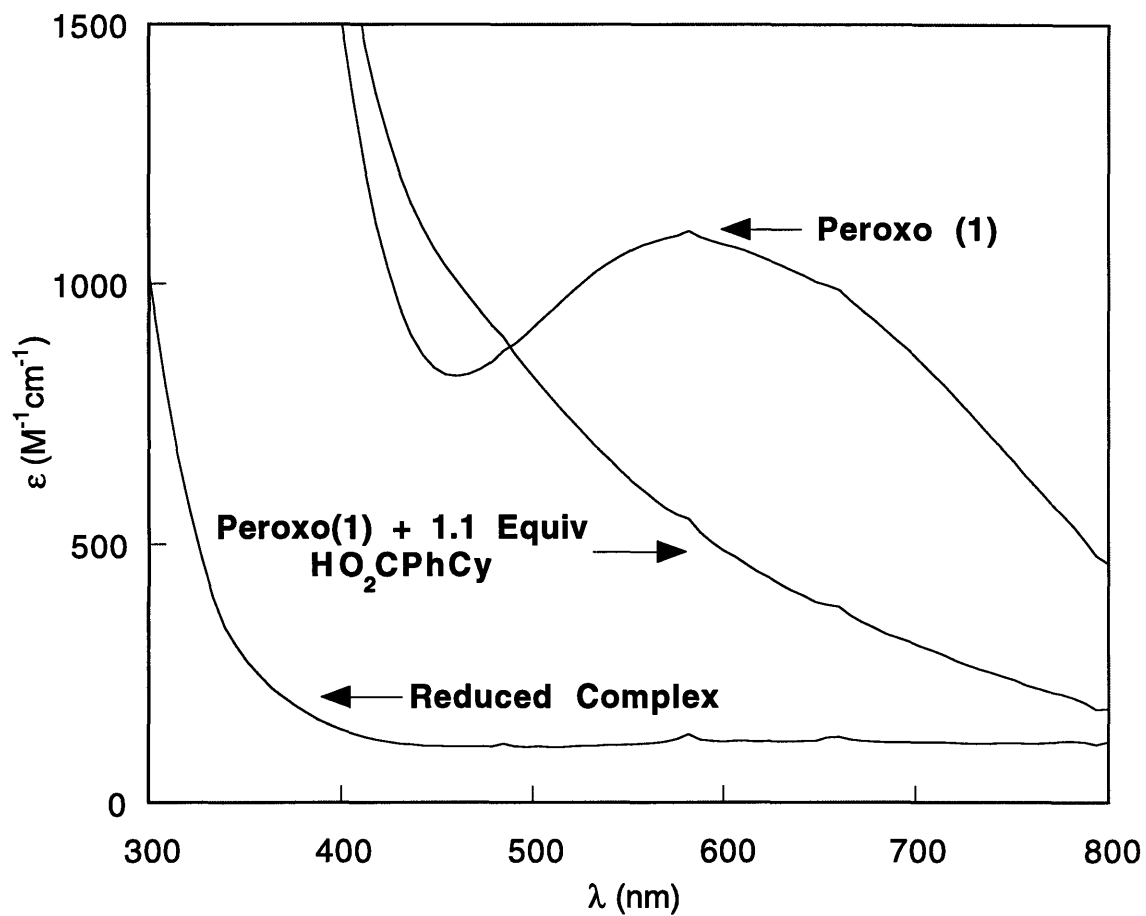


Figure 4.8. Electronic absorption spectrum of 1 in toluene at $-77\text{ }^\circ\text{C}$ (0.86 mM), and after 1.1 equiv of HO_2CPhCy was added. Decomposition to the room-temperature stable product occurred at $-77\text{ }^\circ\text{C}$.

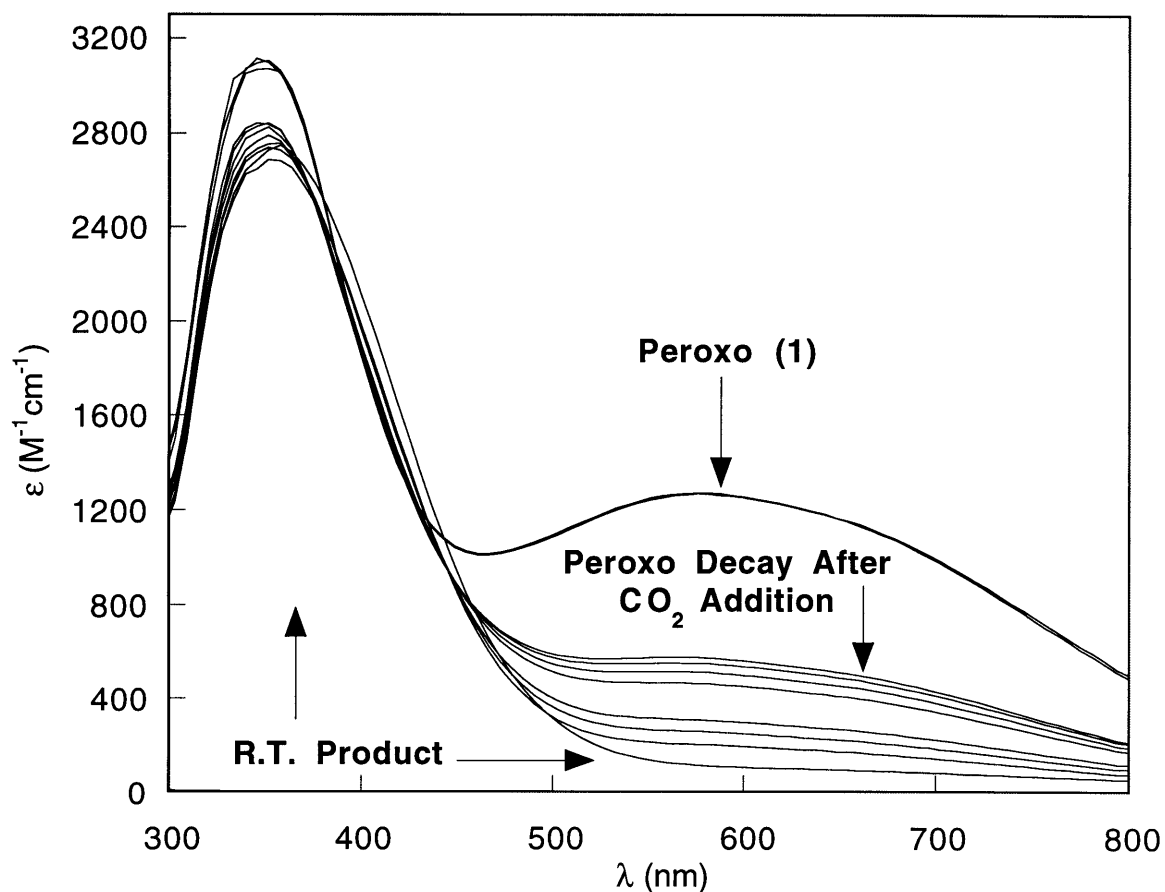


Figure 4.9. Electronic absorption spectrum of **1** in Et₂O at -77 °C (0.98 mM) and ten traces qualitatively tracking the decay of the peroxy upon addition of CO₂. Decomposition to the room-temperature stable product occurred at -77 °C.

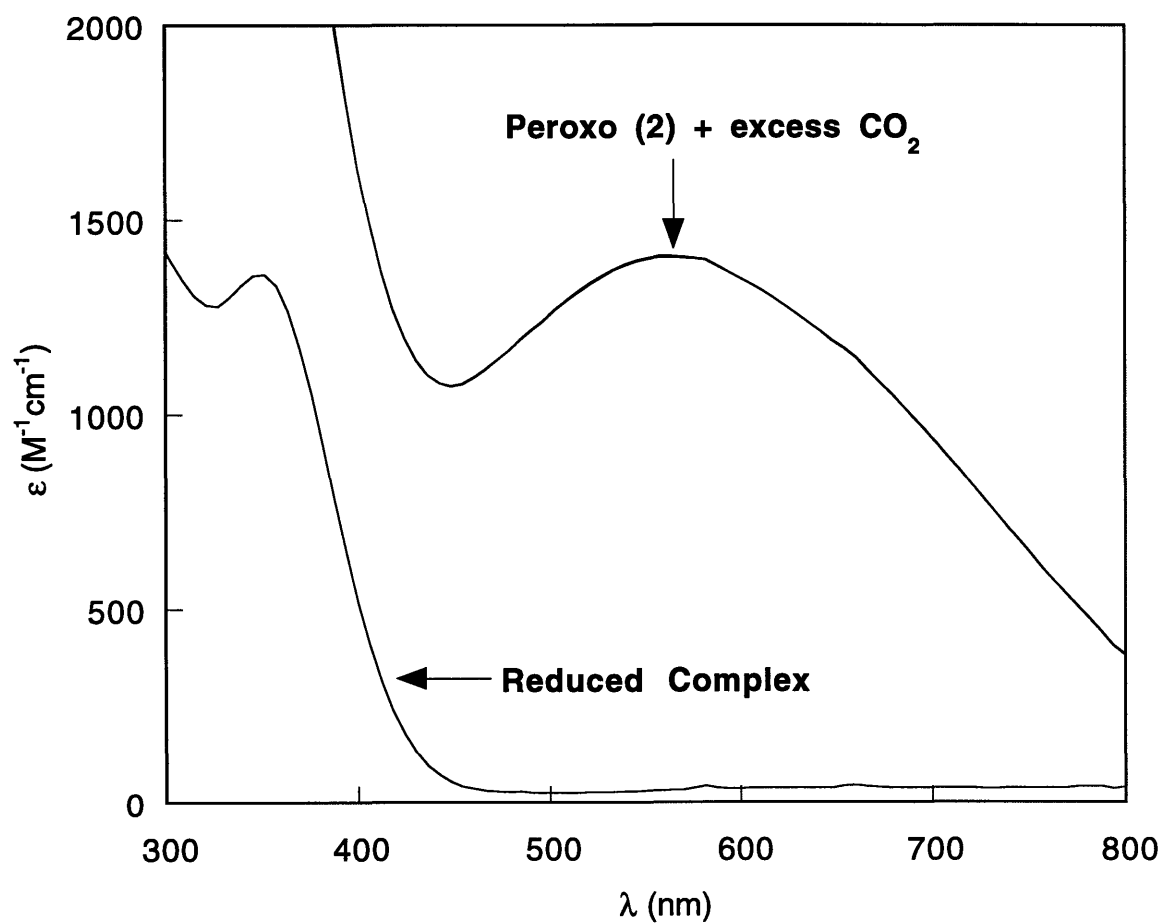


Figure 4.10. Electronic absorption spectrum of **2** in CH_2Cl_2 at -77°C (0.82 mM) in the presence of excess CO_2 .

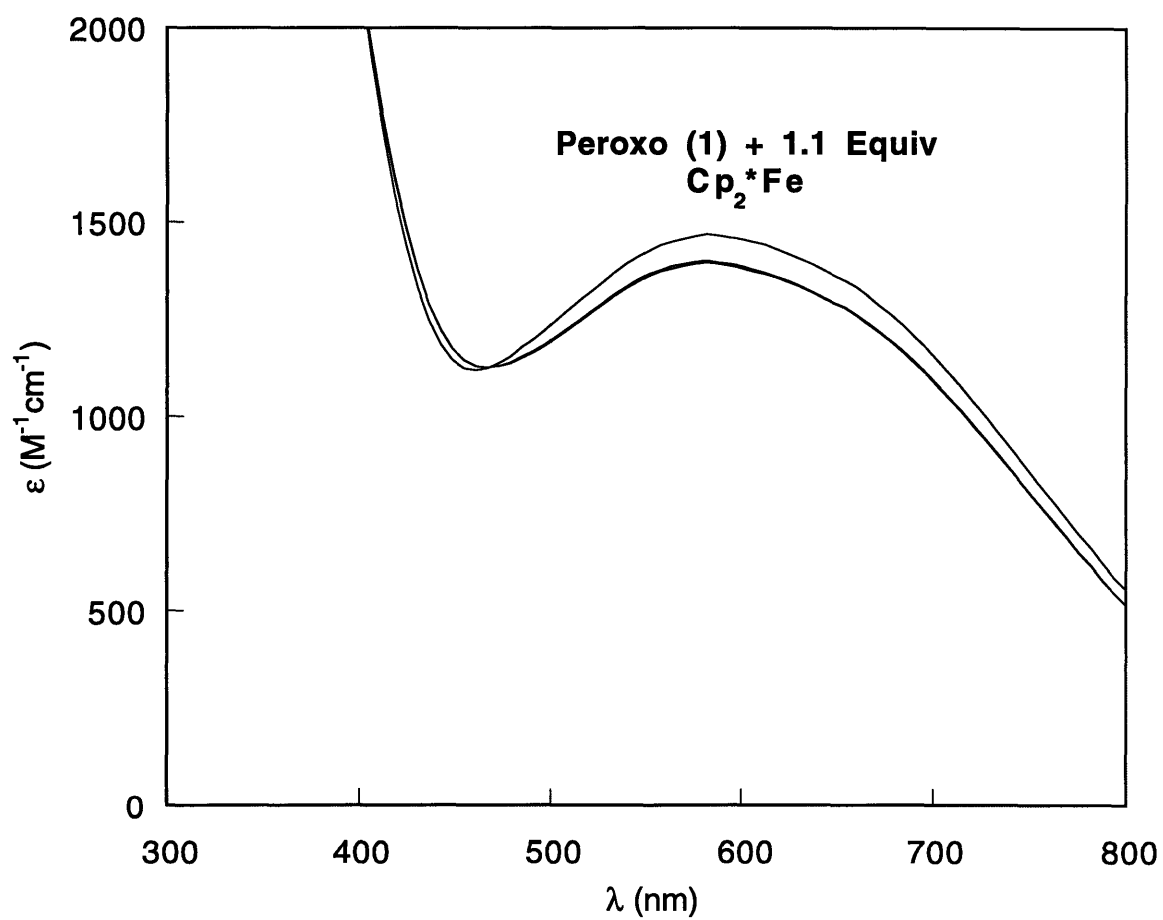


Figure 4.11. Electronic absorption spectrum of 1 in Et_2O at -77°C (0.79 mM), and in the presence of 1.1 equiv of Cp_2^*Fe .

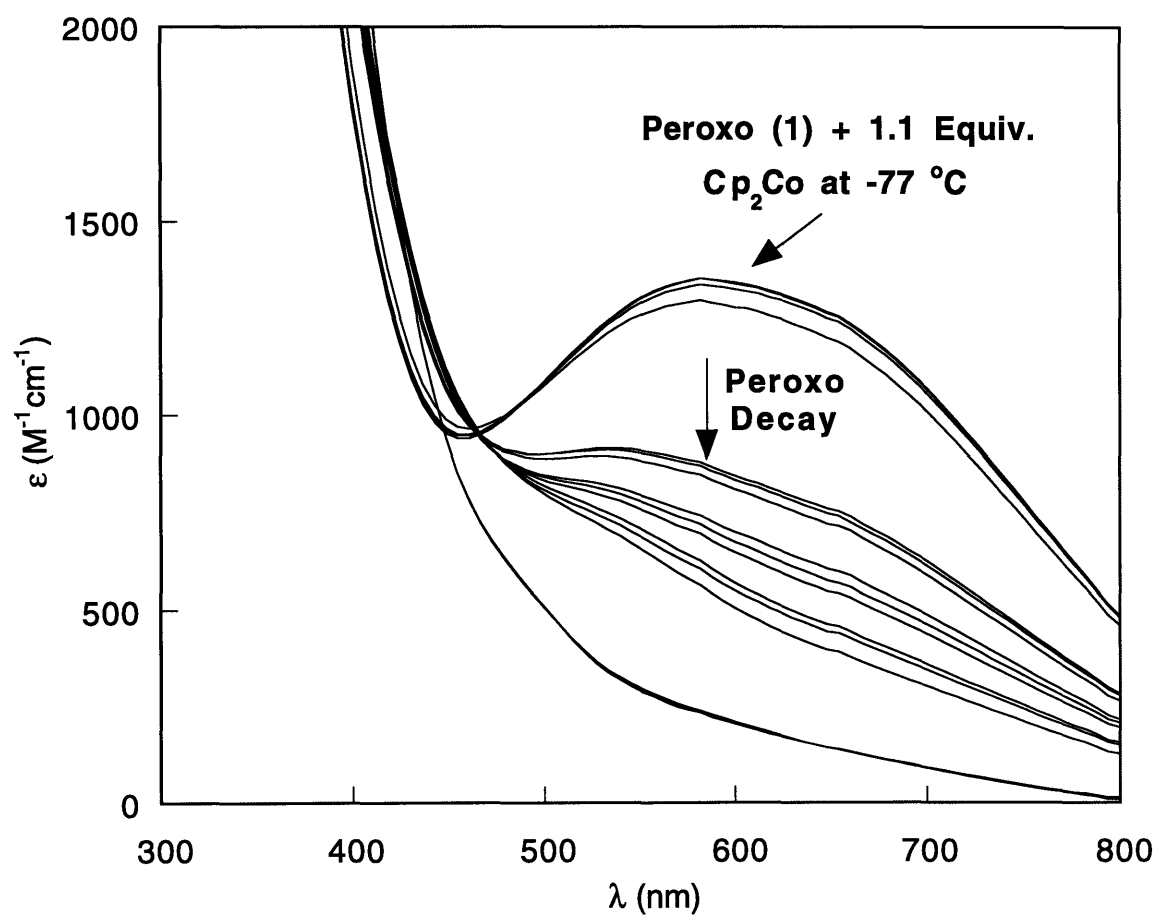


Figure 4.12. Electronic absorption spectrum of 1 in THF at -77 °C (0.79 mM), and after 1.1 equiv of Cp₂Co was added. Decomposition to the room-temperature stable product occurred at -77 °C and it was followed qualitatively.

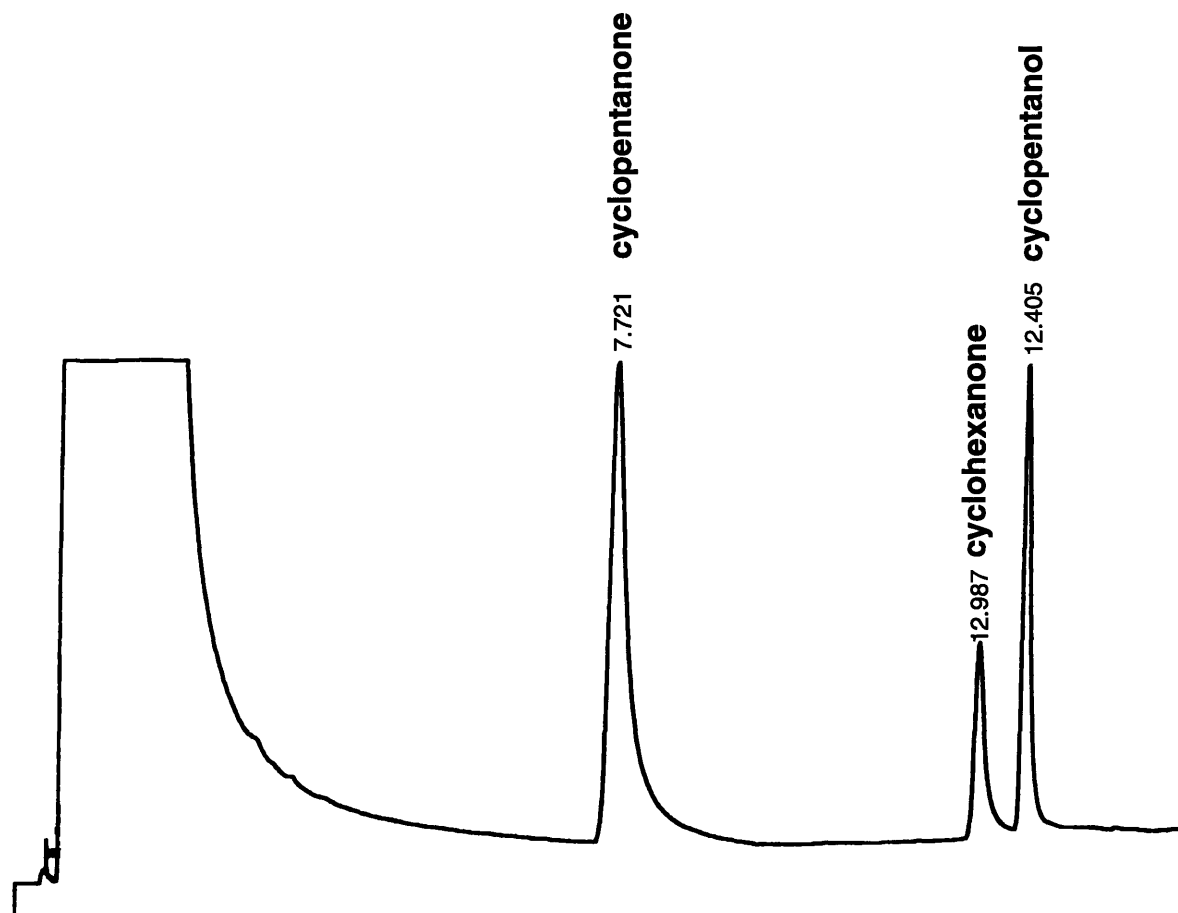


Figure 4.13. A representative GC chromatogram for cyclopentane oxidation reactions with peroxy 1. The sample used for this run was derived from a crude reaction mixture. The cyclohexanone is an internal standard.

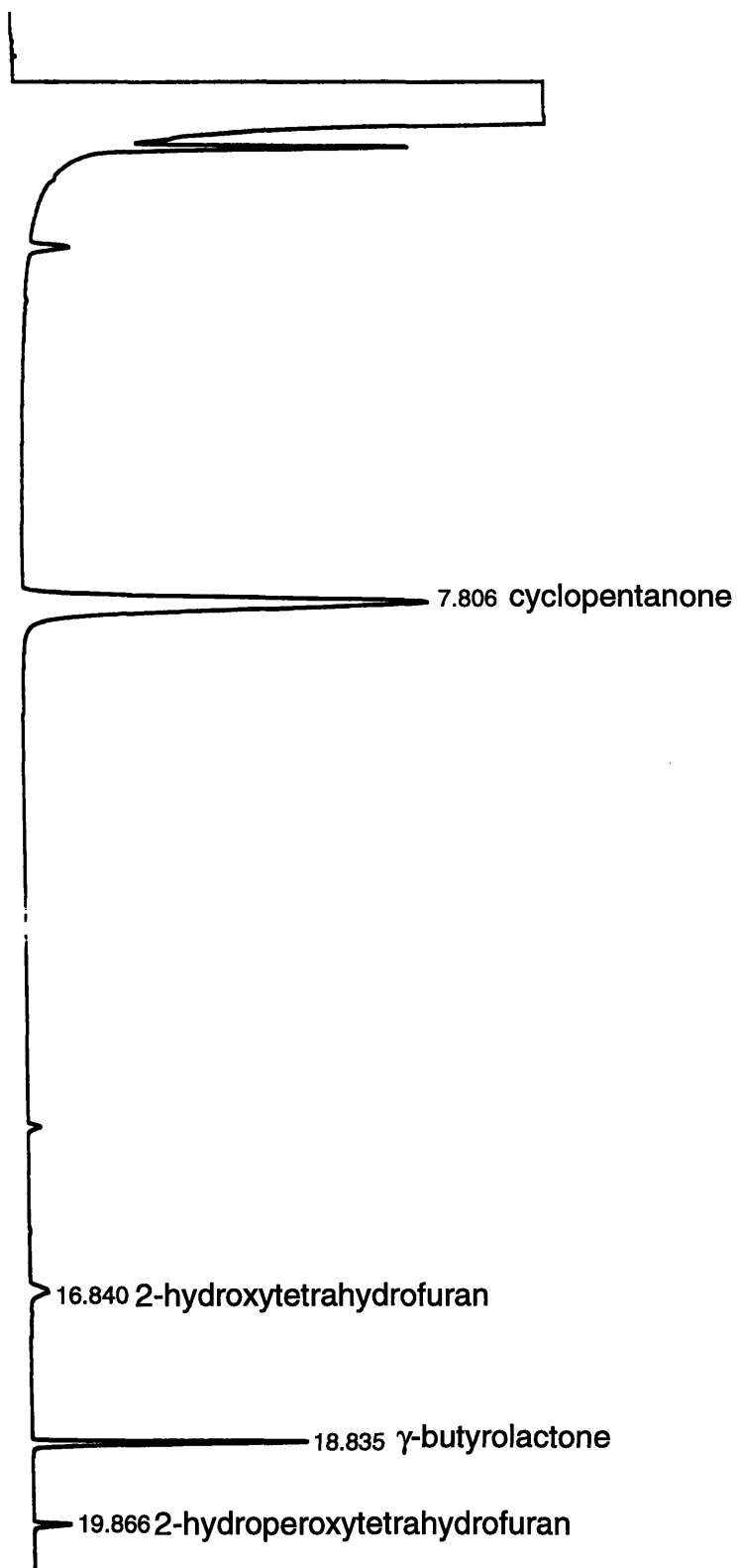


Figure 4.14. A representative GC chromatogram for THF oxidation reactions with peroxy **1**. The sample used for this run was derived from a crude reaction mixture. The cyclopentanone is an internal standard.

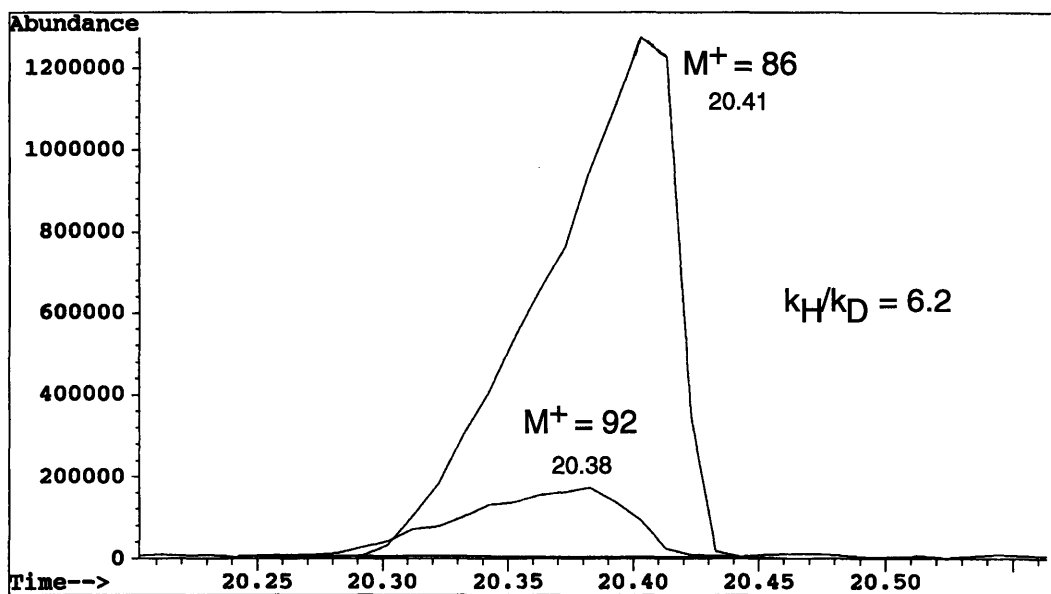


Figure 4.15. A GC-MS chromatogram for the parent ions of h⁶- and d⁶- γ -butyrolactone, a competitive deuterium isotope effect measurement for THF oxidation by peroxy **1**.

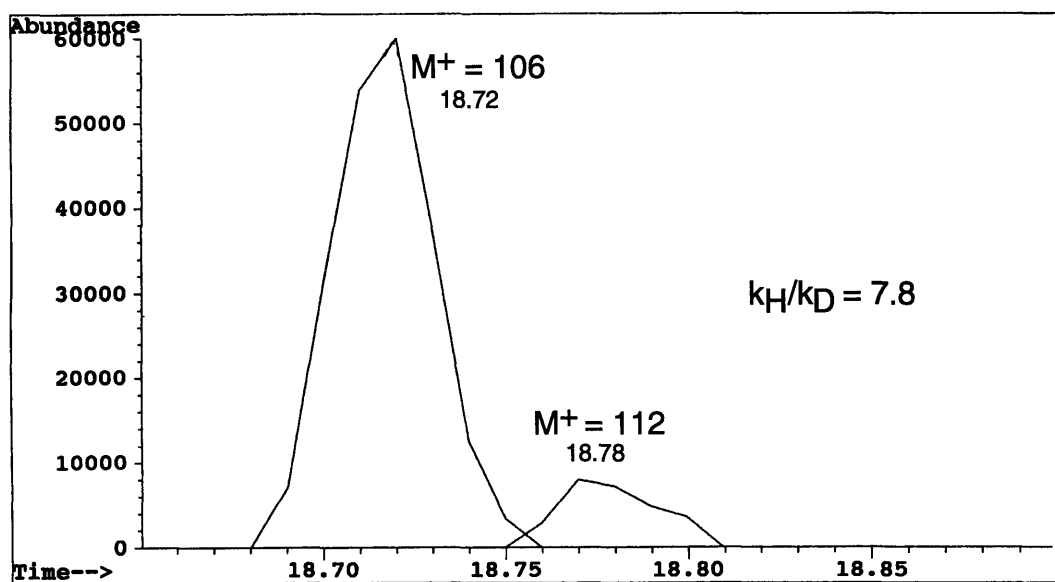


Figure 4.16. A GC-MS chromatogram for the parent ions of h^6 - and d^6 - benzaldehyde, a competitive deuterium isotope effect measurement for toluene oxidation by peroxy 1.

Biographical Note

The author was born in Madison, WI on April 6, 1970. After spending a short amount of time there and in Illinois, California, and Ohio, he resided in Racine, WI for the remainder of his primary and all of his secondary education, which culminated in graduation from J. I. Case High School in 1988. From there he went on to the University of Minnesota-Twin Cities, where Professor William B. Tolman provided him with such remarkable undergraduate research opportunities in chemistry that he decided to pursue his doctorate in this field instead of medicine. Following his graduate studies at MIT, the author plans to work as a postdoctoral fellow with Professor Erick M. Carreira at the California Institute of Technology.